Acta Pharmacologica Sinica (2011) 32: 1431–1432
 1671-4083/11 $32.00
www.nature.com/aps

Research Highlight

Cell adhesion, inflammation and therapy: Old ideas and a significant step forward

Roberto GONZÁLEZ-AMARO*

Acta Pharmacologica Sinica (2011) 32: 1431–1432; doi: 10.1038/aps.2011.154; published online 31 Oct 2011

Cell-to-cell adhesion as well as the interaction of cells with the extracellular matrix are key phenomena in different physiological and pathological conditions, including embryogenesis, blood coagulation, lymphocyte homing, immune response, angiogenesis, metastasis, thrombosis and inflammation[1, 2]. Thus, it has been widely proposed that cell adhesion molecules are an important therapeutic target in a wide array of diseases with high impact on public health, including atherosclerosis, thromboembolic disorders, cancer, graft rejection and autoimmune inflammatory conditions[1, 2]. However, anti-adhesion therapy with either biological agents (mainly blocking monoclonal antibodies, mAb's) or chemical inhibitors (mainly synthetic peptides) has not yet fulfilled these expectations and has not been devoid of undesirable effects[3, 4]. In this context, the research team of Gupta at the University of Miami, recently published an interesting article employing an alternative approach for the pharmacological inhibition of leukocyte extravasation, thus blocking the inflammatory phenomenon[5]. According to this report, novel pharmacological agents ("leukadherins") effectively inhibit the inflammatory phenomenon, with no apparent toxicity, which may constitute a major step ahead in this area.

The interaction between leukocytes and endothelial cells (EC), an essential step in the process of extravasation of these cells to an inflammatory focus, is mainly mediated by cell adhesion receptors that belong to the selectin, integrin and immunoglobulin superfamilies[1–3]. According to the sequential model of leukocyte extravasation (Figure 1)[6], activated endothelial cells favor their initial interaction with leukocytes (*tethering* or first step) through selectins (CD62L, CD62P and CD62E) and their ligands, a phenomenon that is followed by the *rolling* of leukocytes on endothelium (second step). Then, leukocytes slow

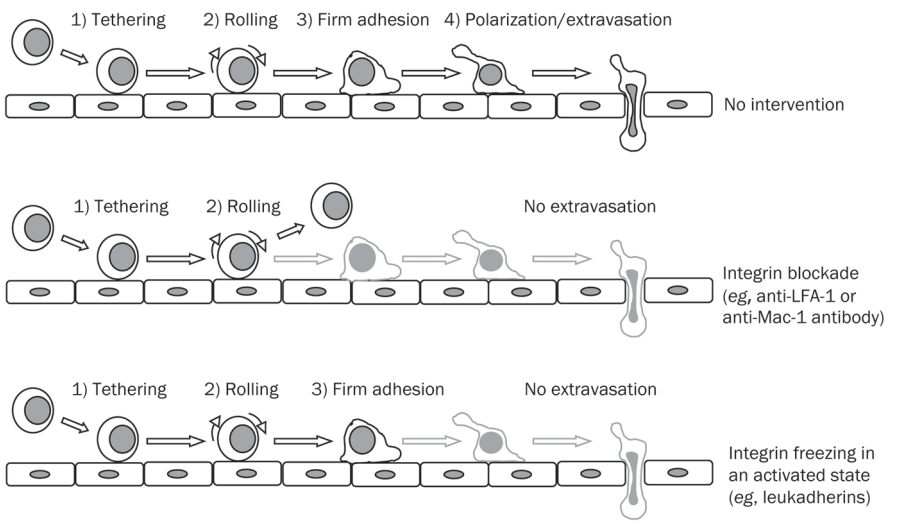

Figure 1. The migration of leukocytes towards an inflammatory focus is a sequential process that includes the tethering of leukocytes with endothelial cells (1st step), the rolling of leukocytes on endothelium (2nd step), the transient firm adhesion of leukocytes (3rd step), and their polarization and extravasation (4th step), reaching thus the inflamed tissue (upper panel). When LFA-1 or Mac-1 integrins are blocked with antibodies of synthetic peptides, the firm adhesion of leukocytes is inhibited and these cells return to the bloodstream (middle panel), but when these integrins are induced to activate, increasing their avidity for their endothelial ligands (ICAM-1, -2), leukocytes remain firmly adhered to endothelium, with no progression to the 4th step or extravasation (lower panel). As stated in the text, leukadherins exert the latter effect, and are able to inhibit the inflammatory phenomenon.

Department of Immunology, School of Medicine, Universidad Autónoma de San Luis Potosí, San Luis Potosí, México
*Correspondence: Prof Roberto González-Amaro (rgonzale@uaslp.mx)

their motion and transiently remain adhered to the EC (*firm adhesion*, third step), which is followed by their polarization and migration through the EC monolayer (*extravasation*, fourth step), mainly by a paracellular route (through the EC junctions). The firm adhesion of leukocytes to endothelium is mainly mediated by LFA-1 and Mac-1 integrins (also called CD11a/CD18 and CD11b/CD18), which during the rolling are able to activate, changing their conformation and significantly increasing their affinity for their different ligands expressed by EC cells (mainly ICAM-1 and -2). In addition, it has been shown that α4β1 and α4β7 integrins are also able to mediate both the initial and late steps of EC-leukocyte interaction[3, 6]. As expected, in order to extravasate leukocytes must exert a very dynamic regulation of their adhesiveness to endothelium mediated by integrins, allowing their detachment from the luminal side of EC cells. In this regard, Kuijpers *et al* demonstrated, more than 15 years ago, that the freezing of the α4β1 integrin in an activated state promotes the adhesion of eosinophils to endothelium but inhibits their extravasation[7].

In the work of the research team of Gupta[5], three synthetic compounds called leukadherins-1 to -3 were identified by their ability to increase the adhesion of K562 cells expressing Mac-1 to fibrinogen, a ligand of this integrin. By using different experimental approaches and by in silico analysis, these authors concluded that leukadherins bind to the A domain of Mac-1, inducing a high-affinity conformation of this integrin. Accordingly, leukadherins increased the adhesion of leukocytes mediated by Mac-1 but inhibited their migration and extravasation *in vivo*. Furthermore, leukadherins exerted a significant therapeutic effect in three different models of inflammatory disease (peritonitis, vascular neointimal thickening and glomerulonephritis), with no apparent toxicity on leukocytes or endothelium, nor evidence of side-effects. Interestingly, additional experiments showed that leukadherins were more effective than a blocking anti-Mac-1 mAb. Finally, by using a transgenic zebrafish model of neutrophil recruitment, these authors demonstrated that the effect of leukadherins was transient and reversed by their removal. It was concluded that leukadherins act as Mac-1 agonists, increasing the adhesion of leukocytes but blocking their transendothelial migration and inhibiting thus the inflammatory phenomenon.

As stated above, it has been widely proposed that the anti-adhesion therapy is a rational and effective approach for the treatment of inflammatory conditions[1–4]. As a result of intensive work over a long time, two anti-adhesion biological agents were approved and marketed in 2003–2004, natalizumab (a blocking mAb directed against the common chain of the α4β1 and α4β7 integrins) for the therapy of multiple sclerosis and Crohn's disease, and efalizumab (a blocking mAb directed against the chain of LFA-1) for the treatment of moderate-to-severe chronic plaque psoriasis. However, mainly due to the increased risk of progressive multifocal leukoencephalopathy (PML), natalizumab and efalizumab were withdrawn from the market (2005 and 2009). Natalizumab returned to the market (2006), but only for the therapy of the relapsing-remitting form of multiple sclerosis. With the exception of three inhibitors of the gpIIb/IIIa (CD41/CD61) platelet integrin (abxicimab, integrilin and tirofiban, used for the therapy of thromboembolic disorders), no other anti-integrin agents have reached the market, mainly due to their lack of effect. Thus, it seems very important to generate novel approaches for the therapy of inflammatory diseases based on modulation of cell adhesion receptors. In this regard, the work of Gupta *et al* is an interesting step ahead in this area. However, two important issues should be addressed during the long trip of leukadherins to the market: the possible consequences of their prolonged administration and the potential cytotoxic effect of leukocytes on EC, as a result of the sustained interaction of these cells induced by the leukadherins. In addition, the possibility of an enhanced risk of PML remains as an important matter. Nevertheless, the results of the work of Gupta *et al* strongly suggest that leukadherins do not promote EC damage and that are well tolerated. In addition, these results indicate that these agents could be more effective than the traditional blockade of integrins. In this regard, it seems evident that the effect of leukadherins could be mediated through the activation of only a fraction of Mac-1 molecules per cell, whereas the effect of blocking antibodies requires their binding to a large fraction of molecules of this integrin. Therefore, this work, relied on an old idea[7], seems to represent a significant step ahead in the therapy of inflammatory diseases based on the modulation of cell adhesion receptors.

1 Frenette PS, Wagner DD. Adhesion molecules — Part 1. N Engl J Med 1996; 334: 1526–9.
2 Frenette PS, Wagner DD. Adhesion molecules — Part II: Blood vessels and blood cells. N Engl J Med 1996; 335: 43–5.
3 Barreiro O, Martín P, González-Amaro R, Sánchez-Madrid F. Molecular cues guiding inflammatory responses. Cardiovasc Res 2010; 86: 174–82.
4 González-Amaro R, Mittelbrunn M, Sánchez-Madrid F. Therapeutic anti-integrin (alpha4 and alphaL) monoclonal antibodies: two-edged swords? Immunology 2005; 116: 289–96.
5 Maiguel D, Faridi MH, Wei C, Kuwano Y, Balla KM, Hernandez D, *et al*. Small molecule-mediated activation of the integrin CD11b/CD18 reduces inflammatory disease. Sci Signal 2011; 4: ra57.
6 Ley K, Laudanna C, Cybulsky MI, Nourshargh S. Getting to the site of inflammation: the leukocyte adhesion cascade updated. Nat Rev Immunol 2007; 7: 678–89.
7 Kuijpers TW, Mul EP, Blom M, Kovach NL, Gaeta FC, Tollefson V, *et al*. Freezing adhesion molecules in a state of high-avidity binding blocks eosinophil migration. J Exp Med 1993; 178: 279–84.

Acta Pharmacologica Sinica (2011) 32: 1433–1445
 1671-4083/11 $32.00
www.nature.com/aps

Review

Beneficial effects of mood stabilizers lithium, valproate and lamotrigine in experimental stroke models

Zhi-fei WANG, Emily Bame FESSLER, De-Maw CHUANG*

Molecular Neurobiology Section, National Institute of Mental Health, National Institutes of Health, Bethesda, MD 20892-1363, USA

The mood stabilizers lithium, valproate and lamotrigine are traditionally used to treat bipolar disorder. However, accumulating evidence suggests that these drugs have broad neuroprotective properties and may therefore be promising therapeutic agents for the treatment of neurodegenerative diseases, including stroke. Lithium, valproate and lamotrigine exert protective effects in diverse experimental stroke models by acting on their respective primary targets, ie, glycogen synthase kinase-3, histone deacetylases and voltage-gated sodium channels, respectively. This article reviews the most recent findings regarding the underlying mechanisms of these phenomena, which will pave the way for clinical investigations that use mood stabilizers to treat stroke. We also propose several future research avenues that may extend our understanding of the benefits of lithium, valproate and lamotrigine in improving stroke outcomes.

Keywords: lithium; valproate; lamotrigine; stroke; brain ischemia; glycogen synthase kinase-3; histone deacetylase; apoptosis; neurogenesis; angiogenesis

Acta Pharmacologica Sinica (2011) 32: 1433–1445; doi: 10.1038/aps.2011.140; published online 7 Nov 2011

Introduction

Stroke is a major cause of serious long-term disability in adults and the second leading cause of death worldwide. Approximately 85% of all strokes are ischemic[1]. To date, thrombolysis with intravenous recombinant tissue plasminogen activator (rtPA) is the only Food and Drug Administration (FDA)-approved treatment for acute ischemic stroke in the United States[2]. Thrombolysis improves patient outcome by facilitating reperfusion of ischemic brain tissue before irreversible damage occurs and must be administered within 4.5 h of symptom onset[3]. Given this narrow therapeutic window, as well as the associated risk of intracerebral hemorrhage[4], the estimated rate of rtPA use is quite low, only 1.8% to 2.1% of all ischemic stroke patients[5]. Thus, there is an urgent need to develop novel treatment options for stroke.

A promising therapeutic direction has emerged from an unexpected field: psychiatry. The mood stabilizing drugs lithium, valproate (VPA) and lamotrigine (see Figure 1 for chemical structures) are FDA-approved treatments for bipolar disorder (BD). This severe psychiatric illness affects 1%–3% of the world's population and is characterized by cyclic episodes of mania and depression. While the etiology of BD remains elusive, increasing evidence suggests that it is associated with neuroanatomical and neurophysiological anomalies, neurocognitive deficits, and dysregulated signaling pathways and gene expression[6]. Lithium, which has a well-established safety profile, has been used to treat BD for more than 60 years. It is an effective treatment for mania and is also used as prophylactic therapy to prevent the recurrent manic and depressive episodes that characterize BD. Anticonvulsants, notably VPA and lamotrigine, are more effective than lithium in treating rapid-cycling bipolar patients. While lamotrigine has more robust effects against bipolar depression, VPA, like lithium, has strong anti-manic effects but is less effective in treating depressive episodes. Although these mood stabilizers have long been the mainstay drugs for BD, their underlying

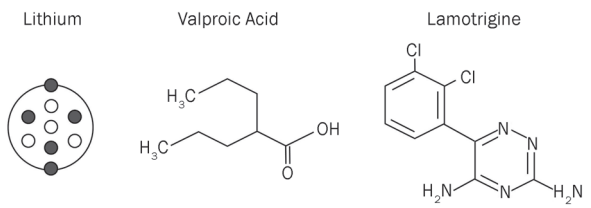

Figure 1. The chemical structures of lithium, VPA and lamotrigine.

* To whom correspondence should be addressed.
E-mail chuang@mail.nih.gov
Received 2011-06-22 Accepted 2011-09-22

therapeutic mechanisms remain largely unknown.

Brain imaging and postmortem investigations have demonstrated regional brain volume reductions, decreased cell number and density, and neuronal atrophy in patients with BD[7, 8]. Structural imaging studies have also shown that patients with BD have a particular pattern of brain abnormalities that includes widespread cortical thinning; morphological abnormalities in the amygdala, basal ganglia and thalamus; reduced gray matter volume in the prefrontal cortex, ventral striatum, and hippocampus; and enlarged lateral ventricles[9, 10]. Notably, chronic treatment with lithium was found to significantly increase brain gray matter volume in BD patients[11]. Another study found that VPA-treated patients had larger cingulate gyrus volumes, including both cortex and white matter, than unmedicated BD patients[12]. In light of these observations, the beneficial effects of mood stabilizing drugs are now recognized to involve neurotrophic and neuroprotective mechanisms with broad applications beyond the treatment of psychiatric illnesses. The extant evidence suggests that these mood stabilizing drugs activate neurotrophic and neuroprotective pathways, highlighting their therapeutic potential for the treatment of a variety of neurodegenerative diseases, including stroke[13–15].

In this article, we review the recent findings gleaned from experimental stroke models, with a focus on ischemic stroke, regarding the protective effects of lithium, VPA and lamotrigine. To date, there is a larger body of evidence from these models supporting the protective effects of lithium and VPA compared to lamotrigine. We will address the mechanisms and effects of each mood stabilizer as they are currently understood, and point to areas where further research may extend the potential therapeutic use of mood stabilizing drugs in stroke treatment.

The pathophysiology of ischemic stroke

Ischemic stroke is caused by reduced blood supply to an area of the brain, which initiates an ischemic cascade. Ischemic stroke accounts for 85% of all stroke cases[1]. The pathophysiology of ischemic stroke is complex and involves both early and late phase processes. In the acute phase after stroke, the reduced blood supply depletes oxygen and glucose within the brain and prevents adenosine triphosphate (ATP) production. In turn, ATP depletion impairs ATP-dependent ion pumps and alters Na^+ concentration gradients across neuronal membranes. As a result, glutamate transporters fail, causing excessive synaptic release and accumulation of glutamate. Through interaction with *N*-methyl-*D*-aspartate (NMDA) and alpha-amino-3-hydroxy-5-methyl-4-isoxanole propionate (AMPA) receptors, glutamate overstimulation leads to Ca^{2+} influx, which then drives the activation of damaging Ca^{2+}-mediated intracellular enzymes such as calpains and caspases. These ultimately result in mitochondrial failure, generation of reactive oxygen species, and cell necrosis and apoptosis[16, 17]. Furthermore, the osmotic gradient caused by the ion imbalance leads to an influx of water, which triggers cytotoxic and vasogenic edema[18].

Neuroinflammation has been increasingly implicated in injury progression following stroke. Post-ischemic inflammation is a dynamic process involving a complicated set of interactions between inflammatory cells and molecules[19]. Within hours after ischemic onset, circulating leukocytes adhere to vessel walls, infiltrate ischemic brain tissue, and amplify inflammatory signal cascades, which enhance tissue damage[20–22]. Microglia, the resident macrophages of the brain, are activated after stroke[23, 24]. Activated microglia release additional inflammatory mediators that increase the vulnerability of neurons, stimulate the expression of adhesion molecules, and mediate the adherence and infiltration of leukocytes[20]. Astrocytes are also activated and express cytokines, chemokines and inducible nitric oxide synthase (iNOS)[25]. These cytotoxic factors induce further cell damage, as well as disrupt the blood-brain barrier (BBB) to further exacerbate brain injury and cause brain edema[26].

The BBB is composed of capillary endothelial cells and pericytes, which are surrounded by basal lamina, astrocytic endfeet, and perivascular interneurons[27]. These endothelial cells are stitched together by tight junctions, which act as a highly selective and effective physical barrier to protect the CNS from pathogens and harmful molecules in the bloodstream. Tight junctions consist of transmembrane proteins, including claudins, occludins, and adhesion junction molecules, as well as cytoplasmic accessory proteins such as zonula occludens-1 (ZO-1)[27]. Impairment of tight junctions disrupts BBB integrity and increases its permeability. BBB disruption is a critical event in the pathogenesis of various neurological disorders, including stroke. Loss of BBB integrity following stroke allows the penetration of intravascular proteins and fluid into the cerebral parenchymal extracellular space, resulting in leukocyte infiltration, vasogenic edema and hemorrhage. Matrix metalloproteinases (MMPs) are a family of zinc-dependent endopeptidases that have multiphasic roles in ischemic stroke[28]. Within hours to days after cerebral ischemia, high levels of MMPs, especially MMP-2 and 9, degrade tight junctions and basal lamina proteins, disrupt cell-matrix homeostasis, and breach BBB integrity[28, 29]. In rodent models of ischemic stroke, both MMP-2 and 9 are linked with increased BBB permeability in the acute phase after ischemic stroke (within hours)[30, 31], whereas MMP-9 is responsible for the severe BBB disruption that occurs at 24 to 48 h after ischemia[32]. Similarly, BBB disruption at approximately 24 h after acute stroke onset in humans is associated with increased plasma MMP-9[33]. Elevated leukocytic MMP-9 is also closely tied to BBB disruption, as it promotes the degradation of the basal lamina in human brain tissue after stroke[34]. The functional significance of this enzyme has been demonstrated in mice, where genetic knockout of MMP-9 or suppression with an MMP inhibitor confers resistance to cerebral ischemia-induced BBB disruption by preventing degradation of the tight junction protein ZO-1[35, 36].

Neurovascular repair and regeneration take place in the chronic phase after stroke and determine the ultimate extent of the damage. The primary neurovascular responses during stroke recovery involve angiogenesis and neurogen-

esis. Angiogenesis is the process by which new capillaries are formed through directed proliferation and migration of endothelial progenitor cells from pre-existing blood vessels. Neurogenesis is the process of generating new neurons from neural stem and progenitor cells. Increasing evidence gleaned from human stroke patients and experimental stroke models suggests that endogenous angiogenesis and neurogenesis occur in the penumbra region days to weeks after stroke onset[37]. A close link between these two processes exists following stroke, as they share growth factors and signaling pathways for cell formation and migration, as well as common physical space as a result of parallel anatomic patterning and development[38]. Pharmacological therapies that enhance endogenous angiogenesis and neurogenesis following stroke have been shown to promote the recovery of neurological function in experimental stroke models[39–41]. Thus, enhancement of angiogenesis and neurogenesis may be a promising avenue for improving post-stroke clinical outcomes and functional recovery.

Genes participating in post-ischemic neurovascular regeneration have been extensively studied in experimental stroke models. Vascular endothelial growth factor (VEGF) and MMPs are two key factors involved in this neurovascular recovery process, and both have biphasic functions in the neurovascular response to stroke. VEGF and MMPs increase BBB permeability in the acute phase but accelerate angiogenesis and neurogenesis in the later phases[42]. In the delayed phase of ischemic recovery, VEGF can induce proliferation, inhibit apoptosis, and increase survival in both endothelial and neural cells[43–44], while MMPs can interact with extracellular matrix and growth factors or cytokine substrates to modulate neurovascular plasticity[28]. In addition, a feedback loop may exist between VEGF and MMPs, in which MMPs process pro-forms of matrix-bound VEGF into freely diffusible bioactive forms of VEGF[45]. This notion is based on findings from a mouse stroke model showing that MMP inhibition reduced endogenous VEGF signals, whereas exogenous VEGF prevented MMP inhibition-induced infarct exacerbation[46].

As we review below, accumulating evidence demonstrates that the mood stabilizers lithium, VPA and lamotrigine exert protective effects throughout the pathophysiological processes of stroke.

The effects of mood stabilizing drugs in experimental stroke models

Lithium

Therapeutic benefits

The neuroprotective effects of lithium against cerebral ischemia were first demonstrated by Nonaka and Chuang in a rat model of focal cerebral ischemia[47]. Chronic pretreatment with lithium significantly improved neurological deficit scores and reduced brain infarct volume in ischemic animals. In a gerbil global cerebral ischemic model, lithium pretreatment at 3 mEq/kg for seven days suppressed neuronal cell death in the hippocampal CA1 region and protected against hyperactivity and memory impairment[48]. In addition to pre-insult treatment, post-insult lithium administration at therapeutically relevant doses (ie, 0.5 or 1.0 mEq/kg, sc) has also been shown to reduce brain infarct volume and facilitate neurological (motor, sensory and reflex) recovery in a rat model of middle cerebral artery occlusion (MCAO)[49]. It is worth noting that because lithium offers beneficial effects when administered at least three hours after ischemic onset, it has great clinical potential for the treatment of acute stroke[49].

Primary target: glycogen synthase kinase-3

Pioneering studies demonstrated that lithium directly inhibits glycogen synthase kinase-3 (GSK-3)[50, 51]. This enzyme has been further established as a crucial target for lithium's cellular effects[13, 52]. GSK-3, consisting of α and β isoforms, is a serine/threonine kinase that regulates diverse cellular and neurophysiological processes. Lithium competes with magnesium to directly inhibit GSK-3 by binding to the active site of the enzyme and limiting its catalytic activity[53]. Lithium also indirectly inhibits GSK-3 activity by enhancing phosphorylation of GSK-3α at Ser21 and GSK-3β at Ser9 via activation of phosphatidylinositol 3-kinase (PI3-K)/Akt, protein kinase A and protein kinase C[13, 54]. In addition, lithium has been shown to increase the activities of two transcription factors, activator protein-1 (AP-1) and cyclic AMP-response element binding protein (CREB), both *in vivo* and *in vitro*[55]. Lithium also activates the mitogen-activated protein (MAP) kinase pathway[56].

Anti-excitotoxic effects

The beneficial effects of lithium in experimental cerebral ischemia may partially occur through the inhibition of excessive NMDA receptor-mediated Ca^{2+} influx into neurons[57]. Specifically, brain ischemia stimulates NMDA receptor subunit 2A (NR2A) and NR2B activation by increasing tyrosine phosphorylation[58]. Lithium has been shown to reduce the activation of NR2A and 2B by inhibiting tyrosine phosphorylation without affecting total protein levels[59, 60]. Furthermore, because long-term lithium treatment was required for robust neuroprotection, these findings suggest that the anti-excitotoxic effects of lithium also involve altered signaling pathways and gene expression. Supporting this notion, long-term pretreatment with lithium was found to enhance brain-derived neurotrophic factor (BDNF)/TrkB signaling, activate the PI3-K/Akt cascade, and suppress the activation of MAP kinases in cultured neurons under glutamate challenge[56, 61, 62]. Akt has been shown to induce phosphorylation and inactivation of BAD[63], a pro-apoptotic member of the B-cell lymphoma 2 (Bcl-2) family, and enhance the expression of Bcl-2[64], an antiapoptotic protein. Consistent with its protective effects, lithium treatment promoted Bcl-2 expression but reduced the expression of p53 and Bax in rat cerebellar granule cells under glutamate challenge, thus inhibiting caspase activation[65]. Lithium-mediated Akt activation after glutamate exposure also indirectly inhibited GSK-3 by increasing its serine phosphorylation level[61]. Therefore, modulation of Akt activity appears to play a key role in the neuroprotective effects of lithium against glutamate excitotoxicity.

Anti-apoptotic effects

Following stroke, Ca^{2+} influx leads to the release of pro-apoptotic proteins from the mitochondria to the cytoplasm, thereby inducing apoptosis[66]. Two enzymes activated after diverse apoptotic insults are c-Jun N-terminal kinase (JNK) and p38 MAP kinase[67]. These molecules can act synergistically to enhance the binding activity of AP-1, a dimeric transcription factor involved in the cellular response to stress factors and other signals[68]. Chronic lithium pretreatment attenuated glutamate-induced apoptosis in rat cerebellar granule cells in part by inhibiting the activation of JNK and p38, as well as the subsequent increase in AP-1 binding activity[56]. In a rat focal cerebral ischemia model, chronic pretreatment with lithium suppressed apoptosis in the ischemic penumbra by reducing caspase-3 immunoreactivity, DNA fragmentation, and expression of the AP-1 family member c-Jun[69]. These effects may be linked to lithium's ability to reverse glutamate-induced down-regulation of the anti-apoptotic protein Bcl-2 and overexpression of the pro-apoptotic proteins p53 and Bax[65].

Calpain is a nonlysosomal Ca^{2+}-dependent intracellular cysteine protease, and Ca^{2+} influx-induced calpain over-activation has been implicated in ischemic brain injury[70]. A recent study found that post-insult lithium treatment mitigated apoptosis and brain damage by preventing GSK-3β and ERK dephosphorylation, reducing the activation of calpain and caspase-3, and inhibiting mitochondrial release of apoptosis-inducing factor and cytochrome *c* in a neonatal hypoxic-ischemic rat model[71]. Heat-shock protein 70 (HSP70) is a well-known cytoprotective factor that inhibits apoptosis and is induced in the ischemic penumbra where neuronal recovery takes place. Post-insult treatment with lithium increased the DNA binding activity of heat-shock factor-1 (HSF-1) to the heat-shock element, superinducing HSP70 in neurons to inhibit brain ischemia-induced apoptosis[49]. Lithium's ability to inhibit GSK-3 is likely associated with HSF-1 activation and HSP70 induction[72]. These findings suggest that lithium-induced GSK-3 inhibition contributes to the anti-apoptotic effects of the drug.

Effects on autophagy

Autophagy is a key intracellular catabolic process that involves the bulk degradation of damaged cytoplasmic proteins or organelles[73]. Recently, autophagic activity was shown to be increased at lesion sites after cerebral ischemia[74]. Lithium decreased inositol 1,4,5-trisphosphate levels by inhibiting phosphoinositol phosphatases, a process recently identified as a novel mechanism for inducing autophagy[75]. In contrast, lithium was also shown to reduce autophagy during the late recovery stage after neonatal hypoxia-ischemia[71]. Autophagy may therefore have either deleterious or beneficial effects, depending on the specific cellular context and the stage of the pathological process[76]. Therefore, the role of autophagy in the neuroprotective effects of lithium remains to be elucidated.

Anti-inflammatory effects

The anti-inflammatory effects of lithium in stroke are not well-established. One recent study documented the anti-inflammatory effects of lithium in a neonatal rat hypoxic-ischemic model. Post-insult lithium treatment significantly reduced total tissue loss following hypoxia-ischemia. This beneficial effect of lithium was associated with a suppression of microglial activation and an attenuation in the levels of pro-inflammatory cytokines and chemokines, eg, IL-1β and chemokine ligand 2[77]. Using a model of lipopolysaccharide (LPS)-induced inflammation in cultured astrocytes, one study found that IL-6 production and its potentiation by interferon gamma (IFNγ) were significantly suppressed by treatment with lithium, GSK-3β siRNA, and four other GSK-3 inhibitors [78]. In addition, lithium pretreatment attenuated astrocyte activation and the increase of IL-6 levels in the cerebral cortex and cerebellum of mice treated with LPS[78]. These findings suggest that lithium may exert anti-inflammatory effects via GSK-3 inhibition, a possibility that warrants further study in the context of stroke.

Pro-angiogenic effects

Several lines of evidence support the pro-angiogenic effects of lithium in stroke models. A functional MRI (fMRI) study in rats demonstrated that delayed administration (12 h after ischemic onset) of a therapeutic dose of lithium (1 mEq/kg, sc) followed by daily injections for two weeks enhanced the mean blood oxygenation level dependence (BOLD) response and task-related functional change of cerebral blood volume (fCBV) in the ipsilateral somatosensory cortex[79]. This chronic lithium treatment also significantly increased the distribution and size of the microvasculature as well as the number of GFAP-positive astrocytes, and upregulated MMP-9 expression in both endothelial cells and astrocytes in the penumbra brain regions[79]. These findings suggest that lithium-induced vascular transformation may contribute to the improved outcomes noted with fMRI. In a follow-up *in vitro* study, lithium was shown to increase Ser9 phosphorylation of GSK-3β in a concentration-dependent manner and to promote the expression and secretion of VEGF, but not BDNF, in both endothelial cells and astrocytes[80]. In endothelial cells, VEGF upregulation by lithium was mimicked by SB216763, another GSK-3β inhibitor, whereas PI3-K inhibition by LY294002 suppressed the lithium-induced increase in GSK-3β phosphorylation and VEGF protein levels[80]. However, VEGF levels in astrocytes were not affected by inhibition of either GSK-3β or PI3-K[80]. These data suggest that lithium promotes VEGF expression through distinct pathways in brain endothelium and astrocytes. Although these initial *in vitro* findings require further confirmation, they suggest that growth factor signaling may contribute to lithium's ability to promote neurovascular remodeling during stroke recovery.

Pro-neurogenic effects

As noted above, evidence suggests that neurogenesis contributes to the therapeutic actions of mood stabilizers. In hippocampal neural progenitor/precursor cell cultures, lithium increased proliferation, decreased apoptosis, and selectively

enhanced the neuronal differentiation of these cells[81, 82]. Lithium treatment enhanced ERK and CREB phosphorylation in cultured hippocampal neural progenitor cells; PD98059, a MEK inhibitor, significantly decreased lithium-induced neuronal subtype differentiation[82]. In animal studies, chronic lithium administration enhanced neurogenesis in the dentate gyrus of adult mice by increasing cell proliferation and neuronal differentiation[83]. In a neonatal rat hypoxic-ischemic model, lithium treatment increased both proliferation and survival of neural stem and progenitor cells[77]. The pro-neurogenic effects of lithium have also been demonstrated in a transient global ischemic model, where they contribute to long-term beneficial effects. In this transient four-vessel occlusion model, lithium treatment increased the generation and survival of newborn cells in the hippocampal dentate gyrus and improved spatial learning and memory deficits of ischemic rats[84]. ERK1/2 phosphorylation following ischemia was enhanced by lithium treatment, whereas the ERK1/2 inhibitor U0126 abolished the effects of lithium on increased newborn cell generation and survival as well as behavioral improvement[84]. Research suggests that brain ischemia-induced neurogenesis involves the activation of receptor tyrosine kinases by inducing growth factors (eg, nerve growth factor, BDNF and VEGF) and subsequent stimulation of the downstream PI3-K/AKT and ERK pathways[85]. Taken together, these *in vitro* and *in vivo* findings suggest that lithium promotes post-ischemic hippocampal neurogenesis through ERK1/2-dependent cell signaling pathways and that this process plays an important role in the behavioral improvement seen following lithium treatment in ischemia.

Alternate findings

It is worth noting that a few early studies failed to observe a therapeutic benefit of lithium treatment in cerebral ischemia. For example, one report showed that lithium pretreatment at 5 mEq/kg up to two days prior to ischemia did not prevent the decrease in neuronal density in the hippocampal CA1 region of gerbils subjected to global cerebral ischemia[86]. The discrepancy could be related to the specific lithium treatment conditions and highlights the importance of optimizing dose and timing to maximize the protective effects of lithium and other drugs in stroke therapy.

VPA

Therapeutic benefits

Pioneering work from our laboratory demonstrated that post-insult treatment with VPA (300 mg/kg) reduced brain infarct size and improved functional outcome in both transient and permanent focal cerebral ischemic rat models[87, 88], with a beneficial time window of at least three hours after ischemic onset[88]. Research from another lab confirmed that pretreatment with VPA prior to ischemia attenuated ischemic brain damage and the neurologic deficit in both transient and permanent focal cerebral ischemic mouse models, whereas treatment with VPA immediately after reperfusion reduced the infarct area only in the transient model[89]. Multiple mechanisms are involved in the protective action of VPA against cerebral ischemic injury.

Primary target: histone deacetylases

Studies conducted a decade ago identified histone deacetylases (HDACs) as direct targets of VPA, which is a fatty acid derivative[90, 91]. In humans, HDACs can be divided into four major classes[14]. At clinically relevant levels, VPA binds directly to HDAC active sites to inhibit class I (HDAC1, 2, 3, and 8 isoforms) and class IIa (HDAC4, 5, 7, and 9 isoforms) HDACs, but not class IIb (HDAC6 and 10 isoforms)[90, 91]. This results in histone hyperacetylation and a more relaxed chromatin conformation. Enhanced access to specific gene promoters facilitates transcription factor binding and regulates the expression of numerous genes, notably neurotrophic and neuroprotective factors such as BDNF and Bcl-2[14].

Anti-excitotoxic effects

VPA can block glutamate-induced excitotoxicity in cultured neurons. By inhibiting HDACs, VPA upregulates α-synuclein, which suppresses glutamate neurotoxicity in rat cerebellar granule cells[92]. In addition, VPA has been shown to protect mature cerebellar granule cells from NMDA receptor-mediated excitotoxicity induced by SYM 2081, an inhibitor of excitatory amino acid transporters and an agonist of low-affinity kainate receptors[93]. Another study noted that treatment with lithium or VPA inhibited glutamate-induced excitotoxicity by inhibiting oxidative stress in rat cerebral cortical neurons, as shown by reduced lipid peroxidation and protein oxidation[94]. In addition, co-treatment with lithium and VPA completely blocked glutamate excitotoxicity in aging cerebellar granular cells, whereas treatment with lithium or VPA alone had no such neuroprotective effect[95]. Enhanced GSK-3 inhibition through serine phosphorylation is most likely a molecular target for this synergy[95].

Anti-apoptotic effects

Anti-apoptotic signaling is also involved in VPA's neuroprotective effects against both ischemic and hemorrhagic stroke. In transient and permanent focal cerebral ischemic rat models, post-insult VPA treatment restored the loss of histone acetylation, superinduced HSP70, and suppressed phosphorylated Akt downregulation, caspase-3 activation and p53 overexpression following injury[87, 88]. Similarly, two distinct HDAC inhibitors, sodium butyrate (SB) and hydroxamic acid trichostatin A (TSA) were found to have anti-apoptotic effects in a permanent cerebral ischemic model[88]. The neuroprotective time window for reducing infarct volume and improving neurological performance was approximately three to six hours after ischemic onset for VPA and SB. VPA also exerted anti-apoptotic actions in a rat intracerebral hemorrhagic model of stroke. Here, VPA upregulated Bcl-2/Bcl-xl, downregulated Bax, inhibited caspase activity, and reduced the number of apoptotic TUNEL-positive cells[96]. In this study, VPA also enhanced protein levels of HSP70, phosphorylation of ERK, Akt and CREB, as well as acetylation of histone-H3. Together,

these data suggest that HDAC inhibition is involved in VPA's anti-apoptotic effects.

Anti-inflammatory effects

VPA was first shown to display robust anti-inflammatory effects in midbrain neuron-glia co-cultures stimulated with LPS, as evidenced by the suppression of LPS-induced TNF-α secretion and nitric oxide production[97, 98]. In a rat permanent ischemic model of stroke, post-insult treatment with 300 mg/kg (ip) of VPA or SB strongly suppressed ischemia-induced microglial activation, reduced the number of infiltrating monocytes/macrophages, and inhibited overexpression of the proinflammatory enzymes iNOS and cyclooxygenase-2 (COX-2)[88]. In addition, HDAC inhibitors were found to superinduce HSP70, preserve levels of phosphorylated Akt, and inhibit ischemia-induced overexpression of p53 in the ischemic brain[87, 88, 99]. VPA-induced HSP70 is triggered by acetylation and recruitment of the transcription factor Sp1 to the HSP70 promoter via inhibition of Class I HDACs[100]. Recent work demonstrated that histone 3 lysine 4 methylation levels at the HSP70 promoter were enhanced by VPA-induced HDAC inhibition in both neurons and astrocytes[101]. A study in a mouse MCAO model found that HSP70 overexpression inactivated the key inflammatory transcription factor nuclear factor-κB (NF-κB) by stabilizing the NF-κB-IκB complex, thus preventing nuclear translocation of activated NF-κB subunits[102]. Furthermore, VPA and SB significantly inhibited MCAO-induced NF-κB activation in a transient MCAO rat model[103]. Hence, it is likely that superinduction of endogenous HSP70 by HDAC inhibition contributes to the anti-inflammatory effects of VPA via NF-κB inhibition.

VPA also exerted anti-inflammatory effects in an intracerebral hemorrhagic model of stroke[96]. Post-insult VPA treatment alleviated cerebral inflammation by inhibiting neutrophil infiltration, suppressing microglial activation, and downregulating mRNA levels of pro-inflammatory cytokines such as Fas ligand and IL-6[96]. VPA treatment markedly upregulated acetylated histone H3 levels in both cerebral ischemic and hemorrhagic models[88, 96, 103]. These findings strongly support the anti-inflammatory effects of HDAC inhibition.

Blood-brain barrier protection

A recent study from our laboratory reported that post-insult treatment with VPA (200 and 300 mg/kg, ip) attenuated BBB disruption and brain edema in a rat model of transient focal cerebral ischemia[103]. VPA-induced BBB protection was dose-dependent and persisted for at least three days after cerebral ischemia and reperfusion. Notably, VPA administered at the beginning of reperfusion following a 60-min MCAO also significantly protected BBB integrity, although this effect was not as robust as that seen when VPA was given immediately after occlusion[103]. By restoring histone acetylation, VPA strongly inhibited cerebral ischemia-induced nuclear translocation of NF-κB, upregulation of MMP-9, degradation of tight junctions, and brain edema[103]. Moreover, the HDAC inhibitor SB was similarly found to have protective effects against BBB disruption, NF-κB activation, and MMP-9 upregulation[103]. It thus appears that in ischemic animal models, the BBB protection by VPA likely involves the initial inhibition of HDACs followed by suppression of NF-κB activation and MMP-9 overexpression, resulting in overall beneficial effects.

Pro-angiogenic effects

Recent work from our laboratory found that chronic post-ischemic VPA treatment enhanced post-ischemic angiogenesis, reduced brain infarction, and improved rotarod performance in an experimental ischemic stroke model (unpublished results). Chronic VPA treatment increased microvascular endothelial cell proliferation and enhanced the relative cerebral blood flow in the penumbra cortex, as detected by perfusion-weighted MRI. The pro-angiogenic effects of VPA may be attributable to HDAC inhibition-triggered upregulation of VEGF and MMP-9. Together, these findings lend further support to the notion that mood stabilizers promote post-ischemic angiogenesis in experimental stroke models, and suggest that these pro-angiogenic effects may contribute to their beneficial effects on long-term functional recovery after stroke.

Pro-neurogenic effects

VPA was found to promote cortical neurogenesis in primary cultures and to enhance hippocampal neurogenesis in adult mice by activating the ERK1/2 pathway[104]. The initial mechanism by which VPA activates the ERK pathway is unlikely to be mediated solely by HDAC inhibition, as its effects are not fully mimicked by TSA, another HDAC inhibitor[104]. However, it has been shown that treatment with the HDAC inhibitors VPA, SB or TSA largely promoted neuronal differentiation in cultured hippocampal neural progenitor cells[105]. Therefore, the ERK pathway is not exclusively responsible for the neuronal differentiation observed in neural progenitor cells.

Chronic treatment with the HDAC inhibitors SB (300 mg/kg, sc) and TSA (0.2 mg/kg, sc) was also found to significantly enhance post-ischemic cell proliferation and neurogenesis in a rat model of permanent cerebral ischemia. This occurred not only in the SVZ and SGZ but also in the ischemic cortex and striatum[106]. SB treatment upregulated levels of BDNF, phospho-CREB and GFAP in multiple brain regions after ischemia [106]. In addition, intracerebral injection of K252a, a TrkB tyrosine kinase inhibitor, blocked SB-induced cell proliferation, neuronal differentiation and CREB activation in multiple brain regions, in addition to blocking the overall behavioral benefits of this agent[106]. These findings suggest that HDAC inhibitor-induced cell proliferation, neuronal differentiation and migration require BDNF-TrkB signaling, which may contribute to the long-term beneficial effects on behavioral performance observed after ischemic injury. Notably, lithium, through GSK-3 inhibition, and VPA, by HDAC inhibition, have both been shown to selectively activate BDNF promoter IV activity in rat cortical neurons[107].

Effects on stem cell migration

For the past decade, stem cell therapy has been investigated

as a potential treatment for stroke. Mesenchymal stem cells (MSCs) derived from bone marrow have been employed in experimental stroke models and shown to improve the functional recovery of neurological deficits induced by cerebral ischemia[108]. However, it is increasingly recognized that the poor homing and migratory abilities of transplanted MSCs limit the effectiveness of this treatment strategy. Our recent *in vitro* findings demonstrated that treatment with lithium or VPA enhanced MSC migration by elevating MMP-9 levels through GSK-3β inhibition or by increasing CXC chemokine receptor 4 (CXCR4) via HDAC inhibition, respectively[109]. Furthermore, combined treatment with lithium and VPA was found to have additive effects on MSC migration[109]. In a follow-up *in vivo* study, MSCs were primed with lithium and/or VPA and then transplanted into transient focal cerebral ischemic rats at 24 h after ischemic onset[110]. Lithium or VPA priming significantly increased the number of MSCs homing to brain infarct regions two weeks after transplantation. Ischemic rats receiving lithium- and/or VPA-primed MSCs showed improved functional recovery, reduced infarct volume, and enhanced angiogenesis in the penumbra regions. Notably, MSCs co-primed with lithium and VPA showed remarkable improvement in homing ability and contributed robustly to functional recovery after transplantation into ischemic rats. These beneficial effects of lithium and VPA priming were reversed by pharmacological inhibition of MMP-9 and CXCR4, respectively, suggesting that the underlying mechanisms likely involved lithium-induced MMP-9 upregulation and VPA-induced CXCR4 overexpression. Together, these findings suggest the potential utility of priming MSCs with GSK-3 and HDAC inhibitors to enhance the migration and homing capacity after transplantation into stroke victims.

Lamotrigine

Therapeutic benefits

Lamotrigine has been demonstrated to exert neuroprotective actions in focal and global cerebral ischemic models. In a permanent MCAO rat model, post-insult treatment with this drug attenuated the neurological deficit and reduced the infarct volume at 24 h after MCAO at a narrow dose range between 8 and 20 mg/kg[111]. Lamotrigine at 20 mg/kg still showed protective effects when given one hour after MCAO. Lamotrigine also provided significant histological and behavioral protection in a gerbil global ischemic model[112, 113]. Lamotrigine treatment completely preserved hippocampal CA3 cell loss and greatly attenuated damage to CA1 and CA3 cells. These effects contributed to its behavioral benefits against ischemia-induced cognitive deficits[113]. Cerebral vasospasm occurs a few days after subarachnoid hemorrhage and results in ischemic neurologic deficits. It has also been shown that oral administration of lamotrigine had marked neuroprotective effects and significantly attenuated cerebral vasospasm after experimental subarachnoid hemorrhage in rabbits[114].

Primary target: voltage-gated sodium channels

Lamotrigine blocks voltage-gated sodium channels (VGSCs), which are key mediators of intrinsic neuronal and muscle excitability. A growing body of evidence implicates abnormal VGSC activity as central to the pathophysiology of epileptic seizures as well as the pathophysiology of diverse neurological disorders, including stroke[15]. Ischemia-induced energy depletion leads to decreased Na^+/K^+-ATPase pump activity, membrane depolarization, persistent inward Na^+ currents, and abnormal intracellular accumulation of Na^+. An overload of Na^+ drives the Na^+/Ca^{2+} exchanger to import Ca^{2+}, triggers glutamate release, and causes further neuronal damage[15]. Hence, VGSC blockers such as lamotrigine might be effective in preventing neuronal injuries caused by decreased oxygen supply. Lamotrigine has been shown to mitigate neuronal excitability by blocking VGSCs, inhibiting presynaptic release of glutamate, and affecting downstream intracellular signaling pathways[115, 116].

Anti-excitotoxic effects

Na^+ influx following cerebral ischemia partially contributes to excessive glutamate release. As a VGSC blocker, lamotrigine may act at these channels to stabilize neuronal membranes, inhibit glutamate transmitter release, and protect the brain from excitotoxic injury[115]. Lamotrigine effectively inhibited extracellular glutamate accumulation after transient global cerebral ischemia in rabbits[117]. In addition, selective neuronal damage in the hippocampal CA1 region of gerbils occurred two to three days after transient cerebral ischemia[118]. Lamotrigine treatment attenuated this injury by preventing the ischemia-induced increase in post-synaptic intrinsic excitability of CA1 pyramidal neurons, thus mitigating glutamate excitotoxicity and cell loss[119]. In addition, a microdialysis study found a significant reduction in the ischemia-induced glutamate surge in lamotrigine-treated ischemic animals[112]. In a rat model of neonatal hypoxic-ischemic encephalopathy, lamotrigine also reduced the hippocampal tissue levels of glutamate and aspartate, but did not affect GABA or glutamine levels[120]. Taken together, these findings support the notion that the neuroprotective effects of lamotrigine against ischemic injury are at least partially mediated by a reduction in excitatory amino acids.

Anti-apoptotic effects

The anti-apoptotic effects of lamotrigine in stroke treatment were reported in a rat model of neonatal hypoxia-ischemia. In this study, lamotrigine protected neurons from necrosis and apoptosis, as indicated by significantly fewer TUNEL-positive cells in the cortex and dentate gyrus of the ischemic hemisphere following lamotrigine administration[121]. In human neuroblastoma cells, chronic treatment with lamotrigine, like lithium and VPA, protected against GSK-3β-facilitated apoptosis, as measured by reduced caspase-3 activity[122]. Therefore, it appears that the GSK-3β signaling system might be involved in the protective effects of multiple mood stabilizers. Furthermore, chronic lamotrigine administration increased Bcl-2 mRNA and protein levels in the frontal cortex of rats, suggesting that upregulation of this anti-apoptotic factor may

contribute to its protective effects[123].

Effects on neurogenesis

After seven consecutive daily injections in 21-day postnatal rats, lamotrigine, but not VPA, increased the number of BrdU-labeled cells in the granule cell layer of the dentate gyrus, suggesting increased neurogenesis[124]. In cultured adult dentate gyrus-derived neural precursor cells, lithium, VPA and lamotrigine decreased staurosporine-induced apoptosis[81]. VPA also reversed the decrease in proliferation induced by dexamethasone, while lamotrigine had no such effect. However, unlike lithium, VPA and lamotrigine elevated the ratio of astroglial differentiation to neuronal differentiation under retinoic acid stimulation[81]. The reason(s) for the different mechanisms of action of these three mood stabilizers requires further investigation.

Conclusions and future directions

In this review, we have discussed recent preclinical advances in understanding the neuroprotective effects of the mood stabilizers lithium, VPA and lamotrigine in experimental stroke models. Accumulating evidence strongly supports the notion that these mood stabilizers exert multiple effects aimed at diverse aspects of stroke pathophysiology, leading to significant protection following insult.

GSK-3 and HDACs are the primary targets of lithium and VPA, respectively, and initiate transcriptional activation of abundant downstream molecules in the ischemic brain, including neuroprotective and neurotrophic gene products, as illustrated in Figure 2. In line with this notion, several other pharmacological GSK-3 inhibitors[125–128] and HDAC inhibitors[14] have been shown to exert beneficial effects against cerebral ischemia. Bcl-2 is transcriptionally activated by lithium through direct or indirect inhibition of GSK-3, while VPA induces Bcl-2 by direct HDAC inhibition. HSP70 expression can be enhanced by lithium-induced HSF-1 and VPA-induced

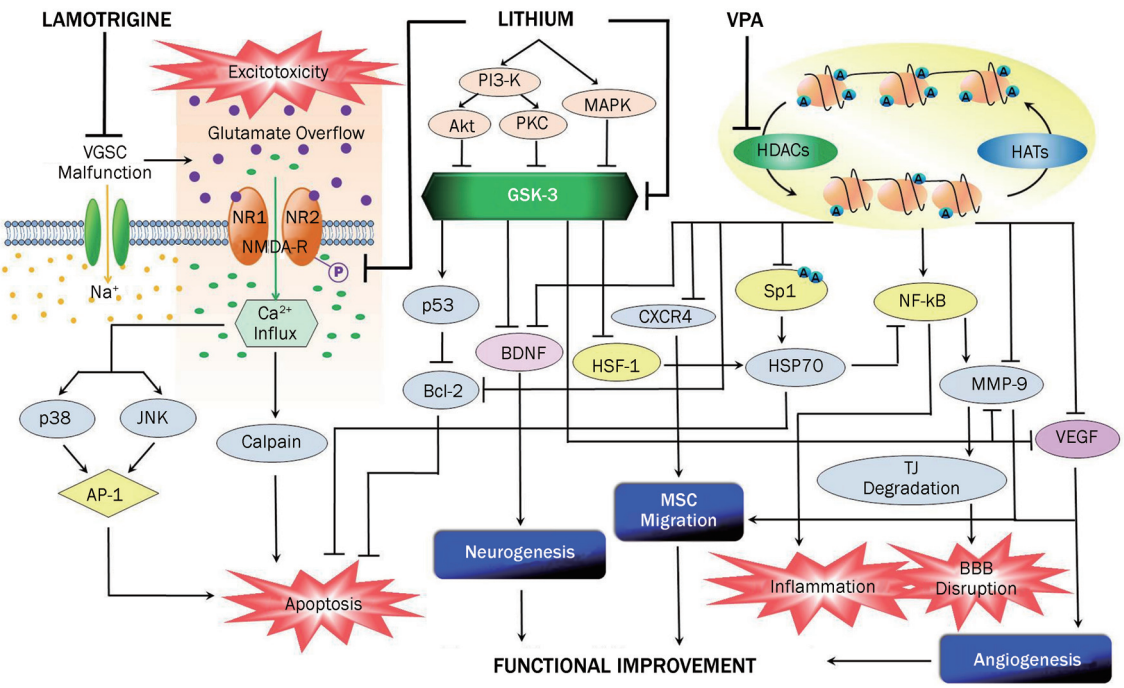

Figure 2. An overview of the proposed signaling mechanisms underlying the protective effects of mood stabilizing drugs against experimental stroke. Lithium, VPA and lamotrigine inhibit glutamate excitotoxicity-induced neuronal apoptosis by different mechanisms. Lithium inhibits stroke-induced NMDA receptor overactivation by decreasing NR2 subunit tyrosine phosphorylation. This suppresses excitotoxicity-induced activation of either calpain or p38, JNK and subsequently AP-1 to block neuronal apoptosis. VPA suppresses glutamate excitotoxicity via regulation of gene expression, among other mechanisms. As a VGSC blocker, lamotrigine attenuates stroke-induced VGSC malfunction, prevents extracellular glutamate overflow, and consequently mitigates excitotoxicity and apoptosis. Lithium and VPA inhibit GSK-3 and HDACs, respectively, to transcriptionally regulate various downstream neuroprotective and neurotrophic factors, as well as to enhance mesenchymal stem cell migration. Bcl-2, an antiapoptotic factor, is upregulated by lithium and VPA under experimental stroke conditions. Expression of the neuroprotective molecule HSP70 is enhanced by lithium and VPA through HSF-1 and Sp1 activation, respectively. HSP70 is also proposed to exert anti-inflammatory effects by inhibiting NF-κB activity. VPA attenuates BBB disruption by downregulating MMP-9 via NF-κB inhibition and preventing tight junction protein degradation shortly after ischemia. Long-term VPA treatment potentiates post-ischemic angiogenesis through upregulating VEGF and MMP-9 expression. Lithium also enhances VEGF and MMP-9 expression following long-term treatment. BDNF is activated by lithium and VPA, and the BDNF-TrkB signaling pathway is essential for enhancing post-ischemic neurogenesis and functional recovery. HAT: histone acetyltransferase; TJ: tight junctions; lines with solid arrows represent stimulatory effects; lines with flattened ends represent inhibitory effects; A: acetylated Lys residues of histone-tail proteins.

Sp1 acetylation to enhance its promoter activity. Both Bcl-2 and HSP70 play prominent protective roles against glutamate excitotoxicity following stroke. HSP70 is likely a key player in the anti-inflammatory effects of VPA by inhibiting ischemia-induced NF-κB activation. The latter action may be involved in VPA's suppression of ischemia-induced short-term upregulation of MMP-9, which contributes to BBB disruption. Delayed increases in MMP-9 and VEGF induced by VPA are likely mediators of angiogenesis. BDNF can also be induced by lithium and VPA through their respective inhibition of GSK-3 and HDACs, and the BDNF signaling pathway is critical for HDAC inhibition-induced neurogenesis and functional improvement. In addition, lithium inhibits the NMDA receptor-mediated Ca^{2+} influx, presumably by decreasing receptor tyrosine phosphorylation. This, in turn, decreases excitotoxicity-induced activation of calpain, as well as p38 and JNK and downstream AP-1 signaling, thus protecting neurons from apoptosis. Lamotrigine similarly protects against ischemia-induced excitotoxicity, but this likely involves VGSC inhibition, which decreases synaptic glutamate accumulation and receptor overexcitation (Figure 2). It remains to be explored whether additional targets are involved in lamotrigine's neuroprotective effects. Since the direct targets that lithium, VPA and lamotrigine engage to elicit beneficial effects in experimental stroke models have recently become clear, further preclinical and clinical stroke studies using other specific agents that specifically inhibit these targets are suggested.

Compelling evidence supports the notion that HDAC inhibition by VPA and other compounds elicits strong anti-inflammatory effects in experimental stroke models. GSK-3β inhibition has been demonstrated to have anti-inflammatory effects, as shown by reduced TNF-α production via attenuated activation of NF-κB and JNK signaling cascades[129], and induction of the anti-inflammatory cytokine IL-10[130]. In light of these findings, the anti-inflammatory effects of lithium in stroke conditions are recommended for future investigation. Emerging evidence suggests that specific microRNAs are regulated by mood stabilizers, and are involved in the translational suppression of multiple targets with major neurophysiological functions[131]. MicroRNAs have already been implicated in the pathogenesis of stroke[132, 133]; thus, further investigation along these lines will not only provide new insights into the neuroprotective effects of mood stabilizers, but also determine the potential utility of targeting specific microRNAs for stroke therapy.

Taken together, the promising preclinical evidence reviewed here, combined with these agents' long history of safe use in humans, suggests that long-term and large-scale clinical trials of mood stabilizers in stroke management are warranted.

Acknowledgements

This work was supported by the Intramural Research Program of the National Institute of Mental Health (NIMH), National Institutes of Health, and the Hsu family gift fund. The authors wish to thank Ioline Henter of the NIMH for her editorial assistance in the preparation of this manuscript.

References

1 Roger VL, Go AS, Lloyd-Jones DM, Adams RJ, Berry JD, Brown TM, *et al*. Heart disease and stroke statistics–2011 update: a report from the American Heart Association. Circulation 2011; 123: e18–e209.
2 Tissue plasminogen activator for acute ischemic stroke. The National Institute of Neurological Disorders and Stroke rt-PA Stroke Study Group. N Engl J Med 1995; 333: 1581–7.
3 Del Zoppo GJ, Saver JL, Jauch EC, Adams HP Jr. Expansion of the time window for treatment of acute ischemic stroke with intravenous tissue plasminogen activator: a science advisory from the American Heart Association/American Stroke Association. Stroke 2009; 40: 2945–8.
4 Barber PA, Zhang J, Demchuk AM, Hill MD, Buchan AM. Why are stroke patients excluded from TPA therapy? An analysis of patient eligibility. Neurology 2001; 56: 1015–20.
5 Kleindorfer D, Lindsell CJ, Brass L, Koroshetz W, Broderick JP. National US estimates of recombinant tissue plasminogen activator use: ICD-9 codes substantially underestimate. Stroke 2008; 39: 924–8.
6 Bearden CE, Woogen M, Glahn DC. Neurocognitive and neuroimaging predictors of clinical outcome in bipolar disorder. Curr Psychiatry Rep 2010; 12: 499–504.
7 Chuang DM. Neuroprotective and neurotrophic actions of the mood stabilizer lithium: can it be used to treat neurodegenerative diseases? Crit Rev Neurobiol 2004; 16: 83–90.
8 Chuang DM. The antiapoptotic actions of mood stabilizers: molecular mechanisms and therapeutic potentials. Ann N Y Acad Sci 2005; 1053: 195–204.
9 Manji HK, Drevets WC, Charney DS. The cellular neurobiology of depression. Nat Med 2001; 7: 541–7.
10 Chuang DM, Manji HK. In search of the Holy Grail for the treatment of neurodegenerative disorders: has a simple cation been overlooked? Biol Psychiatry 2007; 62: 4–6.
11 Moore GJ, Bebchuk JM, Wilds IB, Chen G, Manji HK. Lithium-induced increase in human brain grey matter. Lancet 2000; 356: 1241–2.
12 Atmaca M, Ozdemir H, Cetinkaya S, Parmaksiz S, Belli H, Poyraz AK, *et al*. Cingulate gyrus volumetry in drug free bipolar patients and patients treated with valproate or valproate and quetiapine. J Psychiatr Res 2007; 41: 821–7.
13 Chiu CT, Chuang DM. Molecular actions and therapeutic potential of lithium in preclinical and clinical studies of CNS disorders. Pharmacol Ther 2010; 128: 281–304.
14 Chuang DM, Leng Y, Marinova Z, Kim HJ, Chiu CT. Multiple roles of HDAC inhibition in neurodegenerative conditions. Trends Neurosci 2009; 32: 591–601.
15 Mantegazza M, Curia G, Biagini G, Ragsdale DS, Avoli M. Voltage-gated sodium channels as therapeutic targets in epilepsy and other neurological disorders. Lancet Neurol 2010; 9: 413–24.
16 Deb P, Sharma S, Hassan KM. Pathophysiologic mechanisms of acute ischemic stroke: An overview with emphasis on therapeutic significance beyond thrombolysis. Pathophysiology 2010; 17: 197–218.
17 Allen CL, Bayraktutan U. Oxidative stress and its role in the pathogenesis of ischaemic stroke. Int J Stroke 2009; 4: 461–70.
18 Ito U, Ohno K, Nakamura R, Suganuma F, Inaba Y. Brain edema during ischemia and after restoration of blood flow. Measurement of water, sodium, potassium content and plasma protein permeability. Stroke 1979; 10: 542–7.
19 Iadecola C, Alexander M. Cerebral ischemia and inflammation. Curr Opin Neurol 2001; 14: 89–94.

20 Wang Q, Tang XN, Yenari MA. The inflammatory response in stroke. J Neuroimmunol 2007; 184: 53–68.
21 Danton GH, Dietrich WD. Inflammatory mechanisms after ischemia and stroke. J Neuropathol Exp Neurol 2003; 62: 127–36.
22 Garcia JH, Liu KF, Yoshida Y, Lian J, Chen S, del Zoppo GJ. Influx of leukocytes and platelets in an evolving brain infarct (Wistar rat). Am J Pathol 1994; 144: 188–99.
23 Schilling M, Besselmann M, Leonhard C, Mueller M, Ringelstein EB, Kiefer R. Microglial activation precedes and predominates over macrophage infiltration in transient focal cerebral ischemia: a study in green fluorescent protein transgenic bone marrow chimeric mice. Exp Neurol 2003; 183: 25–33.
24 Zhang Z, Chopp M, Powers C. Temporal profile of microglial response following transient (2 h) middle cerebral artery occlusion. Brain Res 1997; 744: 189–98.
25 Dong Y, Benveniste EN. Immune function of astrocytes. Glia 2001; 36: 180–90.
26 Sandoval KE, Witt KA. Blood-brain barrier tight junction permeability and ischemic stroke. Neurobiol Dis 2008; 32: 200–19.
27 Cecchelli R, Berezowski V, Lundquist S, Culot M, Renftel M, Dehouck MP, *et al*. Modelling of the blood-brain barrier in drug discovery and development. Nat Rev Drug Discov 2007; 6: 650–61.
28 Rosell A, Lo EH. Multiphasic roles for matrix metalloproteinases after stroke. Curr Opin Pharmacol 2008; 8: 82–9.
29 Rosenberg GA, Navratil M, Barone F, Feuerstein G. Proteolytic cascade enzymes increase in focal cerebral ischemia in rat. J Cereb Blood Flow Metab 1996; 16: 360–6.
30 Fujimura M, Gasche Y, Morita-Fujimura Y, Massengale J, Kawase M, Chan PH. Early appearance of activated matrix metalloproteinase-9 and blood-brain barrier disruption in mice after focal cerebral ischemia and reperfusion. Brain Res 1999; 842: 92–100.
31 Heo JH, Lucero J, Abumiya T, Koziol JA, Copeland BR, del Zoppo GJ. Matrix metalloproteinases increase very early during experimental focal cerebral ischemia. J Cereb Blood Flow Metab 1999; 19: 624–33.
32 Park KP, Rosell A, Foerch C, Xing C, Kim WJ, Lee S, *et al*. Plasma and brain matrix metalloproteinase-9 after acute focal cerebral ischemia in rats. Stroke 2009; 40: 2836–42.
33 Barr TL, Latour LL, Lee KY, Schaewe TJ, Luby M, Chang GS, *et al*. Blood-brain barrier disruption in humans is independently associated with increased matrix metalloproteinase-9. Stroke 2010; 41: e123–8.
34 Rosell A, Cuadrado E, Ortega-Aznar A, Hernandez-Guillamon M, Lo EH, Montaner J. MMP-9-positive neutrophil infiltration is associated to blood-brain barrier breakdown and basal lamina type IV collagen degradation during hemorrhagic transformation after human ischemic stroke. Stroke 2008; 39: 1121–6.
35 Asahi M, Wang X, Mori T, Sumii T, Jung JC, Moskowitz MA, *et al*. Effects of matrix metalloproteinase-9 gene knock-out on the proteolysis of blood-brain barrier and white matter components after cerebral ischemia. J Neurosci 2001; 21: 7724–32.
36 Yang Y, Estrada EY, Thompson JF, Liu W, Rosenberg GA. Matrix metalloproteinase-mediated disruption of tight junction proteins in cerebral vessels is reversed by synthetic matrix metalloproteinase inhibitor in focal ischemia in rat. J Cereb Blood Flow Metab 2007; 27: 697–709.
37 Lo EH. A new penumbra: transitioning from injury into repair after stroke. Nat Med 2008; 14: 497–500.
38 Lok J, Gupta P, Guo S, Kim WJ, Whalen MJ, van Leyen K, *et al*. Cell-cell signaling in the neurovascular unit. Neurochem Res 2007; 32: 2032–45.
39 Jin K, Sun Y, Xie L, Childs J, Mao XO, Greenberg DA. Post-ischemic administration of heparin-binding epidermal growth factor-like growth factor (HB-EGF) reduces infarct size and modifies neurogenesis after focal cerebral ischemia in the rat. J Cereb Blood Flow Metab 2004; 24: 399–408.
40 Chen J, Zhang ZG, Li Y, Wang Y, Wang L, Jiang H, *et al*. Statins induce angiogenesis, neurogenesis, and synaptogenesis after stroke. Ann Neurol 2003; 53: 743–51.
41 Wang L, Zhang Z, Wang Y, Zhang R, Chopp M. Treatment of stroke with erythropoietin enhances neurogenesis and angiogenesis and improves neurological function in rats. Stroke 2004; 35: 1732–7.
42 Zhang ZG, Zhang L, Jiang Q, Zhang R, Davies K, Powers C, *et al*. VEGF enhances angiogenesis and promotes blood-brain barrier leakage in the ischemic brain. J Clin Invest 2000; 106: 829–38.
43 Fagan SC, Hess DC, Hohnadel EJ, Pollock DM, Ergul A. Targets for vascular protection after acute ischemic stroke. Stroke 2004; 35: 2220–5.
44 Hansen TM, Moss AJ, Brindle NP. Vascular endothelial growth factor and angiopoietins in neurovascular regeneration and protection following stroke. Curr Neurovasc Res 2008; 5: 236–45.
45 Lee S, Jilani SM, Nikolova GV, Carpizo D, Iruela-Arispe ML. Processing of VEGF-A by matrix metalloproteinases regulates bioavailability and vascular patterning in tumors. J Cell Biol 2005; 169: 681–91.
46 Zhao BQ, Wang S, Kim HY, Storrie H, Rosen BR, Mooney DJ, *et al*. Role of matrix metalloproteinases in delayed cortical responses after stroke. Nat Med 2006; 12: 441–5.
47 Nonaka S, Chuang DM. Neuroprotective effects of chronic lithium on focal cerebral ischemia in rats. Neuroreport 1998; 9: 2081–4.
48 Bian Q, Shi T, Chuang DM, Qian Y. Lithium reduces ischemia-induced hippocampal CA1 damage and behavioral deficits in gerbils. Brain Res 2007; 1184: 270–6.
49 Ren M, Senatorov VV, Chen RW, Chuang DM. Postinsult treatment with lithium reduces brain damage and facilitates neurological recovery in a rat ischemia/reperfusion model. Proc Natl Acad Sci U S A 2003; 100: 6210–5.
50 Klein PS, Melton DA. A molecular mechanism for the effect of lithium on development. Proc Natl Acad Sci U S A 1996; 93: 8455–9.
51 Stambolic V, Ruel L, Woodgett JR. Lithium inhibits glycogen synthase kinase-3 activity and mimics wingless signalling in intact cells. Curr Biol 1996; 6: 1664–8.
52 Jope RS. Lithium and GSK-3: one inhibitor, two inhibitory actions, multiple outcomes. Trends Pharmacol Sci 2003; 24: 441–3.
53 Ryves WJ, Harwood AJ. Lithium inhibits glycogen synthase kinase-3 by competition for magnesium. Biochem Biophys Res Commun 2001; 280: 720–5.
54 Chuang DM, Wang Z, Chiu CT. GSK-3 as a target for lithium-induced neuroprotection against excitotoxicity in neuronal cultures and animal models of ischemic stroke. Front Mol Neurosci 2011; 4: 15.
55 Ozaki N, Chuang DM. Lithium increases transcription factor binding to AP-1 and cyclic AMP-responsive element in cultured neurons and rat brain. J Neurochem 1997; 69: 2336–44.
56 Chen RW, Qin ZH, Ren M, Kanai H, Chalecka-Franaszek E, Leeds P, *et al*. Regulation of c-Jun N-terminal kinase, p38 kinase and AP-1 DNA binding in cultured brain neurons: roles in glutamate excitotoxicity and lithium neuroprotection. J Neurochem 2003; 84: 566–75.
57 Nonaka S, Hough CJ, Chuang DM. Chronic lithium treatment robustly protects neurons in the central nervous system against excitotoxicity by inhibiting *N*-methyl-*D*-aspartate receptor-mediated calcium influx. Proc Natl Acad Sci U S A 1998; 95: 2642–7.

58 Takagi N, Shinno K, Teves L, Bissoon N, Wallace MC, Gurd JW. Transient ischemia differentially increases tyrosine phosphorylation of NMDA receptor subunits 2A and 2B. J Neurochem 1997; 69: 1060–5.
59 Hashimoto R, Hough C, Nakazawa T, Yamamoto T, Chuang DM. Lithium protection against glutamate excitotoxicity in rat cerebral cortical neurons: involvement of NMDA receptor inhibition possibly by decreasing NR2B tyrosine phosphorylation. J Neurochem 2002; 80: 589–97.
60 Ma J, Zhang GY. Lithium reduced *N*-methyl-*D*-aspartate receptor subunit 2A tyrosine phosphorylation and its interactions with Src and Fyn mediated by PSD-95 in rat hippocampus following cerebral ischemia. Neurosci Lett 2003; 348: 185–9.
61 Chalecka-Franaszek E, Chuang DM. Lithium activates the serine/threonine kinase Akt-1 and suppresses glutamate-induced inhibition of Akt-1 activity in neurons. Proc Natl Acad Sci U S A 1999; 96: 8745–50.
62 Hashimoto R, Takei N, Shimazu K, Christ L, Lu B, Chuang DM. Lithium induces brain-derived neurotrophic factor and activates TrkB in rodent cortical neurons: an essential step for neuroprotection against glutamate excitotoxicity. Neuropharmacology 2002; 43: 1173–9.
63 Datta SR, Dudek H, Tao X, Masters S, Fu H, Gotoh Y, *et al*. Akt phosphorylation of BAD couples survival signals to the cell-intrinsic death machinery. Cell 1997; 91: 231–41.
64 Skorski T, Bellacosa A, Nieborowska-Skorska M, Majewski M, Martinez R, Choi JK, *et al*. Transformation of hematopoietic cells by BCR/ABL requires activation of a PI-3K/Akt-dependent pathway. EMBO J 1997; 16: 6151–61.
65 Chen RW, Chuang DM. Long term lithium treatment suppresses p53 and Bax expression but increases Bcl-2 expression. A prominent role in neuroprotection against excitotoxicity. J Biol Chem 1999; 274: 6039–42.
66 Broughton BR, Reutens DC, Sobey CG. Apoptotic mechanisms after cerebral ischemia. Stroke 2009; 40: e331–9.
67 Mielke K, Herdegen T. JNK and p38 stresskinases--degenerative effectors of signal-transduction-cascades in the nervous system. Prog Neurobiol 2000; 61: 45–60.
68 Whitmarsh AJ, Davis RJ. Transcription factor AP-1 regulation by mitogen-activated protein kinase signal transduction pathways. J Mol Med 1996; 74: 589–607.
69 Xu J, Culman J, Blume A, Brecht S, Gohlke P. Chronic treatment with a low dose of lithium protects the brain against ischemic injury by reducing apoptotic death. Stroke 2003; 34: 1287–92.
70 Camins A, Crespo-Biel N, Junyent F, Verdaguer E, Canudas AM, Pallas M. Calpains as a target for therapy of neurodegenerative diseases: putative role of lithium. Curr Drug Metab 2009; 10: 433–47.
71 Li Q, Li H, Roughton K, Wang X, Kroemer G, Blomgren K, *et al*. Lithium reduces apoptosis and autophagy after neonatal hypoxia-ischemia. Cell Death Dis 2010; 1: e56.
72 Bijur GN, Jope RS. Opposing actions of phosphatidylinositol 3-kinase and glycogen synthase kinase-3beta in the regulation of HSF-1 activity. J Neurochem 2000; 75: 2401–8.
73 Klionsky DJ, Emr SD. Autophagy as a regulated pathway of cellular degradation. Science 2000; 290: 1717–21.
74 Wen YD, Sheng R, Zhang LS, Han R, Zhang X, Zhang XD, *et al*. Neuronal injury in rat model of permanent focal cerebral ischemia is associated with activation of autophagic and lysosomal pathways. Autophagy 2008; 4: 762–9.
75 Sarkar S, Floto RA, Berger Z, Imarisio S, Cordenier A, Pasco M, *et al*. Lithium induces autophagy by inhibiting inositol monophosphatase. J Cell Biol 2005; 170: 1101–11.
76 Rubinsztein DC, DiFiglia M, Heintz N, Nixon RA, Qin ZH, Ravikumar B, *et al*. Autophagy and its possible roles in nervous system diseases, damage and repair. Autophagy 2005; 1: 11–22.
77 Li H, Li Q, Du X, Sun Y, Wang X, Kroemer G, *et al*. Lithium-mediated long-term neuroprotection in neonatal rat hypoxia-ischemia is associated with antiinflammatory effects and enhanced proliferation and survival of neural stem/progenitor cells. J Cereb Blood Flow Metab 2011; 31: 2106–15.
78 Beurel E, Jope RS. Lipopolysaccharide-induced interleukin-6 production is controlled by glycogen synthase kinase-3 and STAT3 in the brain. J Neuroinflammation 2009; 6: 9.
79 Kim YR, van Meer MP, Tejima E, Murata Y, Mandeville JB, Dai G, *et al*. Functional MRI of delayed chronic lithium treatment in rat focal cerebral ischemia. Stroke 2008; 39: 439–47.
80 Guo S, Arai K, Stins MF, Chuang DM, Lo EH. Lithium upregulates vascular endothelial growth factor in brain endothelial cells and astrocytes. Stroke 2009; 40: 652–5.
81 Boku S, Nakagawa S, Masuda T, Nishikawa H, Kato A, Toda H, *et al*. Effects of mood stabilizers on adult dentate gyrus-derived neural precursor cells. Prog Neuropsychopharmacol Biol Psychiatry 2011; 35: 111–7.
82 Kim JS, Chang MY, Yu IT, Kim JH, Lee SH, Lee YS, *et al*. Lithium selectively increases neuronal differentiation of hippocampal neural progenitor cells both *in vitro* and *in vivo*. J Neurochem 2004; 89: 324–36.
83 Chen G, Rajkowska G, Du F, Seraji-Bozorgzad N, Manji HK. Enhancement of hippocampal neurogenesis by lithium. J Neurochem 2000; 75: 1729–34.
84 Yan XB, Hou HL, Wu LM, Liu J, Zhou JN. Lithium regulates hippocampal neurogenesis by ERK pathway and facilitates recovery of spatial learning and memory in rats after transient global cerebral ischemia. Neuropharmacology 2007; 53: 487–95.
85 Shioda N, Han F, Fukunaga K. Role of Akt and ERK signaling in the neurogenesis following brain ischemia. Int Rev Neurobiol 2009; 85: 375–87.
86 Yoshida S, Kirino T, Tamura A, Basugi N, Sano K. Lithium ion does not protect brain against transient ischemia in gerbils. Stroke 1991; 22: 84–9.
87 Ren M, Leng Y, Jeong M, Leeds PR, Chuang DM. Valproic acid reduces brain damage induced by transient focal cerebral ischemia in rats: potential roles of histone deacetylase inhibition and heat shock protein induction. J Neurochem 2004; 89: 1358–67.
88 Kim HJ, Rowe M, Ren M, Hong JS, Chen PS, Chuang DM. Histone deacetylase inhibitors exhibit anti-inflammatory and neuroprotective effects in a rat permanent ischemic model of stroke: multiple mechanisms of action. J Pharmacol Exp Ther 2007; 321: 892–901.
89 Qian YR, Lee MJ, Hwang S, Kook JH, Kim JK, Bae CS. Neuroprotection by valproic Acid in mouse models of permanent and transient focal cerebral ischemia. Korean J Physiol Pharmacol 2010; 14: 435–40.
90 Gottlicher M, Minucci S, Zhu P, Kramer OH, Schimpf A, Giavara S, *et al*. Valproic acid defines a novel class of HDAC inhibitors inducing differentiation of transformed cells. EMBO J 2001; 20: 6969–78.
91 Phiel CJ, Zhang F, Huang EY, Guenther MG, Lazar MA, Klein PS. Histone deacetylase is a direct target of valproic acid, a potent anticonvulsant, mood stabilizer, and teratogen. J Biol Chem 2001; 276: 36734–41.
92 Leng Y, Chuang DM. Endogenous alpha-synuclein is induced by valproic acid through histone deacetylase inhibition and participates in neuroprotection against glutamate-induced excitotoxicity. J

Neurosci 2006; 26: 7502–12.
93 Kanai H, Sawa A, Chen RW, Leeds P, Chuang DM. Valproic acid inhibits histone deacetylase activity and suppresses excitotoxicity-induced GAPDH nuclear accumulation and apoptotic death in neurons. Pharmacogenomics J 2004; 4: 336–44.
94 Shao L, Young LT, Wang JF. Chronic treatment with mood stabilizers lithium and valproate prevents excitotoxicity by inhibiting oxidative stress in rat cerebral cortical cells. Biol Psychiatry 2005; 58: 879–84.
95 Leng Y, Liang MH, Ren M, Marinova Z, Leeds P, Chuang DM. Synergistic neuroprotective effects of lithium and valproic acid or other histone deacetylase inhibitors in neurons: roles of glycogen synthase kinase-3 inhibition. J Neurosci 2008; 28: 2576–88.
96 Sinn DI, Kim SJ, Chu K, Jung KH, Lee ST, Song EC, *et al*. Valproic acid-mediated neuroprotection in intracerebral hemorrhage via histone deacetylase inhibition and transcriptional activation. Neurobiol Dis 2007; 26: 464–72.
97 Peng GS, Li G, Tzeng NS, Chen PS, Chuang DM, Hsu YD, *et al*. Valproate pretreatment protects dopaminergic neurons from LPS-induced neurotoxicity in rat primary midbrain cultures: role of microglia. Brain Res Mol Brain Res 2005; 134: 162–9.
98 Chen PS, Peng GS, Li G, Yang S, Wu X, Wang CC, *et al*. Valproate protects dopaminergic neurons in midbrain neuron/glia cultures by stimulating the release of neurotrophic factors from astrocytes. Mol Psychiatry 2006; 11: 1116–25.
99 Faraco G, Pancani T, Formentini L, Mascagni P, Fossati G, Leoni F, *et al*. Pharmacological inhibition of histone deacetylases by suberoylanilide hydroxamic acid specifically alters gene expression and reduces ischemic injury in the mouse brain. Mol Pharmacol 2006; 70: 1876–84.
100 Marinova Z, Ren M, Wendland JR, Leng Y, Liang MH, Yasuda S, *et al*. Valproic acid induces functional heat-shock protein 70 via class I histone deacetylase inhibition in cortical neurons: a potential role of Sp1 acetylation. J Neurochem 2009; 111: 976–87.
101 Marinova Z, Leng Y, Leeds P, Chuang DM. Histone deacetylase inhibition alters histone methylation associated with heat shock protein 70 promoter modifications in astrocytes and neurons. Neuropharmacology 2011; 60: 1109–15.
102 Zheng Z, Kim JY, Ma H, Lee JE, Yenari MA. Anti-inflammatory effects of the 70 kDa heat shock protein in experimental stroke. J Cereb Blood Flow Metab 2008; 28: 53–63.
103 Wang Z, Leng Y, Tsai LK, Leeds P, Chuang DM. Valproic acid attenuates blood-brain barrier disruption in a rat model of transient focal cerebral ischemia: the roles of HDAC and MMP-9 inhibition. J Cereb Blood Flow Metab 2011; 31: 52–7.
104 Hao Y, Creson T, Zhang L, Li P, Du F, Yuan P, *et al*. Mood stabilizer valproate promotes ERK pathway-dependent cortical neuronal growth and neurogenesis. J Neurosci 2004; 24: 6590–9.
105 Hsieh J, Nakashima K, Kuwabara T, Mejia E, Gage FH. Histone deacetylase inhibition-mediated neuronal differentiation of multipotent adult neural progenitor cells. Proc Natl Acad Sci U S A 2004; 101: 16659–64.
106 Kim HJ, Leeds P, Chuang DM. The HDAC inhibitor, sodium butyrate, stimulates neurogenesis in the ischemic brain. J Neurochem 2009; 110: 1226–40.
107 Yasuda S, Liang MH, Marinova Z, Yahyavi A, Chuang DM. The mood stabilizers lithium and valproate selectively activate the promoter IV of brain-derived neurotrophic factor in neurons. Mol Psychiatry 2009; 14: 51–9.
108 Borlongan CV. Bone marrow stem cell mobilization in stroke: a 'bonehead' may be good after all! Leukemia 2011. doi: 10.1038/leu.2011.167
109 Tsai LK, Leng Y, Wang Z, Leeds P, Chuang DM. The mood stabilizers valproic acid and lithium enhance mesenchymal stem cell migration via distinct mechanisms. Neuropsychopharmacology 2010; 35: 2225–37.
110 Tsai LK, Wang Z, Munasinghe J, Leng Y, Leeds P, Chuang DM. Mesenchymal stem cells primed with valproate and lithium robustly migrate to infarcted regions and facilitate recovery in a stroke model. Stroke 2011; 42: 2932–9.
111 Smith SE, Meldrum BS. Cerebroprotective effect of lamotrigine after focal ischemia in rats. Stroke 1995; 26: 117–21; discussion 21–2.
112 Shuaib A, Mahmood RH, Wishart T, Kanthan R, Murabit MA, Ijaz S, *et al*. Neuroprotective effects of lamotrigine in global ischemia in gerbils. A histological, *in vivo* microdialysis and behavioral study. Brain Res 1995; 702: 199–206.
113 Wiard RP, Dickerson MC, Beek O, Norton R, Cooper BR. Neuroprotective properties of the novel antiepileptic lamotrigine in a gerbil model of global cerebral ischemia. Stroke 1995; 26: 466–72.
114 Seckin H, Yigitkanli K, Besalti O, Kosemehmetoglu K, Ozturk E, Simsek S, *et al*. Lamotrigine attenuates cerebral vasospasm after experimental subarachnoid hemorrhage in rabbits. Surg Neurol 2008; 70: 344–51; discussion 51.
115 Leach MJ, Marden CM, Miller AA. Pharmacological studies on lamotrigine, a novel potential antiepileptic drug: II. Neurochemical studies on the mechanism of action. Epilepsia 1986; 27: 490–7.
116 Kuo CC, Lu L. Characterization of lamotrigine inhibition of Na^+ channels in rat hippocampal neurones. Br J Pharmacol 1997; 121: 1231–8.
117 Bacher A, Zornow MH. Lamotrigine inhibits extracellular glutamate accumulation during transient global cerebral ischemia in rabbits. Anesthesiology 1997; 86: 459–63.
118 Kirino T. Delayed neuronal death in the gerbil hippocampus following ischemia. Brain Res 1982; 239: 57–69.
119 Fan Y, Deng P, Wang YC, Lu HC, Xu ZC, Schulz PE. Transient cerebral ischemia increases CA1 pyramidal neuron excitability. Exp Neurol 2008; 212: 415–21.
120 Papazisis G, Kallaras K, Kaiki-Astara A, Pourzitaki C, Tzachanis D, Dagklis T, *et al*. Neuroprotection by lamotrigine in a rat model of neonatal hypoxic-ischaemic encephalopathy. Int J Neuropsychopharmacol 2008; 11: 321–9.
121 Yi YH, Guo WC, Sun WW, Su T, Lin H, Chen SQ, *et al*. Neuroprotection of lamotrigine on hypoxic-ischemic brain damage in neonatal rats: Relations to administration time and doses. Biologics 2008; 2: 339–44.
122 Li X, Bijur GN, Jope RS. Glycogen synthase kinase-3beta, mood stabilizers, and neuroprotection. Bipolar Disord 2002; 4: 137–44.
123 Chang YC, Rapoport SI, Rao JS. Chronic administration of mood stabilizers upregulates BDNF and bcl-2 expression levels in rat frontal cortex. Neurochem Res 2009; 34: 536–41.
124 Kondziella D, Strandberg J, Lindquist C, Asztely F. Lamotrigine increases the number of BrdU-labeled cells in the rat hippocampus. Neuroreport 2011; 22: 97–100.
125 Collino M, Thiemermann C, Mastrocola R, Gallicchio M, Benetti E, Miglio G, *et al*. Treatment with the glycogen synthase kinase-3beta inhibitor, TDZD-8, affects transient cerebral ischemia/reperfusion injury in the rat hippocampus. Shock 2008; 30: 299–307.
126 Kelly S, Zhao H, Hua Sun G, Cheng D, Qiao Y, Luo J, *et al*. Glycogen synthase kinase 3beta inhibitor Chir025 reduces neuronal death resulting from oxygen-glucose deprivation, glutamate excitotoxicity, and cerebral ischemia. Exp Neurol 2004; 188: 378–86.
127 Koh SH, Yoo AR, Chang DI, Hwang SJ, Kim SH. Inhibition of GSK-

3 reduces infarct volume and improves neurobehavioral functions. Biochem Biophys Res Commun 2008; 371: 894–9.

128 Valerio A, Bertolotti P, Delbarba A, Perego C, Dossena M, Ragni M, *et al*. Glycogen synthase kinase-3 inhibition reduces ischemic cerebral damage, restores impaired mitochondrial biogenesis and prevents ROS production. J Neurochem 2011; 116: 1148–59.

129 Wang MJ, Huang HY, Chen WF, Chang HF, Kuo JS. Glycogen synthase kinase-3beta inactivation inhibits tumor necrosis factor-alpha production in microglia by modulating nuclear factor kappaB and MLK3/JNK signaling cascades. J Neuroinflammation 2010; 7: 99.

130 Huang WC, Lin YS, Wang CY, Tsai CC, Tseng HC, Chen CL, *et al*. Glycogen synthase kinase-3 negatively regulates anti-inflammatory interleukin-10 for lipopolysaccharide-induced iNOS/NO biosynthesis and RANTES production in microglial cells. Immunology 2009; 128: e275–86.

131 Zhou R, Yuan P, Wang Y, Hunsberger JG, Elkahloun A, Wei Y, *et al*. Evidence for selective microRNAs and their effectors as common long-term targets for the actions of mood stabilizers. Neuropsychopharmacology 2009; 34: 1395–405.

132 Tan JR, Koo YX, Kaur P, Liu F, Armugam A, Wong PT, *et al*. microRNAs in stroke pathogenesis. Curr Mol Med 2011; 11: 76–92.

133 Jeyaseelan K, Lim KY, Armugam A. MicroRNA expression in the blood and brain of rats subjected to transient focal ischemia by middle cerebral artery occlusion. Stroke 2008; 39: 959–66.

Acta Pharmacologica Sinica (2011) 32: 1446–1453
 1671-4083/11 $32.00
www.nature.com/aps

Original Article

Scutellarin protects against Aβ-induced learning and memory deficits in rats: involvement of nicotinic acetylcholine receptors and cholinesterase

Li-li GUO[1], Zhi-zhong GUAN[1, 2, *], Yong-lin WANG[3]

[1]Pathological Department of Affiliated Hospital, [2]Key Lab of Molecular Biology and [3]Department of Pharmacology in Guiyang Medical College, Guiyang 550004, China

Aim: To examine the protective effects of scutellarin (Scu) on rats with learning and memory deficit induced by β-amyloid peptide (Aβ).
Methods: Fifty male Wistar rats were randomly divided into 5 groups: control, sham operation, Aβ, Aβ+Scu, and Aβ+piracetam groups. $Aβ_{25–35}$ was injected into the lateral ventricle (10 μg each side). Scu (10 mg/2 mL) or piracetam (10 mg/2 mL was intragastrically administered per day for 20 consecutive days following Aβ treatment. Learning and memory was assessed with Morris water maze test. The protein and mRNA levels of nicotinic acetylcholine receptor (nAChR) α4, α7, and β2 subunits in the brain were examined using Western blotting and real-time PCR, respectively. The activities of acetylcholinesterase (AChE) and butyrylcholinesterase (BuChE) in the brain and plasma were measured using Ellman's colorimetric method.
Results: In Aβ group, the escape latency period and first platform cross was significantly increased, and the total number of platform crossings was significantly decreased, as compared with the control and the sham operation groups. Both Scu and piracetam treatment significantly reduced the escape latency period and time to cross platform, and increased the number of platform crosses, but there were no significant differences between Aβ+Scu and Aβ+piracetam groups. In Aβ group, the protein levels of nAChR α4 and α7 subunits in the cerebral cortex were significantly decreased by 42%–47% and 58%–61%, respectively, as compared to the control and the sham operation groups. Scu treatment caused upregulation of α4 and α7 subunit proteins by around 24% and 30%, respectively, as compared to Aβ group, but there were no significant differences between Aβ+Scu and Aβ+piracetam groups. The protein level of nAChR β2 subunit had no significant difference among different groups. The mRNA levels of nAChR α4, α7, and β2 subunits were not significantly changed. In Aβ group, the activities of AChE and BuChE in the brain were significantly increased, but were significantly decreased in the plasma, as compared to the control and the sham operation groups. Scu or piracetam treatment restored the activities in brain and plasma nearly to the levels in the control group.
Conclusion: The results suggest that Scu may rescue some of the deleterious effects of Aβ, possibly by stimulating nAChR protein translation and regulating cholinesterase activity.

Keywords: scutellarin; piracetam; β-amyloid peptide; learning and memory; cholinesterase; nicotinic acetylcholine receptor

Acta Pharmacologica Sinica (2011) 32: 1446–1453; doi: 10.1038/aps.2011.115; published online 10 Oct 2011

Introduction

Herba Erigerontis (HE), a Chinese medicinal herb derived from *Erigeron breviscapus* (vant) Hand-Mazz, has been used to effectively treat brain and cardiovascular disorders[1]. Flavonoids, a large group of natural compounds found in HE, have been considered as substitutes for estrogen[2] and proven to have neuroprotective effects[3–6]. Interestingly, scutellarin (Scu) is a major component of flavonoids in HE (over 40% of the total flavonoids: 5,6,4′,7-glucuronyl oxyflavone). Several basic research and clinical studies have shown that Scu plays an important role in combating neurotoxicity[1, 7, 8].

Alzheimer's disease (AD) is one of the most devastating diseases of the central nervous system (CNS). Neuropathologically, it is characterized by amyloid plaques composed primarily of β-amyloid peptide (Aβ) aggregates, neurofibrillary tangles comprised of hyperphosphorylated tau protein, and extensive neuronal loss that is particularly pronounced in the cholinergic system[9]. Aβ, a protein fragment derived from sequential proteolytic cleavage by β- and γ-secretases on amyloid precursor protein (APP), is one of the key events leading to neuronal dysfunction and cognitive decline in the progression of AD[10]. It has been hypothesized that the altered pro-

* To whom correspondence should be addressed.
E-mail zhizhongguan@yahoo.com
Received 2011-03-24 Accepted 2011-07-22

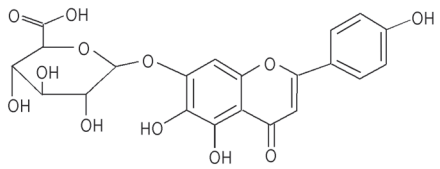

Chemical structure of scutellarin.

cessing of APP results in the accumulation and aggregation of neurotoxic forms of Aβ[11] that induces neurotoxic effects via signaling cascades[12].

The cholinergic neurotransmitter system in the brain is critical for the processing of information related to cognitive function[13]. Indeed, AD dysfunction is marked by conspicuous decreases in choline acetyltransferase activity and acetylcholine (ACh) release, significant loss of cholinergic neurons and depletion of cholinergic acetylcholine receptors[9, 14]. Within the cholinergic system, nicotinic acetylcholine receptors (nAChRs), which are members of the superfamily of ligand-gated ion channels, are important components involved in a wide range of brain activities and functions, including cognitive enhancement and neuroprotection[15]. Within the last decade, experimental evidence has accumulated supporting nAChRs as direct therapeutic targets to improve cognitive function and slow neurodegenerative progression in AD patients[16]. Accordingly, some of the interventions to prevent or treat the development and progression of AD have focused on enhancing cholinergic transmission, either through increasing ACh synthesis or inhibiting the activities of acetylcholinesterase (AChE) and butyrylcholinesterase (BuChE), enzymes responsible for ACh hydrolysis[17, 18].

At present, there are no effective pharmacological interventions that prevent or stall AD. In researching alternative therapeutic agents against the disease, HE was found to inhibit aggregation of Aβ[19], and Scu may prevent neuronal death induced by Aβ[3]. In this study, we investigated the potential mechanisms underlying the effects of Scu on learning and memory, expression of nAChRs and the activity of ChE by using the dementia model of rats produced by intracerebroventricular (icv) injection of Aβ.

Materials and methods

Preparation of Scu

HE, whole grass of the perennial Erigeron breviscapus (vant) Hand-Mazz, was collected from the Leisan County, Guizhou Province in China, and the identity of plant materials was verified morphologically. A voucher specimen was deposited in Guiyang Medical College (accession number EB20070730). Plant material was sun-dried and ground.

Scu was derived from extraction of HE, and its purity above 95% was determined by ultra performance liquid chromatography (UPLC). Each killogram of air-dried powder produced from whole HE was decocted with 10 L of water 3 times for 30 min each, for a total time of 1.5 h. Individual batches of the decoction were combined, filtered, and concentrated to obtain a relative density (or specific gravity) of 1.10 (50 °C) and then adjusted to an ethanol content of 55% with 95% ethanol. The resulting mixture was stirred for 30 min and then kept at 50 °C for 12 h. The filtrate thus obtained was first concentrated under reduced atmospheric pressure to yield a relative density of 1.11 (50 °C) and then adjusted to pH 2 with hydrochloric acid. The mixture was kept at 55 °C for 6 h, filtered, and finally vacuum-dried to yield Scu used in subsequent studies.

Chemicals

The chemical reagents including $A\beta_{25-35}$, mouse monoclonal anti-β-actin antibody, and AChE and BuChE were purchased from Sigma-Aldrich Co (St Louis, MO, USA). Goat polyclonal anti-α4 and -β2 antibodies, mouse monoclonal anti-α7 antibody, and secondary anti-goat and anti-mouse IgG conjugated with horseradish peroxidase were purchased from Santa Cruz Biotechnology Inc (Santa Cruz, CA, USA). Piracetam was purchased from the Hangzhou Minsheng Pharmaceutical Group Co (Hangzhou, China). Hyper Performance Chemiluminescence film and ECL Plus reagent were obtained from Amersham (Uppsala, Sweden). Real-time PCR reagents were obtained from Promega Co (Madison, WI, USA) and the Taqman probe was from Applied Biosystems Co (Foster City, CA, USA).

Aβ aggregation

$A\beta_{25-35}$ was dissolved in 10% dimethyl sulfoxide (DMSO) to a final concentration of 5 μg/μL (4.7 mmol/L), and the solution was incubated at 37 °C for 3 d to induce a conformational transformation from a soluble form to insoluble β-sheets, thus increasing the neurotoxicity of the peptide.

Experimental animals

Male Wistar rats [Grade II; Certificate No: SCXK (Q) 200220001], 300–350 g, were purchased from the Experimental Animal Center in Guizhou province, China, and the experiments were approved by the regional ethical committee for animal studies in Guizhou. The rats were acclimated for one month in a controlled housing facility (humidity 30%–55% and temperature 22–25 °C) prior to use in experiments.

Surgery and drug administration

Fifty rats with similar learning and memory ability as determined by the Morris water maze test were randomly divided into 5 groups: control (no operation), sham operation, learning and memory deficit model (Aβ icv), Aβ+Scu and Aβ+piracetam (which received Aβ icv before treatment with Scu or piracetam) groups. Ten animals were used for each group. During the study, the rats were given water and food *ad libitum*. The learning and memory deficit model with AD-like dementia was produced by bilateral icv injection with $A\beta_{25-35}$. Rats were anesthetized with chloral hydrate (0.3 g/kg, ip) and placed in a stereotaxic apparatus. Referring

to the atlas of Paxinos and Watson[20], the coordinates were located for lateral ventricle injection (anterior-posterior, 3.0 mm; medial-lateral, 2.0 mm; dorsal-ventral, 3.3 mm from the bregma). Two microliters of $A\beta_{25-35}$ (10 μg) were gradually delivered into each lateral ventricle via a microsyringe with a stainless steel needle within 5 min. The sham operation was identical except sterile saline was used in place of $A\beta_{25-35}$ solution. No procedure was performed on the control group. The rats in the Aβ+Scu or Aβ+piracetam group were treated with the same protocol as the learning and memory deficit model, but five days after icv the animals were additionally treated with 10 mg/2 mL per day of Scu or piracetam by intragastric administration (ig) for 20 consecutive days. At the end of the experiment, the rats were assessed with the Morris water maze test and then sacrificed by femoral artery exsanguination. Blood samples were collected, and brains, including whole cerebral cortices, were removed and stored at -80 °C for later analysis.

Examination of spatial learning and memory

Spatial learning and memory was evaluated with the Morris water maze test[21]. As described previously[22], each rat was placed facing the pool from different quadrants at the start of a trial and subjected to 4 trials each day with a 30-min interval of rest between trials for a training period of 4 d. Their movement was monitored with Videotrack Software (View Point). During the navigation test, the time required to locate the escape platform (escape latency) was determined. The 4 trials on each individual day were averaged for statistical analysis. Furthermore, on d 5, the platform was removed, and the time that the animal first crossed the platform site and the total number of crosses within 60 s were recorded. All of these behavioral tests were conducted in a quiet environment with subdued lighting.

Protein levels of α4, α7, and β2 nAChR subunits detected by Western blotting

The cerebral cortices were homogenized, and the protein concentrations of the resulting supernatant were determined[22]. The proteins in the solubilized membrane fraction recovered in the supernatant were separated by 10% SDS-PAGE and transferred to polyvinylidene difluoride (PVDF) membranes. For the quantification of nAChR subunits and β-actin, the PVDF membranes were incubated with appropriate antibodies for corresponding proteins: nAChR subunit α4 (1:300), α7 (1:500) and β2 (1:300) and β-actin (1:10000) at 4 °C overnight. After washing, the membranes were incubated with HRP-conjugated anti-goat IgG (1:5000) or anti-mouse IgG (1:3000), respectively, for 60 min. Finally, these membranes were incubated in ECL Plus reagent for 5 min and the signals were visualized by exposure to Hyper Performance Chemiluminescence film. For the calculation of Western blotting results, we used β-actin (a housekeeping gene) as an internal standard. The resultant values (as compared with β-actin) were expressed as a percentage of the average value for controls.

The mRNA levels of α4, α7, and β2 nAChR subunits determined by real-time PCR

Total RNA in the cerebral cortices was isolated by TRIzol reagents (Invitrogen, Carlsbad, CA, USA). cDNA was generated from 3 μg of total RNA by utilizing a cDNA synthesis kit (Promega, Madison, WI, USA)[23], and the reaction mixture was incubated in a Mastercycler 5700 (Eppendorf, Hamburg, Germany) at 37 °C for 1 h, then at 70 °C for 15 min and at 4 °C for 1 min. The primers and probes for α4 (Rn 00577436), α7 (Rn 00563223), β2 (Rn 00570733) nAChR subunits, and β-actin (4352931E; as an internal standard) were purchased from Applied Biosystems (Foster City, CA, USA) (Table 1). Reactions were performed with the Universal TaqMan 2X PCR master mix (Applied Biosystems, Foster City, USA) in a 20 μL reaction volume. The detailed procedure was performed as described in the manufacturer's protocol. After an initial denaturation at 50 °C for 120 s, 40 cycles were performed consisting of 95 °C for 600 s, 55 °C for 15 s followed by a final extension at 60 °C for 60 s. The experiments were repeated at least three times. The results are expressed as the ratio of detected signal for each nAChR subunit to the β-actin signal, and the CT values were calculated as percentages of the controls (as 100%).

Table 1. Sequences of PCR primers and product length.

Gene	Primers sequences	Length
nAChR α4	CTCAGCTCATTGACGTGGACGAGAA	65
nAChR α7	TGCTGCACGTGTCCCTGCAAGGCGA	72
nAChR β2	ACCAGAGTGTGAGGGAGGACTGGAA	63
β-actin	CCTTCCTTCCTGGGTATGGAATCCT	91

AChE and BuChE activities in brain and plasma

The cerebral cortical tissues were homogenized 1:9 (*w/v*) of 0.9% saline. The resulting brain homogenate supernatants were diluted with PBS by 1:15, and plasma was diluted 1:13. Activities of AChE and BuChE in these solutions were determined by an improved Ellman's colorimetric method[24], employing acetylthiocholine (ATC) and butyrylthiocholine (BTC), respectively, as substrates for the reactions. Activities were calculated with the following formula:

$$\text{ChE (nmol·min}^{-1}\text{·mL}^{-1}\text{)} = OD_{\text{(sample-control)}} \times 0.588 \times \text{diluted multiple}$$

The data were normalized to the amount of protein measured by the Lowry method, using the Bio-Rad DC protein assay and bovine serum albumin as the standard.

Statistical analysis

The results were expressed as the mean±SD. Groups were assessed for significant differences with analysis of variance (ANOVA) and Tukey-Kramer *post-hoc* tests using SPSSv11.5 software (SPSS Inc, USA). $P<0.05$ was considered statistically

significant.

Results

Learning and memory dysfunction in response to Aβ treatment

Rats given Aβ icv had increased values for the escape latency period and first platform cross, and the total number of platform crossings was significantly lower than the control and the sham operation groups (Figure 1).

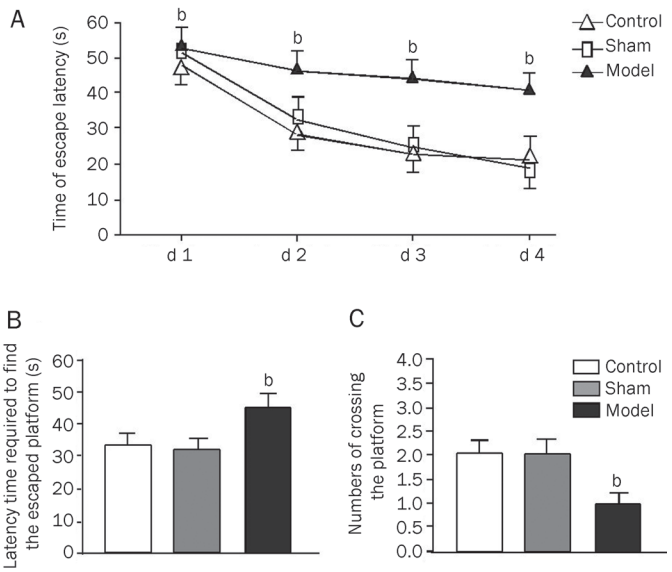

Figure 1. Spatial learning and memory of rats with cerebroventricular injection of Aβ and the rats as sham operation and control. Spatial learning and memory were tested in a Morris Water Maze involving a circular pool 180 cm in diameter. Following four trials daily for 4 d, the average escaping latency of rats in different groups during training session was conducted (A); on d 5 the platform was removed, and latency trials (B) and the number of times the central platform was crossed was counted (C). Values in the bar graphs are means±SD of 10 rats. $^{b}P<0.05$ as compared to normal groups and sham operation groups, as determined by an analysis of the variance ANOVA with Tukey-Kramer using SPSS15.0 software.

Effect of Scu on the rats treated with Aβ

Compared to the learning and memory deficit group, rats additionally treated with Scu showed decreases in escape latency period and time to cross platform, as well as a higher number of platform crosses. There were no significant differences between Aβ+Scu and Aβ+piracetam treatment groups (Figure 2).

Protein and mRNA levels of α4, α7, and β2 nAChR subunits

The protein levels of the α4 and α7 nAChR subunits in the cerebral cortex were significantly decreased by 42%–47% and 58%–61%, respectively, in the learning and memory deficit model group as compared to the control and the sham operation groups (Figure 3). Interestingly, Scu treatment resulted in an upregulation by 24% and 30% in α4 and α7 nAChR subunit proteins, respectively, as compared to the learning and

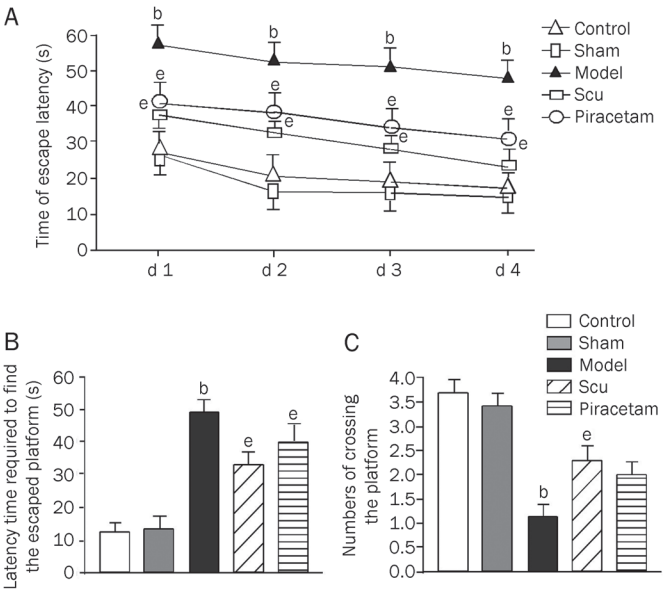

Figure 2. Effects of Scu and piracetam on spatial learning and memory of rats treated previously with Aβ injection. Spatial learning and memory were tested in a Morris Water Maze involving a circular pool 180 cm in diameter. Following four trials daily for 4 d, the average escaping latency of rats in different groups during training session was conducted (A); on d 5 the platform was removed, and latency trials (B) and the number of times the central platform was crossed was counted (C). Values in the bar graphs are means±SD of 10 rats. $^{b}P<0.05$ as compared to normal groups and sham operation groups. $^{e}P<0.05$ as compared to model groups, as determined by an analysis of the variance ANOVA with Tukey-Kramer using SPSS15.0 software.

memory deficit model group, while no significant difference of these receptor levels was observed when compared to the piracetam treatment. There was no change in β2 nAChR subunit protein level among different groups (Figure 3). No significant changes in the mRNA levels of α4, α7, and β2 nAChR subunits were observed (Figure 4).

Activities of AChE and BuChE in brain and plasma

The activities of AChE and BuChE in the brain were significantly increased in the learning and memory deficit model group as compared to the control and the sham operation groups. However, the activities in both enzymes in plasma were significantly lower in the learning and memory deficit model group than those in the control and the sham operation groups. However, treatment by Scu or piracetam restored the activities in brain and plasma to near those of the control group (Figure 5).

Discussion

Aβ, the major component in amyloid plaques of AD brains, is a 39- to 43-amino acid peptide derived from APP. Numerous groups have demonstrated that icv injection of several types of Aβ, including $Aβ_{1–42}$, $Aβ_{1–40}$, and $Aβ_{25–35}$ (the neurotoxic domain of the full-length Aβ), into rats or mice impairs

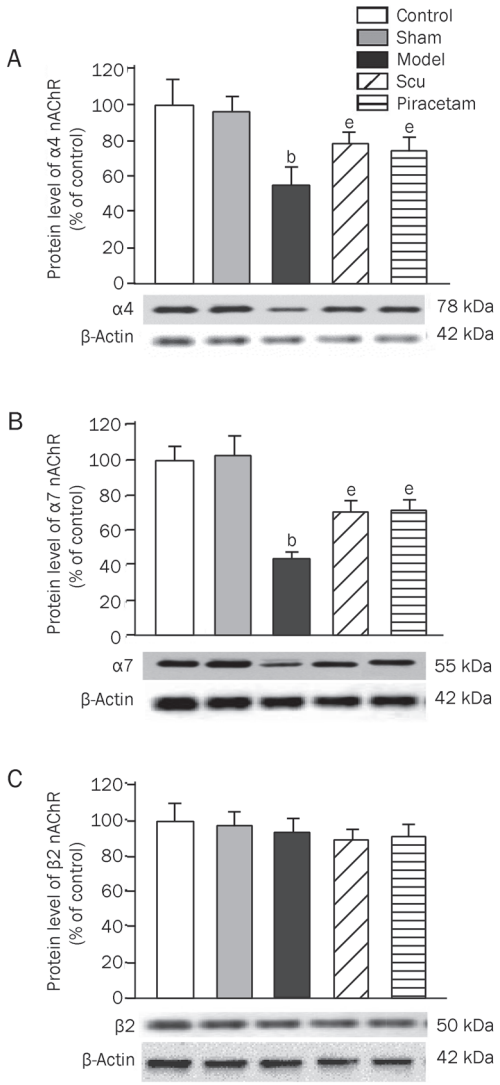

Figure 3. Expressions of α4, α7, and β2 nAChR subunits at protein level in the rat brains. The nAChR α4 (A), α7 (B), and β2 (C) subunit proteins in the rat brains as well as β-actin (as an internal standard) were measured by Western blotting. For the calculation of Western blotting results, β-actin (a house-keeping gene) was used as an internal standard, and the resultant values (as compared with β-actin) were expressed as a percentage of the average value for controls (as 100%). $^{b}P<0.05$ as compared to normal group and sham operation group. $^{e}P<0.05$ as compared to model group as determined by an analysis of the variance ANOVA with Tukey-Kramer using SPSS15.0 software.

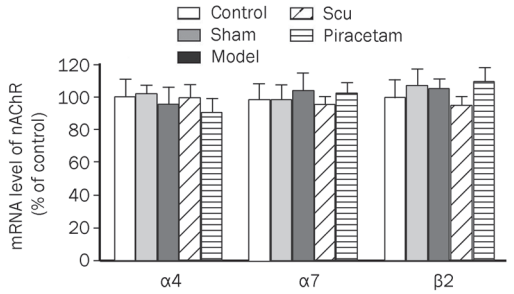

Figure 4. Expressions of α4, α7, and β2 nAChR subunits at mRNA level in the rat brains. The mRNAs of nAChR α4, α7, and β2 subunits as well as β-actin (as an internal standard) were measured by real-time PCR. The results are expressed as the ratio of detected signal for each mRNA of nAChR subunit to their respective β-actin signal and then the CT values were calculated as the percentages of controls (as 100%). The data were analyzed by an analysis of the variance ANOVA with Tukey-Kramer using SPSS15.0 software.

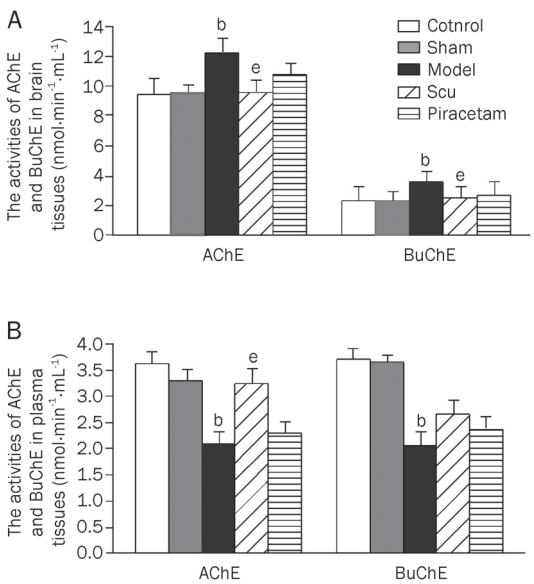

Figure 5. Activities of AChE and BuChE in the rat brains (A) and plasma (B). The activities of AChE and BuChE were determined by the improved Ellman's colorimetric method. $^{b}P<0.05$ as compared to normal and sham operation groups. $^{e}P<0.05$ as compared to model group as determined by an analysis of the variance ANOVA with Tukey-Kramer using SPSS15.0 software.

learning and memory[25–28]. We have previously reported high levels of apoptosis in neuronal cultures induced by $A\beta_{1-40}$ and $A\beta_{25-35}$, while the reversed sequence $A\beta_{35-25}$ had no effect[29]. In this study, we observed that the rats treated with $A\beta_{25-35}$ icv exhibited impaired learning and memory, as demonstrated by increases in the escape latency period and the time required to pass the platform, and the decrease in the numbers of crossing the platform.

The nAChRs are ligand-gated ion channels consisting of five subunits that form a central, cation-permeable channel[30]. The nAChRs are generated from α (α2–α10) and β (β2–β4) subunits[31] and the most abundant nAChR subtypes in brains are α4β2 and α7[32]. A number of studies have indicated that deficient numbers of nAChRs play an important role in AD pathogenesis, specifically, a resultant decrease in α7, α4, and α3 nAChR subunit proteins, but the amount of β2 does not change in models of AD or AD brains[33]. Interestingly, changed α3 and β2 nAChR subunits, but not α4, were observed in the brains of patients with Parkinson disease[34]. For this study, goat polyclonal anti-α4 and -β2 antibodies and

mouse monoclonal anti-α7 antibody were purchased from Santa Cruz Biotechnology Inc to detect the level of nAChR proteins. In our previous publications, the specific immunoreactivity of these antibodies has been well characterized and could identify the different nAChR subunits[33]. In this study, decreased expression of α4 and α7 nAChR subunits was observed in the brains of rats treated with Aβ, suggesting a toxic effect of Aβ on the receptors. Meanwhile, consistent with previous reports, no change occurred in β2 nAChR subunit[35], in which the mechanism may be related to that the β subunit is considered as a structural rather than functional part and less influenced by Aβ[35]. In addition, despite differences in protein levels, we did not find any significant changes of α4, α7, or β2 nAChR subunit mRNA among the different groups, suggesting that the Aβ-mediated effect on nAChRs may be post-translational[36].

ChEs are a group of serine hydrolases with two major forms, AChE and BuChE. The two enzymes differ in substrate specificity, kinetics and activity in different brain regions[37], but they work synergistically to terminate ACh signaling by hydrolyzing, and thereby inactivating the transmitter. It has been proposed that AChE may interact with Aβ to promote fibrillogenesis and the deposition of amyloid plaques[38], which might induce ACh downregulation and the degeneration or death of cholinergic neurons[14]. BuChE is biochemically related to AChE, and in particular, catalyzes the hydrolysis of ACh along with AChE, and thus serves as a co-regulator of cholinergic transmission[39]. Activities of both AChE and BuChE were reduced in plasma from AD patients. In our previous study, we also found the decreased activity of AChE in plasma of AD patients, which may reflect the altered central cholinergic function[40]. However, it has been reported that despite an overall decrease in the amount of AChE, the activity of the enzyme is increased around Aβ plaques in AD brains[41, 42]. This paradoxical finding may be due to the toxic Aβ affecting the catalysis of ACh. In this study, the activities of AChE and BuChE were significantly decreased in plasma but increased in brain tissues of the rats from the learning and memory deficit group, findings that correlate with previously reported results.

To date, there are no effective pharmacological interventions for AD, a fact that has stimulated interest in alternative therapies[43], including traditional Chinese medicines[44]. HE is produced mainly in the Chinese regions of Hunan, Guizhou, Yunnan and Tibet and has been extensively used to treat brain injury, cardiovascular disorders and other diseases. It has been reported that a commercial herbal extract of HE, breviscapine (in which Scu is a major active principle), can improve learning and memory and protect against brain injury[45, 46]. In addition, flavones, one of the major components of HE, have been shown to possess neuroprotective effects[9] and inhibit formation of reactive oxygen species[47–50]. Furthermore, Scu can inhibit Aβ aggregation and prevent cell death induced by Aβ in cultured PC12 cells[1, 3].

In this study, the rats were injected with Aβ to induce learning and memory dysfunction and then treated with Scu extracted from HE in order to investigate the effects of the compound on learning and memory function, expression of nAChRs and the activity of ChE. The results we obtained here showed that Scu rescued behavioral deficits induced by icv injected Aβ. This treatment also prohibited the decreased expression of α4 and α7 nAChR subunit proteins and recovered the activities of AChE and BuChE to normal levels in the AD animal model. Because the functions of nAChRs and ChE are believed to be integral to the processes of learning and memory, the results here indicate that Scu may stimulate cholinergic neuroprotective effects to ameliorate learning and memory dysfunction. Another possibility is that the positive effect of Scu on the cognitive deficits of the animals might be mediated via a direct or indirect effect through nAChRs against Aβ toxicity[29], a hypothesis we plan to investigate in future studies.

Preclinical research suggests that piracetam, a neurotropic drug, may improve cognitive functions in AD patients[51], possibly due to its ability to bind several central nervous system neurotransmitter receptors to protect against neuronal damage[52]. Therefore, we utilized the drug as a positive drug control in the study. The results here also showed that Scu and piracetam had similar effects. For some of the results, such as the rescue of cognitive deficits and enhanced activity of ChE, Scu was more effective than piracetam.

In summary, an acute Aβ treatment can induce learning and memory dysfunction in rats, inhibit expression of nAChR subunit proteins in the brain, and affect activity levels of AChE and BuChE in the brain or plasma. Importantly, Scu may reverse some of these outcomes. The results suggest that the mechanism concerning the protective effect of Scu on learning and memory deficit of rats induced by Aβ might involve stimulating expression of nAChRs and regulating activity of ChE, an insight that may provide an important therapeutic strategy for AD.

Acknowledgements

This work was financed by grants from the National Natural Science Foundation (No 30870986), the Foundations in the Ministry of Science and Technology of China (2006DFA33530), and the Foundations in the Guizhou Province of China.

Author contribution

Li-li GUO performed experiments, analyzed data and wrote the paper; Zhi-zhong GUAN designed research, performed revisions, and approved the final version to be published; Yong-lin WANG carried out the isolation and the analysis of Scu.

References

1 Zhu JT, Choi RC, Li J, Xie HQ, Bi CW, Cheung AW, *et al*. Estrogenic and neuroprotective properties of scutellarin from erigeron breviscapus: a drug against postmenopausal symptoms and Alzheimer's disease. Planta Med 2009; 75: 1489–93.

2 Miksicek RJ. Commonly occurring plant flavonoids have estrogenic activity. Mol Pharmacol 1993; 44: 37–43.

3 Zhu JT, Choi RC, Chu GK, Cheung AW, Gao QT, Li J, *et al*. Flavonoids possess neuroprotective effects on cultured pheochromocytoma PC12 cells: a comparison of different flavonoids in activating estrogenic effect and in preventing beta-amyloid-induced cell death. J Agric Food Chem 2007; 55: 2438–45.
4 Wang CN, Chi CW, Lin YL, Chen CF, Shiao YJ. The neuroprotective effects of phytoestrogens on amyloid beta protein-induced toxicity are mediated by abrogating the activation of caspase cascade in rat cortical neurons. J Biol Chem 2001; 276: 5287–95.
5 Kim H, Park BS, Lee KG, Choi CY, Jang SS, Kim YH, *et al*. Effects of naturally occurring compounds on fibril formation and oxidative stress of beta-amyloid. J Agric Food Chem 2005; 53: 8537–41.
6 Henderson VW, Paganini-Hill A, Miller BL, Elble RJ, Reyes PF, Shoupe D, *et al*. Estrogen for Alzheimer's disease in women: randomized, double-blind, placebo-controlled trial. Neurology 2000; 54: 295–301.
7 Zhang HF, Hu XM, Wang LX, Xu SQ, Zeng FD. Protective effects of scutellarin against cerebral ischemia in rats: evidence for inhibition of the apoptosis-inducing factor pathway. Planta Med 2009; 75: 121–6.
8 Lin LL, Liu AJ, Yu XH, Qin LP, Su DF. Protective effects of scutellarin and breviscapine on brain and heart ischemia in rat. J Cardiovasc Pharmacol 2005; 50: 327–32.
9 Barrantes FJ, Borroni V, Vallés S. Neuronal nicotinic acetylcholine receptor–cholesterol crosstalk in Alzheimer's disease. FEBS Lett 2010; 584: 1856–63.
10 Bayer TA, Wirths O. Intracellular accumulation of amyloid-beta-a predictor for synaptic dysfunction and neuron loss in Alzheimer's disease. Front Aging Neurosci 2010; 10: 2–8.
11 Guglielmotto M, Giliberto L, Tamagno E, Tabaton M. Oxidative stress mediates the pathogenic effect of different Alzheimer's disease risk factors. Front Aging Neurosci 2010; 9: 2–3.
12 Kubo T, Nishimura S, Kumagae Y, Kaneko I. *In vivo* conversion of racemized beta-amyloid ([D-Ser 26] A beta 1–40) to truncated and toxic fragments ([D-Ser 26]A beta 25–35/40) and fragment presence in the brains of Alzheimer's patients. J Neurosci Res 2002; 70: 474–83.
13 Perry E, Walker M, Grace J, Perry R. Acetylcholine in mind: a neurotransmitter correlate of consciousness? Trends Neurosci 1999; 22: 273–80.
14 Mesulam M. The cholinergic lesion of Alzheimer's disease: pivotal factor or side show? Learn Mem 2004; 11: 43–9.
15 Paterson D, Nordberg A. Neuronal nicotinic receptors in the human brain. Prog Neurobiol 2000; 61: 75–111.
16 Lippiello P, Letchworth SR, Gatto GJ, Traina VM, Bencherif M. Ispronicline: a novel alpha4beta2 nicotinic acetylcholine receptor-selective agonist with cognition-enhancing and neuroprotective properties. J Mol Neurosci 2006; 30: 19–20.
17 Viegas C Jr, Bolzani Vda S, Barreiro EJ, Fraga CA. New anti-Alzheimer drugs from biodiversity: the role of the natural acetylcholinesterase inhibitors. Mini Rev Med Chem 2005; 5: 915–26.
18 Kamal MA, Qu X, Yu QS, Tweedie D, Holloway HW, Li Y, *et al*. Tetrahydrofurobenzofuran cymserine, a potent butyrylcholinesterase inhibitor and experimental Alzheimer drug candidate, enzyme kinetic analysis. J Neural Transm 2008; 115: 889–98.
19 Zhao B, Yang HJ, Zhao J. Development of an assay for screening beta-amyloid aggregation inhibitors *in vitro* and study on inhibitive activity of fridelin. Chin Pharm J 2005; 40: 1474–7.
20 Paxinos G, Watson C. The rat brain in stereotaxic coordinates. New York: Academic Press; 1982.
21 Morris R. Developments of a water-maze procedure for studying spatial learning in the rat. J Neurosci Methods 1984; 11: 47–60.
22 Liu RY, Gu R, Qi XL, Tang Z, Zhao Y, He Y, *et al*. Decreased nicotinic receptors and cognitive deficit in rats intracerebroventricularly injected with beta-amyloid peptide(1–42) and fed a high-cholesterol diet. J Neurosci Res 2008; 86: 183–93.
23 An Y, Qi XL, Pei JJ, Tang Z, Xiao Y, Guan ZZ. Amyloid precursor protein gene mutated at Swedish 670/671 sites *in vitro* induces changed expression of nicotinic acetylcholine receptors and neurotoxicity. Neurochem Int 2010; 57: 647–54.
24 Ellman G, Courtney D, Andres V, Feather RM. A new and rapid colorimetric determination of acetylcholinesterase activity. Biochem Pharmacol 1961; 7: 88–95.
25 Yamaguchi Y, Miyashita H, Tsunekawa H, Mouri A, Kim HC, Saito K, *et al*. Effects of a novel cognitive enhancer, spiro[imidazo-[1,2-a] pyridine-3,2-indan]-2(3*H*)-one (ZSET1446), on learning impairments induced by amyloid-beta1–40 in the rat. J Pharmacol Exp Ther 2006; 317: 1079–87.
26 Mazzola C, Micale V, Drago F. Amnesia induced by beta-amyloid fragments is counteracted by cannabinoid CB1 receptor blockade. Eur J Pharmacol 2003; 477: 219–25.
27 Wang CN, Chi CW, Lin YL, Chen CF, Shiao YJ. The neuroprotective effects of phytoestrogens on amyloid beta protein-induced toxicity are mediated by abrogating the activation of caspase cascade in rat cortical neurons. J Biol Chem 2001; 276: 5287–95.
28 Jhoo JH, Kim HC, Nabeshima T, Yamada K, Shin EJ, Jhoo WK, *et al*. Beta-amyloid (1–42)-induced learning and memory deficits in mice: involvement of oxidative burdens in the hippocampus and cerebral cortex. Behav Brain Res 2004; 155: 185–96.
29 Guan ZZ, Miao H, Tian JY, Unger C, Nordberg A, Zhang X. Suppressed expression of nicotinic acetylcholine receptors by nanomolar? amyloid peptides in PC12 cells. J Neural Transm 2001; 108: 1417–33.
30 Steven DB, Andrew KJ, Laurence AB, David BS. Nicotinic acetylcholine receptor signalling: roles in Alzheimer's disease and amyloid neuroprotection. Pharmacol Rev 2009; 61: 39–61.
31 Dani JA, Bertrand D. Nicotinic acetylcholine receptors and nicotinic cholinergic mechanisms of the central nervous system. Annu Rev Pharmacol Toxicol 2007; 47: 699–729.
32 Lindstrom JM. Nicotinic acetylcholine receptors of muscles and nerves: comparison of their structures, functional roles, and vulnerability to pathology. Ann N Y Acad Sci 2003; 998: 41–52.
33 Guan ZZ, Zhang X, Ravid R, Nordberg A. Decreased protein levels of nicotinic receptor subunits in the hippocampus and temporal cortex of patients with Alzheimer's disease. J Neurochem 2000; 74: 237–43.
34 Guan ZZ, Nordberg A, Mousavi M, Rinne JO, Hellström-Lindahl E. Selective changes in the levels of nicotinic acetylcholine receptor protein and of corresponding mRNA species in the brains of patients with Parkinson's disease. Brain Res 2002; 956: 358–66.
35 Court J, Martin-Ruiz C, Piggott M. Nicotinic receptor abnormalities in Alzheimer's disease. Biol Psychiatry 2001; 49: 175–84.
36 Kihara T, Shimohama S. Alzheimer's disease and acetylcholine receptors. Acta Neurobiol Exp 2004; 64: 99–105.
37 Patocka J, Kuca K, Jun D. Acetylcholinesterase and butyrylcholinesterase–important enzymes of human body. Acta Medica (Hradec Kralove) 2004; 47: 215–28.
38 Rees T, Hammond PI, Soreq H, Younkin S, Brimijoin S. Acetylcholinesterase promotes beta-amyloid plaques in cerebral cortex. Neurobiol Aging 2003; 24: 777–87.
39 Geula C, Darvesh S. Butyrylcholinesterase, cholinergic neurotransmission and the pathology of Alzheimer's disease. Drugs Today (Barc) 2004; 40: 711–21.
40 Zhang LJ, Xiao Y, Qi XL, Shan KR, Pei JJ, Kuang SX, *et al*. Cholinesterase activity and mRNA level of nicotinic acetylcholine receptors (alpha4 and beta2 Subunits) in blood of elderly Chinese diagnosed as

Alzheimer's disease. J Alzheimers Dis 2010; 19: 849–58.
41 Mesulam MM, Asuncion Morán M. Cholinesterases within neurofibrillary tangles related to age and Alzheimer's disease. Ann Neurol 1987; 22: 223–8.
42 Ulrich J, Meier-Ruge W, Probst A, Meier E, Ipsen S. Senile plaques: staining for acetylcholinesterase and A4 protein: a comparative study in the hippocampus and entorhinal cortex. Acta Neuropathol 1990; 80: 624-8.
43 Melnikova I. Therapies for Alzheimer's disease. Nat Rev Drug Discov 2007; 6: 341–2.
44 Howes MJ, Houghton PJ. Plants used in Chinese and Indian traditional medicine for improvement of memory and cognitive function. Pharmacol Biochem Behav 2003; 75: 513–27.
45 Liu JX, Liu Y, Chen XL, Zhao JJ, Song TS, Qian YH. Breviscapine improves functions of spatial learning and memory of focal cerebral ischemia rats. Zhong Yao Cai (Chinese) 2009; 32: 548–56.
46 Xiong Z, Liu C, Wang F, Li C, Wang W, Wang J, *et al*. Protective effects of breviscapine on ischemic vascular dementia in rats. Biol Pharm Bull 2006; 29: 1880–5.
47 Liu H, Yang XL, Zhou LZ, Xu HB. Study on reactive oxygen species scavenging effects of scutellarin. J Chin Med Mat 2002; 25: 491–3.
48 Liu H, Yang XL, Wang Y, Tang XQ, Jiang DY, Xu HB. Protective effects of scutellarin on superoxide-induced oxidative stress in rat cortical synaptosomes. Acta Pharmacol Sin 2003; 24: 1113–7.
49 Xu W, Zha RP, Wang WY, Wang YP. Effects of scutellarin on PKC in PC12 cell injury induced by oxygen and glucose deprivation. Acta Pharmacol Sin 2007; 28: 1573–9.
50 Hong H, Liu GQ. Protection against hydrogen peroxide-induced cytotoxicity in PC12 cells by scutellarin. Life Sci 2004; 74: 2959–73.
51 Croisile B, Trillet M, Fondarai J, Laurent B, Mauguière F, Billardon M. Long-term and high-dose piracetam treatment of Alzheimer's disease. Neurology 1993; 43: 301–5.
52 Bering B, Muller WE. Interaction of piracetam with several neurotransmitter receptors in the central nervous system. Arzneim Forsch 1985; 35: 1350–2.

Acta Pharmacologica Sinica (2011) 32: 1454–1459
 1671-4083/11 $32.00
www.nature.com/aps

Original Article

Magnesium sulfate enhances non-depolarizing muscle relaxant vecuronium action at adult muscle-type nicotinic acetylcholine receptor *in vitro*

Hong WANG[1, 2], Qi-sheng LIANG[1], Lan-ren CHENG[1], Xiao-hong LI[1], Wei FU[1], Wen-tao DAI[1], Shi-tong LI[2, *]

[1]*Department of Anesthesiology, the First Affiliated Hospital of Bengbu Medical College, Bengbu 233000, China;* [2]*Department of Anesthesiology, First People's Hospital, School of Medicine, Shanghai Jiaotong University, Shanghai 200030, China*

Aim: To investigate the effect of magnesium sulfate and its interaction with the non-depolarizing muscle relaxant vecuronium at adult muscle-type acetylcholine receptors *in vitro*.
Methods: Adult muscle-type acetylcholine receptors were expressed in HEK293 cells. Drug-containing solution was applied via a gravity-driven perfusion system. The inward currents were activated by brief application of acetylcholine (ACh), and recorded using whole-cell voltage-clamp technique.
Results: Magnesium sulfate (1–100 mmol/L) inhibited the inward currents induced ACh (10 μmol/L) in a concentration-dependent manner (IC_{50}=29.2 mmol/L). The inhibition of magnesium sulfate was non-competitive. In contrast, vecuronium produced a potent inhibition on the adult muscle-type acetylcholine receptor (IC_{50}=8.7 nmol/L) by competitive antagonism. Magnesium sulfate at the concentrations of 1, 3, and 6 mmol/L markedly enhanced the inhibition of vecuronium (10 nmol/L) on adult muscle-type acetylcholine receptors.
Conclusion: Clinical enhancement of vecuronium-induced muscle relaxation by magnesium sulfate can be attributed partly to synergism between magnesium sulfate and non-depolarizing muscle relaxants at adult muscle-type acetylcholine receptors.

Keywords: magnesium sulfate; non-depolarizing muscle relaxant; vecuronium; adult muscle-type acetylcholine receptor; synergism

Acta Pharmacologica Sinica (2011) 32: 1454–1459; doi: 10.1038/aps.2011.117; published online 10 Oct 2011

Introduction

Magnesium sulfate ($MgSO_4$) has long been used in the treatment of eclampsia or placenta previa, which leads anesthesiologists to more frequent encounters with obstetric patients with hypermagnesemia. The choice of anesthetic techniques for Cesarean sections in such patients is the subject of intense debate[1–3]. Although anesthesiologists prefer epidural anesthesia in hypermagnesemic parturients, the risk of coagulopathy or hemodynamic catastrophe often requires anesthesiologists to proceed with urgent general anesthesia.

However, some studies have shown that hypermagnesemia increases the potency of non-depolarizing muscle relaxants, even magnesium, in the range of therapeutic serum concentrations[4–6]. Krendal[7] suggested that magnesium sulfate has a pre-synaptic effect by inhibiting acetylcholine release at motor nerve terminals, effects that may be responsible for the interaction with vecuronium. Furthermore, some studies have shown that increasing extracellular magnesium reduces the size of acetylcholine-evoked responses and the single-channel conductance of nicotinic acetylcholine receptors at the mouse end-plate[8–10].

However, no data regarding a combined effect of magnesium sulfate and non-depolarizing muscle relaxants on nicotinic acetylcholine receptors are available in the literature. To evaluate the mechanism of inhibition of magnesium sulfate and non-depolarizing muscle relaxants on nicotinic acetylcholine receptors, we heterologously expressed nicotinic acetylcholine receptors in human embryonic kidney 293 (HEK293) cells and studied the discrete and combined effects of magnesium sulfate with vecuronium, a non-depolarizing muscle relaxant that is often used in general anesthesia.

Materials and methods

Cell culture and transfection

Expression plasmids [Psp65α, Psp65β, Psp65δ, and Pbssk(+) ε], encoding complementary DNA sequences for the mouse

* To whom correspondence should be addressed.
E-mail lishitongs@163.com
Received 2011-06-16 Accepted 2011-07-20

muscle nicotinic acetylcholine receptor subunits (α, β, δ, and ε, respectively), were provided by the Salk Institute, USA. These coding sequences were subcloned into pcDNA3.1$^+$ (Invitrogen Life Technologies, Carlsbad, CA, USA). Human embryonic kidney 293 (HEK293) cells were cultured in Dulbecco's modified Eagle's medium (Invitrogen, Grand Island, NY, USA) supplemented with 10% calf serum (Invitrogen, Grand Island, NY, USA), 100 units/mL of penicillin, and 100 μg/mL of streptomycin at 37 °C in a 5% CO_2 incubator. The HEK293 cells were stably transfected with Lipofectamine 2000 according to the manufacturer's protocol (Invitrogen Life Technologies, Carlsbad, CA, USA). After transfection, the positive cell clones were selected with G418, an aminoglycoside related to gentamicin, which is commonly used as a selective agent for eukaryotic cells. The transfected cells were then incubated for 24 h before the recordings were made.

Electrophysiology

HEK293 cells were voltage-clamped using the whole-cell patch-clamp technique. Pipettes were pulled from borosilicate glass tubes with a P-97 electrode puller (Sutter Instrument Co, Novato, CA, USA) at a resistance of 2–3 MΩ. The pipette electrode was filled with the following solution (mmol/L): CsCl, 140; $MgCl_2$, 0.8; HEPES-CsOH, 10; EGTA, 0.5; and Na-ATP, 4 (pH 7.3). The external solution contained the following (mmol/L): NaCl, 140; KCl, 2.5; $CaCl_2$, 2; $MgCl_2$, 0.8; HEPES-NaOH, 10; and glucose, 10 (pH 7.3). The $MgSO_4$ solution was composed of the following (mmol/L): NaCl, 140; KCl, 2.5; $MgSO_4$, 1, 10, 30, 50, and 100; HEPES-NaOH, 10; and glucose, 10 (pH 7.3). The cells were voltage-clamped at -80 mV in the whole-cell configuration, and all of the experiments were performed at room temperature (20–24 °C). The currents were measured with an EPC10 amplifier (HEKA Elektronik, Germany) and PatchMaster software (HEKA Elektronik, Germany), sampled at 20 kHz and stored on a computer.

Acetylcholine and magnesium sulfate were purchased from Sigma (Sigma Chemical Co, St Louis, MO, USA). Vecuronium (NV; Organon, the Netherlands) was obtained in preparations for clinical use, dissolved in the external solution or $MgSO_4$ solution and applied by a gravity-driven perfusion system. The solutions and dilutions for the experimental concentrations were prepared immediately before the experiments. The test solutions, containing either acetylcholine alone or in combination with various concentrations of vecuronium or/and magnesium sulfate, were applied for 1 s to the HEK293 cells, and the peak current was then determined. To evaluate the effect of the antagonist on the acetylcholine-elicited current, the solution containing vecuronium or/and magnesium sulfate was perfused on the HEK293 cells for 1 min prior to the application of acetylcholine in the presence of the antagonist. The washout time between each drug application was at least 60 s to minimize the amount of desensitization throughout the course of the experiment. Current was generated in five HEK293 cells. The control current in response to acetylcholine alone was repeated after the washout of the antagonist. Taking the mean value of these two acetylcholine applications as the average control current, the antagonist response was calculated (percentage inhibition of average control current) using the following equation:

$$\%\ \text{Inhibition}=100\times\left(1-\frac{\text{Current in presence of antagonist}}{\text{Average control current}}\right)$$

Statistical analysis

Data analysis was performed offline using Origin 8 (OriginLab, Northampton, MA, USA) and GraphPad Prism 4 (Graphpad Software, Inc, San Diego, CA, USA). Concentration-response curves were fitted to the four-parameter logistic equation by non-linear regression analysis, and the IC_{50} values were determined. The results are expressed as the mean±SD or as the 95% confidence interval (CI). Statistical significance was assessed with paired two-tailed Student's *t*-tests. A $P<0.05$ was considered statistically significant.

Results

Acetylcholine at different concentrations was applied for 1 s to HEK293 cells, which were voltage clamped at -80 mV and expressed the adult muscle-type acetylcholine receptor. The acetylcholine induced inward currents in a dose-dependent fashion. The data were fitted to the logistic equation, and the acetylcholine concentrations producing 50% of the maximal response (EC_{50}) were 19.1 μmol/L (95% CI, 7.9–46.1; Figure 1).

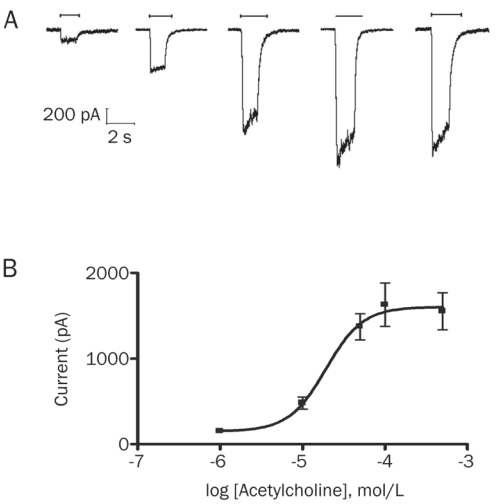

Figure 1. Acetylcholine produces concentration-dependent inward currents in HEK293 cells expressing adult muscle-type acetylcholine receptors. (A) Representative recordings of currents from a single HEK293 cell elicited by 1, 10, 50, 100, and 500 μmol/L acetylcholine (horizontal bars). (B) Concentration-response curve for acetylcholine on adult muscle-type acetylcholine receptor. Data points show the mean±SD of 5 HEK293 cells.

Magnesium sulfate inhibited adult muscle-type acetylcholine receptors

Magnesium sulfate produced a reversible, concentration-

dependent inhibition of 10 μmol/L acetylcholine-induced currents. Fitting the concentration responses of magnesium sulfate to the Hill equation yielded IC_{50} values of 29.2 mmol/L (95% CI, 14.7–58.0; Figure 2). The inhibitory effect of magnesium sulfate on the adult muscle-type acetylcholine receptors was then studied in more detail. The inward currents evoked from the nicotinic acetylcholine receptors at different acetylcholine concentrations, in the absence and presence of magnesium sulfate, are shown in Figure 3. The peak inward currents under control conditions were dependent on the acetylcholine concentration. Doses of 3 mmol/L and 30 mmol/L magnesium sulfate reduced the nicotinic acetylcholine receptor-mediated inward currents at all of the acetylcholine concentrations studied. Increasing the concentrations of acetylcholine did not overcome the inhibition produced by magnesium sulfate.

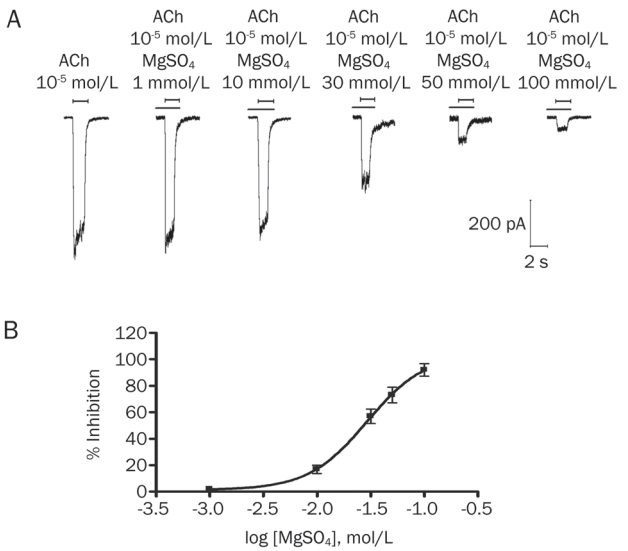

Figure 2. Concentration-dependent effects of magnesium sulphate on adult muscle-type acetylcholine receptors expressed in HEK293 cells. (A) Tracing represent raw currents observed during the application of acetylcholine (ACh; 10 μmol/L for 1 s), either alone or in combination with 1, 10, 30, 50, and 100 mmol/L magnesium sulphate ($MgSO_4$). (B) Concentration-response effect for $MgSO_4$ for inhibition of acetylcholine-induced (10 μmol/L) inward currents mediated by adult muscle-type acetylcholine receptor. Data points show the mean±SD of 5 HEK293 cells.

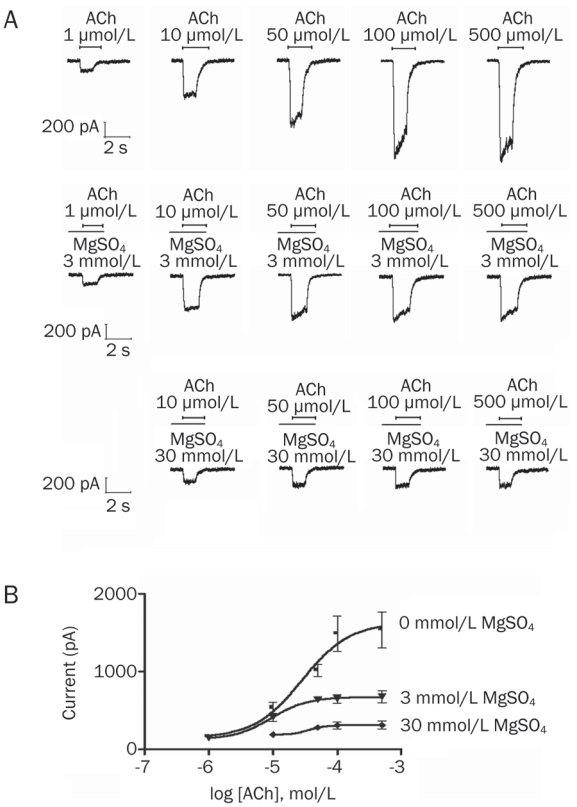

Figure 3. Effect of magnesium sulphate ($MgSO_4$) on the concentration-response of acetylcholine (ACh) on adult muscle-type acetylcholine receptor. (A) Inward currents evoked by superfusion of 1, 10, 50, 100, and 500 μmol/L ACh alone (as indicated by horizontal bars) during control conditions and co-application of 3 and 30 mmol/L $MgSO_4$. $MgSO_4$ was pre-applied for 60 s before co-application with 1, 10, 50, 100, and 500 μmol/L ACh. (B) The effect on inward currents mediated by adult muscle-type acetylcholine receptor over a range of acetylcholine concentrations in the presence of 0, 3, and 30 mmol/L magnesium sulphate ($MgSO_4$). Data points represent the mean±SD of 5 HEK293 cells.

Vecuronium inhibited adult muscle-type acetylcholine receptor

Vecuronium also produced a potent inhibition of the adult muscle-type acetylcholine receptors. Fitting the concentration responses of vecuronium to the Hill equation yielded IC_{50} values of 8.7 nmol/L (95% CI, 5.5–13.6; Figure 4). Furthermore, at increasing acetylcholine concentrations, there was a significant decrease in the inhibition of the acetylcholine currents produced by 10 nmol/L vecuronium. At an agonist concentration of 1 μmol/L acetylcholine, 10 nmol/L vecuronium produced an inhibition of 91%±7% (n=5), whereas at 100 μmol/L acetylcholine, the inhibition was only 9%±2% (n=5), consistent with a competitive inhibition (Figure 5).

Interaction between magnesium sulfate and vecuronium on adult muscle-type acetylcholine receptors

To explore the interaction between magnesium sulfate and vecuronium on the function of the adult muscle-type acetylcholine receptor, we co-applied magnesium sulfate and vecuronium at different concentrations to adult muscle-type acetylcholine receptors. The different concentrations of magnesium sulfate resulted in a strong enhancement of the 10 nmol/L vecuronium-induced inhibition (P<0.01; Figure 6). Representative recordings of the raw data for both magnesium sulfate and vecuronium are shown in Figure 7.

Discussion

It has been shown that the action of non-depolarizing muscle relaxants is significantly prolonged in the presence of therapeutic serum levels of magnesium[11]. The mechanism of inter-

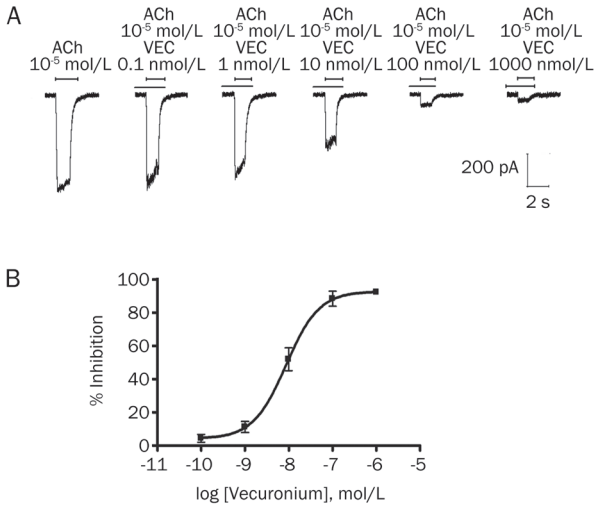

Figure 4. Concentration-dependent effects of vecuronium on adult muscle-type acetylcholine receptors expressed in HEK293 cells. (A) Tracing represent raw currents observed during the application of acetylcholine (ACh; 10 μmol/L for 1 s), either alone or in combination with 0.1, 1, 10, 100, and 1000 nmol/L vecuronium (VEC). (B) Concentration-response effect for vecuronium for inhibition of acetylcholine (10 μmol/L)-induced inward currents mediated by adult muscle-type acetylcholine receptor. Data points show the mean±SD (error bars) of 5 HEK293 cells.

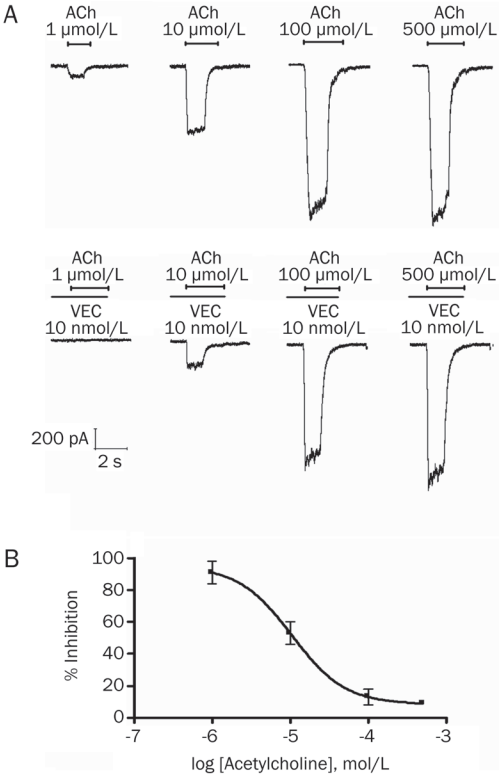

Figure 5. Effect of vecuronium (VEC) on the concentration-response of acetylcholine (ACh) on adult muscle-type acetylcholine receptor. (A) Inward currents evoked by superfusion of 1, 10, 100, and 500 μmol/L ACh alone (as indicated by horizontal bars) during control conditions and co-application of 10 nmol/L vecuronium. Vecuronium was pre-applied for 60 s before co-application with 1, 10, 100, and 500 μmol/L ACh. (B) The effect on inward currents mediated by adult muscle-type acetylcholine receptor over a range of acetylcholine concentrations in the presence of 10 nmol/L vecuronium. Data points represent the mean±SD (error bars) of 5 HEK293 cells.

action for this process was considered to be the pre-synaptic effects of magnesium sulfate; however, this study found that this potentiation of non-depolarizing muscle relaxants by magnesium can be attributed in part to a combined effect on adult muscle-type acetylcholine receptors.

Our study showed that magnesium sulfate produced a concentration-dependent inhibition of the adult muscle-type acetylcholine receptor-mediated inward currents. The IC_{50} value of magnesium sulfate was 29.2 mmol/L, which far exceeds the serum magnesium concentrations in therapeutic ranges[5, 6] and suggested that, in the range of therapeutic concentrations, magnesium alone could not attain a clinically acceptable neuromuscular inhibition. Our findings also showed that the inhibition of the nicotinic acetylcholine receptor function by magnesium sulfate was insurmountable by merely increasing the concentrations of acetylcholine, indicating that magnesium sulfate acts as a non-competitive inhibitor of the adult muscle-type acetylcholine receptor. This effect has been ascribed to the high-affinity interactions of divalent cations with negative residues in the channel that decrease the local ion concentration[12].

Consistent with previous studies[13–15], our study also showed that vecuronium potently inhibited the adult muscle-type acetylcholine receptor. It is widely recognized that non-depolarizing muscle relaxants inhibit nicotinic acetylcholine receptors by a competitive mechanism[16, 17]. In this study, an increasing acetylcholine concentration up to 500 μmol/L was able to overcome the inhibition of vecuronium on adult muscle-type acetylcholine receptors, confirming that vecuronium acts in a competitive manner.

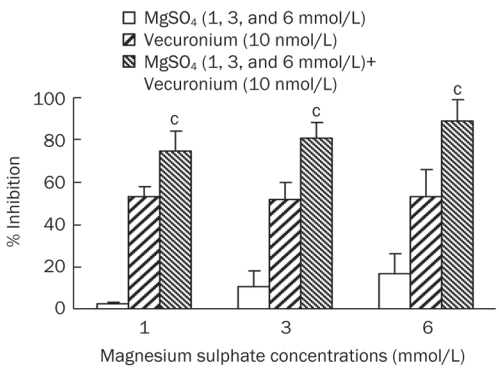

Figure 6. Graphic representation of the enhancement of percentage inhibition of acetylcholine-induced (10 μmol/L) currents with vecuronium and magnesium sulphate ($MgSO_4$). $^cP<0.01$ *vs* vecuronium.

To determine whether magnesium sulfate and vecuronium have an interactive effect, we observed the interaction between

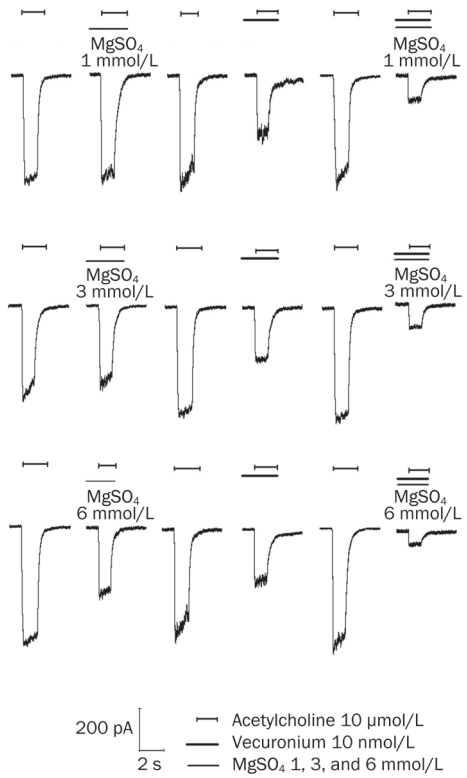

Figure 7. Effect of 10 nmol/L vecuronium and 1, 3, and 6 mmol/L magnesium sulphate ($MgSO_4$) alone and in combination on acetylcholine-induced (10 μmol/L) inward currents mediated by adult muscle-type acetylcholine receptor. Horizontal bars indicate drug applications. $MgSO_4$, vecuronium, and the combination of both drugs were pre-applied for 60 s before co-application with 10 μmol/L acetylcholine. After each drug application, a 10 μmol/L acetylcholine-induced inward current was obtained as a control (last control not shown).

three different concentrations of magnesium sulfate (1, 3, and 6 mmol/L) and vecuronium (10 nmol/L). Consistent with previous work[4–6], our findings also showed a marked enhancement of the potency of vecuronium by magnesium sulfate with all three of the concentrations tested. Fuchs-Buder *et al*[6] reported that an intravenous infusion of magnesium at 40 mg/kg significantly potentiated the neuromuscular blockage of vecuronium, and plasma magnesium concentrations increased from a baseline concentration of 0.9±0.06 to 1.08±0.07 mmol/L 15 min after the magnesium sulfate infusion ($P<0.05$). Although this increase in plasma concentration of magnesium in patients pre-treated with magnesium sulfate was statistically significant, the administration of these doses was deemed clinically safe, as no symptoms of muscle weakness were reported by the patients. In addition, Baraka and Yazigi[18] found no clinical or electromyographic signs of muscle weakness, even at slightly higher plasma magnesium concentrations (1.7–2.5 mmol/L). Thus, in the present study, the potentiation of vecuronium by a 1 mmol/L magnesium may have more clinical significance.

During the course of our study, we used a concentration of 10 μmol/L of acetylcholine as an agonist. This concentration can ensure sufficient acetylcholine current responses and minimize the desensitization of the nicotinic acetylcholine receptor that resulted from the repetitive application of acetylcholine[13, 14]. In this study, the HEK293 cells were clamped at -80 mV because the antagonistic effects of non-depolarizing muscle relaxants are independent of the holding voltages that range from -100 to -40 mV[13, 15, 19, 20].

Conclusion

In conclusion, our results demonstrate that the presence of magnesium in the range of therapeutic serum concentrations could significantly intensified the potency of vecuronium on adult muscle-type acetylcholine receptors. These results suggest that the interaction between magnesium and non-depolarizing muscle relaxants on adult muscle-type acetylcholine receptors can partly explain how magnesium enhances a non-depolarizing muscle relaxant-induced neuromuscular blockade.

Acknowledgements

This work was supported by the National Natural Science Foundation of China (No 30571796).

Author contribution

Hong WANG and Shi-tong LI designed the research; Hong WANG and Qi-sheng LIANG performed the research; Xiao-hong LI and Lan-ren CHENG analyzed the data; and Hong WANG, Wei FU, and Wen-tao DAI wrote the paper.

Abbreviations

$MgSO_4$, magnesium sulfate; HEK293, human embryonic kidney 293; nAChR, nicotinic acetylcholine receptor; IC_{50}, half-maximal response; DMEM, Dulbecco's modified Eagle's medium; ACh, acetylcholine; VEC, vecuronium.

References

1 Howell P. Spinal anesthesia in severe preclampsia: time for reappraisal or time for caution? Int J Obstet Anesth 1998; 7: 217–9.
2 Aya AG, Mangin R, Vialles NV, Ferrer JM, Robert C, Ripart J, *et al*. Patients with severe preeclampsia experience less hypotension during spinal anesthesia for elective cesarean delivery than healthy patients: a prospective cohort comparison. Anesth Analg 2003; 97: 867–72.
3 Lipman S, Carvalho B, Brock-Utne J. The demise of general anesthesia in obstetrics revisited: prescription for a cure. Int J Obstet Anesth 2005; 14: 2–4.
4 Ross RM, Backer T. An effect of magnesium on neuromuscular function in parturients. J Clin Anesth 1996; 8: 202–4.
5 Yoshida A, Itoh Y, Nagaya K, Takino K, Sugawara J, Murakami T, *et al*. Prolonged relaxant effects of vecuronium in patients with deliberate hypermagnesemia: time for caution in cesarean section. J Anesth 2006; 20: 33–5.
6 Fuchs-Buder T, Wilder-Smith OH, Borgeat A, Tassonyi E. Interaction of magnesium sulphate with vecuronium-induced neuromuscular block. Br J Anaesth 1995; 74: 405–9.
7 Krendal DA. Hypermagnesemia and neuromuscular transmission. Semin Neurol 1990; 10: 42–5.

8 McLarnon JG, Quastel DM. Postsynaptic effects of magnesium and calcium at the mouse neuromuscular junction. J Neurosci 1983; 3: 1626–33.
9 Del Castillo J, Engbaek L. The nature of the neuromuscular block produced by magnesium. J Physiol 1954; 124: 370–84.
10 Grassi F, Degasperi V. Modulation of fetal and adult acetylcholine receptors by Ca^{2+} and Mg^{2+} at developing mouse end-plates. Pflugers Arch 2000; 440: 704–9.
11. James MFM. Magnesium in obstetric anesthesia. Int J Obstet Anesth 1988; 7: 115–23.
12 Imoto K, Busch C, Sakmann B, Mishina M, Konno T, Nakai J, *et al*. Rings of negatively charged amino acids determine the acetylcholine receptor channel conductance. Nature 1998; 335: 645–51.
13 Paul M, Kindler CH, Fokt RM, Dresser MJ, Dipp NC, Yost CS. The potency of new muscle relaxants on recombinant muscle-type acetylcholine receptors. Anesth Analg 2002; 94: 597–603.
14 Wang H, Zhang Y, Li ST. The effect of local anesthetics on the inhibition of adult muscel-type nicotinic acetylcholine receptors by nondepolarizing muscle relaxants. Eur J Pharmacol 2010; 630: 29–33.
15 Garland CM, Foreman RC, Chad JE, Holden-Dye L, Walker RJ. The actions of muscle relaxants at nicotinic acetylcholine receptor isoforms. Eur J Pharmacol 1998; 357: 83–92.
16 Sine SM, Taylor P. Relationship between reversible antagonist occupany and the functional capacity of the acetylcholine receptor. J Biol Chem 1981; 256: 6692–9.
17 Fletcher GH, Steinbach JH. Ability of nondepolarizing neuromuscular blocking drugs to act as partial agonists at fetal and adult mouse muscle nicotinic receptors. Mol Pharmacol 1996; 49: 938–47.
18 Baraka A, Yazigi A. Neuromuscular interaction of magnesium with succinylcholine-vecuronium sequence in the eclamptic parturient. Anesthesiology 1987; 67: 806–8.
19 Wang H, Yang B, Xu YF, Yan T, Li ST. Magnitude differences of resistance to different nondepolarizing muscle relaxants in the denervated mouse skeletal muscle. Acta Pharmacol Sin 2010; 31: 399–404.
20 Wang H, Yang B, Han GW, Li ST. Potency of nondepolarizing muscle relaxants at muscle-type acetylcholine receptors in denervated mouse skeletal muscle. Acta Pharmacol Sin 2010; 31: 1541–6.

Acta Pharmacologica Sinica (2011) 32: 1460–1465
 1671-4083/11 $32.00
www.nature.com/aps

Original Article

Differential involvement of $GABA_A$ and $GABA_B$ receptors in propofol self-administration in rats

Bo YANG[1], Ben-fu WANG[1], Miao-jun LAI[2], Fu-qiang ZHANG[2], Xiao-wei YANG[1], Wen-hua ZHOU[2, *], Qing-quan LIAN[1, *]

[1]Department of Anesthesiology of the 2nd Affiliated Hospital and Institute of Neuroendocrinology, Wenzhou Medical College, Wenzhou 325000, China; [2]Ningbo Addiction Research and Treatment Center, School of Medicine, Ningbo University, Ningbo 315010, China

Aim: Propofol has shown abuse potential. The aim of the present study is to investigate the effects of $GABA_A$ antagonist and $GABA_B$ agonist on propofol reinforcement.
Methods: Sprague-Dawley rats were trained to self-administer propofol at a dose of 1.7 mg/kg per infusion under a fixed ratio (FR1) schedule of reinforcement for 14 d. In a separate set of experiments, food-maintained self-administration under a fixed ratio (FR5) schedule and locomotor activities of Sprague-Dawley rats were examined.
Results: $GABA_A$ receptor antagonist bicuculline (0.25 mg/kg, ip) significantly increased the number of injections and active responses. Pretreatment with $GABA_B$ receptor agonist baclofen (3 mg/kg, ip) significantly decreased the number of active responses and total infusions of propofol during the training session. Moreover, microinjection of baclofen (50 and 100 ng/side) into the ventral tegmental area (VTA) significantly decreased the number of active responses and total infusions of propofol. Neither baclofen (1–3 mg/kg, ip) nor bicuculline (0.25–1 mg/kg, ip) affected food-maintained responses or motor activities.
Conclusion: Propofol maintains its reward properties partially through $GABA_A$ receptor activation. Stimulation of $GABA_B$ receptors in VTA may counteract the reinforcing properties of propofol.

Keywords: addiction; propofol; drug abuse; GABA receptors; baclofen; bicuculline; ventral tegmental area (VTA); locomotor activity

Acta Pharmacologica Sinica (2011) 32: 1460–1465; doi: 10.1038/aps.2011.123; published online 10 Oct 2011

Introduction

Propofol (2, 6-disopropylphenol) is an intravenous, short-acting anesthetic that has been widely used for sedation and anesthesia. Clinical surveys reveal that propofol may have abuse potential and dependency[1]. The abuse potential of propofol has also been demonstrated in preclinical studies using conditioned place preference (CPP)[2, 3] and self-administration[4], which are the classic methods for the evaluation of the psychodependence of drugs.

There are two types of neurons within the ventral tegmental area (VTA), primary dopaminergic projection neurons and secondary γ-aminobutyric acid (GABA) inhibitory interneurons. The mesolimbic dopamine system, which originates in the VTA and connects to the nucleus accumbens (NAc), is a critical component of reward and addiction. All drugs of abuse enhance the activity of the mesolimbic dopaminergic circuit of reward, which leads to the release of dopamine (DA) in the NAc[5, 6]. The release of DA in the NAc indicates that the reinforcement potential of propofol may account for the regulation of the activity of the reward pathway. Both $GABA_A$ and $GABA_B$ receptor subtypes have been identified within the VTA. The activation of $GABA_A$ on GABAergic interneurons increases the activity of dopamine neurons in the VTA through disinhibition[7, 8]. In contrast, GABAergic neurons dampen DA neurons via inhibitory $GABA_B$ receptors on dopaminergic VTA neurons[9]. The microinjection of baclofen, a $GABA_B$ receptor agonist, into the VTA reduces heroin-induced DA release in the NAc and inhibits heroin and morphine self-administration in a dose-dependent manner[10]. However, the role of each GABA receptor subtype in propofol reinforcement is not clear. Therefore, the present study examined the effects of baclofen and bicuculline on propofol reinforcement using intravenous self-administration.

Materials and methods

Animals

Experiments were performed in male Sprague-Dawley rats (280–300 g) that were purchased from the Experimental Animal Center of Zhejiang Province (Hangzhou, China). Rats

* To whom correspondence should be addressed.
E-mail lianqingquan@yahoo.com.cn (Qing-quan LIAN);
whzhou@vip.163.com (Wen-hua ZHOU)
Received 2011-03-20 Accepted 2011-08-08

were housed individually in home cages in a temperature-controlled ventilated colony room with a reversed 12–12 h light/dark cycle (lights on at 7:00 pm). *Ad libitum* food and water were provided in the home cage. The Institutional Animal Care and Use Committee of Zhejiang Province approved all procedures. Animal care was provided by trained vivarium staff at the Laboratory of Ningbo Addiction Research and Treatment Center (Ningbo, China). All animals were euthanized by carbon dioxide inhalation after pentobarbital anesthesia at the termination of experiments.

Drugs

Propofol (10 mg/mL; Diprivan, Astrazeneca, Italy) was prepared immediately before use and was injected intravenously. The propofol dose (1.7 mg/kg per infusion) that was used for the self-administration experiments was based on a previous study[4]. Baclofen and bicuculline were purchased from Sigma Chemical Co (St Louis, USA). Both drugs were dissolved in sterile saline.

Apparatus

Thirty-two custom-made operant Plexiglas boxes (Ningbo Addiction Research and Treatment Center, China) were used for propofol training as described previously[10]. Briefly, each box was equipped with two nose-poke apparatuses that were located 5 cm above the floor. There was a green LED light inside of each nose-poke hole. A house light (28 V, 0.1 mA) was situated on the wall above the nose-poke holes. Drug solution was delivered through Tygon tubing that was protected by a leash assembly and suspended through the ceiling of the chamber from a plastic fluid swivel. The leash assembly was modified to fit a custom-made fluid connector that was fixed on the animal's jacket. The Tygon tubing was attached to a syringe pump that delivered fluid at a speed of 1.2 mL/min using a 5-mL syringe. Experimental events were controlled by an IBM-compatible PC using an MED Associates interface and running self-programmed software written in Borland Delphi 6.0.

Surgery

The rats were surgically implanted with chronic indwelling intravenous catheters under sodium pentobarbital anesthesia using a previously described method[10]. The catheters were flushed daily with a 0.2 mL saline-heparin solution (25 U/mL heparin) to maintain catheter patency. The rats were treated post-surgically with penicillin B for 5 d to prevent infection. All of the animals were allowed to recover for at least 7 d[10].

In some experiments, bilateral guide cannulae (20-gauge Small Parts Inc, Roanoke, VA, USA) were implanted in the VTA (6.0 mm posterior to bregma, 1.0 mm lateral to midline, and 7.8 mm ventral to the surface of the cortex using a 10° angle) according to a previously described method[11]. Guide cannulae were lowered into place and attached to the skull via dental acrylic. Obturators were extended 0.5 mm beyond the tip of each cannula to prevent obstruction by debris.

Microinjection procedure

Animals that had been trained for 14 d received microinjections beginning on d 15. Obturators were removed, and bilateral infusion cannulae were inserted to extend 0.5 mm beyond the tip of the guide cannulae. All injections into the VTA were delivered using a microinjection pump (MD-1001, Bioanalytical System Inc, West Lafayette, IN, USA) in a volume of 0.5 μL/side over 5 min.

Propofol self-administration training

The rats were trained to self-administer drugs as described previously[10]. For each daily 3 h training session, the rats were moved from their home cages to the operant chambers, and their connectors were attached to the infusion lines. Each session started with the illumination of the green light inside of the active nose-poke hole. The rats received a single propofol infusion (1.7 mg/kg per infusion) following the completion of the ratio requirement (FR1) in the active nose-poke hole. Each infusion was paired with a 5 s illumination of the house light and the noise of the infusion pump. A time-out period was imposed for 30 s, during which further responses produced no programmed consequences. However, these responses were recorded. Illumination of the green light in the active nose-poke hole signaled the end of the 30 s timeout period. Responses in the inactive nose-poke hole produced no programmed consequences. The sessions ended after 3 h or 50 propofol infusions, which ever event occurred first.

Sucrose self-administration training

The rats were trained to nose poke for sucrose pellets under a fixed ratio (FR5) schedule of reinforcement daily 1-h session for 7 d. The paradigm for sucrose self-administration was similar to the paradigm for heroin self-administration except that rats received a 45 mg sucrose pellet (Dustless precision pellets, Bio-Serv, NJ) that was delivered via a sucrose cup. During the session, each nose-poke in the active hole resulted in the delivery of a food pellet only. Nose pokes in the inactive hole had no programmed consequence. Active nose-poke responses, inactive nose-poke responses, and the number of sucrose pellets that were earned during each training session were recorded by a computer. Twenty minutes prior to the session on d 8, the trained rats received saline, baclofen (1.0, 2.0 or 3.0 mg/kg, ip), or bicuculline (0.25, 0.5, or 1.0 mg/kg, ip).

Locomotor test after withdrawal

We examined the effects of the intraperitoneal administration of either baclofen or bicuculline on locomotion in a novel context to further assess the possible nonspecific effects of baclofen or bicuculline on general activity. The locomotor activity of naïve rats (n=8 in each groups) was monitored for 3 h. The total distance traveled was recorded and analyzed as the measure of locomotion using MED Associates SOF-811 Open-field Activity Software.

Histology

The rats were anesthetized and transcardially perfused with

phosphate-buffered saline followed by a 4% polyformaldehyde solution. The brains were sectioned in the coronal plane to a thickness of 50 μm using a Cryostat Microtome (Leica CM1850; Leica, Wetzlar, Germany). The placement of the cannula tip for infusions was located using light microscopy and mapped onto a schematic diagram of the rat brain using a previously published method[11]. Only animals with a proper functioning cannula and a correct location of the probe were included in the study.

Specific experiments

Experiment 1

Rats were trained for propofol self-administration (1.7 mg/kg per infusion) for 14 d. The rats (n=24) were randomly assigned to one of 4 groups and were injected with vehicle, 1.0 mg/kg, 2.0 mg/kg, or 3.0 mg/kg (ip) baclofen 20 min prior to testing.

Experiment 2

The rats (n=24) underwent the 14-d training and were then injected with vehicle or 0.25 mg/kg, 0.5 mg/kg, or 1.0 mg/kg (ip) bicuculline 20 min prior to testing.

Experiment 3

Bilateral microinjections were performed into VTA as described above. The rats (n=6 in each group) were placed into the self-administration chambers 10 min after intra-VTA baclofen (50 and 100 ng/side) or vehicle injection. Self-administration was examined as described above.

Statistical analysis

The number of infusions or responses in active or inactive holes during self-administration was analyzed using one-way ANOVA. A Newman-Keuls multiple comparison with an alpha level of 0.05 was used for *post hoc* comparisons between group means.

Results

Systemic pretreatment with baclofen decreased propofol self-administration

The animals exhibited reliable propofol self-administration, which was indicated by the increase in active responses and infusions during the acquisition, and maintained stable self-administration during the late training sessions. ANOVA revealed a significant main effect of baclofen treatment on the number of active responses [$F_{(3, 20)}$=3.32, P<0.05] (Figure 1A) and the number of infusions [$F_{(3, 20)}$=8.1, P<0.05] (Figure 1B). There was no significant difference in the number of inactive nose-poke responses between the groups [$F_{(3, 20)}$=0.99, P>0.05] (Figure 1A). Multiple comparisons showed that 3.0 mg/kg baclofen decreased the number of active responses compared to the control group (P<0.01) (Figure 1A). Baclofen at doses of 2.0 or 3.0 mg/kg decreased the number of infusions compared to the control group (P<0.05, P<0.01) (Figure 1B).

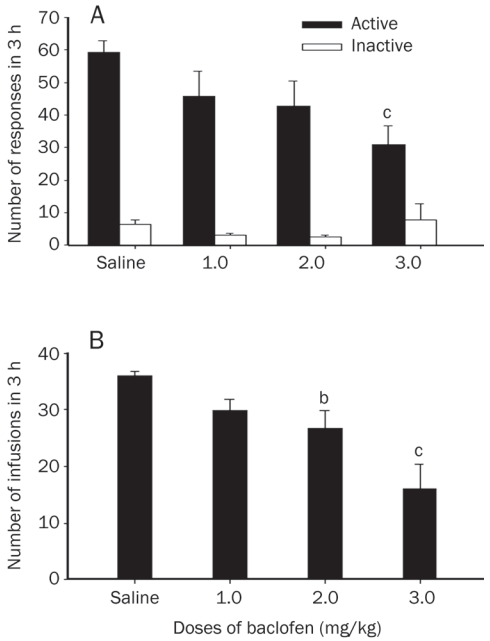

Figure 1. Effect of baclofen on intravenous propofol self-administration under an FR1 schedule. Baclofen (vehicle, 1.0, 2.0, or 3.0 mg/kg, n=6 in each group) was injected ip 20 min before training. Results represent the mean±SEM of the number of total active and inactive responses (A) and infusions (B) in rats. ^{b}P<0.05, ^{c}P<0.01 compared to the saline group.

Systemic pretreatment with bicuculline enhanced propofol self-administration

ANOVA revealed a main effect of bicuculline treatment in the number of active responses [$F_{(3, 20)}$=3.66, P<0.05] (Figure 2A) and the number of infusions [$F_{(3, 20)}$=3.18, P<0.05] (Figure 2B). There was no difference of the number of inactive nose-poke responses between the groups [$F_{(3, 20)}$=1.43, P>0.05] (Figure 2A). Multiple comparisons demonstrated that 0.25 mg/kg bicuculline increased the number of active responses compared to the control group (P<0.01) (Figure 2A). Bicuculline at doses of 0.25 or 0.5 mg/kg increased the number of infusions compared to the control group (P<0.01, P<0.05) (Figure 2B).

Microinjection of baclofen into the VTA inhibited propofol self-administration

ANOVA revealed a main effect of baclofen infusion into the VTA on the number of active responses [$F_{(2, 15)}$=21.23, P<0.05] (Figure 3A) and the number of infusions [$F_{(2, 15)}$=63.51, P<0.05] (Figure 3B). There was no difference in the number of inactive nose-poke responses among the groups [$F_{(2, 15)}$=0.081, P>0.05] (Figure 3A). Multiple comparisons demonstrated that both doses of baclofen significantly decreased the number of active responses (P<0.01) (Figure 3A) and the number of infusions (P<0.01) (Figure 3B).

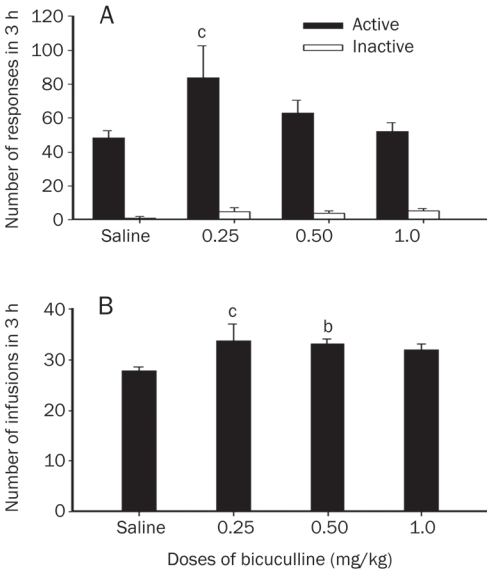

Figure 2. Effect of bicuculline on intravenous propofol self-administration under an FR1 schedule. Bicuculline (vehicle, 0.25, 0.50, or 1.0 mg/kg, n=6 in each group) was injected ip 20 min before training. Results represent the mean±SEM of the number of total active and inactive responses (A) and infusions (B) in rats. ^{b}P<0.05, ^{c}P<0.01 compared to the saline group.

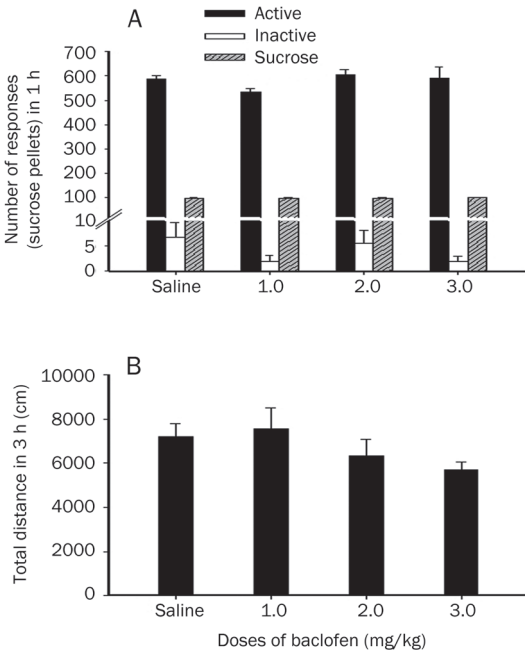

Figure 4. Effects of baclofen on food-maintained self-administration and locomotor activities (A). Baclofen (vehicle, 1.0, 2.0, or 3.0 mg/kg, n=7 in each group) was administered systemically 20 min prior to training. Results represent the mean±SEM number of the total active and inactive responses and sucrose pellets in rats. (B) Baclofen (vehicle, 1.0, 2.0, or 3.0 mg/kg, n=8 in each group) was administered systemically 20 min prior to testing. Each bar represents the mean±SEM distance of rats.

Neither baclofen nor bicuculline affected food-maintained behavior or locomotor activity

One-way ANOVA revealed no apparent variance of baclofen treatment on the number of active [$F_{(3, 24)}$=1.27, P>0.05] or inactive nose-poke responses [$F_{(3, 24)}$=1.36, P>0.05] or the number of sucrose pellets in food-maintained testing [$F_{(3, 24)}$=0.32, P>0.05] (Figure 4A). Pretreatment with bicuculline did not alter the number of active [$F_{(3, 24)}$=0.94, P>0.05] or inactive nose-poke responses [$F_{(3, 24)}$=1.9, P>0.05) or the number of sucrose pellets in food-maintained testing [F(3, 24)=0.32, P>0.05] (Figure 5A). Pretreatment with either baclofen [$F_{(3, 28)}$=1.53, P>0.05] (Figure 4B) or bicuculline [$F_{(3, 28)}$=0.60, P>0.05] (Figure 5B) did not affect the locomotor activity.

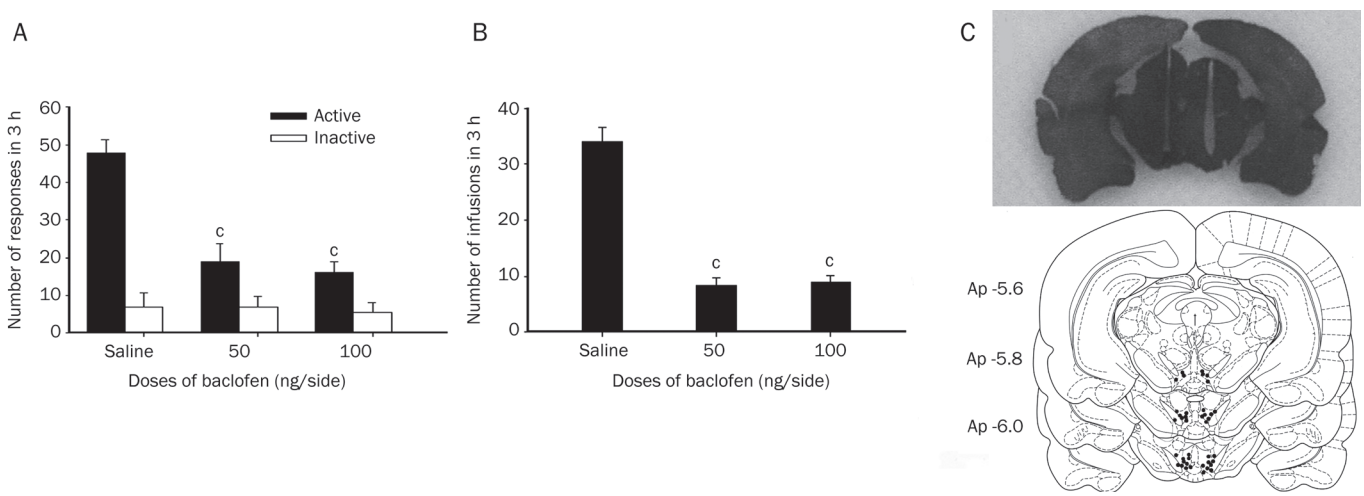

Figure 3. Effect of the microinjection of baclofen into the VTA on intravenous propofol self-administration under an FR1 schedule. Baclofen (vehicle, 50, or 100 ng/side, n=6 in each group) was injected intra-VTA before the beginning of training. Results represent the mean±SEM number of active and inactive responses (A) and infusions (B) in rats. (C) Location of cannula tips in the VTA. Symbols (black spots) indicate where the cannula tips were placed. ^{c}P<0.01 compared to the saline group.

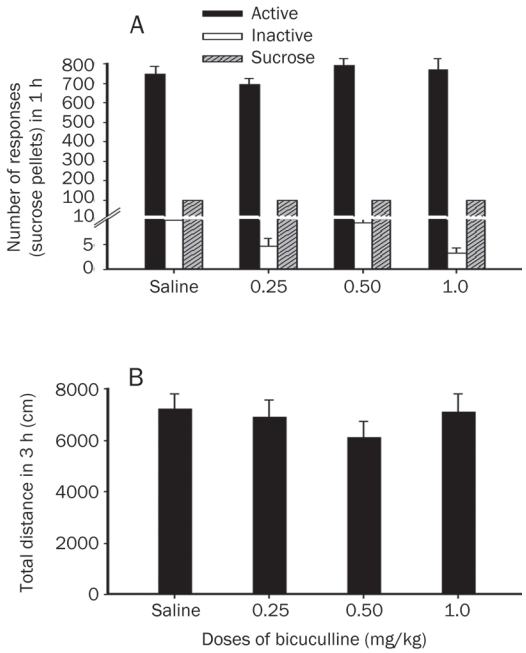

Figure 5. Effects of bicuculline on food-maintained self-administration and locomotor activities (A). Bicuculline (vehicle, 0.25, 0.50, or 1.0 mg/kg, *n*=7 in each group) was administered systemically 20 min prior to training. Results represent the mean±SEM number of the total active and inactive responses and sucrose pellets in rats. (B) Bicuculline (saline, 0.25, 0.50, or 1.0 mg/kg, *n*=8 in each group) was administered systemically 20 min prior to testing. Each bar represents the mean±SEM distance of rats.

Discussion

The main findings of this study are that bicuculline pretreatment at a lower dose increased the active responses and infusions of propofol self-administration. However, baclofen pretreatment using a systemic or intra-VTA infusion reduced the active responses and infusions of propofol self-administration in a dose-dependent manner in rats. Neither bicuculline nor baclofen affected food-maintained responses or locomotor activities. These results suggest that the action of bicuculline or baclofen on propofol reinforcement cannot account for the impairment of coordinated motor ability.

Drugs of abuse enhance DA release in the NAc via a disinhibition of GABAergic neurons in the VTA[12]. Propofol is a positive allosteric modulator of the $GABA_A$ receptor. Benzodiazepines have recently been shown to increase the firing of DA neurons in the VTA via the positive modulation of $GABA_A$ receptors on nearby interneurons[7]. In the present study, a low dose of bicuculline, an antagonist of $GABA_A$ receptors, significantly increased propofol self-administration, which suggests a compensatory enhanced behavioral response as a result of the partial reversal of $GABA_A$ activation by propofol. Both pre-synaptic and post-synaptic $GABA_A$ receptors exist in the VTA. The activation of pre-synaptic $GABA_A$ receptors leads to a decrease in GABA release from GABAergic interneurons and a subsequent increase in dopaminergic neurons. However, the activation of post-synaptic $GABA_A$ receptors may reduce the activity of dopaminergic neurons[13]. A large dose of bicuculline did not affect propofol reinforcement, which may be explained by the blockade of post-synaptic $GABA_A$ receptors. The present results are consistent with previous reports that the disinhibition of $GABA_A$ receptors triggers drug-evoked synaptic plasticity in excitatory afferents that synapse on dopaminergic neurons, which underlies drug reinforcement[7, 14].

The capacity of $GABA_B$ receptors to modulate the DA projection from the VTA to the NAc has been the subject of much research. $GABA_B$ receptor agonists reduce the activity of the mesolimbic DA system via direct actions on dopaminergic VTA neurons[15, 16]. The present results showed that the systemic administration of the $GABA_B$ receptor agonist baclofen inhibited propofol self-administration in a dose-dependent manner. This result suggests that $GABA_B$ receptors regulate the reinforcement of propofol. The results of this study are consistent with those of previous studies of other addictive drugs[17–20]. For example, baclofen inhibits morphine and heroin self-administration in rats[10, 21]. Additionally, baclofen pretreatment antagonizes the morphine-induced increase in DA levels in the NAc, which is mediated by $GABA_B$ receptors[22]. The majority of VTA $GABA_B$ receptors are localized on dopaminergic neurons[23]. The present results also showed that an intra-VTA injection of baclofen reduced propofol self-administration, which is consistent with a previous report that the microinjection of baclofen into the VTA, but not into the NAc, decreases opiate reinforcement[21, 24]. The inhibitory action of baclofen was blocked by an intra-VTA infusion of a $GABA_B$ receptor antagonist[21]. Moreover, the inhibitory action of systemically administered baclofen suggests that baclofen acted on $GABA_B$ receptors on dopaminergic neurons within the VTA to inhibit propofol reinforcement.

In conclusion, the present data provided evidence that propofol maintains its reward properties partially through the activation of $GABA_A$ receptors, but stimulation of the $GABA_B$ receptors in the VTA may counteract the reinforcing of properties of propofol.

Acknowledgements

This study was supported in part by the National Natural Science Foundation of China (30972840) to QL, ZJNSF (Z2101211), QL, WZKJ (Y20100046) BW, and the ZJNSF (D2080515) to WZ.

Author contribution

Bo YANG, Wen-hua ZHOU, and Qing-quan LIAN designed the studies; Bo YANG, Ben-fu WANG, Miao-jun LAI, Fu-qiang ZHANG, and Xiao-wei YANG performed the studies; Bo YANG, and Wen-hua ZHOU analyzed the data; Bo YANG, Wen-hua ZHOU, and Qing-quan LIAN wrote the manuscript.

References

1 Roussin A, Montastruc JL, Lapeyre-Mestre M. Pharmacological and clinical evidences on the potential for abuse and dependence of propofol: a review of the literature. Fundam Clin Pharmacol 2007; 21:

459–66.
2 Pain L, Oberling P, Sandner G, Di Scala G. Effect of propofol on affective state as assessed by place conditioning paradigm in rats. Anesthesiology 1996; 85: 121–8.
3 Pain L, Oberling P, Sandner G, Di Scala G. Effect of midazolam on propofol-induced positive affective state assessed by place conditioning in rats. Anesthesiology 1997; 87: 935–43.
4 LeSage MG, Stafford D, Glowa JR. Abuse liability of the anesthetic propofol: self-administration of propofol in rats under fixed-ratio schedules of drug delivery. Psychopharmacology (Berl) 2000; 153: 148–54.
5 Wise RA. Dopamine, learning and motivation. Nat Rev Neurosci 2004; 5: 483–94.
6 Pain L, Gobaille S, Schleef C, Aunis D, Oberling P. *In vivo* dopamine measurements in the nucleus accumbens after nonanesthetic and anesthetic doses of propofol in rats. Anesth Analg 2002; 95: 915–9.
7 Tan KR, Brown M, Labouèbe G, Yvon C, Creton C, Fritschy JM, *et al*. Neural bases for addictive properties of benzodiazepines. Nature 2010; 463: 769–74.
8 Xi ZX, Stein EA. Nucleus accumbens dopamine release modulation by mesolimbic $GABA_A$ receptors–an *in vivo* electrochemical study. Brain Research 1998;798: 156–65
9 Cousins MS, Roberts DC, de Wit H. $GABA_B$ receptor agonists for the treatment of drug addiction: a review of recent findings. Drug Alcohol Depend 2002; 65: 209–20.
10 Yoon SS, Lee BH, Kim HS, Choi KH, Yun J, Jang EY, *et al*. Potential roles of GABA receptors in morphine self-administration in rats. Neurosci Lett 2007; 428: 33–7.
11 Zhou W, Liu H, Zhang F, Tang S, Zhu H, Lai M, *et al*. Role of acetylcholine transmission in nucleus accumbens and ventral tegmental area in heroin-seeking induced by conditioned cues. Neuroscience 2007; 144: 1209–18.
12 Johnson SW, North RA. Opioids excite dopamine neurons by hyperpolarization of local interneurons. J Neurosci 1992; 12: 483–8.
13 McBride WJ, Murphym JM, Ikemoto S. Localization of brain reinforcement mechanisms: intracranial self-administration and intracranial place-conditioning studies. Behav Brain Res 1999; 101: 129–52.
14 Laviolette, SR, Gallegos RA, Henriksen SJ, van der Kooy D. Opiate state controls bi-directional reward signaling via $GABA_A$ receptors in the ventral tegmental area. Nature Neurosci 2004; 7: 160–9
15 Panagis G, Kastellakis A. The effects of ventral tegmental administration of $GABA_A$, $GABA_B$, NMDA and AMPA receptor agonists on ventral pallidum self-stimulation. Behav Brain Res 2002; 131: 115–23.
16 Westerink BH, Enrico P, Feimann J, De Vries JB. The pharmacology of mesocortical dopamine neurons: a dual-probe microdialysis study in the ventral tegmental area and prefrontal cortex of the rat brain. J Pharmacol Exp Ther 1998; 285: 143–54.
17 Roberts DC, Andrews MM. Baclofen suppression of cocaine self-administration: demonstration using a discrete trials procedure. Psychopharmacology (Berl) 1997; 131: 271–7.
18 Shoaib M, Swanner LS, Beyer CE, Goldberg SR, Schindler CW. The $GABA_B$ agonist baclofen modifies cocaine self-administration in rats. Behav Pharmacol 1998; 9: 195–206.
19 Walker BM, Koob GF. The gamma-aminobutyric acid-B receptor agonist baclofen attenuates responding for ethanol in ethanol-dependent rats. Alcohol Clin Exp Res 2007; 31: 11–8.
20 Brebner K, Phelan R, Roberts DC. Intra-VTA baclofen attenuates cocaine self-administration on a progressive ratio schedule of reinforcement. Pharmacol Biochem Behav 2000; 66: 857–62.
21 Xi ZX, Stein EA. Baclofen inhibits heroin self-administration behavior and mesolimbic dopamine release. J Pharmacol Exp Ther 1999; 290: 1369–74.
22 Fadda P, Scherma M, Fresu A, Collu M, Fratta W. Baclofen antagonizes nicotine-, cocaine-, and morphine-induced dopamine release in the nucleus accumbens of rat. Synapse 2003; 50: 1–6.
23 Margeta-Mitrovic M, Mitrovic I, Riley RC, Jan LY, Basbaum AI. Immunohistochemical localization of $GABA_B$ receptors in the rat central nervous system. J Com Neurol 1999; 405: 299–321
24 Sahraei H, Amiri YA, Haeri-Rohani A, Sepehri H, Salimi SH, Pourmotabbed A, *et al*. Different effects of GABAergic receptors located in the ventral tegmental area on the expression of morphine-induced conditioned place preference in rat. Eur J Pharmacol 2005; 524: 95–101.

Acta Pharmacologica Sinica (2011) 32: 1466–1474
 1671-4083/11 $32.00
www.nature.com/aps

Original Article

The novel ATP-sensitive potassium channel opener iptakalim prevents insulin resistance associated with hypertension via restoring endothelial function

Yu WANG[1, #], Fu-hu ZENG[2, #], Chao-liang LONG[1, #], Zhi-yuan PAN[1, #], Wen-yu CUI[1], Ru-huan WANG[3], Guo-shu LIU[2], Hai WANG[1, 3, *]

[1]*Cardiovascular Drug Research Center, Institute of Health and Environmental Medicine, Academy of Military Medical Sciences, Beijing 100850, China;* [2]*Department of Cardiology, Chinese People's Liberation Army General Hospital, Beijing 100853, China;* [3]*Thadweik Academy of Medicine, Beijing 100039, China*

Aim: To investigate the effects of iptakalim on endothelial dysfunction induced by insulin resistance (IR) and to determine whether iptakalim improved IR associated with hypertension in fructose-fed rats (FFRs) and spontaneously hypertensive rats (SHRs).
Methods: Human umbilical vein endothelial cells (HUVECs) were used for *in vitro* study. The levels of endothelial vasoactive mediators and eNOS protein expression were determined using radioimmunoassays, ELISAs, colorimetric assays or Western blotting. Sprague-Dawley rats were fed with a high-fructose diet. In both FFRs and SHRs, tail-cuff method was used to measure systolic blood pressure (SBP), and hyperinsulinemic-euglycemic clamp was used to evaluate IR states.
Results: (1) Cultured HUVECs incubated with the PI3-kinase inhibitor wortmannin (50 nmol/L) and insulin (100 nmol/L) induced endothelial dysfunction characterized by significantly reduced release of NO and expression of eNOS protein, and significantly increased production of ET-1. Pretreatment with iptakalim (0.1–10 μmol/L) could prevent the endothelial dysfunction. (2) In FFRs, the levels of SBP, fasting plasma glucose and insulin were significantly elevated, whereas the glucose infusion rate (GIR) and insulin sensitive index (ISI) were significantly decreased, and the endothelium-dependent vascular relaxation response to ACh was impaired. These changes could be prevented by oral administration of iptakalim (1, 3, or 9 mg·kg^{-1}·d^{-1}, for 4 weeks). The imbalance between serum NO and ET-1 was also ameliorated by iptakalim. (3) In 2–4 month-old SHRs (IR was established at the age of 4 months), oral administration of iptakalim (1, 3, or 9 mg·kg^{-1}·d^{-1}, for 8 weeks) significantly ameliorated hypertension and increased the GIR to the normal level.
Conclusion: These results demonstrate that iptakalim could protect against IR-induced endothelial dysfunction, and ameliorate IR associated with hypertension, possibly via restoring the balance between NO and ET-1 signaling.

Keywords: endothelial dysfunction; insulin resistance; hypertension; ATP-sensitive potassium channel opener; iptakalim; spontaneously hypertensive rats; fructose-fed rats

Acta Pharmacologica Sinica (2011) 32: 1466–1474; doi: 10.1038/aps.2011.129; published online 7 Nov 2011

Introduction

Epidemiological evidence has demonstrated that insulin resistance (IR) and compensatory hyperinsulinemia play important roles in the onset and persistence of essential hypertension[1–4]. IR has been reported in several animal models of hypertension, including spontaneously hypertensive rats (SHRs) and fructose-fed hypertensive rats (FFRs)[5]. Humans with a genetic predisposition to hypertension tend to develop IR with hyperinsulinemia[6]. Because IR and hypertension often co-existed, the effects of antihypertensive drugs on IR have been highlighted. Of the first-line antihypertensive drugs, only angiotensin-converting enzyme (ACE) inhibitors and angiotensin II (Ang II) type 1 (AT1) receptor antagonists have been reported to have benefits in patients with IR[7]. However, despite intense research, studies identifying drugs able to lower blood pressure and reverse IR are still lacking.

Recent research indicates that endothelial dysfunction plays a key role in linking the pathogenesis of hypertension and IR, and the vicious circle involving hypertension, IR, and endothelial dysfunction has been documented[8–11]. Endothelial dysfunction associated with hypertension and IR is often characterized by an imbalance between NO and ET-1 signaling[12]. Therefore, restoration of endothelial function may be

# These authors contributed equally to this work.
* To whom correspondence should be addressed.
E-mail wh9588@yahoo.com.cn
Received 2011-04-18 Accepted 2011-08-30

a useful way to inhibit the development of IR in hypertensive patients.

The pharmacological approach to restoring the balance between nitric oxide (NO) and endothelin-1 (ET-1) signaling in the endothelium has been well documented[13]. A promising candidate in this field is iptakalim, a novel adenosine triphosphate (ATP)-sensitive potassium (K_{ATP}) channel opener that has been shown to have antihypertensive effects in different animals models of hypertension and in humans[14, 15]. Our laboratory has recently demonstrated that iptakalim can protect against endothelial dysfunction induced by cardiovascular risk factors, such as homocysteine, hyperglycemia, and hyperuricemia, by activating the SUR2B/Kir6.1 subtype of K_{ATP} channels in endothelial cells[16–19]. Because iptakalim has highly efficacious antihypertensive and potent endothelial protective effects, we hypothesized that iptakalim treatment has beneficial effects on the IR associated with hypertension, through protecting endothelial function.

Here, we first investigated the protective effects of K_{ATP} activation by iptakalim on endothelial dysfunction induced by insulin and wortmannin in human umbilical vein endothelial cells (HUVECs) and then explored its effects on IR associated with hypertension in fructose-fed rats (FFRs) and spontaneously hypertensive rats (SHRs). We found that iptakalim improved the IR associated with hypertension by restoring the balance between nitric oxide and endothelin-1 signaling, which was a different mechanism than that of drugs affecting the renin-angiotensin system (RAS). These investigations provide experimental evidence for a novel strategy to treat the IR associated with hypertension.

Materials and methods

Chemicals

Iptakalim was synthesized by the Thadweik Academy of Medicine (Beijing, China). Rosiglitazone, insulin, wortmannin, and glibenclamide were purchased from Sigma-Aldrich (St Louis, MO, USA). Benazepril was a gift from Novartis (Beijing, China).

Endothelial dysfunction induced by insulin resistance with hyperinsulinemia *in vitro*

Human umbilical vein cells (HUVECs) were obtained from Cascade Biologics (Portland, OR, USA). Cells from the third to fourth passage were used for experiments. To mimic IR, wortmannin, a partial inhibitor of phosphoinositide 3-kinase (PI3-kinase), and an high concentration of insulin were added to the cells[20]. Briefly, HUVECs were preincubated with or without iptakalim (10 nmol/L–100 μmol/L) for 6 h and then incubated with wortmannin (50 nmol/L) and insulin (100 nmol/L) for 20 h. Glibenclamide (10^{-5} mol/L) was added 1 h before iptakalim pretreatment. The medium was collected for the NO, ET-1, 6-Keto-PGF1α (namely 6-keto, a PGI_2 metabolite) and PAI-1 assays. The level of NO, including nitrite and nitrate, was measured using a commercial kit (Nanjing Jiancheng Bioengineering Institute, Nanjing, China); PAI-1 was measured by ELISA using a commercial kit (Beijing BIO-LAB Materials Institute, Beijing, China); and the other substances were measured using a commercial radioimmunoassay kit (Eastern Asia Radioimmunity Research Institute, Beijing, China) according to the manufacturer's instructions. The expression of eNOS protein was detected using Western blot analysis. The methods for cell lysis and Western blot analysis have been described previously[21]. The monoclonal anti-eNOS antibody was used at the manufacturers' suggested concentration. A secondary antibody (rat anti-rabbit IgG-horseradish peroxidase) and an enhanced chemiluminescence kit were used to visualize the immunoreactive bands. Multiple exposures of films were obtained to determine the optimal exposure time. The protein bands were scanned by a densitometer, and the relative intensities were quantified using ImageQuant software.

Animals and drug treatments

Six-week-old male Sprague-Dawley (SD) rats were provided by the Experimental Animal Center of the Beijing Institute of Pharmacology and Toxicology. Male SHRs and normotensive Wistar-Kyoto (WKY) rats of various ages were obtained from the Institute of Cardiovascular Diseases, Chinese Academy of Medical Sciences (Beijing, China). The rats were housed in groups of five, under a 12-h light/dark cycle at a temperature of 24±1 °C and relatively humidity of 56%±10%, with free access to water and a normal diet (22% protein). All animal procedures were performed in accordance with the Declaration of the National Institutes of Health Guide and Use of Laboratory Animals (Publication 85–23, revised 1985) and approved by the local animal care and use committee.

Six-week-old male Sprague-Dawley rats were divided into 7 groups (n=14 per group) and fed *ad libitum* one of the following diets for 8 weeks: standard chow (control rats), standard chow with iptakalim (9 $mg \cdot kg^{-1} \cdot d^{-1}$), a high-fructose diet (fructose-fed rats), or a high-fructose diet with iptakalim (1, 3, or 9 $mg \cdot kg^{-1} \cdot d^{-1}$) or rosiglitazone (5 $mg \cdot kg^{-1} \cdot d^{-1}$). During the last 4 weeks, all the medications were given daily by gavage. In a separate study, the effect of iptakalim (3 mg/kg) on endothelial function in the fructose-fed rats during the last 4 weeks was compared to enalapril (3 mg/kg). The high-fructose diet contained 60% fructose, 13% fat, and 20% protein by calories. Body weight, systolic blood pressure (SBP), and heart rate (HR) were determined every week throughout the study. The SBP and HR were measured using a tail-cuff method in conscious rats.

Both SBP and HR were elevated, while IR was not established in the 2- and 3-month-old SHRs. IR was established in the 4-month-old SHRs. The therapeutic arrangement was carried out before (2–3 months of age) and after (4 months of age) IR was established. SHRs aged 2, 3, or 4 months were randomized into five groups (n=5 rats/group) and treated daily for 8 weeks by gavage with iptakalim (1, 3, or 9 $mg \cdot kg^{-1} \cdot d^{-1}$), benazepril (6 $mg \cdot kg^{-1} \cdot d^{-1}$), or vehicle. Six age-matched WKY rats were given vehicle alone for 8 weeks.

Hyperinsulinemic-euglycemic clamp

Euglycemic-hyperinsulinemia clamp analysis was performed as described previously[22]. Briefly, at the end of 8 weeks, rats were fasted for 12 h before the start of the experimental protocol. Then, they were anesthetized by an intraperitoneal injection of pentobarbital sodium (50 mg/kg). The left carotid artery (for blood sampling) and both femoral veins (left femoral vein for exogenous glucose infusion and right femoral vein for insulin infusion) were cannulated with silastic catheters. The catheters were flushed periodically with heparinized saline to maintain patency. At the beginning, blood samples were collected to measure basal plasma glucose concentrations, and then a constant infusion of insulin at a rate of 10 mU·kg^{-1}·min^{-1} was performed. Meanwhile, a variable infusion of 10% dextrose was adjusted based on 5-min blood samples to maintain the plasma glucose at the target value. A stable plasma glucose concentration and an exogenous glucose infusion rate (GIR) were generally achieved within 70 to 90 min, at which time 6 blood samples (200 μL) were collected at 5-min intervals to determine the GIR.

Metabolic and endothelial function measurements

Blood samples were obtained from the retro-orbital sinus from rats that were fasted overnight and euthanized with ether. Plasma glucose levels were determined with an automated biochemical analyzer (7600-DDP-ISE; Hitachi Software Engineering, Yokohama, Japan). The concentration of insulin, NO, ET-1, and Ang II levels in the plasma were measured using a commercial radioimmunoassay kit (Eastern Asia Radioimmunity Research Institute, Beijing, China) according to the manufacturer's instructions. The NO level was measured using a commercial kit (Nanjing Jiancheng Bioengineering Institute, Nanjing, China). Insulin sensitivity was assessed using the quantitative insulin sensitivity index [ISI=-ln(fasting glucose level×fasting insulin level)].

Determination of the endothelium-dependent vascular relaxation

The thoracic aorta was isolated and removed from high-fructose diet rats after 4 weeks of vehicle or drug therapy. Acetylcholine-induced endothelium-dependent vascular relaxation was tested as described previously[23].

Statistical analysis

The data are expressed as the mean±SD, and *n* indicates the number of experiments. For multiple comparisons, the results were analyzed by factorial ANOVA using the Statistical Analysis System software (SAS8.00). A value of $P<0.05$ was considered to be statistically significant.

Results

Activation of K_{ATP} reverses endothelial dysfunction *in vitro*

The experiments were carried out in cultured HUVECs to investigate the improvement in K_{ATP} channel activation by iptakalim *in vitro*. Endothelial dysfunction was induced with wortmannin to block PI3-kinase-dependent signaling, and meanwhile, the cells were exposed to high concentrations of insulin[20, 24]. The release of NO (Figure 1A) and 6-keto-$F_{1\alpha}$ (Figure 1B) decreased, and the levels of ET-1 (Figure 1C) and PAI-1 (Figure 1D) increased in the HUVECs incubated with wortmannin and insulin at concentrations of 50 and 100 nmol/L, respectively, for 20 h. Pretreatment with iptakalim at concentrations ranging from 10 nmol/L–10 μmol/L for 6 h increased NO release (Figure 1A) and prevented ET-1 formation (Figure 1C). Iptakalim had mild effects on 6-keto-$F_{1\alpha}$ release only at the high concentration of 10 μmol/L, which was 100 times greater than the effective concentration for increasing NO release (Figure 1B) but had no effect on the API-1 level (Figure 1D). The effect of iptakalim on NO release was abolished by glibenclamide (10 μmol/L), a specific blocker of K_{ATP} channels (Figure 1E). In addition, eNOS protein expression in HUVECs was decreased when incubated with wortmannin and insulin, while pretreatment with iptakalim could significantly increase eNOS expression (Figure 2). These results suggested that iptakalim protects against endothelial dysfunction mainly by restoring the balance between NO and ET-1 via opening the SUR2B/Kir6.1 subtype of K_{ATP} channel in the endothelium, which is consistent with a previous report from our lab[16].

Iptakalim improves IR associated with hypertension *in vivo*

First, the effect of K_{ATP} activation by iptakalim on the progression of IR associated with hypertension was investigated in SHRs. SBP, HR, and the GIR were compared between the SHRs and age-matched Wistar-Kyoto rats (WKY). SBP and GIR in the 1-month-old SHRs and age-matched WKY rats were comparable. SBP was elevated, and GIR was normal in the 2-3-month-old SHRs. SBP was elevated, the GIR was decreased, and hypertension and IR developed in the 4-6-month-old SHRs (Figure 3A). The effect of treatment with iptakalim at doses of 1, 3, or 9 mg·kg^{-1}·d^{-1} for 8 weeks in SHRs before or after IR had developed was evaluated. SBP decreased, and GIR increased in the SHRs treated with iptakalim at 2, 3, or 4 months of age. Treatment with iptakalim improved IR associated with hypertension, whereas treatment with benazepril at a dose of 6 mg·kg^{-1}·d^{-1} for 8 weeks decreased the SBP but did not improve the decrease in the GIR (Figure 3B).

Second, we investigated the effects of iptakalim on IR associated with hypertension in the FFRs. Food intake was significantly lower in the FFRs compared to the control rats. Iptakalim treatment did not affect food consumption in either the normal chow-fed or fructose-fed rats, but rosiglitazone treatment significantly increased food intake in the fructose-fed rats. Iptakalim treatment did not affect body weight or food consumption in either the normal chow-fed or fructose-fed rats (data not shown). IR associated with hypertension in the FFRs was characterized by an elevated SBP, decreased GIR, and insulin sensitive index (ISI) with diabetic manifestations of increased fasting blood levels of insulin (FBI) and glucose (FBG). Treatment with iptakalim at a dose of 1, 3, or 9 mg·kg^{-1}·d^{-1} or the PPARγ agonist rosiglitazone at 5 mg·kg^{-1}·d^{-1} for 4 weeks prevented IR associated with hypertension and hyperinsulinemia, and the SBP (Figure 4A), FBI (Figure 4B),

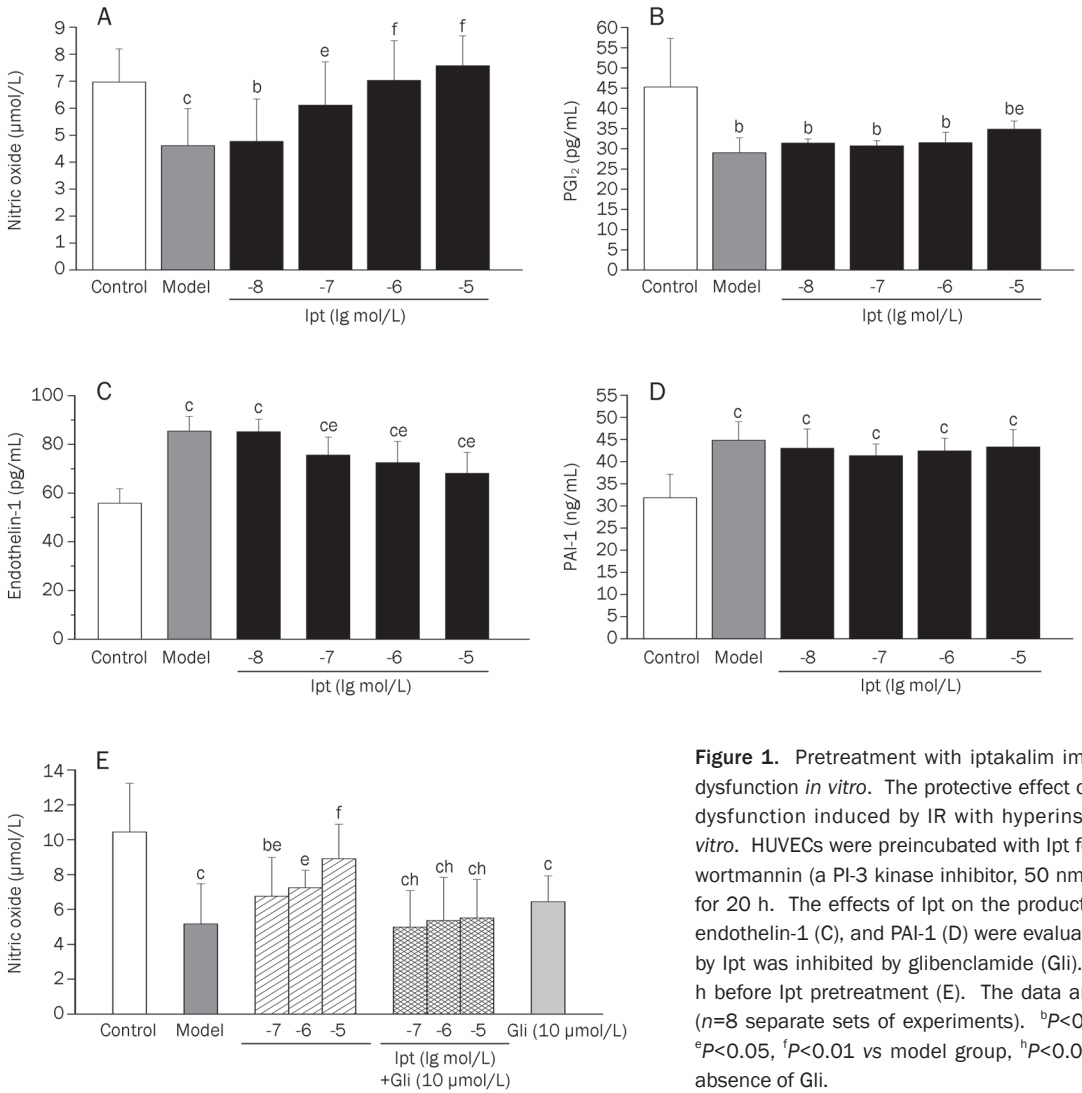

Figure 1. Pretreatment with iptakalim improves IR-induced endothelial dysfunction *in vitro*. The protective effect of iptakalim (Ipt) on endothelial dysfunction induced by IR with hyperinsulinemia was investigated *in vitro*. HUVECs were preincubated with Ipt for 6 h and then incubated with wortmannin (a PI-3 kinase inhibitor, 50 nmol/L) and insulin (100 nmol/L) for 20 h. The effects of Ipt on the production of nitric oxide (A), PGI_2 (B), endothelin-1 (C), and PAI-1 (D) were evaluated. The increased NO release by Ipt was inhibited by glibenclamide (Gli). Gli (10^{-5} mol/L) was added 1 h before Ipt pretreatment (E). The data are expressed as the mean±SD (n=8 separate sets of experiments). $^{b}P<0.05$, $^{c}P<0.01$ *vs* control group; $^{e}P<0.05$, $^{f}P<0.01$ *vs* model group, $^{h}P<0.05$ *vs* the data obtained in the absence of Gli.

FBG (Figure 4C), GIR (Figure 4D), and ISI (Figure 4E) were normalized. In addition, iptakalim had no effect on the above parameters in the control rats fed a normal diet.

Activation of K_{ATP} ameliorates fructose-induced endothelial dysfunction *in vivo*

Endothelial dysfunction was characterized by impaired vascular relaxation induced by acetylcholine in aorta from the FFRs. The endothelium-dependent vascular relaxation induced by acetylcholine at concentrations of 0.1, 1, 10, or 100 μmol/L was significantly decreased in the *in vitro* aortic preparations isolated from the FFRs. This change was significantly improved by treatment with iptakalim at the doses of 1, 3, or 9 $mg{\cdot}kg^{-1}{\cdot}d^{-1}$ for 4 weeks or by treatment with rosiglitazone (Figure 5). Serum levels of NO (Figure 6A) decreased, whereas ET-1 (Figure 6B) increased in the FFRs, which was improved by treatment with iptakalim at a dose of 3 $mg{\cdot}kg^{-1}{\cdot}d^{-1}$ for 4 weeks. These findings suggest that endothelial dysfunction can be restored by treatment with iptakalim *in vivo*.

In addition, serum levels of angiotensin II increased from 597.63±55.97 (n=10) to 796.48±113.62 (n=10) ng/mL ($P<0.01$ *vs* normal control group) in the FFRs. However, these increased levels of angiotensin II were not influenced by treatment with iptakalim at a dose of 3 mg/kg po qd for 4 weeks, and the serum content of angiotensin II remained high at 808.30±87.03 ng/mL (n=10, $P>0.05$ *vs* model group). However, the levels of angiotensin II decreased to 589.78±67.96 (10) ng/mL ($P<0.01$ *vs* model group; $P>0.05$ *vs* normal control group) with treatment with enalapril at a dose of 3 $mg{\cdot}kg^{-1}{\cdot}d^{-1}$ (Figure 6C). These results are consistent with those observed in hypertensive renal damage and renal injury induced by hyperuricemia[25, 26]. Because iptakalim has no effect on the renin-angiotensin system, its benefit on IR associated with hypertension is entirely different from those of drugs acting on the RAS.

Discussion

Essential hypertension and insulin resistance are inextricably linked[1]. Approximately 50 percent of patients with hypertension can be considered to have insulin resistance and hyperinsulinemia[27]. Studies in both hypertensive humans and rodent

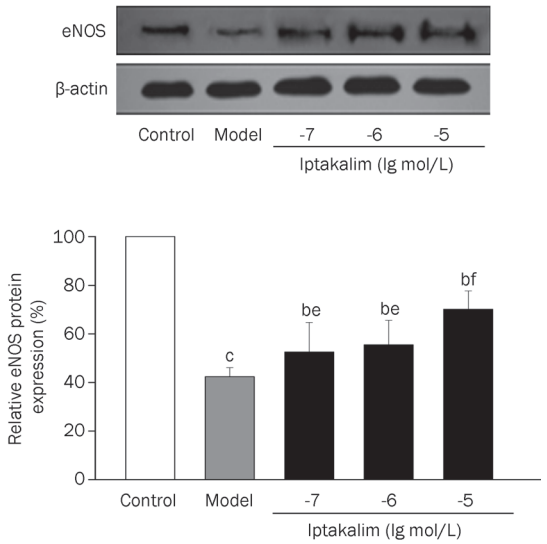

Figure 2. Effect of iptakalim on eNOS protein expression in HUVECs. Western blot analysis of eNOS protein expression in endothelial cells was performed with a rabbit monoclonal anti-eNOS antibody. An equal amount of protein was loaded in each lane. The density of the bands was quantified by densitometric scanning, and the relative density was calculated by setting the density of the control band as 100%. The data are expressed as the mean±SD (n=3 separate sets of experiments). $^{b}P<0.05$, $^{c}P<0.01$ compared to the control group. $^{e}P<0.05$, $^{f}P<0.01$ compared to the model group.

models of hypertension suggest that IR and/or compensatory hyperinsulinemia have an important role in blood pressure regulation and may predispose individuals to develop hypertension. However, an antihypertensive drug that reduces BP does not necessarily improve IR. Of the current first-line antihypertensive agents, β-adrenergic receptor blockers and diuretics can impair insulin sensitivity, and the metabolic effects of calcium channel blockers are still controversial[28]. Only angiotensin-converting enzyme (ACE) inhibitors and angiotensin II (Ang) II type 1 (AT1) receptor antagonists have been reported to be beneficial in patients with IR[7]. Drugs that can lower blood pressure and reverse the associated IR are still lacking, which reveals the need for developing new drugs that can reduce blood pressure and improve IR.

Recent studies have demonstrated that endothelial dysfunction is likely to be one of the most important underlying pathophysiological mechanisms that might serve as the link between IR and hypertension. The endothelium releases many vasoactive mediators that regulate cardiovascular function and, importantly, contribute to maintaining homeostasis. Endothelial dysfunction has been attributed to various cardiovascular risk factors and is mainly characterized by an imbalance between NO and ET-1 signaling, which contributes to further progression of hypertension. Insulin resistance is characterized by pathway-specific impairment in PI3-kinase-dependent signaling, which in the endothelium, may also cause an imbalance between NO and endothelin-1, leading to decreased blood flow and worsening insulin resistance. Therapeutic interventions in animal models and human studies have indicated that improving endothelial dysfunction ameliorates insulin resistance, whereas improving insulin sensitivity ameliorates endothelial dysfunction[11]. Thus, if an antihypertensive agent protects against endothelial dysfunction, it is very likely to improve IR in hypertensive individuals.

Iptakalim is a novel K_{ATP} channel opener with potent antihypertensive properties, which have been confirmed in phase 3 clinical trials in China, and has selective activation of the SUR2B/Kir6.1 channel, resulting in the protection of endothelial function[14–18]. Iptakalim has protective effects against endothelial dysfunction induced by low-density lipoprotein, homocysteine, hyperglycemia, and hypertension[16]. In this study, we demonstrated for the first time that iptakalim improves IR associated with hypertension by restoring the balance between NO and ET-1 signaling in the endothelium.

First, we performed experiments to mimic IR-induced endothelial dysfunction. Simultaneous treatment of endothelial cells with wortmannin and high insulin levels blunts the PI3-kinase-dependent effects of insulin, such as the induction of eNOS expression and the release of NO, and increases the production of ET-1, which is consistent with previous reports[20, 24]. Iptakalim rebalanced the release of NO and the production of ET-1 but had little effects on PGI_2 and PAI-1. The effect of iptakalim on NO release was abolished by glibenclamide, a specific blocker of K_{ATP} channels. Furthermore, iptakalim was able to increase eNOS protein expression in endothelial cells. These observations confirm previous results indicating that iptakalim potently protects against endothelial dysfunction[16–19]. Iptakalim can improve IR-induced endothelial dysfunction and ameliorate the impaired insulin-PI3-Kinase-NO signaling pathway via opening the SUR2B/Kir6.1 subtype of K_{ATP} channel. Thus, we hypothesized that iptakalim could ameliorate IR *in vivo* through endothelial protection induced by activating the SUR2B/Kir6.1 channel.

Several animal models have been used to study the relationship between IR and the development of hypertension, including SHRs and FFRs[29–32]. The SHR is a widely used genetic model of essential hypertension and the associated metabolic disturbances, including IR and endothelial dysfunction. Recent advances in the genetics of the SHR have revealed that there are some specific genes that influence blood pressure and IR[33]. The FFR is another useful model of acquired systolic hypertension that displays numerous features of the metabolic syndrome including IR. Rats fed a high fructose diet exhibit IR/hyperinsulinemia and hypertension, which is independent of genetic contributions[34]. In our study, these two different animal models were used to identify the effect of iptakalim on IR. Because of the effects of ACEIs and γ peroxisome proliferator-activated receptors (PPARγ) agonists on insulin-resistance states have been well documented[35], we chose different ACEIs (benazepril for the SHRs and enalapril for the FFRs), and a PPARγ agonist (rosiglitazone for the FFRs) as positive controls to demonstrate the reliability of the rat models of IR associated with hypertension.

Although growing evidence demonstrates that several

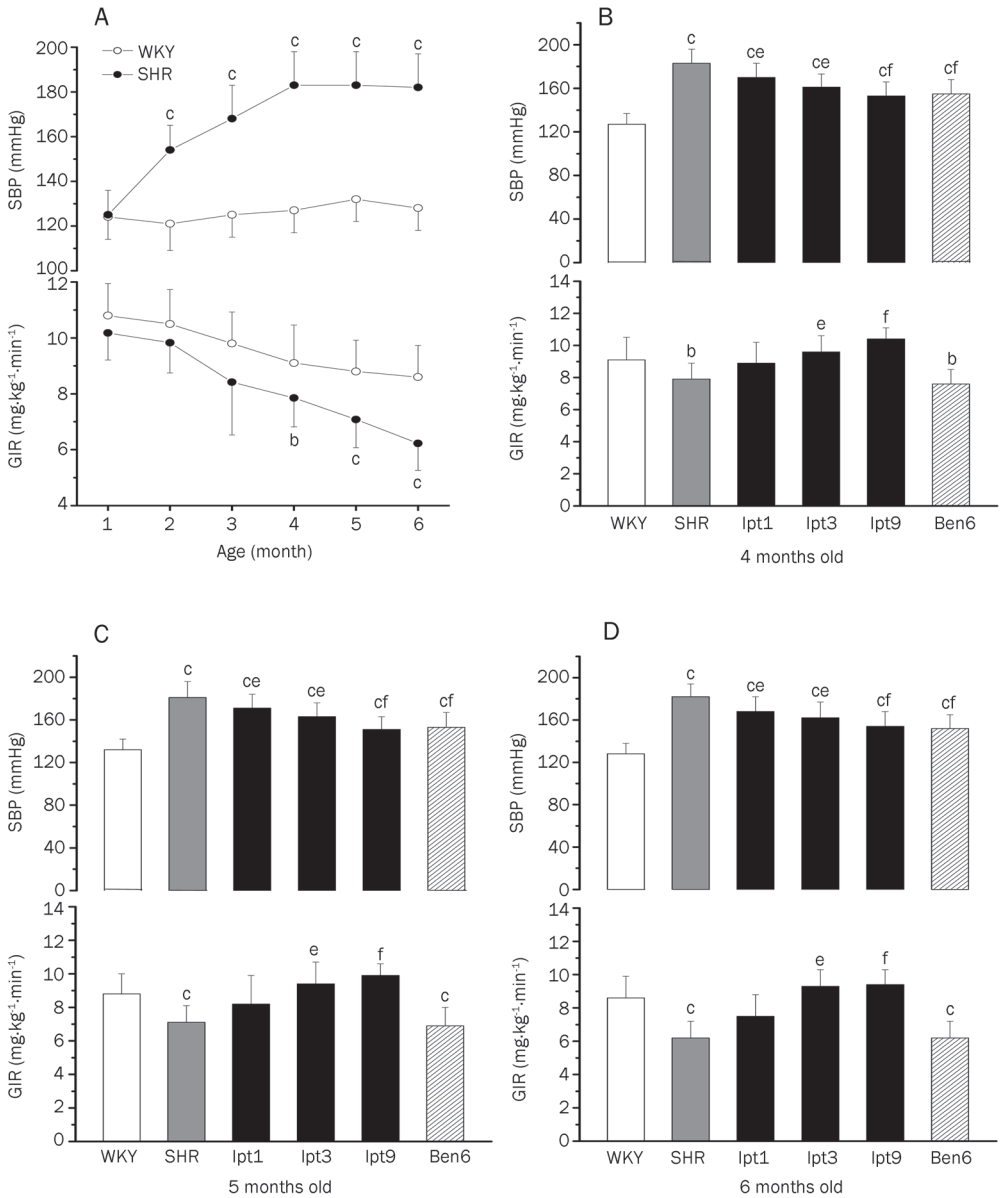

Figure 3. Treatment with iptakalim improves insulin resistance (IR) associated with hypertension in spontaneously hypertensive rats (SHRs). (A) The changes in the systolic blood pressure (SBP) and glucose infusion rate (GIR) in the SHRs and in the age-matched WKY rats at 1, 2, 3, 4, 5, and 6 months of age. (B, C, D) Eight-week treatment with iptakalim reduced the SBP and attenuated IR in SHRs. The daily therapy with vehicle, iptakalim 1, 3, or 9 mg·kg^{-1}·d^{-1} (Ipt1, Ipt3, Ipt9), or benazepril 6 mg·kg^{-1}·d^{-1} (Ben 6) for 8 weeks was performed before (SHRs 2 (B) and 3 (C) months of age) and after (SHRs 4 (D) months of age) IR was established. When the treatments were completed, these SHRs were 4 (B), 5 (C), or 6 (D) months old. The data are expressed as the mean±SD (n=6 per group). $^{b}P<0.05$, $^{c}P<0.01$ *vs* age-matched WKY rats, $^{e}P<0.05$, $^{f}P<0.01$ *vs* age-matched SHRs.

related mechanisms for IR contribute to the pathogenesis of hypertension in the SHRs, the exact cause of this disorder remains unclear. In addition, whether IR is a "reason" or a "result" for the progression of hypertension is yet to be elucidated. Our results indicate that hypertension develops before IR. Furthermore, we have shown for the first time that the GIR was improved after 8 weeks of iptakalim treatment in SHRs. There are at least two reasons that may explain this phenomenon. First, the lower blood pressure may result from iptakalim directly. Another possibility is that the lower blood pressure results from the restoration of endothelial function by iptakalim. Therefore, it is very important to further explore the molecular mechanism by which iptakalim affects IR associated with hypertension in SHRs.

A substantial number of studies suggest a relationship among the occurrence of IR, endothelial dysfunction and hypertension in FFRs, but the cause and effect among them has yet to be elucidated. Katakam and colleagues reported that hyperinsulinemia occurs following 3 d of high fructose feeding, IR develops after 7–10 d, endothelial dysfunction was observed following 18 d and hypertension was found after 4 weeks[33, 36, 37]. Based on the order in which they develop, we designed this study such that the iptakalim treatments were performed after hypertension had developed after 4 weeks of the diet. We found that treating the FFRs with iptakalim for 4 weeks resulted in lower blood pressures and restored the balance between the production of NO and secretion of ET-1. Furthermore, the impaired ACh-induced endothelium-dependent relaxation of aortic tissue derived from the FFRs was improved significantly after 4 weeks of iptakalim administration. In agreement with other reports[31, 38], we have demonstrated that iptakalim has a direct endothelial effect. Thus, the similar *in vivo* and *in vitro* effects of iptakalim indicate that the positive effects of iptakalim on vascular function are mainly

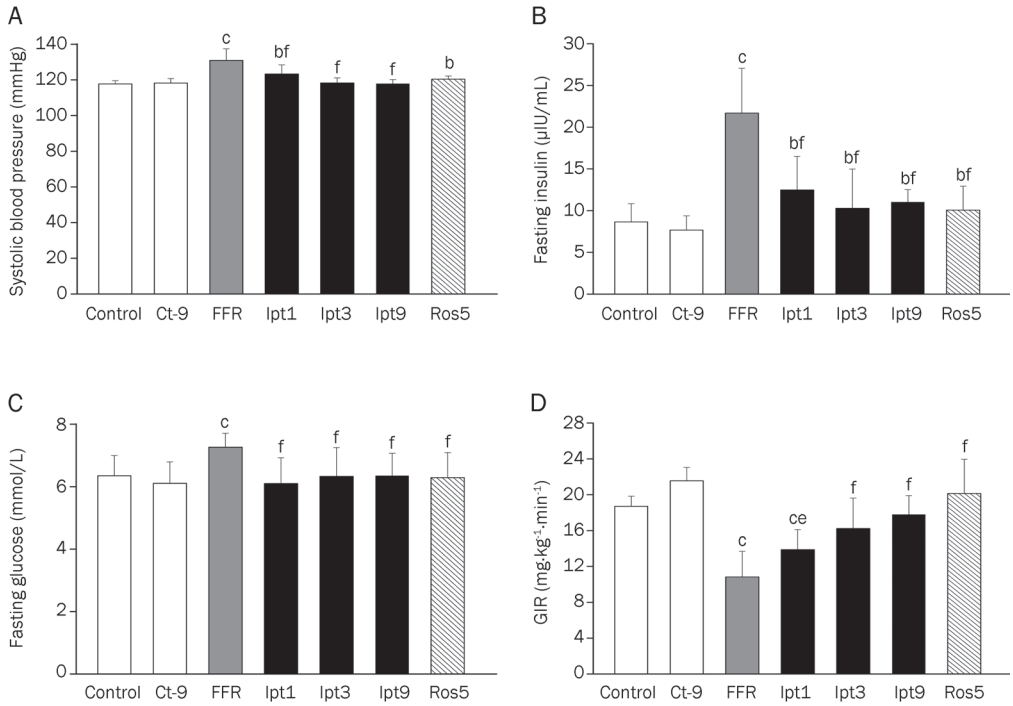

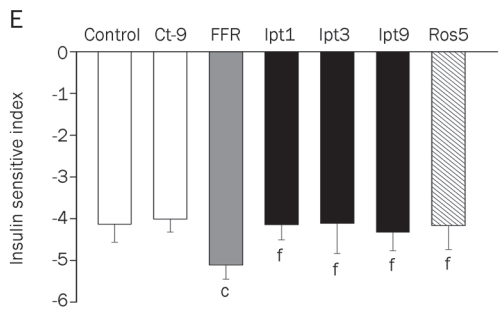

Figure 4. Treatment with iptakalim improved insulin resistance (IR) associated with hypertension in fructose-fed rats (FFR). In Sprague-Dawley rats fed either a normal (Ctrl) or high fructose-fed (FFR) diet for 8 weeks, iptakalim and rosiglitazone were administered orally at 1, 3, or 9 mg·kg^{-1}·d^{-1} (Ipt1, Ipt3, Ipt9) and 5 mg·kg^{-1}·d^{-1} (Ros 5), respectively, for the last 4 weeks in the high-fructose diet group. Iptakalim was administered orally at 9 mg·kg^{-1}·d^{-1} (Ct-9) for the last 4 weeks in the control diet group. At the end of 8 weeks, the SBP (A) was measured using the tail cuff method. Fasting blood samples were obtained to measure insulin (B) and glucose (C). Insulin sensitivity was assessed by the GIR (D) and ISI (E). The data are expressed as the mean±SD (n=14 per group). ^{b}P<0.05, ^{c}P<0.01 *vs* control group. ^{e}P<0.05, ^{f}P<0.01 *vs* model group.

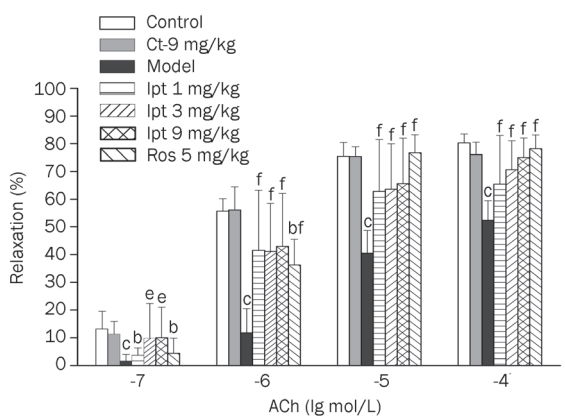

Figure 5. Treatment with iptakalim or rosiglitazone improved acetylcholine-induced endothelium-dependent vascular relaxation in the isolated aortic rings derived from the FFRs. Normal rats (Control), iptakalim control (Ct-9 mg/kg), FFRs (Model), and the FFRs treated with iptakalim (Ipt 1, 3, or 9 mg/kg) and rosiglitazone (Ros-5 mg/kg) for 4 weeks. The data are expressed as the mean±SD (n=6 per group). ^{b}P<0.05, ^{c}P<0.01 *vs* control group. ^{e}P<0.05, ^{f}P<0.01 *vs* model group.

due to its direct effects on endothelial function.

Interestingly, in this study, we have demonstrated that iptakalim treatment improves insulin sensitivity, normalizes the GIR, and decreases plasma insulin levels in FFRs. Because therapeutic interventions in animal models and human studies have confirmed that improving endothelial dysfunction ameliorates insulin resistance[11], it is reasonable to postulate that improvements in IR by iptakalim are due to its amelioration of endothelial dysfunction.

It is well known that ACE inhibitors may directly improve endothelial dysfunction by blocking local endothelial angiotensin II production. Our results showed that enalapril can inhibit the increased serum concentration of Ang II, while iptakalim has no direct effect on this change in the FFRs, which suggests that the mechanism for iptakalim-induced improvement in IR differs from that of enalapril and occurs through a novel molecular pathway.

Based upon the above investigation, it appears reasonable to conclude that iptakalim, a K_{ATP} channel opener, protects against IR-induced endothelial dysfunction by restoring the

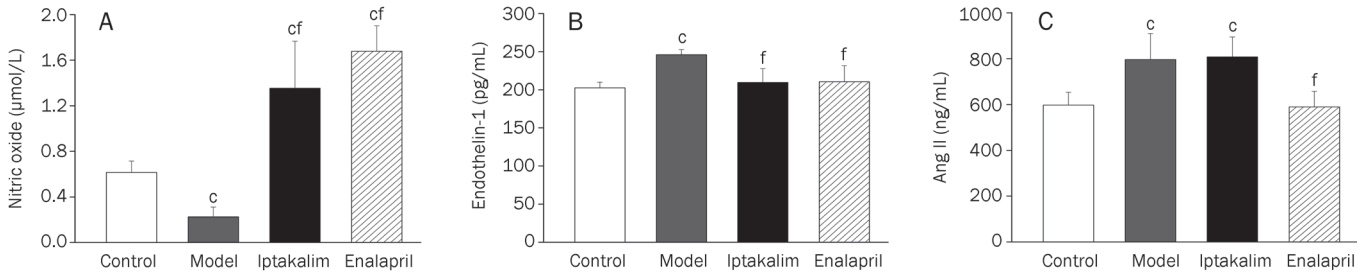

Figure 6. Iptakalim ameliorates endothelial dysfunction in FFRs. Treatment with iptakalim or enalapril 3 mg·kg^{-1}·d^{-1} for 4 weeks increased serum nitric oxide levels and decreased serum endothelin-1 levels in FFRs (A, B). Iptakalim treatment had no effect on the serum angiotensin II (Ang II) level, which was different compared to enalapril (C). The data are expressed as the mean±SD (n=8). ^{c}P<0.01 *vs* control group; ^{f}P<0.01 *vs* model group.

balance between NO and ET-1 signaling, and ameliorates the IR associated with hypertension.

Conclusions

Iptakalim can protect endothelial cells by activating K_{ATP} through the preferential activation of the SUR2B/Kir6.1 subtypes of K_{ATP} expressed in the endothelium. In this study, we first investigated the effects of iptakalim on IR in SHRs and FFRs and then explored the molecular mechanism by which it protects against endothelial dysfunction *in vivo* and *in vitro*. These findings suggest that iptakalim improves the IR associated with hypertension through restoring the balance between NO and ET-1 signaling and that targeting the SUR2B/Kir6.1 subtype of K_{ATP} is a new strategy for ameliorating the IR associated with hypertension.

Acknowledgements

This study was supported by grants from the National New Drug Research and Development Key Project (No 2008ZX09101-006, 2008ZXJ09004-018 and 2009ZX09301-002), the State Key Basic Research and Development from the Ministry of Science and Technology of China (No GT1998051112), the 863-High Technology Research and Development Program Plan (No 2002AA2Z3137), the National 1035 Project (No 969010101) of China and the New Drug Development of Beijing Key Project (No D0204003040721).

Author contribution

Hai WANG and Guo-shu LIU designed the research. Yu WANG, Fu-hu ZENG, Zhi-yuan PAN, Wen-yu CUI, and Ruhuan WANG performed the research. Yu WANG and Fu-hu ZENG analyzed the data. Yu WANG, Chao-liang LONG, and Zhi-yuan PAN wrote the paper.

Abbreviations

K_{ATP}, ATP-sensitive potassium channel; IR, insulin resistance; SHR, spontaneously hypertensive rat; FFR, fructose-fed rat; GIR, glucose infusion rate; SBP, systolic blood pressure; HUVEC, human umbilical vein endothelial cells; NO, nitric oxide; ET-1, endothelin-1; Ang II, angiotensin II; ACEI, angiotensin-converting enzyme inhibitor; 6-Keto-$PGF_{1\alpha}$, 6-Keto-prostaglandin-$F_{1\alpha}$; PAI-1, plasminogen activator inhibitor-1; PPARγ, γ peroxisome proliferator-activated receptors.

References

1 Ferrannini E, Buzzigoli G, Bonadonna R, Giorico MA, Oleggini M, Graziadei L, *et al*. Insulin resistance in essential hypertension. N Engl J Med 1987; 317: 350–7.
2 Reddy KJ, Singh M, Bangit JR, Batsell RR. The role of insulin resistance in the pathogenesis of atherosclerotic cardiovascular disease: an updated review. J Cardiovasc Med (Hagerstown) 2010; 11: 633–47.
3 Penesova A, Cizmarova E, Belan V, Blazicek P, Imrich R, Vlcek M, *et al*. Insulin resistance in young, lean male subjects with essential hypertension. J Hum Hypertens 2011; 25: 391–400.
4 Perticone F, Sciacqua A, Maio R, Perticone M, Galiano Leone G, Bruni R, *et al*. Endothelial dysfunction, ADMA and insulin resistance in essential hypertension. Int J Cardiol 2010; 142: 236–41.
5 Higashiura K, Ura N, Takada T, Li Y, Torii T, Togashi N, *et al*. The effects of an angiotensin-converting enzyme inhibitor and an angiotensin II receptor antagonist on insulin resistance in fructose-fed rats. Am J Hypertens 2000; 13: 290–7.
6 Umeda M, Kanda T, Murakami M. Effects of angiotensin II receptor antagonists on insulin resistance syndrome and leptin in sucrose-fed spontaneously hypertensive rats. Hypertens Res 2003; 26: 485–92.
7 Pahor M, Psaty BM, Furberg CD. Treatment of hypertensive patients with diabetes. Lancet 1998; 32: s18–23.
8 Duncan ER, Crossey PA, Walker S, Anilkumar N, Poston L, Douglas G, *et al*. Effect of endothelium-specific insulin resistance on endothelial function *in vivo*. Diabetes 2008; 57: 3307–14.
9 Katakam PV, Ujhelyi MR, Hoenig ME, Miller AW. Endothelial dysfunction precedes hypertension in diet-induced insulin resistance. Am J Physiol 1998; 275: R788–92.
10 Tziomalos K, Athyros VG, Karagiannis A, Mikhailidis DP. Endothelial dysfunction in metabolic syndrome: prevalence, pathogenesis and management. Nutr Metab Cardiovasc Dis 2010; 20: 140–6.
11 Kim JA, Montagnani M, Koh KK, Quon MJ. Reciprocal relationships between insulin resistance and endothelial dysfunction: molecular and pathophysiological mechanisms. Circulation 2006; 113: 1888–904.
12 Potenza MA, Marasciulo FL, Chieppa DM, Brigiani GS, Formoso G, Quon MJ, *et al*. Insulin resistance in spontaneously hypertensive rats is associated with endothelial dysfunction characterized by imbanlace between NO and ET-1 production. Am J Physiol 2005; 289: H813–22.
13 Minamino T, Hori M. Protecting endothelial function: a novel therapeutic target of ATP-sensitive potassium channel openers. Cardiovasc Res 2007; 73: 448–9.
14 Pan Z, Huang J, Cui W, Long C, Zhang Y, Wang H. Targeting hypertension with a new ATP sensitive potassium channel opener iptakalim.

J Cardiovasc Pharmacol 2010; 56: 215–28.
15 Duan RF, Cui WY, Wang H. Association of the antihypertensive response of iptakalim with KCNJ11 (Kir6.2 gene) polymorphisms in Chinese Han hypertensive patients. Acta Pharmacol Sin 2011; 32: 1078–84.
16 Wang H, Long C, Duan Z, Shi C, Jia G, Zhang Y. A new ATP-sensitive potassium channel opener protects endothelial function in cultured aortic endothelial cells. Cardiovasc Res 2007; 73: 497–503.
17 Gao S, Long CL, Wang RH, Wang H. K_{ATP} activation prevents progression of cardiac hypertrophy to failure induced by pressure overload via protecting endothelial function. Cardiovasc Res 2009; 83: 444–56.
18 Tang Y, Long CL, Wang RH, Cui W, Wang H. Activation of SUR2B/Kir6.1 subtype of adenosine triphosphate-sensitive potassium channel improves pressure overload induced cardiac remodeling via protecting endothelial function. J Cardiovasc Pharmacol 2010; 56: 345–53.
19 Zhao RJ, Wang H. Chemerin/ChemR23 signaling axis is involved in the endothelial protection by K_{ATP} channel opener iptakalim. Acta Pharmacol Sin 2011; 32: 573–80.
20 Montagnani M, Golovchenko I, Kim I, Koh GY, Goalstone ML, Mundhekar AN, *et al*. Inhibition of phosphatidylinositol 3-kinase enhances mitogenic actions of insulin in endothelial cells. J Biol Chem 2002; 277: 1794–9.
21 Vaziri ND, Wang XQ. cGMP-mediated negative-feedback regulation of endothelial nitric oxide synthase expression by nitric oxide. Hypertension 1999; 34: 1237–41.
22 Furukawa LN, Kushiro T, Asagami T, Takahashi A, Kanmatsuse K, Ishikawa K. Variations in insulin sensitivity in spontaneously hypertensive rats from different sources. Metabolism 1998; 47: 493–6.
23 Katakam PV, Ujhelyi MR, Hoenig M, Miller AW. Metformin improves vascular function in insulin-resistant rats. Hypertension 2000; 35: 108–12.
24 Li R, Zhang H, Wang W, Wang X, Huang Y, Huang C, *et al*. Vascular insulin resistance in prehypertensive rats: role of PI3-kinase/Akt/eNOS signaling. Eur J Pharmacol 2010; 628: 140–7.
25 Xue H, Zhang YL, Liu GS, Wang H. A new ATP-sensitive potassium channel opener protects the kidney from hypertensive damage in experimental hypertension. J Pharmacol Exp Ther 2005; 315: 501–9.
26 Long CL, Qin XC, Pan ZY, Chen K, Zhang YF, Cui WY, *et al*. Activation of ATP-sensitive potassium channels protects vascular endothelial cells from hypertension and renal injury induced by hyperuricemia. J Hyperten 2008; 26: 2326–38.
27 Pollare T, Lithell H, Berne C. Insulin resistance is a characteristic feature of primary hypertension in dependent of obesity. Metabolism 1990; 39: 167–74.
28 Oron-Herman M, Sela BA, Rosenthal T. Risk reduction therapy for syndrome X: comparison of several treatments. Am J Hypertens 2005; 18: 372–8.
29 Modon CE, Reaven GM. Evidence of abnormalities of insulin metabolism in rats with spontaneously hypertension. J Metabolism 1988; 37: 303–5.
30 Verma S, Yao L, Stewart DJ, Dumont AS, Anderson TJ, McNeill JH. Endothelin antagonism uncovers insulin-mediated vasorelaxation *in vitro* and *in vivo*. Hypertension 2001; 37: 328–33.
31 Misurski DA, Wu SQ, McNeill JR, Wilson TW, Gopalakrishnan V. Insulin-induced biphasic response in rat mesenteric vascular bed: role of endothelin. Hypertension 2001; 37: 1298–302.
32 Verma S, Bhanot S, McNeill JH. Effects of chronic endothelin blockade in hyperinsulinemia hypertensive rats. Am J Physiol 1995; 269: H2017–21.
33 Kurtz TW. Recent advances in genetics of the spontaneously hypertensive rat. Curr Hypertens Rep 2010; 12: 5–9.
34 Tran LT, Yuen VG, McNeill JH. The fructose-fed rats: a review on the mechanism of fructose-induced insulin resistance and hypertension. Mol Cell Biochem 2009; 332: 145–59.
35 Potenza MA, Marasciulo FL, Tarquinio M, Quon MJ, Montagnani M. Treatment of spontaneously hypertensive rats with rosiglitazone and/or enalapril restores balance between vasodilator and vasoconstrictor actions of insulin with simultaneous improvement in hypertension and insulin resistance. Diabetes 2006; 55: 3594–603.
36 Katakam PV, Ujhelyi MR, Hoenig ME, Miller AW. Endothelial dysfunction precedes hypertension in diet-induced insulin resistance. Am J Physiol 1998; 275: R788–92.
37 Hwang IS, Ho H, Hoffman BB, Reaven GM. Fructose-induced insulin resistance and hypertension in rats. Hypertension 1987; 10: 512–6.
38 Wilkes JJ, Hevener A, Olefsky J. Chronic endothelin-1 treatment leads to insulin resistance *in vivo*. Diabetes 2003; 52: 1904–9.

Acta Pharmacologica Sinica (2011) 32: 1475–1482
 1671-4083/11 $32.00
www.nature.com/aps

Original Article

Wogonin ameliorates lipotoxicity-induced apoptosis of cultured vascular smooth muscle cells via interfering with DAG-PKC pathway

Yu-min LIU[1], Xiong WANG[2], Ahmed NAWAZ[3], Zhao-hong KONG[1], Yan HONG[1], Chang-hua WANG[3], Jun-jian ZHANG[1, *]

[1]Department of Neurology, Zhongnan Hospital of Wuhan University, Wuhan 430071, China; [2]Department of Pathophysiology, Hubei University of Medicine, Shiyan 442000, China; [3]Department of Pathophysiology, Wuhan University School of Medicine, Wuhan 430070, China

Aim: To investigate the effects of wogonin (5,7-dihydroxy-8-methoxyflavone) extracted from *Scutellaria baicalensis* Georgi (*S baicalensis*) on lipotoxicity-induced apoptosis of vascular smooth muscle cells (VSMCs) and the underlying mechanisms.
Methods: Cultured VSMCs were used. Apoptosis of VSMCs was induced by palmitate (0.75 mmol/L), and detected using TUNEL assay. The expression levels of protein and phosphorylated protein were measured using Western blot analysis.
Results: Treatment of VSMCs with wogonin (10, 25 and 50 μmol/L) significantly attenuated the apoptosis and endoplasmic reticulum (ER) stress induced by palmitate in concentration- and time-dependent manners. Wogonin (50 μmol/L) decreased palmitate-induced reactive oxygen species (ROS) generation. The ER stress inhibitor 4-phenyl butyric acid (5 mmol/L) significantly decreased palmitate-induced apoptotic cells, and occluded the anti-apoptotic effect of wogonin (25 μmol/L). Wogonin (10, 25 and 50 μmol/L) significantly reduced the intracellular diacylglycerol (DAG) accumulation and expression levels of phosphorylated PKCs in palmitate-treated VSMCs.
Conclusion: Our results suggest that wogonin inhibits lipotoxicity-induced apoptosis of VSMCs via suppressing the intracellular DAG accumulation and subsequent inhibition of PKC phosphorylation. Wogonin has therapeutic potential for the prevention and treatment of atherosclerosis.

Keywords: wogonin; atherosclerosis; vascular smooth muscle cells; apoptosis; endoplasmic reticulum stress; palmitate; diacylglycerol (DAG); PKC

Acta Pharmacologica Sinica (2011) 32: 1475–1482; doi: 10.1038/aps.2011.120; published online 10 Oct 2011

Introduction

Diabetes mellitus is a major contributor to cerebrovascular and cardiovascular disease morbidity and mortality worldwide. Increased free fatty acid (FFA) levels in the plasma caused lipotoxicity, which is a hallmark of diabetes mellitus and leads to an increased risk of atherosclerosis and cardiovascular diseases[1–3]. Strong evidence has suggested that elevated FFA levels in the plasma enhance the intracellular accumulation of diacylglycerol (DAG), which leads to the activation of protein kinase Cs (PKCs), inhibitor kappaB kinase (IKK), or c-Jun N-terminal kinase (JNK), resulting in atherosclerotic plaque development and instability[4, 5]. Therefore, the plasma FFA and intracellular DAG levels represent selective targets to prevent atherosclerosis.

Vascular smooth muscle cells (VSMCs) play a pivotal role in the initiation and early progression of atherosclerosis and plaque rupture[6, 7]. Due to the important function of synthesizing components of the fibrous cap in plaques, VSMCs are responsible for promoting plaque stability in advanced atherosclerotic lesions. Published evidence has shown that VSMC apoptosis precipitates a number of deleterious consequences in atherosclerosis, such as plaque rupture[7–12]. Therefore, anti-apoptotic therapies for VSMCs may benefit the prevention and treatment of atherosclerosis[8, 10].

Scutellaria baicalensis Georgi (*S baicalensis*) is a traditional Chinese herb (Baikal Skullcap) that is widely used for the treatment of inflammation, infection, cancer, hypertension, and cardiovascular disease[13, 14]. Wogonin (5,7-dihydroxy-8-methoxyflavone) is a major bioactive component of the flavonoids from *S baicalensis*. Pharmacological findings have highlighted the therapeutic potential regarding the use of plant-derived wogonin to modulate endothelial cell and VSMC function for the prevention and treatment of atherosclerosis[15–17]. However, the underlying mechanism is poorly understood.

* To whom correspondence should be addressed.
E-mail wdsjkx@163.com
Received 2011-01-08 Accepted 2011-07-25

In this study, our results show that wogonin attenuates lipotoxicity-induced apoptosis and inhibits endoplasmic reticulum (ER) stress by suppressing intracellular DAG accumulation, which perturbs the DAG/PKC pathway in cultured VSMCs. This novel finding supplies evidence for the potential administration of wogonin for the treatment of atherosclerosis.

Materials and methods

Materials and reagents

Biochemical reagents were obtained from the following sources: palmitic acid, tunicamycin, wogonin ($C_{16}H_{12}O_5$) (Figure 1), 4-phenyl butyric acid (4-PBA) from Sigma (St Louis, MO, USA); the anti-CHOP antibody, anti-cleaved caspase-3 antibody, anti-cleaved caspase-6 antibody, anti-eIF2α antibody, anti-phosphorylated-eIF2α Ser51 antibody, anti-Bcl-2 antibody, anti-Bax antibody, PKC isoform antibody sampler kit, and phosphorylated-PKC isoform antibody sampler kit from Cell Signaling Technology; and secondary antibodies that were conjugated to alkaline phosphatase from Promega. The APO-BrdUTM TUNEL Assay Kit was purchased from Invitrogen. The ELISA Kit for DAG was obtained from Uscn Life Science, Inc (Wuhan, China).

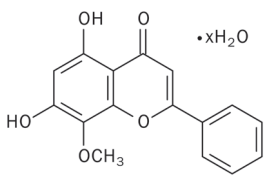

Figure 1. Chemical structure of wogonin.

Cell culture and treatment

Vascular smooth muscle cells (SV40LT-SMC Clone HEP-SA, ATCC CRL-2018™) were cultured in growth medium (Dulbecco's modified Eagle's medium with 4 mmol/L *L*-glutamine, which was adjusted to contain 1.5 g/L sodium bicarbonate and 4.5 g/L glucose, 0.2 mg/mL G418, and 10% bovine calf serum). A10 VSMCs (ATCC CRL-1476™) were incubated in DMEM (ATCC 30-2002) containing 10% FBS and 1.0 g/L sodium bicarbonate. The culture conditions were 37.0 °C, 95% O_2, and 5% CO_2. For treatment, the cells were serum-starved for 6 h and then incubated with palmitate and/or wogonin for the desired exposure time. The preparation of palmitate was as described in our previous study[18]. Briefly, palmitic acid was dissolved in ethanol, mixed with 20% BSA and then incubated overnight at 4 °C. The solution was filtered, stored at -20 °C and used within 2 weeks. The same concentration of ethanol was mixed with 20% BSA and used as a control.

Western blot analysis

The cells were lysed with lysis buffer (50 mmol/L Hepes, pH 7.6, 150 mmol/L NaCl, 1% Triton X-100, 10 mmol/L NaF, 20 mmol/L sodium pyrophosphate, 20 mmol/L β-glycerol phosphate, 1 mmol/L sodium orthovanadate, 10 μg/mL leupeptin, 10 μg/mL aprotinin, and 1 mmol/L phenylmethanesulfonyl fluoride). The cell lysates were incubated on ice for 10 min and then centrifuged at 14000×*g* for 10 min at 4 °C. The supernatants were mixed with equal volumes of 2×SDS-PAGE sample loading buffer. After heating at 95 °C for 4 min, the proteins were separated using a SDS-PAGE gel, transferred to a nitrocellulose membrane, and detected with the aforementioned antibodies.

Apoptosis determination

Terminal deoxynucleotidyl transferase-mediated dUTP-biotin nick end-labeling (TUNEL) was performed to detect cells undergoing apoptosis according to the manufacturer's protocol. Briefly, VSMCs were treated with palmitate and/or wogonin, washed with cold PBS three times and then fixed with 1% of paraformaldehyde on ice for 1 h. After washing three times with PBS, the cells were treated with 70% ethanol and incubated at -20 °C for 24 h. The cells were washed with wash buffer 3 times and incubated in DNA-labeling solution (including terminal deoxynucleotidyl transferase enzyme and BrdU triphosphate) at 37 °C for 1 h. The cells were rinsed with PBS, collected by centrifugation, and incubated in anti-BrdU-staining mix for 45 min at room temperature. The apoptotic nuclei containing nicked DNA were stained brown. To calculate the apoptosis rate, 1000 nuclei were identified in 20 random high power fields per slide.

Extraction and measurement of DAG

Total DAG levels were measured using an ELISA Assay Kit (Uscn Life Science Inc, Wuhan, China) according to the manufacturer's protocol. Briefly, the serum-starved VSMCs (1×10^6 cells/well in 6-well dishes) were incubated with or without different doses of palmitate and/or wogonin for the desired time. Total cell lipids were extracted with chloroform:methanol (1:2, *v*/*v*) after centrifugation at 5000×*g* for 2 min[19]. The lower chloroform phase was analyzed for DAG contents.

Measurement of reactive oxygen species

Intracellular reactive oxygen species (ROS) production was measured using the method of Shaw *et al*[20]. Briefly, VSMCs were plated in a 24-well plate at a density of 2×10^4 cells/well in DMEM, serum-starved for 6 h, and treated with or without different doses of palmitate and/or wogonin for the desired time. The cells were washed with modified Eagle's medium without phenol red and incubated in the dark for 10 min in Krebs-Ringer solution containing 50 μmol/L DCHF diacetate. Changes in fluorescence intensity were determined using an Flx-800 microplate fluorescence reader (Bio-Tek Instruments) at excitation and emission wavelengths at 485 and 528 nm, respectively[19, 20].

Statistical analysis

Three independent experiments were performed with each sample in triplicate. The data were expressed as the mean±SEM. Statistical analysis was performed using analysis

of variance followed by Student's *t*-test for paired data. $P<0.05$ was considered significant. The figures are representative of at least three independent experiments with similar results.

Results

Effects of wogonin on palmitate-induced apoptosis

Wogonin modulates endothelial cell and VSMC functions to promote its anti-atherosclerotic effects[15–17]. Considering the pivotal roles of VSMC apoptosis[7–12] and the elevated plasma FFA levels[4, 5] in atherosclerotic plaque ruptures, we investigated the potential effects of wogonin on palmitate-induced VSMC apoptosis. The serum-starved VSMCs were treated with different doses of wogonin for the desired time in the presence of 0.75 mmol/L palmitate for 24 h. As shown in Figure 2A and 2B, wogonin significantly attenuated the palmitate-induced apoptosis in a dose- and time-dependent manner. We evaluated the expression levels of cleaved caspase-3 and caspase-6 because activation of the caspase-3 pathway is a hallmark of apoptosis[21–23]. We found that wogonin inhibited the expression of cleaved caspase-3 and caspase-6 in a dose- and time-dependent manner in VSMCs that were pre-treated with 0.75 mmol/L palmitate (Figure 2C and 2D). The anti-apoptotic Bcl-2 and pro-apoptotic Bax proteins are among many key regulators of apoptosis. Therefore, we investigated the effects of wogonin on these regulatory proteins. We treated A10 VSMCs with 0.75 mmol/L palmitate for 12 h followed by treatment with 25 μmol/L wogonin for an additional 12 h. We found that wogonin restored Bcl-2 expression and decreased Bax expression, which consequently restored the ratio of Bcl-2 to Bax (Figure 3). These data suggest that wogonin protects VSMCs from palmitate-induced apoptosis.

Effects of wogonin on palmitate-induced ER stress

To identify the signaling pathway that initialized apoptosis, VSMCs were serum-starved by culturing in serum-free medium. Serum-starved VSMCs were treated with wogonin in a dose- and time-dependent manner in culture medium with 0.75 mmol/L palmitate. The levels of CHOP expression and eIF2α phosphorylation for these cells were analyzed using the Western blot analysis as stated under the Materials and methods. As shown in Figure 4A and 4B, palmitate-induced CHOP expression and eIF2α phosphorylation were suppressed by wogonin in a dose- and time-dependent manner similar to that observed in wogonin-mediated suppression of cleaved caspase-3 and caspase-6 expression and apoptosis. Apoptosis is initialized by extrinsic (activated by death ligands), intrinsic (mitochondrial pathway), or ER stress pathways[21–23]. We treated VSMCs to discover the potential anti-apoptotic effects of wogonin so that we could determine whether ER stress mediated the inhibitory effects of wogonin on apoptosis. 4-PBA (5 mmol/L) was used to inhibit ER stress in A10 VSMCs that were treated with 0.75 mmol/L palmitate and/or 25 mmol/L wogonin. We found that administration of 4-PBA significantly decreased the number of apoptotic cells in A10 VSMCs that were treated with palmitate and that wogonin treatment did not further enhance the inhibitory

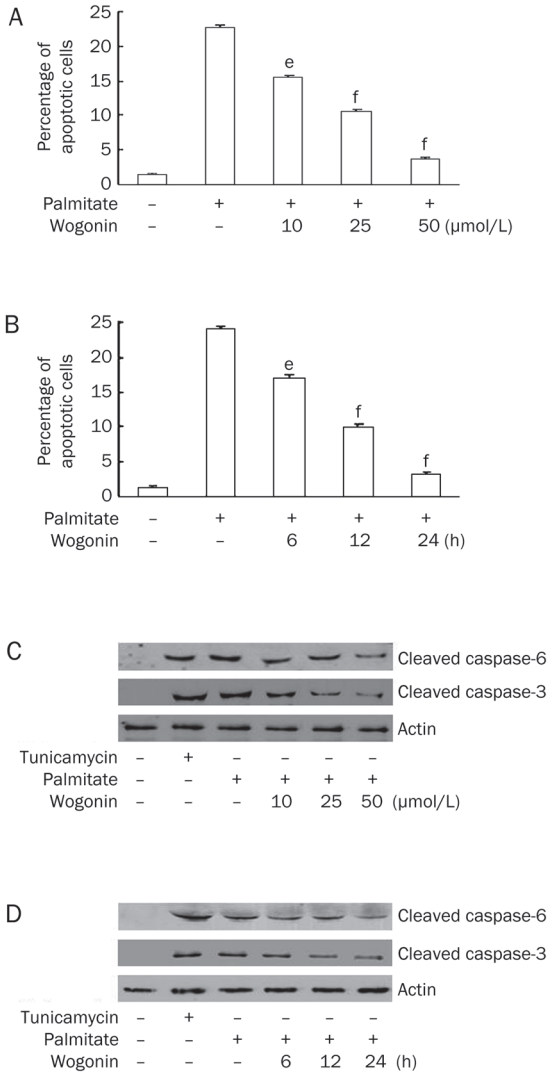

Figure 2. Wogonin prevented palmitate-induced apoptosis. VSMCs were cultured in serum-free medium for 6 h and treated with or without 0.75 mmol/L of palmitate for 12 h, followed by a second treatment with or without 10, 25, and 50 μmol/L of wogonin for an additional 12 h (A and C) or 25 μmol/L of wogonin for 6, 12, and 24 h (B and D). (A and B) The effects of wogonin on the percentage of apoptotic cells. Apoptotic cells were visualized using TUNEL methods. $^{e}P<0.05$; $^{f}P<0.01$ compared with the palmitate-treated group. (C and D) The effects of wogonin on cleaved caspase-3 and caspase-6 expression. In total, 5 μg/mL of tunicamycin (18 h) was used as a positive control. The expression levels of cleaved caspase-3 and caspase-6 were detected using Western blotting. The figures are representative of at least three independent experiments with similar results.

effects (Figure 5). These data suggest that palmitate-induced apoptosis and wogonin-mediated protection against apoptosis are mediated by ER stress. Taken together, these data indicate that wogonin promotes anti-apoptotic effects via inhibition of ER stress.

Effects of wogonin on palmitate-induced ROS generation

Over-generation of ROS is responsible for apoptosis in FFA-

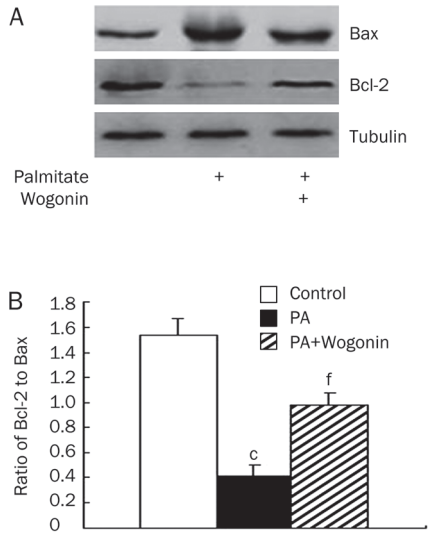

Figure 3. Wogonin restored the ratio of Bcl-2 to Bax. A10 VSMCs were cultured in serum-free medium for 6 h and treated with 0.75 mmol/L of palmitate (PA) for 12 h, followed by a second treatment with or without 25 μmol/L of wogonin for an additional 12 h. (A) Bcl-2 and Bax protein expression. (B) Bar graph for the ratio of Bcl-2 to Bax. Western blot was performed to detect the expression levels of Bcl-2 and Bax. The figures are representative of at least three independent experiments with similar results. $^{c}P<0.01$ compared with the control group. $^{f}P<0.01$ compared with the palmitate-treated group.

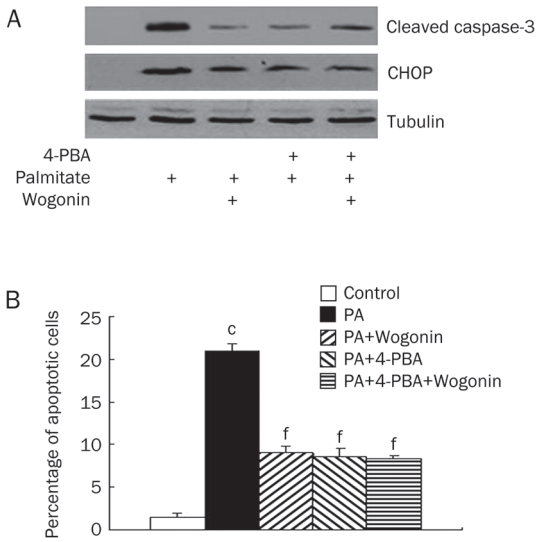

Figure 5. The effects of combined treatment of 4-PBA and wogonin on apoptosis. A10 VSMCs were cultured in serum-free medium for 6 h and treated with or without 4-PBA (5 mmol/L) for 1 h, followed by treatment with or without 25 μmol/L of wogonin for 12 h in the presence of 0.75 mmol/L of palmitate (PA) for 24 h. (A) CHOP and cleaved caspase-3 protein expression. (B) Bar graph for percentage of apoptotic cells. Western blot was performed to detect the expression levels of CHOP and cleaved caspase-3. The figures are representative of at least three independent experiments with similar results. $^{c}P<0.01$ compared with the control group; $^{f}P<0.01$ compared with the palmitate-treated group.

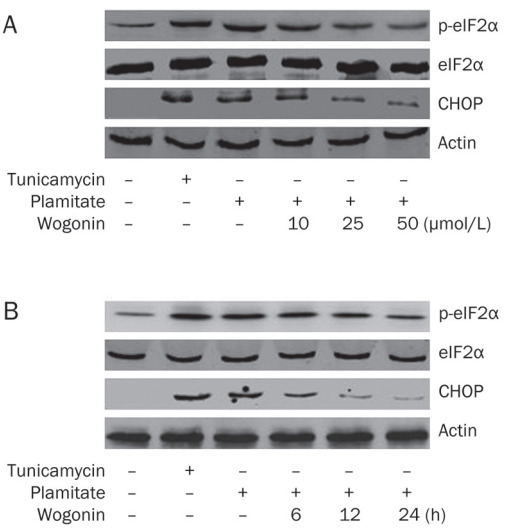

Figure 4. Wogonin inhibited palmitate-induced ER stress. VSMCs were cultured in serum-free medium for 6 h and treated with or without differential doses of wogonin for the indicated time in the presence of 0.75 mmol/L of palmitate or 10 μg/mL of the ER inducer tunicamycin for 24 h. (A) Dose course. In total, 10, 25, or 50 μmol/L of wogonin was added to the culture medium for 24 h. (B) Time course. In total, 50 μmol/L of wogonin was added to the culture medium for 6, 12, or 24 h. Western blot was performed to detect the expression levels of CHOP, eIF2α, and phosphorylated eIF2α. The figures are representative of at least three independent experiments with similar results.

treated cells[24–27]. We addressed whether wogonin has any effects on palmitate-mediated ROS generation. Serum-starved VSMCs were treated with wogonin in a dose- and time-dependent manner in culture medium with 0.75 mmol/L palmitate and evaluated to measure ROS generation. As shown in Figure 6A and 6B, ROS generation was increased in cells that were treated with palmitate and suppressed after a high dose (50 μmol/L) of wogonin treatment ($P<0.05$) and long exposure time (24 h) ($P<0.05$). These results indicate that the inhibition of ROS generation by wogonin is not a major mechanism for its anti-apoptotic effects.

Effects of wogonin on the DAG/PKC pathway

Accumulating evidence suggests that the DAG/PKC pathway contributes to deleterious consequences in cells, including apoptosis in response to FFA administration[28–35]. Based on this evidence, we hypothesized that wogonin-mediated suppression of apoptosis might counter this mechanism and improve cell survival. To confirm this hypothesis, serum-starved VSMCs were treated with wogonin in a dose- and time-dependent manner in culture medium with 0.75 mmol/L of palmitate and evaluated to measure intracellular levels of DAG. As expected, palmitate significantly increased the intracellular contents of DAG, which were suppressed by wogonin administration (Figure 7A and 7B). In addition, the administration of wogonin at a dose of 25 μmol/L for 24 h inhibited palmitate-induced PKC phosphorylation for mul-

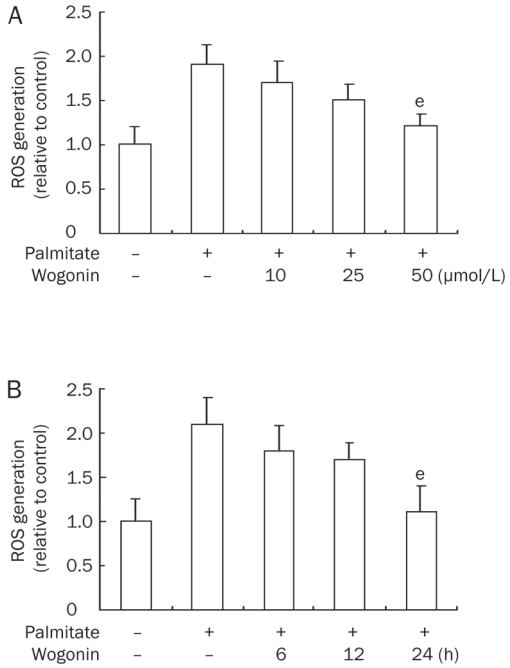

Figure 6. Wogonin suppressed palmitate-induced ROS generation. VSMCs were cultured in serum-free medium for 6 h and treated with or without different doses of wogonin for the indicated time in the presence of 0.75 mmol/L of palmitate for 24 h. (A) Dose course. In total, 10, 25, or 50 μmol/L of wogonin was added to the culture medium for 24 h. (B) Time course. In total, 50 μmol/L of wogonin was added to the culture medium for 6, 12, or 24 h. The production of ROS was determined as described in the Materials and methods section. $^{e}P<0.05$, $^{f}P<0.01$ compared with the palmitate-treated group.

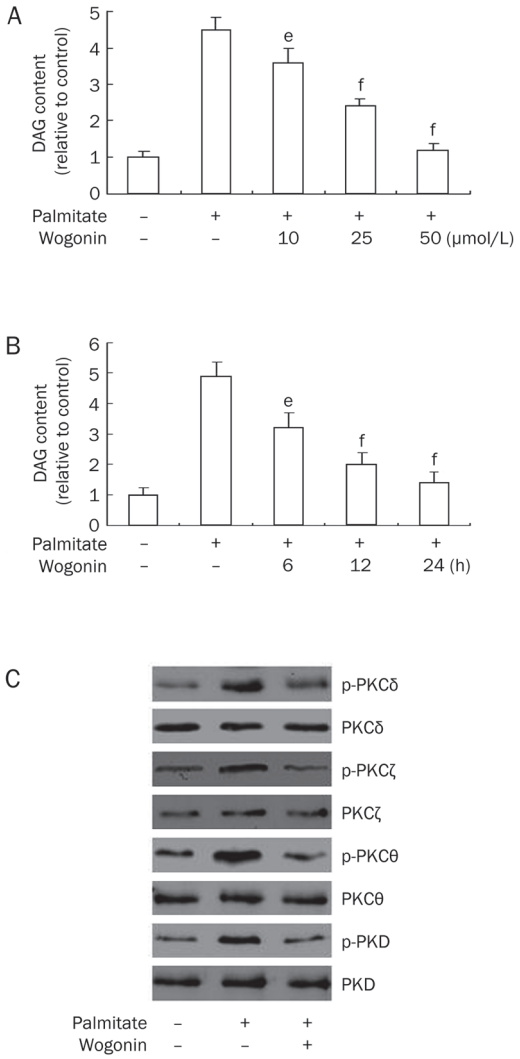

Figure 7. Wogonin ameliorated intracellular DAG accumulation and attenuated PKC phosphorylation. (A and B) VSMCs were cultured in serum-free medium for 6 h and treated with or without 0.75 mmol/L of palmitate for 12 h, followed by a second treatment with or without 10, 25, and 50 μmol/L of wogonin for an additional 12 h (A) or 25 μmol/L of wogonin for 6, 12, and 24 h (B). DAG content in the cells was determined as described in the Materials and methods section. $^{e}P<0.05$, $^{f}P<0.01$ compared with the palmitate-treated group. (C) VSMCs were cultured in serum-free medium for 6 h and treated with or without 25 μmol/L of wogonin for 12 h in the presence of 0.75 mmol/L of palmitate for 24 h. Western blot analysis was performed to detect the expression levels of total and phosphorylated PKC isoforms. The figures are representative of at least three independent experiments with similar results.

tiple PKC-isozymes (Figure 7C). These observations suggest that wogonin inhibits the DAG/PKC pathway, and attenuates apoptosis when combined with palmitate treatment.

Discussion

In this study, we demonstrate a protective effect of wogonin on palmitate-induced VSMC apoptosis. Palmitate-induced apoptosis of VSMCs was attenuated by wogonin administration in a dose- and time-dependent manner. The administration of wogonin inhibits the DAG/PKC pathway by down-regulating intracellular DAG accumulation and attenuating ER stress.

It is well documented that obese and diabetic patients have increased FFA levels, which induce atherosclerotic vascular disease. Previous studies have shown that even minute increases in plasma FFA may initiate early vascular abnormalities that promote atherosclerosis and cardiovascular disease (CVD)[1]. The most abundant saturated fatty acid in the plasma is palmitate. Studies have indicated that palmitate is involved in atherogenesis by increasing the extent of plaque formation (or plaque score)[36] and inducing extracellular matrix alterations[37]. In this study, we found that the administration of palmitate induced VSMC apoptosis (Figure 2). VSMCs synthesize components of the fibrous cap in plaques. Therefore, VSMC apoptosis may result in plaque ruptures[7–12]. Our results indicate a potential mechanism for FFA-induced plaque rupture.

Apoptosis can be initialized through an extrinsic pathway that is activated via death ligands, the intrinsic pathway (mitochondrial pathway), or the ER stress pathway that converges on the activation of caspase-3[21–23]. Our results confirm that palmitate significantly increases CHOP protein expression and

eIF2α phosphorylation (Figure 4).

We detected the increased expression of cleaved caspase-3 and caspase-6 (Figure 2), and the decreased ratio of anti-apoptotic protein Bcl-2 to pro-apoptotic protein Bax (Figure 3). Furthermore, the ER stress inhibitor 4-PBA prevented palmitate-induced apoptosis (Figure 5), which indicated that palmitate-induced apoptosis of VSMCs was mediated by ER stress. These data are congruent with previous studies showing that palmitate is a potent inducer of ER stress[38]. Recent evidence shows that atherosclerosis is associated with ER dysfunction and the accumulation of unfolded proteins[39–43]. Suppressing ER-stress signaling significantly attenuates accelerated atherogenesis[40]. The results of the current study suggest that increased FFA levels enhance ER stress, which may be an important risk factor in the induction of VSMC apoptosis in atherosclerosis.

Wogonin has recently been shown to be toxic in malignant cells but has no or little toxicity in normal cells[44–46]. Wogonin selectively induces apoptosis in tumor cells but has protective effects on glucocorticoid-induced apoptosis in normal rat thymocytes[46]. This selective antitumor function is largely due to its abilities to reduce inflammation, scavenge oxidative radicals, attenuate NF-κB activity, inhibit several genes that are important for regulation of the cell cycle, suppress COX-2 gene expression, block NO, and prevent viral infections[13, 47–49]. Our results demonstrate that wogonin attenuates palmitate-induced apoptosis of VSMCs in a dose- and time-dependent manner (Figure 2), which is accompanied by the suppression of ER stress (Figure 4). When ER stress was inhibited by 4-PBA, the administration of wogonin did not enhance its protective effects on apoptosis (Figure 5). Therefore, these data confirm that the inhibitory effects of wogonin on apoptosis are mediated by the suppression of ER stress.

ER and oxidative stresses are common manifestations in cells that are treated with FFA. The effect of FFA on ROS production has been examined in numerous cell types[50, 51]. ER stress and ROS are proposed to be involved in cell death. Nevertheless, their relative involvements in the processes leading to cell apoptosis are not well elucidated. Research groups have confirmed that over-generation of intracellular ROS might induce apoptosis in endothelial cells, beta cells, and retinal pericytes[24–27]. In contrast, some data shows that apoptosis may not be caused by increased ROS in VSMCs and neonatal cardiomyocytes that are incubated with palmitate[52, 53]. Our results show that palmitate increases ROS generation (Figure 6). Although the administration of wogonin at doses of 10 μmol/L and 25 μmol/L significantly reduced apoptosis (Figure 2), no effects where observed on ROS generation (Figure 6). These results suggest that palmitate-induced ROS generation may not be the major cause of apoptosis in VSMCs.

Furthermore, we found that palmitate increased the intracellular accumulation of DAG and consequently enhanced PKC phosphorylation (Figure 7). This result coincides with previous studies showing that saturated non-esterified fatty acids stimulate an increase in *de novo* intramuscular synthesis and accumulation of DAG[31, 32] and the subsequent activation of PKCs[28–30, 33–35]. Our results show that pre-treatment with wogonin significantly reduces the intracellular DAG levels and attenuates PKC phosphorylation (Figure 7). Because activated PKCs may contribute to altered cellular functions such as regulating signaling function of the ER[54, 55] and enhancing ROS production[51], our data suggest that the DAG/PKC pathway mediates palmitate-induced apoptosis and over-generated ROS production in VSMCs, and that wogonin ameliorates palmitate-induced ER stress by inhibiting the DAG-PKC pathway.

In conclusion, we provide novel evidence that wogonin attenuates lipotoxicity-induced apoptosis by suppressing intracellular DAG accumulation and inhibiting PKC phosphorylation in cultured VSMCs. However, further studies are necessary to determine whether the administration of wogonin will protect *in vivo* VSMCs from apoptosis and the subsequent rupture of advanced atherosclerotic plaques. Additional research into wogonin is also required to investigate the underlying mechanisms that suppress intracellular DAG accumulation in VSMCs.

Acknowledgements

We would like to thank Levi FROKE and Michael FREITAG (University of South Dakota, USA) for editing the manuscript for English grammar.

Author contribution

Yu-min LIU, Chang-hua WANG, and Jun-jian ZHANG designed the research; Xiong WANG, Ahmed NAWAZ, and Zhao-hong KONG performed the research; Yan HONG contributed new reagents and analytic tools; Yu-min LIU and Yan HONG analyzed the data; and Chang-hua WANG and Jun-jian ZHANG wrote the paper.

Abbreviations

DAG, diacylglycerol; DMEM, Dulbecco's modified Eagle's medium; ER, endoplasmic reticulum; FBS, fetal bovine serum; FFA, free fatty acid; PKC, protein kinase C; ROS, reactive oxygen species; VSMC, vascular smooth muscle cell; PBS, phosphate-buffered saline.

References

1 Mathew M, Tay E, Cusi K. Elevated plasma free fatty acids increase cardiovascular risk by inducing plasma biomarkers of endothelial activation, myeloperoxidase and PAI-1 in healthy subjects. Cardiovasc Diabetol 2010; 9: 9.

2 Gade W, Schmit J, Collins M, Gade J. Beyond obesity: the diagnosis and pathophysiology of metabolic syndrome. Clin Lab Sci 2010; 23: 51–61.

3 Boden G. Obesity and free fatty acids. Endocrinol Metab Clin North Am 2008; 37: 635–46.

4 Pilz S, März W. Free fatty acids as a cardiovascular risk factor. Clin Chem Lab Med 2008; 46: 429–34.

5 Montecucco F, Steffens S, Mach F. Insulin resistance: a proinflammatory state mediated by lipid-induced signaling dysfunction and involved in atherosclerotic plaque instability. Mediators Inflamm 2008; 2008: 767623.

6 Doran AC, Meller N, McNamara CA. Role of smooth muscle cells in the initiation and early progression of atherosclerosis. Arterioscler Thromb Vasc Biol 2008; 28: 812–9.
7 Rudijanto A. The role of vascular smooth muscle cells on the pathogenesis of atherosclerosis. Acta Med Indones 2007; 39: 86–93.
8 Clarke M, Bennett M. The emerging role of vascular smooth muscle cell apoptosis in atherosclerosis and plaque stability. Am J Nephrol 2006; 26: 531–5.
9 Clarke M, Bennett M. Defining the role of vascular smooth muscle cell apoptosis in atherosclerosis. Cell Cycle 2006; 5: 2329–31.
10 Stoneman VE, Bennett MR. Role of apoptosis in atherosclerosis and its therapeutic implications. Clin Sci (Lond) 2004; 107: 343–54.
11 Newby AC, Libby P, van der Wal AC. Plaque instability: the real challenge for atherosclerosis research in the next decade? Cardiovasc Res 1999; 41: 321–2.
12 Bennett MR. Apoptosis of vascular smooth muscle cells in vascular remodelling and atherosclerotic plaque rupture. Cardiovasc Res 1999; 41: 361–8.
13 Li-Weber M. New therapeutic aspects of flavones: the anticancer properties of Scutellaria and its main active constituents Wogonin, Baicalein and Baicalin. Cancer Treat Rev 2009; 35: 57–68.
14 Huang Y, Tsang SY, Yao X, Chen ZY. Biological properties of baicalein in cardiovascular system. Curr Drug Targets Cardiovasc Haematol Disord 2005; 5: 177–84.
15 Lee SO, Jeong YJ, Yu MH, Lee JW, Hwangbo MH, Kim CH, *et al*. Wogonin suppresses TNF-alpha-induced MMP-9 expression by blocking the NF-kappaB activation via MAPK signaling pathways in human aortic smooth muscle cells. Biochem Biophys Res Commun 2006; 351: 118–25.
16 Chang YL, Shen JJ, Wung BS, Cheng JJ, Wang DL. Chinese herbal remedy wogonin inhibits monocyte chemotactic protein-1 gene expression in human endothelial cells. Mol Pharmacol 2001; 60: 507–13.
17 Huang HC, Wang HR, Hsieh LM. Antiproliferative effect of baicalein, a flavonoid from a Chinese herb, on vascular smooth muscle cell. Eur J Pharmacol 1994; 251: 91–3.
18 Wang C, Liu M, Riojas RA, Xin X, Gao Z, Wu J, *et al*. Protein Kinase C {theta} (PKC{theta})-dependent phosphorylation of PDK1 at Ser504 and Ser532 contributes to palmitate-induced insulin resistance. J Biol Chem 2009; 284: 2038–44.
19 Ramana KV, Friedrich B, Tammali R, West MB, Bhatnagar A, Srivastava SK. Requirement of aldose reductase for the hyperglycemic activation of protein kinase C and formation of diacylglycerol in vascular smooth muscle cells. Diabetes 2005; 54: 818–29.
20 Shaw S, Wang X, Redd H, Alexander GD, Isales CM, Marrero MB. High glucose augments the angiotensin II-induced activation of JAK2 in vascular smooth muscle cells via the polyol pathway. J Biol Chem 2003; 278: 30634–41.
21 Hitomi J, Katayama T, Eguchi Y, Kudo T, Taniguchi M, Koyama Y, *et al*. Involvement of caspase-4 in endoplasmic reticulum stress-induced apoptosis and Abeta-induced cell death. J Cell Biol 2004; 165: 347–56.
22 Morishima N, Nakanishi K, Takenouchi H, Shibata T, Yasuhiko Y. An endoplasmic reticulum stress-specific caspase cascade in apoptosis. Cytochrome c-independent activation of caspase-9 by caspase-12. J Biol Chem 2002; 277: 34287–94.
23 Nakagawa T, Zhu H, Morishima N, Li E, Xu J, Yankner BA, *et al*. Caspase-12 mediates endoplasmic-reticulum-specific apoptosis and cytotoxicity by amyloid-beta. Nature 2000; 403: 98–103.
24 Kim JE, Kim YW, Lee IK, Kim JY, Kang YJ, Park SY. AMP-activated protein kinase activation by 5-aminoimidazole-4-carboxamide-1-beta-D-ribofuranoside (AICAR) inhibits palmitate-induced endothelial cell apoptosis through reactive oxygen species suppression. J Pharmacol Sci 2008; 106: 394–403.
25 Cai Y, Martens GA, Hinke SA, Heimberg H, Pipeleers D, Van de Casteele M. Increased oxygen radical formation and mitochondrial dysfunction mediate beta cell apoptosis under conditions of AMP-activated protein kinase stimulation. Free Radic Biol Med 2007; 42: 64–78.
26 Iverson SL, Orrenius S. The cardiolipin-cytochrome c interaction and the mitochondrial regulation of apoptosis. Arch Biochem Biophys 2004; 423: 37–46.
27 Yamagishi S, Okamoto T, Amano S, Inagaki Y, Koga M, Choei H, *et al*. Palmitate-induced apoptosis of microvascular endothelial cells and pericytes. Mol Med 2002; 8: 179–84.
28 Erion DM, Shulman GI. Diacylglycerol-mediated insulin resistance. Nat Med 2010; 16: 400–2.
29 Das Evcimen N, King GL. The role of protein kinase C activation and the vascular complications of diabetes. Pharmacol Res 2007; 55: 498–510.
30 Wang QJ. PKD at the crossroads of DAG and PKC signaling. Trends Pharmacol Sci 2006; 27: 317–23.
31 Lee JS, Pinnamaneni SK, Eo SJ, Cho IH, Pyo JH, Kim CK, *et al*. Saturated, but not n-6 polyunsaturated, fatty acids induce insulin resistance: role of intramuscular accumulation of lipid metabolites. J Appl Physiol 2006; 100: 1467–74.
32 Gaster M, Rustan AC, Beck-Nielsen H. Differential utilization of saturated palmitate and unsaturated oleate: evidence from cultured myotubes. Diabetes 2005; 54: 648–56.
33 Yu HY, Inoguchi T, Kakimoto M, Nakashima N, Imamura M, Hashimoto T, *et al*. Saturated non-esterified fatty acids stimulate *de novo* diacylglycerol synthesis and protein kinase c activity in cultured aortic smooth muscle cells. Diabetologia 2001; 44: 614–20.
34 Way KJ, Katai N, King GL. Protein kinase C and the development of diabetic vascular complications. Diabet Med 2001; 18: 945–59.
35 Lee IK, Koya D, Ishi H, Kanoh H, King GL. d-Alpha-tocopherol prevents the hyperglycemia induced activation of diacylglycerol (DAG)-protein kinase C (PKC) pathway in vascular smooth muscle cell by an increase of DAG kinase activity. Diabetes Res Clin Pract 1999; 45: 183–90.
36 Ebbesson SO, Roman MJ, Devereux RB, Kaufman D, Fabsitz RR, Maccluer JW, *et al*. Consumption of omega-3 fatty acids is not associated with a reduction in carotid atherosclerosis: the Genetics of Coronary Artery Disease in Alaska Natives study. Atherosclerosis 2008; 199: 346–53.
37 Rodríguez-Lee M, Ostergren-Lundén G, Wallin B, Moses J, Bondjers G, Camejo G. Fatty acids cause alterations of human arterial smooth muscle cell proteoglycans that increase the affinity for low-density lipoprotein. Arterioscler Thromb Vasc Biol 2006; 26: 130–5.
38 Rho MC, Ah Lee K, Mi Kim S, Sik Lee C, Jeong Jang M, Kook Kim Y, *et al*. Sensitization of vascular smooth muscle cell to TNF-alpha-mediated death in the presence of palmitate. Toxicol Appl Pharmacol 2007; 220: 311–9.
39 Kedi X, Ming Y, Yongping W, Yi Y, Xiaoxiang Z. Free cholesterol overloading induced smooth muscle cells death and activated both ER- and mitochondrial-dependent death pathway. Atherosclerosis 2009; 207: 123–30.
40 Khan MI, Pichna BA, Shi Y, Bowes AJ, Werstuck GH. Evidence supporting a role for endoplasmic reticulum stress in the development of atherosclerosis in a hyperglycaemic mouse model. Antioxid Redox Signal 2009; 11: 2289–98.
41 Cheng WP, Hung HF, Wang BW, Shyu KG. The molecular regulation of GADD153 in apoptosis of cultured vascular smooth muscle cells by

cyclic mechanical stretch. Cardiovasc Res 2008; 77: 551–9.
42 Chin TY, Lin HC, Kuo JP, Chueh SH. Dual effect of thapsigargin on cell death in porcine aortic smooth muscle cells. Am J Physiol Cell Physiol 2007; 292: C383–95.
43 Werstuck GH, Khan MI, Femia G, Kim AJ, Tedesco V, Trigatti B, *et al*. Glucosamine-induced endoplasmic reticulum dysfunction is associated with accelerated atherosclerosis in a hyperglycemic mouse model. Diabetes 2006; 55: 93–101.
44 Baumann S, Fas SC, Giaisi M, Müller WW, Merling A, Gülow K, *et al*. Wogonin preferentially kills malignant lymphocytes and suppresses T-cell tumor growth by inducing PLC{gamma}1- and Ca^{2+}-dependent apoptosis. Blood 2008; 111: 2354–63.
45 Lee DH, Kim C, Zhang L, Lee YJ. Role of p53, PUMA, and Bax in Wogonin induced apoptosis in human cancer cells. Biochem Pharmacol 2008; 75: 2020–33.
46 Enomoto R, Sugahara C, Suzuki C, Nagase I, Takamura Y, Yoshikawa A, *et al*. Wogonin prevents glucocorticoid-induced thymocyte apoptosis without diminishing its anti-inflammatory action. J Pharmacol Sci 2007; 104: 355–65.
47 Havsteen BH. The biochemistry and medical significance of the flavonoids. Pharmacol Ther 2002; 96: 67–202.
48 Rice-Evans CA, Miller NJ, Paganga G. St ructure-antioxidant activity relationships of flavonoids and phenolic acids. Free Radic Biol Med 1996; 20: 933–56.
49 Cao G, Sofic E, Prior RL. Antioxidant and prooxidant behavior of flavonoids: structure-activity relationships. Free Radic Biol Med 1997; 22: 749–60.
50 Lambertucci RH, Hirabara SM, Silveira Ldos R, Levada-Pires AC, Curi R, Pithon-Curi TC. Palmitate increases superoxide production through mitochondrial electron transport chain and NADPH oxidase activity in skeletal muscle cells. J Cell Physiol 2008; 216: 796–804.
51 Inoguchi T, Li P, Umeda F, Yu HY, Kakimoto M, Aoki T, *et al*. High glucose level and free fatty acid stimulate reactive oxygen species production through protein kinase C-dependent activation of NAD(P)H oxidase in cultured vascular cells. Diabetes 2000; 49: 1939–45.
52 Mattern HM, Hardin CD. Vascular metabolic dysfunction and lipotoxicity. Physiol Res 2007; 56: 149–58.
53 Hickson-Bick DL, Sparagna GC, Buja LM, McMillin JB. Palmitate-induced apoptosis in neonatal cardiomyocytes is not dependent on the generation of ROS. Am J Physiol Heart Circ Physiol 2002; 282: H656–64.
54 Pino SC, O'Sullivan-Murphy B, Lidstone EA, Thornley TB, Jurczyk A, Urano F, *et al*. Protein kinase C signaling during T cell activation induces the endoplasmic reticulum stress response. Cell Stress Chaperones 2008; 13: 421–34.
55 Lee W, Kim DH, Boo JH, Kim YH, Park IS, Mook-Jung I. ER stress-induced caspase-12 activation is inhibited by PKC in neuronal cells. Apoptosis 2005; 10: 407–15.

Acta Pharmacologica Sinica (2011) 32: 1483–1490
 1671-4083/11 $32.00
www.nature.com/aps

Original Article

Nerve growth factor induces cord formation of mesenchymal stem cell by promoting proliferation and activating the PI3K/Akt signaling pathway

Wen-xia WANG[1], Xin-yang HU[1, 2], Xiao-jie XIE[1, 2], Xian-bao LIU[1, 2], Rong-rong WU[1], Ya-ping WANG[1], Feng GAO[1], Jian-an WANG[1, 2, *]

[1]*Cardiovascular Key Lab of Zhejiang Province,* [2]*Department of Cardiology, Second Affiliated Hospital, College of Medicine, Zhejiang University, Hangzhou 310009, China*

Aim: To investigate whether nerve growth factor (NGF) induced angiogenesis of bone marrow mesenchymal stem cells (MSCs) and the underlying mechanisms.
Methods: Bone marrow MSCs were isolated from femors or tibias of Sprague-Dawley rat, and cultured. The cells were purified after 3 to 5 passages, seeded on Matrigel-coated 24-well plates and treated with NGF. Tube formation was observed 24 h later. Tropomyosin-related kinase A (TrkA) and p75NTR gene expression was examined using PCR analysis and flow cytometry. Growth curves were determined via cell counting. Expression of VEGF and pAkt/Akt were analyzed with Western blot.
Results: NGF (25, 50, 100 and 200 μg/L) promoted tube formation of MSCs. The tubular length reached the maximum of a 2.24-fold increase, when the cells were treated with NGF (50 μg/L). NGF (50 μg/L) significantly enhanced Akt phosphorylation. Pretreatment with the specific PI3K inhibitor LY294002 (10 μmol/L) blocked NGF-stimulated Akt phosphorylation, tube formation and angiogenesis. NGF (25–200 μg/L) did not affect the expression of TrkA and vascular endothelial growth factor (VEGF), but significantly suppressed the expression of p75NTR. NGF (50 μg/L) markedly increased the proliferation of MSCs.
Conclusion: NGF promoted proliferation of MSCs and activated the PI3K/Akt signaling pathway, which may be responsible for NGF induction of MSC angiogenesis.

Keywords: nerve growth factor; mesenchymal stem cells; angiogenesis; PI3K/Akt signaling pathway; TrkA; p75 neurotrophin receptor

Acta Pharmacologica Sinica (2011) 32: 1483–1490; doi: 10.1038/aps.2011.141

Introduction

Stem cell transplantation is one of newest therapeutic methods proposed to improve the outcome of patients with heart failure or infarctions[1, 2]. Mesenchymal stem cells (MSCs) are a group of clonogenic cells capable of multilineage differentiation and self-reproduction. They can differentiate into mesoderm-type cells, such as osteoblasts, adipocytes and chondrocytes. MSCs are present in adult tissues, most notably in bone marrow stroma[3, 4]. MSC transplantation could improve the outcomes of patients with myocardial infarction. The cause of improvement from this method is still unknown, but autocrine and paracrine growth mechanisms and angiogenesis are likely candidates[5].

In the peripheral and central nervous systems, NGF plays a crucial role in regulating growth, differentiation and survival of neurocytes[6, 7]. These physiological effects are mediated by two types of membrane receptors: tyrosine kinase receptor A (*TrkA*), which shows a high affinity for NGF, and *p75* neurotrophin receptor (*p75NTR*), which exhibits a low affinity for NGF[8]. The cellular effects of NGF are mediated mainly by the high affinity receptor, *TrkA*[9].

The physiological effect of NGF on the survival and differentiation of neurons has been well described, and there is now growing evidence that NGF displays potential for inducing angiogenesis in physiological and pathological conditions[10–13]. However, whether NGF could enhance angiogenesis in MSCs remains unclear.

In this study, we investigated the effect of NGF on MSC angiogenesis. Our findings indicated that NGF could promote MSC angiogenesis *in vitro* by promoting proliferation and activating the PI3K/Akt signaling pathway.

* To whom correspondence should be addressed.
E-mail wang_jian_an@tom.com
Received 2011-02-19 Accepted 2011-09-26

Materials and methods

MSC isolation and expansion

MSCs were isolated and harvested as previously described[14]. Briefly, male Sprague-Dawley rats (weight: 80 g, 2–3 weeks) were sacrificed, and we collected bone marrow samples by flushing their femoral and tibial cavities with low glucose Dulbecco's modified Eagle's medium (DMEM-LG). Samples were transferred to sterile centrifuge tubes. Tubes were centrifuged at 900×*g* for 5–8 min. The precipitate was resuspended in DMEM-LG containing 10% fetal bovine serum (FBS) (Sijiqing, Zhejiang, China), penicillin (100 U/mL) and streptomycin (100 g/L), then seeded into 25-cm^2 flasks (Falcon, Oxnard, CA, USA) and cultured at 37 °C in humidified air with 5% CO_2. After 24 h, the media was replaced and nonadherent hematopoietic cells were removed. Spindle-shaped adherent MSCs were expanded and purified with 3 to 5 passages after initial plating.

Flow cytometry analysis

Flow cytometry analysis was performed to identify MSC surface markers and to examine *p75* expression. MSCs were lifted with 0.25% trypsin and rinsed with phosphate buffered saline (PBS). Cells were centrifuged for 5 min at 900×*g*, resuspended in 0.5 mL PBS, and primary antibody was added (CD34, CD45: Santa Cruz, CA. CD29-PE: eBioscience, USA. CD31-PE, CD90-FITC: BD, USA. *P75*: Abcam, Cambridge, UK). Samples were incubated at room temperature for 1 h. After the cells were washed with PBS, they were incubated with secondary antibody for 1 h and then analyzed by flow cytometry.

Differentiation

Adipogenic differentiation

Passage p5 MSCs were seeded at 5×10^4 cells on culture plates in DMEM-LG. The following day, the medium was replaced with adipogenic induction medium composed of high glucose DMEM (DMEM-HG) with 1 μmol/L dexamethasone (Sigma-Aldrich, St Louis, MO, USA), 0.2 mmol/L indomethacin (Sigma), and 1×liquid media supplement (ITS) (Sigma). Media were changed every three days. After induction for 10 d, Oil Red O staining (Sigma) was used to examine adipogenic differentiation. Cells were observed and photographed with an inverted microscope.

Chondrocyte differentiation

Chondrocyte differentiation was performed using cell adherent culture methods. MSCs were cultured with DMEM-HG with 10 μg/L transforming growth factor β 3 (Santa Cruz), 100 μmol/L dexamethasone and 50 μmol/L ascorbic acid (Sigma). Media were changed every three days. After 14 d, toluidine blue staining was used to examine chondrocyte differentiation.

Matrigel assay

Cord formation was induced using Matrigel (Sigma)[15]. For the MSC cord formation assay, 200 μL of Matrigel was paved on a well of a 24-well plate and incubated for 1 h at 37 °C. MSCs were then trypsinized, resuspended and seeded onto the Matrigel (1×10^5 cells/well). MSCs were treated with NGF (R&D Systems, Minneapolis, MN) at different concentrations (0, 25, 50, 100, and 200 μg/L) with or without the PI3K specific inhibitor, LY294002 (10 μmol/L) (Sigma). The ability of MSC cord formation was observed and photographed using an inverted phase contrast microscope after 24 h. Pictures were taken from triplicate experiments and the tubular lengths of the MSCs were measured using Image-Pro Plus.

Immunocytochemistry

MSCs were cultured on Matrigel on 24-well plates, gently pulled off media and washed twice with PBS. Cells were fixed in 10% paraformaldehyde (dissolved in PBS) for 30 min at 37 °C, and permeabilized by immersion in 0.5% TritonX-100 for 15 min. After washing with PBS, the cells were blocked with 5% FBS/PBS for 1 h, and then labeled with appropriate primary antibodies (vWF: Santa Cruz, GAP43: Abcam). After overnight incubation at 4 °C, the cells were rinsed and incubated with TRITC-conjugated secondary antibodies for 1 h at RT, then washed and incubated with Hoechst 33258 (Invitrogen, CA, USA). Cells were analyzed using a fluorescent microscope (Olympus, Tokyo, Japan).

Reverse transcription-polymerase chain reaction (RT-PCR) and real-time PCR analysis

Total RNA was extracted using Trizol reagent (Invitrogen, USA) to analyze gene expression in the MSCs. RNA was reverse-transcribed to obtain cDNA. The sequences of PCR primers for *p75* were: 5′ TTGCTTGCTGTTGGAATGAG 3′ (forward), 5′ AGCTCCTGGGGAGGAAAATA 3′ (reverse) (Sangon, Shanghai, China). The sequences of *TrkA* primers were 5′ GTCTGGTGGGTCAGGGACTA 3′ (forward), 5′ GGGTTGCTTTCCATAGGTGA 3′ (reverse) (Sangon). The sequences of GAPDH primers were 5′ AGACAGCCGCATCTTCTTGT 3′ (forward), 5′ CTTGCCGTGGGTAGAGTCAT 3′ (reverse) (Sangon). Real-time PCR analysis of *p75* gene expression was performed with the ABI PRISM 7000 Sequence Detection System using the SYBR Green I Real Time PCR Kit (Bioer, Hangzhou, China). Relative quantification of gene expression was performed using the $2^{-\Delta\Delta Ct}$ method. Analysis of *TrkA* gene expression was performed by RT-PCR. Agarose gel electrophoresis (1.7 %) was performed to analyze the products.

Western blot analysis

MSCs were collected in an Eppendorf tube, then lysed with RIPA lysis buffer (Beyotime, Shanghai, China) for 30 min. Cell and nuclear lysates were centrifuged at 13 000×*g* for 25 min at 4 °C. Samples containing equal amounts (60 μg) of protein were run on SDS-PAGE gels and transferred onto PVDF membranes. Membranes were blocked with 0.1% Tween-20 TBS (TBS-T) containing 1% BSA for 1 h. Then the membrane was incubated in diluted primary antibodies (VEGF and β-actin: Santa Cruz, USA. Akt, pAkt: Cell Signaling Technology, Beverly, MA, USA). After washing in 0.1% TBS-T, the membranes were incubated for 2 h with HRP-conjugated secondary anti-

bodies. Bands were visualized by ECL. Quantity One software was used to semi-quantify protein levels in every lane.

Cell growth curve

Equal numbers (5×10^3) of MSCs with or without NGF were plated on 24-well plates. Cell number was determined using a cell counting chamber at 0, 1, 2, 3, 4, and 5 d after cell plating. Triplicate wells were used for each time point.

Statistical analysis

Data were expressed as the mean±SD and analyzed with SPSS 16.0 statistical software (SPSS Inc, Chicago, IL). Statistical analysis was performed by one-way ANOVA, and a P value <0.05 was considered statistically significant.

Results

Characterization of MSCs

To demonstrate that the cells isolated from rat bone marrow were indeed MSCs, we examined their differentiation capacity and phenotypic markers. MSCs appeared spindle-shaped and adhered to the bottom of the culture-flask (Figure 1A). After adipogenic induction for 10 d, MSCs contained abundant amounts of vacuoles, and Oil Red O staining demonstrated that these vacuoles contained neutral lipids (Figure 1B). After chondrogenic induction, MSCs showed metachromasia following toluidine blue treatment (Figure 1C). These results indicate that the MSCs differentiated into adipocytes and chondrocytes. Flow cytometry demonstrated that the MSCs were negative for the hematopoietic markers CD31, CD34, and CD45 but were positive for the MSC markers CD29 and CD90 (Figure 1D).

NGF promoted cord formation of MSCs in Matrigel

3-D Matrigel basement models closely mimic the structure, composition, physical properties and functional characteristics of the neovascularization microenvironment. To assess the effect of NGF on angiogenesis in MSCs, Matrigel assays were performed. After incubation for 24 h, MSCs formed tubes and networks on the Matrigel basement models *in vitro* (Figure 2A). After culturing with NGF for 24 h, the ability of the MSCs to form tubes was enhanced. As shown in Figure 2B–2E, the number of tubes, and the tubular lengths, were promoted in groups of NGF-treated MSCs compared to controls. NGF 50 and 100 μg/L enhanced cord formation in MSCs (P<0.05) (Figure 2F). The tubular length of 50 μg/L NGF-treated MSCs was 2.24-fold greater than controls. As such, the following experiments were performed using 50 μg/L NGF.

MSCs cultured in Matrigel may differentiate into endothelial cells

Matrigel has been widely used in cell-culture applications, and the Matrigel assay is commonly recognized as an angiogenesis model *in vitro*. Von Willebrand Factor (vWF) is a surface marker used to identify endothelial cells. The MSCs that formed tubes in Matrigel expressed vWF, which was used as a specific marker of endothelial cells (Figure 3B). However, the MSCs that did not form tubes were negative for vWF. This result indicated that tubes formed in Matrigel may differentiate into endothelial cells. Because the Matrigel can also support neuronal differentiation of neural precursor cells[16], we examined whether the MSCs differentiated into neurocytes. MSCs were positively expressing early neuronal markers and some mature neuronal markers. Immunofluorescence analyses showed that the MSCs were negative for GAP43

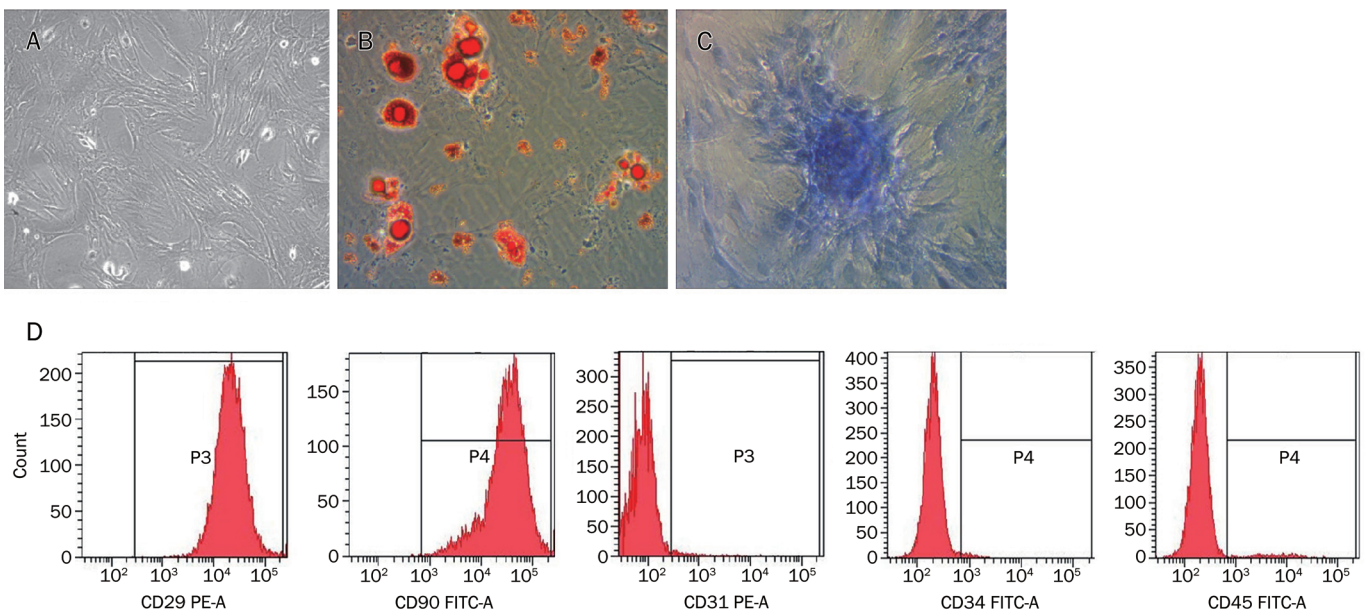

Figure 1. Characterization of mesenchymal stem cells (MSCs). (A) Representative morphological image of MSCs. Magnification×100. (B) Oil Red O staining of the adipogenic induction of MSCs. Magnification×200. (C) Toluidine blue staining of the chondrogenic induction medium-induced MSCs. Magnification×200. (D) Expression of cell surface markers on cultured MSCs. Flow cytometry analysis showed that the positivity of selected markers were as follows: CD29 99.6%, CD90 99.3%, CD31 2.4%, CD34 1.5%, CD45 3.2%.

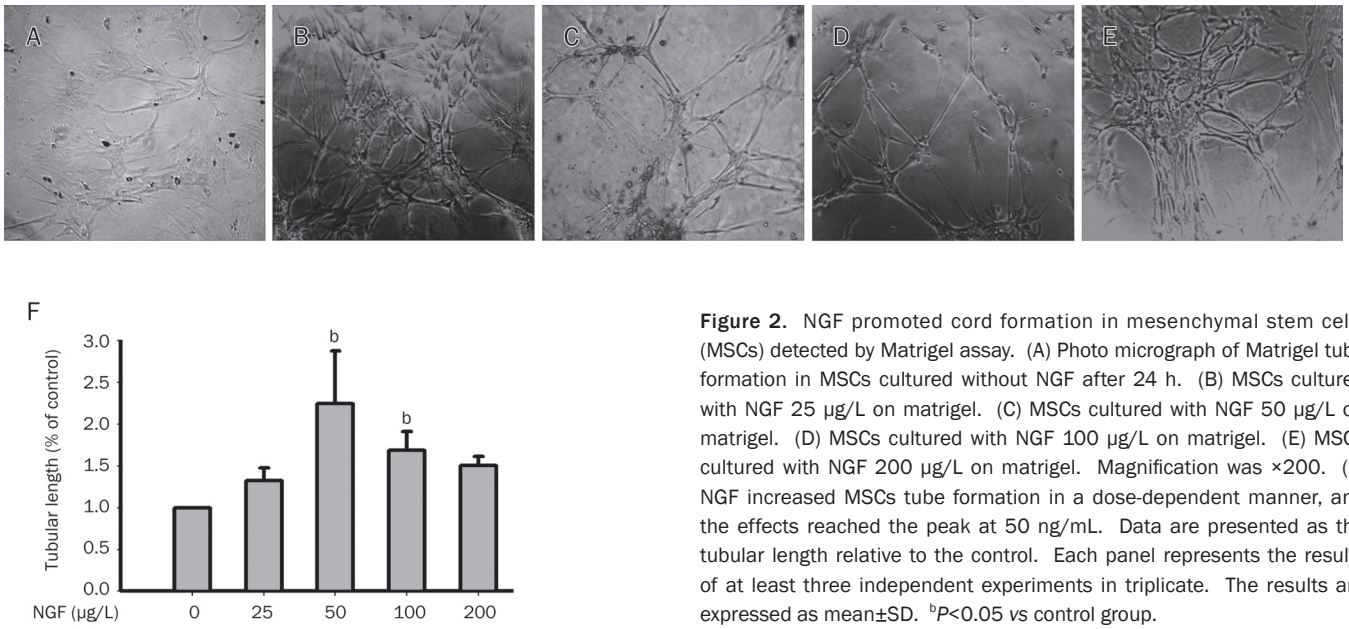

Figure 2. NGF promoted cord formation in mesenchymal stem cells (MSCs) detected by Matrigel assay. (A) Photo micrograph of Matrigel tube formation in MSCs cultured without NGF after 24 h. (B) MSCs cultured with NGF 25 μg/L on matrigel. (C) MSCs cultured with NGF 50 μg/L on matrigel. (D) MSCs cultured with NGF 100 μg/L on matrigel. (E) MSCs cultured with NGF 200 μg/L on matrigel. Magnification was ×200. (F) NGF increased MSCs tube formation in a dose-dependent manner, and the effects reached the peak at 50 ng/mL. Data are presented as the tubular length relative to the control. Each panel represents the results of at least three independent experiments in triplicate. The results are expressed as mean±SD. $^{b}P<0.05$ *vs* control group.

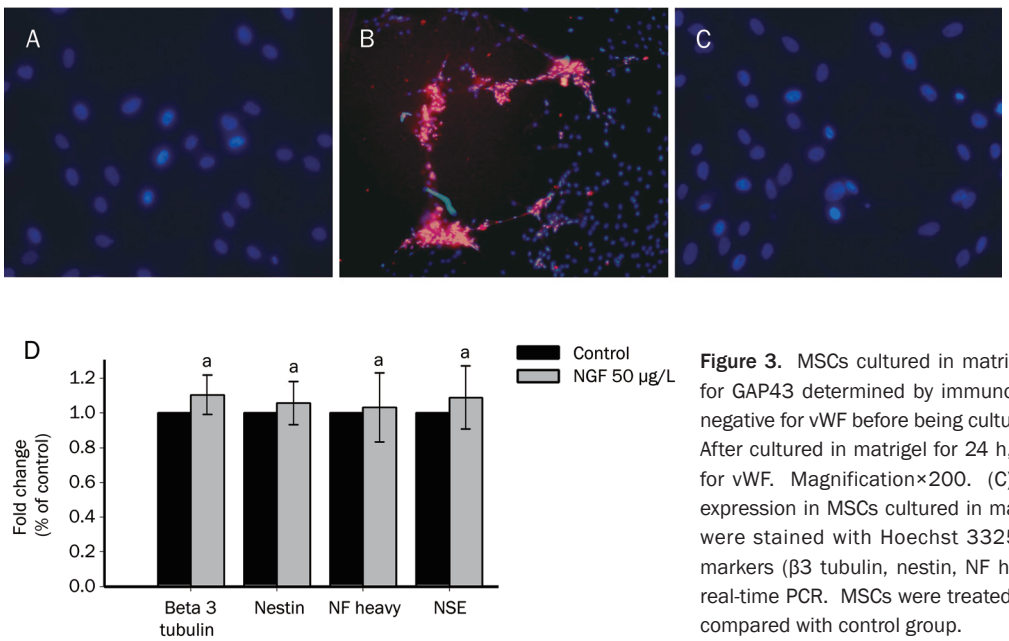

Figure 3. MSCs cultured in matrigel were positive for vWF and negative for GAP43 determined by immunofluorescence analysis. (A) MSCs were negative for vWF before being cultured in matrigel. Magnification×400. (B) After cultured in matrigel for 24 h, MSCs formed tubes and were positive for vWF. Magnification×200. (C) Immunofluoresence image of GAP43 expression in MSCs cultured in matrigel. Magnification×400. Nucleuses were stained with Hoechst 33258. (D) The expressions of neuronal markers (β3 tubulin, nestin, NF heavy, NSE) in MSCs were examined by real-time PCR. MSCs were treated with or without NGF for 24 h. $^{a}P>0.05$ compared with control group.

both before and after culture in Matrigel (Figure 3C). RT-PCR analyses demonstrated that pretreatment with only NGF had no influence on the expression of β3 tubulin, nestin, neurofilament (NF) or neuron-specific enolae (NSE) (Figure 3D).

Influence on TrkA and p75 receptor expression

TrkA gene expression was examined using RT-PCR. Total RNA was extracted after MSCs were either untreated or treated with NGF for 24 h. As shown in Figure 4A, the *TrkA* mRNA expression was barely detectable and was not influenced by NGF at any concentration. However, real-time PCR demonstrated that NGF-treatment decreased the expression of *p75* mRNA (Figure 4B). It induced a 0.27- to 0.55-fold decrease in gene expression in the NGF-treated MSC group when compared with controls, and NGF concentrations of 50 μg/L showed the strongest inhibiting effect. Moreover, flow cytometry further confirmed inhibition of *p75* gene expression by NGF (Figure 4C).

Activation of the PI3K/Akt signaling pathway in MSCs

Western blot experiments were used to identify the downstream signaling pathway involved in NGF-induced cord formation in MSCs. The results revealed that the phosphorylated form of Akt, a downstream target of PI3K, was elevated

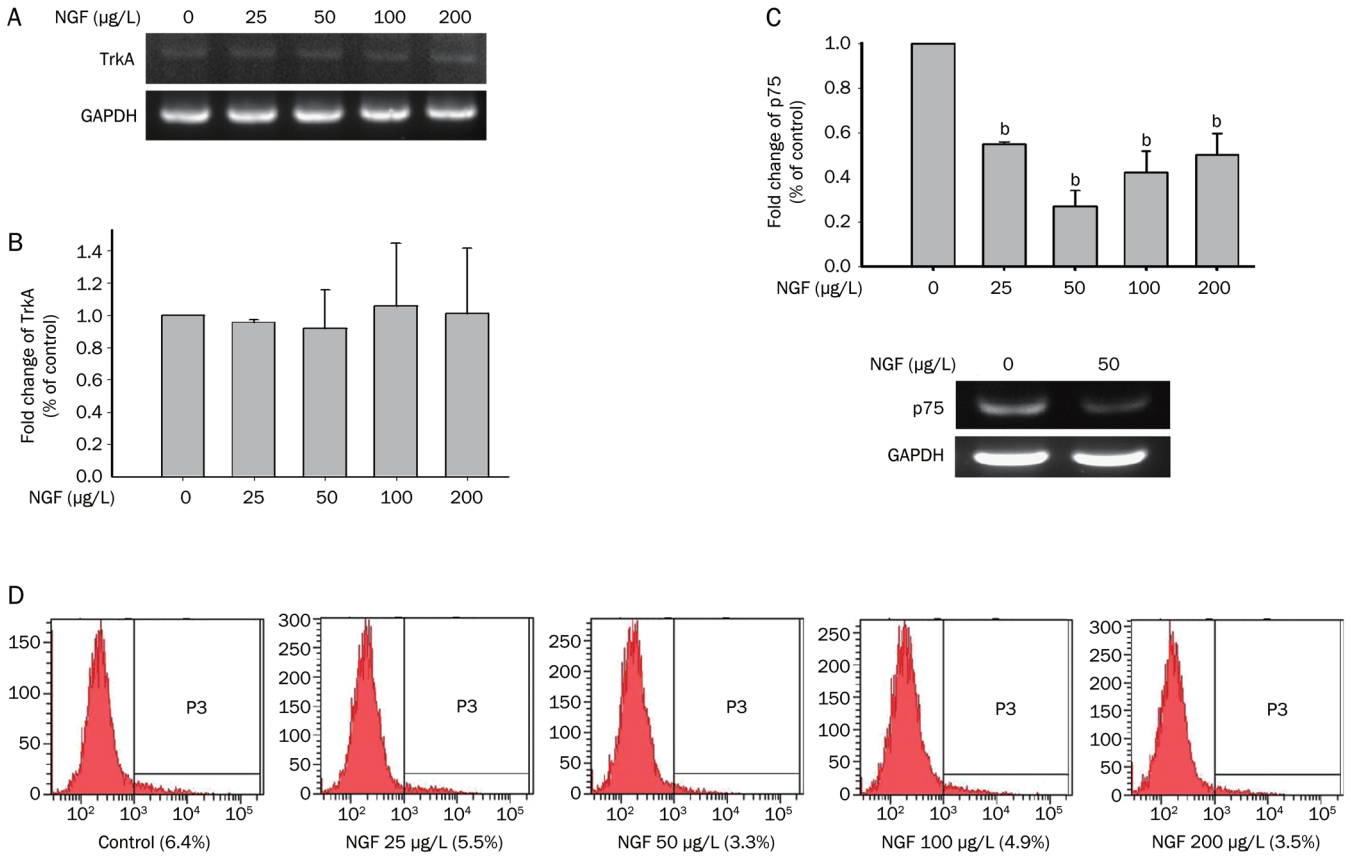

Figure 4. PCR and FACS analysis of TrkA and p75 expression. (A) Total RNA was isolated from MSCs treated or untreated with NGF. TrkA and a housekeeping gene (GAPDH) were analyzed by RT-PCR. (B) Data were expressed as the fold change of TrkA relative to the control. (C) P75NTR and GAPDH gene expressions of MSCs at different concentrations were examined by real-time PCR. Data were represented with mean±SD of three replicates. $^{b}P<0.05$ vs control group. (D) The effect of different concentrations of NGF on P75NTR protein level of MSCs was analyzed by FCS. The percentage of positive cells was listed in parentheses.

in NGF-treated MSCs within 1 h of treatment (Figure 5A). LY294002 was used to inhibit the activation of PI3K, which inhibited the expression of pAkt activated by NGF (Figure 5B). The addition of LY294002 (10 μmol/L) to cultures containg 50 μg/L NGF almost entirely attenuated NGF-induced capillary-like structure formation (Figure 5C–5G).

Enhancement of MSCs proliferation

The increased angiogenesis potential of MSCs after NGF pre-treatment prompted us to investigate whether it was associated with increased proliferation of MSCs. Figure 6 shows the growth curves of untreated MSCs and 50 μg/L NGF-treated MSCs. Following NGF treatment for 1 d, the cell growth was markedly enhanced, and the growth trend increased over time.

NGF had no influence on VEGF expression

To determine whether NGF-promoted MSC cord formation was related to VEGF expression, we determined the level of VEGF expression in treated and untreated MSCs. Figure 7 shows that NGF treatment had no significant effect on the expression level of VEGF in MSCs.

Discussion

The major findings of the present study were as follows: (1) NGF can induce MSC cord formation on Matrigel *in vitro*. (2) NGF had no influence on the expression of *TrkA* mRNA, but could inhibit *p75* expression in MSCs. (3) The effect of NGF-promoted MSC angiogenesis may be mediated by the PI3K/Akt signaling pathway. It also may be associated with the promotion of MSC proliferation, and has no correlation to VEGF expression in MSCs.

MSC transplantation was reported to improve myocardial function following myocardial infarction, but the underlying mechanisms remain to be elucidated[4]. Recent evidence has indicated that intramyocardial implantation of bone marrow MSCs induced revascularization, and these MSCs may differentiate into endothelial cells after myocardial infarction[5, 17]. Enhancing the angiogenesis ability of MSCs may be beneficial to improving myocardial function, and many studies have focused on accomplishing this aim. For instance, Annabi *et al* found hypoxic culture conditions could rapidly induce MSC migration and three-dimensional capillary-like structure formation on Matrigel through paracrine and autocrine regulatory mechanisms[18]. Wu *et al* found that calcium was a

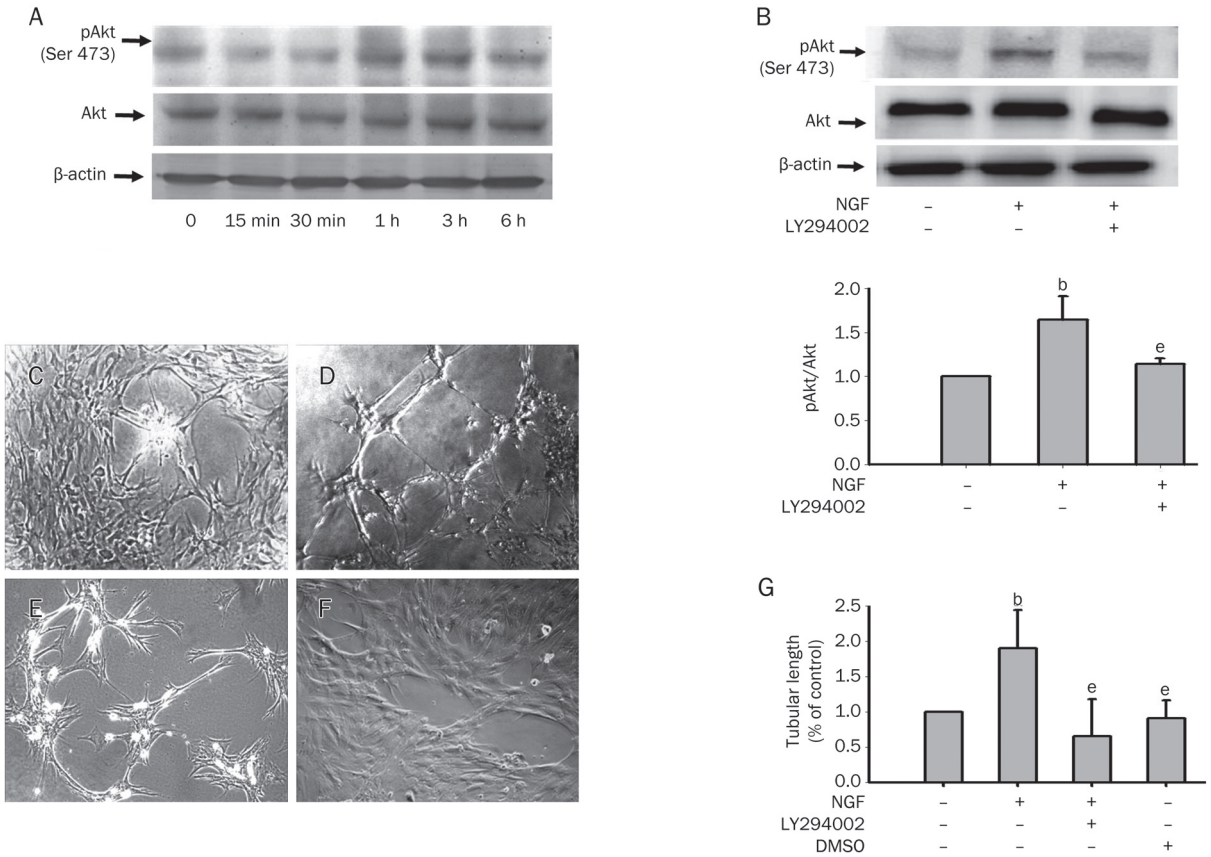

Figure 5. Effect of PI3K/Akt signaling pathway involved in the promotion of cord formation. (A) Western blot analysis of pAkt and Akt at the indicated time points after treated with NGF (50 μg/L). (B) Western blot analysis of pAkt and Akt of NGF treated MSCs. Cells were pretreated with or without LY294002 (10 μmol/L) for 1 h, and then stimulated with or without NGF (50 μg/L) for 1 h. $^{b}P<0.05$ *vs* control group. $^{e}P<0.05$ *vs* NGF treated MSCs. (C) Photomicrograph shows the matrigel tube formation of MSCs cultured without NGF. (D) MSCs cultured with NGF (50 μg/L) on matrigel for 24 h. (E) MSCs pretreated with LY294002 (10 μmol/L) for 1 h and cultured with NGF (50 μg/L) for 24 h on matrigel. Magnification×200. (F) MSCs cultured with DMSO (1 μmol/L) for 24 h on matrigel. (Because LY294002 was reconstituted in DMSO, so we evaluated the effect of DMSO on MSCs cord formation.) (G) LY294002 attenuated the angiogenic effect of NGF. Data were representative of three independent experiments. The results are expressed as mean±SD. $^{b}P<0.05$ *vs* control group. $^{e}P<0.05$ *vs* NGF treated MSCs.

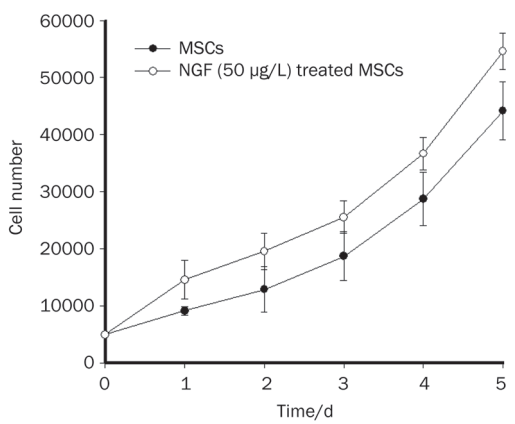

Figure 6. Growth curves of MSCs with or without NGF. Cell counting method was applied to examine the proliferation ability of MSCs. Data were representative of three independent experiments.

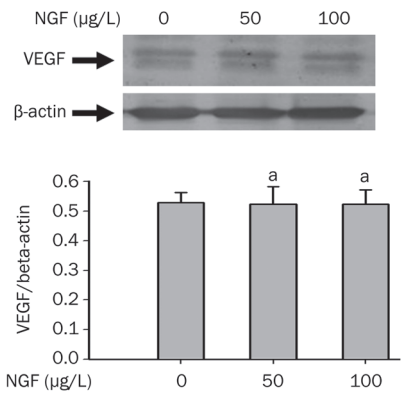

Figure 7. NGF treatment had no influence on the expression level of VEGF in MSCs. Western blot was performed to evaluate the expression of VEGF in MSCs after treatment with or without NGF (50 and 100 μg/L). Western blot image and quantitation of VEGF was normalized by β-actin. $^{a}P>0.05$ *vs* control group.

positive regulator of CXCR4 expression that enhanced bone marrow stem cell pro-angiogenesis therapy[19]. In the present study, we focused on NGF regulation of MSC tube formation and investigated the possible mechanism behind it.

NGF has been shown to trigger angiogenesis both directly and indirectly. NGF may induce expression of specific proteins, including VEGF and MMP-2, and may contribute to the maintenance, survival, and function of endothelial cells[10–13, 20, 21]. We found that NGF promoted MSC cord formation when grown on Matrigel, as evidenced by a 2.24-fold increase in tubular length when grown with a concentration of 50 μg/L NGF.

The Matrigel assay is commonly considered to be an experimental method that measures the ability of cells to promote angiogenesis *in vitro*[15] and is also used to support the differentiation of neural precursor cells into neuronal cells[16]. NGF is a common neurotrophic factor, so we needed to exclude the possibility that MSCs normally have the ability to differentiate into neuronal cells. Immunofluorescence analyses showed MSC-formed tubes may have differentiated into endothelial cells. MSCs were negative for GAP43 before and after culture in Matrigel. Because of the positive expression of early neuronal markers and a few mature markers, it is difficult to use immunofluorescence to judge whether the cells have a tendency to differentiate into neurocytes. Real-time PCR demonstrated that pretreatment with NGF had no influence on the expression of neuronal markers. Therefore, we believe that the cells were not differentiating into neurons.

Results indicated that tubular lengths responded to increasing concentrations of NGF in a pattern similar to a Gaussian distribution. It is unknown whether this distribution was caused by regulation of the NGF receptors. *TrkA* is a specific receptor of NGF and is involved in angiogenesis[22]. Myung-Jin Park *et al* demonstrated that *TrkA* activation induces endothelial cell invasion and cord formation[20]. However, our results showed *TrkA* mRNA were hardly detectable in MSCs, and NGF treatment had no significant effect on *TrkA* expression levels. Western blot analyses further confirmed that MSCs had low levels of *TrkA* protein expression (data not shown). *P75NTR* is a low affinity NGF receptor. To our surprise, real-time PCR and flow cytometry analyses both demonstrated that NGF could inhibit *p75* receptor expression in MSCs, and *p75*-positive cells only comprised 6.4% of the population. Previous studies show that *p75NTR* over-expression can promote apoptosis. We found that *TrkA* and *p75* were scarcely expressed in bone marrow MSCs, so we postulated that the inhibition of *p75* may be related to the effect of NGF in promoting MSC proliferation, and its association with MSC angiogenesis. Because our experiments show low levels of *TrkA* and *p75NTR* expression, there may be other mechanisms involved that require further study.

The PI3K/Akt signaling pathway is reported to be involved in angiogenesis in endothelial cells, and it plays an important role in the physiological effect of NGF, especially in the angiogenesis process[22]. Park *et al* demonstrated that NGF stimulates endothelial cell invasion and cord formation, and that the PI3K/Akt signaling pathway may be responsible for triggering angiogenesis[20].

Many reports have shown that the PI3K/Akt signaling pathway is critical for MSC proliferation, anti-apoptosis and migration, and promoted angiogenesis through specific stimulation[23, 24]. Activating PI3K could induce the assembly of receptor-PI3K complexes, followed by activation of Akt by a second messenger. Through phosphorylation, activated Akt mediated the activation and inhibition of several targets, resulting in cellular growth, survival and proliferation through various mechanisms[25].

Our Western blot analysis results showed that NGF stimulated Akt phosphorylation in MSCs. LY294002 inhibition of the catalytic activity of the p110 subunit of PI3K have been widely used *in vitro* for many years[25]. The Matrigel assay showed that NGF-induced MSC tube formation was completely blocked by LY294002. Using the specific kinase inhibitor, we showed that the PI3K/Akt signaling pathway was critical for NGF-induced MSC tube formation on Matrigel *in vitro*.

Cell proliferation plays an important role in angiogenesis. We used a cell growth curve method to evaluate whether the increased angiogenic potential of NGF-treated MSCs was associated with increased proliferation. We found that NGF could markedly promote MSC proliferation. During angiogenesis, NGF may promote MSC sprouting and proliferation during tube formation.

It has been reported that NGF up-regulated VEGF expression both *in vitro* and *in vivo*. NGF may be involved in promoting endothelial cell growth, which is associated with increased expression of VEGF. The result of this increased expression may be capillary sprouting[26]. VEGF is a crucial mediator of vascular hyperpermeability, angiogenesis, and inflammation. These processes are intimately involved in tissue repair and regeneration[27]. NGF played a functional role in reparative neovascularization through a VEGF-mediated mechanism[10]. Park *et al* showed that NGF may induce reparative angiogenesis during thymic regeneration in adults through the up-regulation of VEGF expression[13]. Wu *et al* showed that bone marrow MSCs stimulated endothelial cell proliferation, migration, and organization into tubules through the expression of high levels of VEGF[28]. Our data showed that MSCs could synthesize VEGF. However, the expression of VEGF was not different in both the NGF-treated and control groups. Our findings were different from the studies described above, which may be due to our use of different cells. NGF can promote VEGF expression in vascular endothelial cell and thymic epithelial cells, but it has no effect on VEGF expression in MSCs. Accordingly, we suggested that NGF-induced angiogenesis in MSCs are not related to VEGF expression.

Angiogenesis is very complex and consists of several processes, including proliferation, migration and invasion of endothelial cells, and is necessary for their survival. We investigated the effects of NGF on MSC migration through scratch tests and trans-well assays, but we observed that NGF did not promote migration (data not shown). We presume that

the enhancement of MSC angiogenesis by NGF contributes to increased cell proliferation and cord formation, though there may be other mechanisms involved.

In summary, this study demonstrates that NGF enhances proliferation in MSCs, and activates the PI3K/Akt signaling pathway. These effects may play an important role in angiogenesis, and these results may have value in the treatment of myocardial infarction using MSC transplantation.

Acknowledgements

This study was supported by the National Natural Science Foundation of China (Nos 30670868, 30770887, and 30770887/H0220), the Qianjiang Talent Scheme Foundation of Zhejiang Province (No 2009R10069) and the Key Lab of Traditional Chinese Medicine of Zhejiang Province (No ZK23812).

References

1 Forrester JS, Price MJ, Makkar RR. Stem cell repair of infarcted myocardium: an overview for clinicians. Circulation 2003; 108: 1139–45.
2 Tomita S, Li RK, Weisel RD, Mickle DA, Kim EJ, Sakai T, *et al.* Autologous transplantation of bone marrow cells improves damaged heart function. Circulation 1999; 100: II247–56.
3 Psaltis PJ, Zannettino AC, Worthley SG, Gronthos S. Concise review mesenchymal stromal cells potential for cardiovascular repair. Stem Cells 2008; 2008; 26: 2201–10.
4 Minguell JJ, Erices A. Mesenchymal stem cells and the treatment of cardiac disease. Exp Biol Med (Maywood) 2006; 231: 39–49.
5 Tse HF, Kwong YL, Chan JK, Lo G, Ho CL, Lau CP. Angiogenesis in ischaemic myocardium by intramyocardial autologous bone marrow mononuclear cell implantation. Lancet 2003; 361: 47–9.
6 Levi-Montalcini R, Angeletti PU. Nerve growth factor. Physiol Rev 1968; 48: 534–69.
7 Levi-Montalcini R. The nerve growth factor 35 years later. Science 1987; 237: 1154–62.
8 Chao MV, Hempstead BL. p75 and Trk: a two-receptor system. Trends Neurosci 1995; 18: 321–6.
9 Jing S, Tapley P, Barbacid M. Nerve growth factor mediates signal transduction through Trk homodimer receptors. Neuron 1992; 9: 1067–9.
10 Emanueli C, Salis MB, Pinna A, Graiani G, Manni L, Madeddu P. Nerve growth factor promotes angiogenesis and arteriogenesis in ischemic hindlimbs. Circulation 2002; 106: 2257–62.
11 Cantarella G, Lempereur L, Presta M, Ribatti D, Lombardo G, Lazarovici P, *et al.* Nerve growth factor-endothelial cell interaction leads to angiogenesis *in vitro* and *in vivo*. Faseb J 2002; 16: 1307–9.
12 Han Y, Qi Y, Kang J, Li N, Tian X, Yan C. Nerve growth factor promotes formation of lumen-like structures *in vitro* through inducing apoptosis in human umbilical vein endothelial cells. Biochem Biophys Res Commun 2008; 366: 685–91.
13 Park HJ, Kim MN, Kim JG, Bae YH, Bae MK, Wee HJ, *et al*. Up-regulation of VEGF expression by NGF that enhances reparative angiogenesis during thymic regeneration in adult rat. Biochim Biophys Acta 2007; 1773: 1462–72.
14 Xie XJ, Wang JA, Cao J, Zhang X. Differentiation of bone marrow mesenchymal stem cells induced by myocardial medium under hypoxic conditions. Acta Pharmacol Sin 2006; 27: 1153–8.
15 Shiba Y, Takahashi M, Ikeda U. Models for the study of angiogenesis. Curr Pharm Des 2008; 14: 371–7.
16 Uemura M, Refaat MM, Shinoyama M, Hayashi H, Hashimoto N, Takahashi J. Matrigel supports survival and neuronal differentiation of grafted embryonic stem cell-derived neural precursor cells. J Neurosci Res 2010; 88: 542–51.
17 Orlic D, Kajstura J, Chimenti S, Bodine DM, Leri A, Anversa P. Bone marrow stem cells regenerate infarcted myocardium. Pediatr Transplant 2003; 7: 86–8.
18 Annabi B, Lee YT, Turcotte S, Naud E, Desrosiers RR, Champagne M, *et al.* Hypoxia promotes murine bone-marrow-derived stromal cell migration and tube formation. Stem Cells 2003; 21: 337–47.
19 Wu Q, Shao H, Darwin ED, Li J, Li J, Yang B, *et al.* Extracellular calcium increases CXCR4 expression on bone marrow-derived cells and enhances pro-angiogenesis therapy. J Cell Mol Med 2009; 13: 3764–73.
20 Park MJ, Kwak HJ, Lee HC, Yoo DH, Park IC, Kim MS, *et al.* Nerve growth factor induces endothelial cell invasion and cord formation by promoting matrix metalloproteinase-2 expression through the phosphatidylinositol 3-kinase/Akt signaling pathway and AP-2 transcription factor. J Biol Chem 2007; 282: 30485–96.
21 Nicosia RF, Ottinetti A. Growth of microvessels in serum-free matrix culture of rat aorta. A quantitative assay of angiogenesis *in vitro*. Lab Invest 1990; 63: 115–22.
22 Nico B, Mangieri D, Benagiano V, Crivellato E, Ribatti D. Nerve growth factor as an angiogenic factor. Microvasc Res 2008; 75: 135–41.
23 Wang ZJ, Zhang FM, Wang LS, Yao YW, Zhao Q, Gao X. Lipopolysaccharides can protect mesenchymal stem cells (MSCs) from oxidative stress-induced apoptosis and enhance proliferation of MSCs via Toll-like receptor(TLR)-4 and PI3K/Akt. Cell Biol Int 2009; 33: 665–74.
24 Ryu CH, Park SA, Kim SM, Lim JY, Jeong CH, Jun JA, *et al.* Migration of human umbilical cord blood mesenchymal stem cells mediated by stromal cell-derived factor-1/CXCR4 axis via Akt, ERK, and p38 signal transduction pathways. Biochem Biophys Res Commun 2010; 398: 105–10.
25 Vivanco I, Sawyers CL. The phosphatidylinositol 3-kinase AKT pathway in human cancer. Nat Rev Cancer 2002; 2: 489–501.
26 Calza L, Giardino L, Giuliani A, Aloe L, Levi-Montalcini R. Nerve growth factor control of neuronal expression of angiogenetic and vasoactive factors. Proc Natl Acad Sci U S A 2001; 98: 4160–5.
27 Ferrara N. Role of vascular endothelial growth factor in regulation of physiological angiogenesis. Am J Physiol Cell Physiol 2001; 280: C1358–66.
28 Wu Y, Chen L, Scott PG, Tredget EE. Mesenchymal stem cells enhance wound healing through differentiation and angiogenesis. Stem Cells 2007; 25: 2648–59.

Acta Pharmacologica Sinica (2011) 32: 1491–1497
 1671-4083/11 $32.00
www.nature.com/aps

Original Article

Oxidized low-density lipoprotein and β-glycerophosphate synergistically induce endothelial progenitor cell ossification

Li LIU[1], Zhi-zhong LIU[1], Hui CHEN[2], Guo-jun ZHANG[1], Yu-hua KONG[1], Xi-xiong KANG[1, *]

[1]Center for Laboratory Diagnosis, Beijing Tiantan Hospital Affiliated to Capital Medical University, Beijing 100050, China; [2]Department of Clinical Laboratory, Beijing Boai Hospital, Beijing 100077, China

Aim: To investigate the ability of ox-LDL to induce ossification of endothelial progenitor cells (EPCs) *in vitro* and explored whether oxidative stress, especially hypoxia inducible factor-1α (HIF-1α) and reactive oxygen species (ROS), participate in the ossific process.
Methods: Rat bone marrow-derived endothelial progenitor cells (BMEPCs) were cultured in endothelial growth medium supplemented with VEGF (40 ng/mL) and bFGF (10 ng/mL). The cells were treated with oxidized low-density lipoprotein (ox-LDL, 5 μg/mL) and/or β-glycerophosphate (β-GP, 10 mmol/L). Calcium content and Von Kossa staining were used as the measures of calcium deposition. Ossific gene expression was determined using RT-PCR. The expression of osteocalcin (OCN) was detected with immunofluorescence. Alkaline phosphatase (ALP) activity was analyzed using colorimetric assay. Intercellular reactive oxygen species (ROS) were measured with flow cytometry.
Results: BMEPCs exhibited a spindle-like shape. The percentage of cells that expressed the cell markers of EPCs CD34, CD133, and kinase insert domain-containing receptor (KDR) were 46.2%±5.8%, 23.5%±4.0%, and 74.3%±8.8%, respectively. Among the total cells, 78.3%±4.2% were stained with endothelial-specific fluorescence. Treatment of BMEPCs with ox-LDL significantly promoted calcium deposition, which was further significantly enhanced by co-treatment with β-GP. The same treatments significantly increased the gene expression of core-binding factor a-1 (cbfa-1) and OCN, while decreased the gene expression of osteoprotegerin (OPG). The treatments also significantly enhanced the activity of ALP, but did not affect the number of OCN^+ cells. Furthermore, the treatments significantly increased ROS and activated the hypoxia inducible factor-1α (HIF-1α). In all these effects, ox-LDL acted synergistically with β-GP.
Conclusion: Ox-LDL and β-GP synergistically induce ossification of BMEPCs, in which an oxidizing mechanism is involved.

Keywords: atherosclerosis; vascular calcification; oxidized low-density lipoprotein; β-glycerophosphate; endothelial progenitor cells; ossification; oxidized stress

Acta Pharmacologica Sinica (2011) 32: 1491–1497; doi: 10.1038/aps.2011.128; published online 31 Oct 2011

Introduction

Calcification that occurs in nonosseous tissue is called ectopic calcification. Calcification in vessel walls is primarily thought of as a process of degeneration that follows atherosclerosis. Matrix vesicles containing phosphorites and some bone-associated genes and proteins are found in atherosclerotic areas, which indicates that vascular calcification is a proactive-regulated phenomenon similar to bone formation[1]. Oxidative stress and inflammation are considered the main stimuli of vascular calcification, but the mechanism remains unclear[2].

Smooth muscle cells have been used as an effective model for studying vascular calcification *in vitro*[3]. However, there are other kinds of cells that also contribute to vascular pathology. Stem cells from bone marrow, such as marrow stromal cells (MSCs), endothelial progenitor cells (EPCs) and hematopoietic stem cells (HSCs), have many similar functions and potentials of transdifferentiation. Recent research has shown that EPCs participate in vascular pathology through a diphasic action. On one hand, EPCs homing into lesions and contribute to neovascularization and re-endothelialization after vessel injury. On the other hand, because of their stem cell characteristics, EPCs express phenotypes of fibration or ossification rather than differentiating into functional cells in certain abnormal microenvironments, which could aggravate vascular injury. It has been reported that EPCs express osteocalcin (OCN) in patients with coronary atherosclerosis or

* To whom correspondence should be addressed.
E-mail kangxx@vip.sina.com
Received 2011-05-04 Accepted 2011-08-22

severe aortic valve stenosis[4, 5]. Furthermore, EPCs were found in the areas of calcium deposition[6]. Local calcium deposition and microcalcification in the vessel wall could play a role in the adherence of circulating EPC populations and perhaps their differentiation towards an osteogenic phenotype. The phenotypes expressed by EPCs are determined by the local microenvironment. All of these studies implied a close correlation between endothelial differentiation and calcification. Unfortunately, research has focused only on transdifferentiation of EPCs *in vivo*. Whether EPCs can be induced to ossify *in vitro* and what factors might contribute to the transdifferentiation remains unknown.

Oxidized low-density lipoprotein (ox-LDL) has a dramatic effect on atherosclerosis[7]. Ox-LDL stimuli can cause endothelial cells to lose their vaso-protective effect and damage EPCs by triggering apoptosis, accelerating senescence and inhibiting endothelialization[8-10]. Ox-LDL also induces vascular smooth muscle cells to express genes associated with bone formation by up-regulating osterix[11], which is considered a risk factor for calcification.

In this study, we examined in detail the ability of ox-LDL to induce ossification of EPCs *in vitro* and explored whether oxidative stress, especially hypoxia inducible factor-1α (HIF-1α) and reactive oxygen species (ROS), participate in the ossific process. The results may provide a new understanding of the role of stem cells in vascular calcification.

Materials and methods

Reagents

The materials used in the experiments were from the following sources: Endothelial growth medium was purchased from Cambrex Corporation (Charles, IA, USA). VEGF and bFGF were purchased from PeproTech Asia (Rehovot, Israel). Fluorescein isothiocyanate-labeled lectin from ulex europaeus agglutinin (FITC-UEA-1), 2′,7′-dichlorofluorescin diacetate (DCHF-DA), β-glycerophosphate (β-GP) and fibronectin were all obtained from Sigma-Aldrich (USA). The Reverse Transcription System kit and the GoTaq qPCR Master Mix kit were obtained from Promega (Madison, WI, USA). The Sensolyte pNPP Alkaline Phosphatase ELISA Assay kit was purchased from AnaSpec Company (Fremont, CA, USA). The primary antibodies CD34-PerCP Cy5.5 and KDR-Alexa Fluor 647 were obtained from Becton Dickinson (San Jose, CA, USA). CD133-PE antibody was from eBioscience (San Diego, CA, USA). 1,1′-dioctadecyl-3,3,3′,3′-tetramethyl-indocarbocyanine-labeled acetylated low-density lipoprotein (DiI-ac-LDL) and ox-LDL (MDA=50 nmol/mL) were purchased from XieSheng Biotechnology Limited-liability Company (Beijing, China). Sprague-Dawley rats (SPF/VAF) were purchased from Vital River Laboratories (Beijing, China); the certificate number was SCXX2006-0009.

Ethics

Animal experiments were approved by the Institutional Ethics Committee of Beijing Tiantan Hospital, China. The experiments were performed according to the National Research Council's guidelines.

Cell culture

Bone marrow-derived endothelial progenitor cells (BMEPCs) were cultured as previously described[12]. In brief, bone marrow was aspirated from tibias and femurs of Sprague-Dawley rats (100 g in weight) and washed with Dulbecco's modified Eagle medium (DMEM) containing 5% fetal bull serum. Bone marrow-derived mononuclear cells (BMMNCs) were isolated with Ficoll-Paque (GE Healthcare, Sweden) density-gradient centrifugation. After being washed twice with PBS, BMMNCs (1×10^6/mL) were plated into six-well plates coated with fibronectin and cultured with endothelial growth medium (EGM) supplemented with 40 ng/mL VEGF and 10 ng/mL bFGF. Culture medium was renewed every three days.

Identification of EPCs

To identify their characteristics, the attached cells were trypsinized and labeled directly with three fluorescent antibodies: CD34-PerCP Cy5.5, CD133-PE, and KDR-Alexa Fluor 647. Cell fluorescence was measured by the FACSCalibur flow cytometer (Becton Dickinson). Cellquest software was used to analyze the ratios of positive cells. Additional cells were incubated with 2.4 μg/mL DiI-ac-LDL for 1 h at 37 °C, fixed in 2% paraformaldehyde and stained with 10 μg/mL FITC-UEA-1 for 40 min. The nuclei were stained with Hoechst 33342. Fluorescence microscopy (Olympus, DP71) was used to identify the percentage of dual-positive cells.

Treatment with ox-LDL

The results of preliminary experiments showed that 5 μg/mL ox-LDL had no significant impact on cell survival after 14 d of incubation. This concentration could be used for ossific induction. After attachment, the primary passages were exposed to 5 μg/mL ox-LDL, 10 mmol/L β-GP, or 5 μg/mL ox-LDL plus 10 mmol/L β-GP. Historically, β-GP has been thought to act solely as a phosphate donor and as such was required for the mineralization of primary cell cultures *in vitro*[11]. Cells were maintained in normal growth medium as a control. Osteogenic differentiation was evaluated as explained below.

Calcium staining and quantification

Mineralization in induced cells were investigated using Von Kossa staining as previously described[13]. Briefly, fixed cells were incubated in 5% silver nitrate solution for 30 min in the dark. The cells were then washed with distilled water and exposed to light for 45 min. Calcium particles were observed in visual fields at a magnification of ×40.

The treated cells were washed twice with PBS and rinsed in 0.6 mol/L HCl. Intracellular calcium was extracted after incubating the cells for 24 h at 37 °C with continuous shaking. The supernatant was collected by centrifugation (1000×*g* for 5 min). Calcium concentration was determined by the autobiochemistry analyzer (Roche P800, Switzerland). The calcium content was normalized to total protein content as determined by the Bradford method.

Expression of osteogenic genes

Total RNA isolation and reverse transcription polymerase chain reaction (RT-PCR) were performed. Briefly, the cells of interest were lysed with TRIzol reagent (Invitrogen, CA, USA). The target genes were amplified using the Reverse Transcription System kit and the GoTaq qPCR Master Mix kit. The genes of interest included the following: core-binding factor a-1 (cbfa-1), which serves as the transcription factor triggering the expression of major osteoblast-specific lineage genes; osteoprotegerin (OPG), which acts as a suppressive signal of vascular calcification in normal cells; and OCN, which is the classic and mature marker for bone formation. The primers (Invitrogen, Shanghai, China) are shown in Table 1. The ratios of associated genes to beta-actin were analyzed semiquantitatively with Quantity One software (Bio-Rad, USA).

ALP activity

Alkaline phosphatase (ALP) activity of the induced cells was quantified using the Sensolyte pNPP Alkaline Phosphatase ELISA Assay Kit according to the manufacturer's instructions. The yellow product, p-nitrophenol, was measured by the microplate reader (Thermo, MK3) at a wavelength of 405 nm. ALP activity was standardized according to total protein content.

Immunofluorescence for osteocalcin

Immunofluorescent staining was used to detect osteocalcin. BMEPCs were fixed in 4% paraformaldehyde for 20 min and blocked with anti-serum containing 0.5% Triton for 40 min at room temperature. The cells were then incubated with a primary monoclonal antibody targeted to osteocalcin (Santa Cruz, CA, USA) at 4 °C overnight. The cell were incubated with a secondary antibody, labeled with FITC (Jackson ImmunoResearch, PA, USA), at 37 °C for 40 min. Hoechst 33342 was used to stain cell nuclei. Cells were washed with PBS between each step.

Oxidative stress

Intracellular ROS was detected to evaluate oxidative status. Cells were loaded with 10 μmol/L DCHF-DA at 37 °C for 1 h, washed with PBS and harvested gently. DCHF-DA is a stable fluorescent ROS-sensitive compound, which is oxidized by hydrogen peroxide or low-molecular-weight peroxides to produce the green fluorescence of 2′,7′-dihydrogendichlorofluorescein (DCF). DCF in cells was measured using flow cytometry. Fluorescence intensity represented the level of ROS. The mean fluorescence for each sample was analyzed by Cellquest software.

Statistical analysis

All data were presented as the mean±standard deviation (SD). The differences between groups were analyzed by Student's *t* test. A value of $P<0.05$ was considered statistically significant.

Results

Characteristics of EPCs derived from bone marrow

BMMNCs were cultured in endothelial growth medium for 7 d and exhibited the typical spindle-like shapes of endothelial progenitor cells (Figure 1A). Endothelial characteristics were assessed by the uptake of DiI-ac-LDL and the binding of FITC-UEA-1. Approximately 78.3%±4.2% of total adherent cells were dual-positive (Figure 1B–1D), indicating that they expressed the scavenger receptor for ac-LDL and the ligand for UEA-1. Furthermore, the cell markers of EPCs were displayed. (Figure 1E–1G). The percentages of CD34, CD133, and KDR were 46.2%±5.8%, 23.5%±4.0%, and 74.3%±8.8%, respectively. On the basis of these characteristics, the cells could be considered as BMEPCs[12].

Increased calcium deposition in BMEPCs

Calcium deposition is an early event of ossification. BMEPCs were cultured in 5 μg/mL ox-LDL in the absence or presence of β-GP for 14 d. The concentration of intracellular calcium in control cells was 4.4±0.95 μg/mg protein. Both ox-LDL and β-GP significantly increased intracellular calcium deposition. The values were 12.3±3.2 μg/mg protein ($P<0.05$) and 17.2±2.0 μg/mg protein ($P<0.01$), respectively. When ox-LDL and β-GP were combined, calcium deposition increased 6.1-fold (28.0±2.4 μg/mg protein, $P<0.01$) compared with the control and 2.3-fold compared with ox-LDL alone ($P<0.01$). The

Table 1. Primers for target genes.

Name	Size (bp)	Primers	Locus number
Cbfa-1	200	Forward: 5′-GCAAGGTTCAACGATCTGAG-3′ Reverse: 5′-GAGGCGGTCAGAGAACAAAC-3′	NM_001024630.3
OCN	335	Forward: 5′-CAGCCACCGAGACACCAT-3′ Reverse: 5′-CCAGCAGAGCGACACCCTA-3′	NM_199173.3
OPG	207	Forward: 5′-CCTTGCCCTGACCACTAC-3′ Reverse: 5′-TTGCACCACTCCAAATCC-3′	NM_002546.3
HIF-1α	408	Forward: 5′-AAACCACCTATGACCTGC-3′ Reverse: 5′-GTCGTGCTGAATAATACCACTC-3′	NM-001530.3
Beta-actin	302	Forward: 5′-TCAGGAGGAGCAATGATCTTG-3′ Reverse: 5′-TCCTCCCTGGAGA AGAGCTA-3′	NM_031144.2

Cbfa-1, core-binding factor a 1; HIF-1α, hypoxia inducible factor 1α, OPG: osteoprotegerin; OCN, osteocalcin.

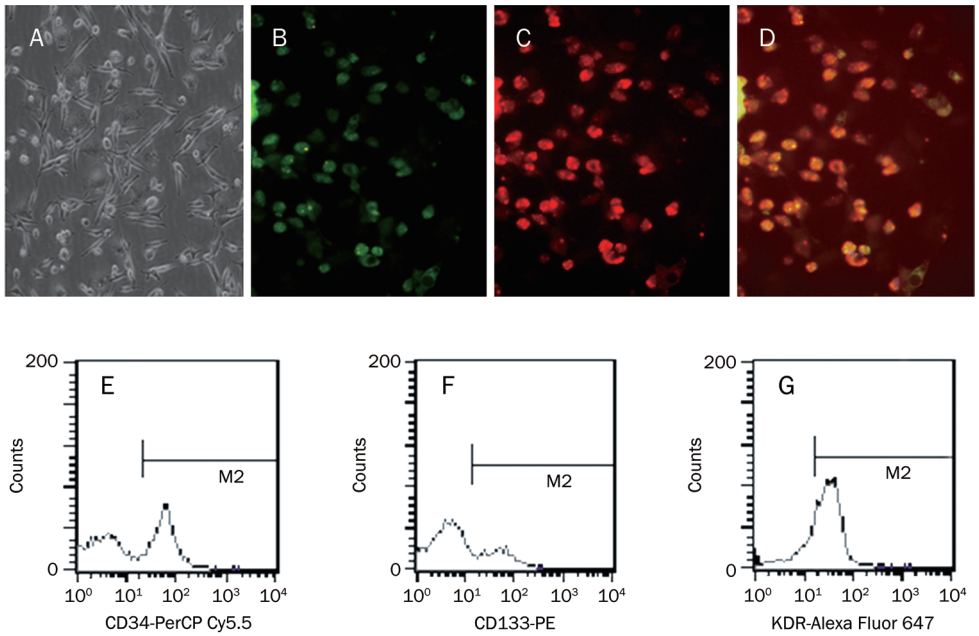

Figure 1. Characterization of EPCs. Mononuclear cells from bone marrow were cultured in endothelial growth medium for 7 d. (A) BMEPCs displayed spindle-like shapes under bright field (100×); (B) Adherent cells with green FITC-UEA-1; (C) Adherent cells with red DiI-ac-LDL; (D) Dual-positive cells with orange were identified as differentiating BMEPCs (200×); (E, F, G) The M2 gate in histograms from flow cytometer showed the percentages of CD34, CD133 and KDR stained with fluoresceins-labeled antibodies. Results were displayed as mean±SD (n=4).

results were consistent with the Von Kossa staining (Figure 2). Ox-LDL not only increased intracellular calcium when used alone but also enhanced the effect of β-GP.

Changes in bone-associated genes in BMEPCs

For the gene expression analyses, BMEPCs were cultured for 7 d in the presence of ox-LDL and/or β-GP. Ox-LDL alone slightly increased cbfa-1, but the increase was not significant compared with the control. Ox-LDL plus β-GP increased the expression of cbfa-1 by 2.2-fold relative to the control. The expression of OPG decreased by approximately 50%–60% in groups treated with ox-LDL (Figure 3A). OCN expression did not change in any of the groups after 7 d of induction. We extended the time of treatment to 10 d and the level of OCN increased approximately 1.6-fold in both ox-LDL and β-GP groups; moreover, there was a 2.8-fold increase in ox-LDL plus β-GP group relative to the control (Figure 3B). The results showed that the expression of certain bone-associated genes in BMEPCs could be changed by treatment with ox-LDL and β-GP. Furthermore, ox-LDL had a synergistic effect with β-GP.

Increased ALP activity in BMEPCs

ALP activity was determined after ox-LDL/β-GP incubation for 11 d by a colorimetric assay. Control cells showed low ALP activity, but treatment with ox-LDL increased ALP activity 1.2-fold, which was similar to β-GP treatment. There was a 1.5-fold increase in cells treated with both ox-LDL and β-GP (Figure 4). ALP is a representative marker of bone formation; therefore, the data suggest that BMEPCs responded to the increased activity of bone-associated proteins.

No difference of OCN$^+$ BMEPCs

Immunofluorescence detection of OCN was performed after

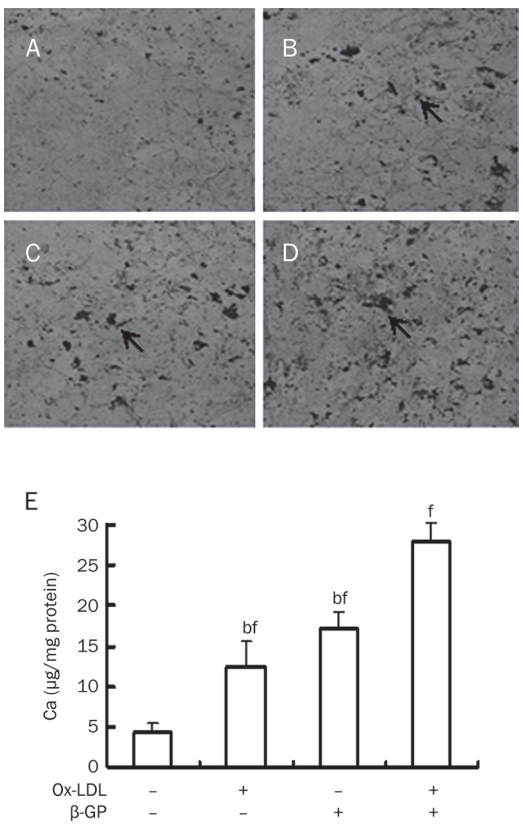

Figure 2. Calcium deposition of BMEPCs. BMEPCs were incubated for 14 d with 5 μg/mL ox-LDL and/or 10 mmol/L β-GP. The effects of ox-LDL on calcification were assessed by the content of calcium and Von Kossa staining. Calcium nodule displayed black or deep-brown granules and local cord-like shapes (×40, pointed out with arrows). (A) Control; (B) Ox-LDL; (C) β-GP; (D) Ox-LDL plus β-GP. Results were displayed as mean±SD (n=3). ^bP<0.05 *vs* ox-LDL plus β-GP group. ^fP<0.01 *vs* control.

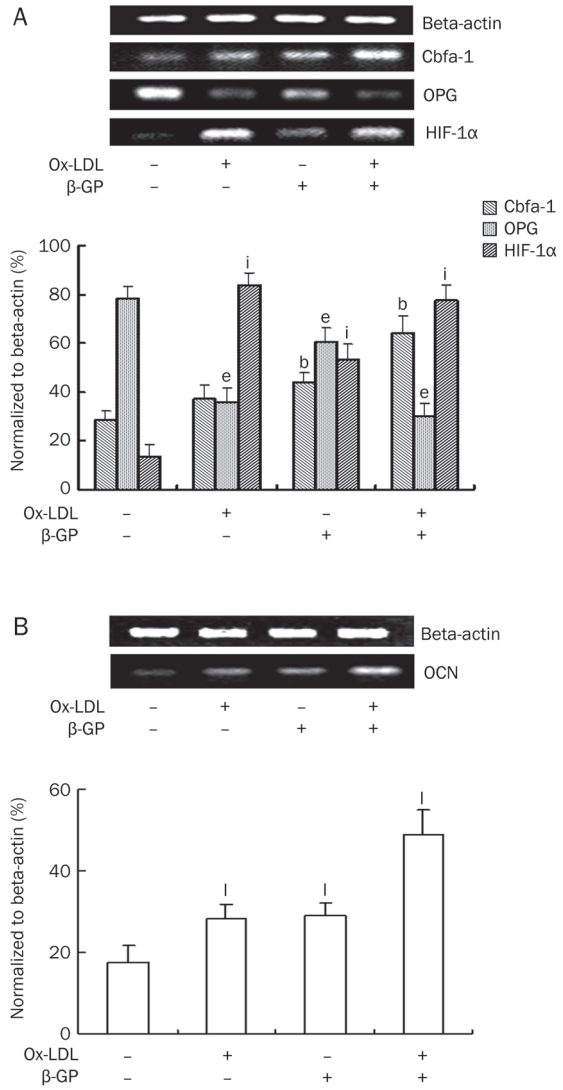

Figure 3. Expression of osteogenic genes. BMEPCs were incubated with 5 μg/mL ox-LDL and/or 10 mmol/L β-GP. The levels of osteogenic genes were assessed by RT-PCR. The ratios were normalized to beta-actin. (A) Genes of 7 d; (B) Genes of 10 d. Results were displayed as mean±SD (n=3–5). ^{b}P<0.05 *vs* cbfa-1 of control. ^{e}P<0.05 *vs* OPG of control. ^{i}P<0.01 *vs* HIF-1α of control. ^{l}P<0.01 *vs* OCN of control.

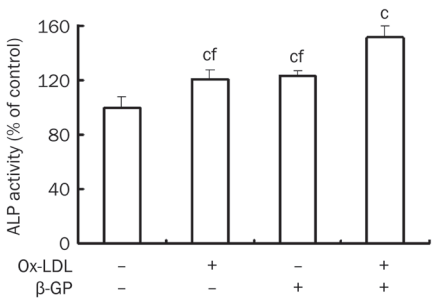

Figure 4. ALP activity. BMEPCs were incubated for 11 d with 5 μg/mL ox-LDL and 10 mmol/L β-GP. ALP activity was determined by colorimetric. Results were displayed as mean±SD (n=3). The activity displayed as the percentage of control. ^{c}P<0.01 *vs* control. ^{f}P<0.01 *vs* ox-LDL plus β-GP group.

14 d of treatment with ox-LDL and β-GP. OCN^{+} cells were counted under the microscope in ten random visual fields at a magnification of 200×. The immunopositive cells were easily identified (Figure 5), but there was no difference among the groups.

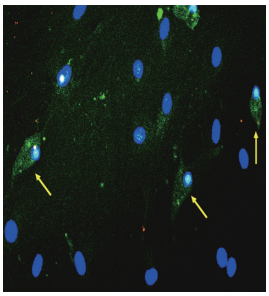

Figure 5. Immunofluorescence for OCN. BMEPCs were incubated for 14 d with 5 μg/mL ox-LDL and/or 10 mmol/L β-GP. Monoclonal antibody and FITC labeled second antibody were used. The positive cells (pointed out with arrows) showed fusiform-like appearance. ×200.

Contribution of oxidative stress to ossification

To assess the mechanism of ossification induced by ox-LDL, intracellular ROS was determined. Fluorescence intensity data are shown as a percentage of the control. During the inducible process, ROS increased persistently, yet it improved at 5 d than at 1 d. In the ox-LDL-treated group, ROS increased 3.8-fold, 2.7-fold and 2.4-fold at 1 d, 3 d, and 5 d, respectively. A similar change occurred in the ox-LDL plus β-GP group. The results showed that the early phase of transdifferentiation induced by ox-LDL was accompanied by high levels of ROS. After 3 d, a relatively stable level of ROS was maintained (Figure 6). Moreover, HIF-1α, which acts as a regulatory factor for differentiation under hypoxia, also increased more than 5-fold in the ox-LDL treated groups after treatment for 7 d (Figure 3A). We also assessed HIF-1α at 1 d and 3 d, but no apparent expression was detected. The results indicate that

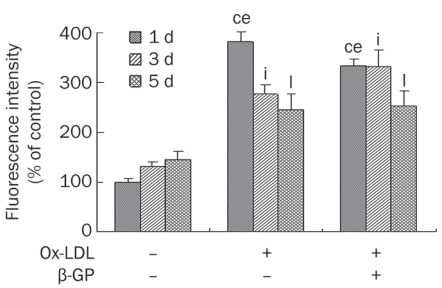

Figure 6. Effects of ox-LDL on ROS production in BMEPCs. BMEPCs were treated for 1 d, 3 d, and 5 d with 5 μg/mL ox-LDL and/or 10 mmol/L β-GP and were stained with DCHF-DA. Flow cytometric analysis was performed to determine the mean fluorescence intensity of DCF-positive cells. Data were shown as the percentage of control. Results were displayed as mean±SD (n=3). ^{c}P<0.01 *vs* control at 1 d. ^{e}P<0.05 *vs* the same group at 5 d. ^{i}P<0.01, ^{l}P<0.01 *vs* control at 3 d and 5 d, respectively.

ROS and HIF-1α were activated successively during the ossification process.

Discussion

EPCs can be isolated from peripheral blood, spleen, bone marrow and adipose tissue. They express cell markers of both stem cells and endothelial cells. Because of different culture conditions, the percentage of cell markers identified was neither exact nor unified. In our study, the medium, which was supplied with a high concentration of VEGF and bFGF, could be used to selectively culture EPCs with spindle morphology and the phagotrophic function of the endothelium. In combination with a special set of cell markers (CD34, CD133, KDR), the cells isolated from bone marrow were mostly identified as a mixture of EPCs and immature endothelial cells. Because endothelial cells do not differentiate, the ossific effects identified in our study came from BMEPCs. Thus, this method could provide another stem cell model for vascular ossification in addition to monocytic progenitor cells and MSCs[14, 15].

Ox-LDL contributes to vascular calcification by inducing smooth muscle cells and foam cells to initiate fibrosis and form atheromas, which is followed by an increase in calcium deposition[16]. There is a positive correlation between coronary calcium or instability of coronary plaques and plasma ox-LDL level[17]. *In vitro* ox-LDL increased ALP activity, induced transient and strong expression of bone morphogenetic protein 2 (BMP2) and matrix gla-protein (MGP) and accelerated mineralization[18]. However, ox-LDL treatment at specified concentrations inhibited Pi-induced UMR106 rat osteoblast mineralization and bone associated proteins, suggesting that ox-LDL would simply be a risk factor for the presence of atherosclerosis, rather than pathological in atherosclerosis complications[19]. Therefore, the effect of ox-LDL on vascular calcification is controversial[20]. In our study, ox-LDL and/or β-GP increased calcium deposition and ALP activity. The results were consistent with other reports[21]. Genes promoting calcification (cbfa-1, OCN) increased and genes inhibiting calcification (OPG) decreased, indicating the ossific process induced by ox-LDL was dual-regulatory. However, the effect on changes in bone gene expression was not strong. One potential explanation is that the culture conditions might require a more complicated microenvironment such as the addition of calcium ions. It was reported that $CD34^+$ cells, pretreated with 5 mmol/L Ca^{2+}, had more changes in bone gene expression than those without Ca^{2+}[4]. In addition, ox-LDL had no apparent effect on increasing the number of OCN^+ cells. There were several possible reasons as for these findings. The complicated process from gene transcription to protein expression may require more regulatory elements. Furthermore, the OCN protein was present in low abundance in BMPECs, meaning that identification of the different concentrations of OCN in the treated groups was challenging.

Vascular calcification and oxidative stress occur in parallel. Low concentrations of H_2O_2 increase ALP activity and potentiate the progression of aortic valve calcification[22, 23]. The levels of expression of mRNAs for OPN and OCN were significantly greater in ROS-treated human dental pulp cells[24]. Thus, rather than simply causing oxidative damage, ROS played a more complex role in cell physiology. HIF-1α is a transcription factor that regulates stem cell differentiation during hypoxia[25]. Overexpression of HIF-1α in mature osteoblasts profoundly increases angiogenesis and osteogenesis[26]. Both of these processes are activated concomitantly to promote intra-plaque angiogenesis and foam cell development[27]. Our results displayed higher levels of early-phase ROS generation followed by a significant increase in the expression of HIF-1α. Thus, it could be speculated that ox-LDL induces ossification of BMEPCs through ROS mediation of an increase in HIF-1α nucleotide level.

The effect of ox-LDL on cell differentiation has been fully explained to different degrees[11, 28]. Our study presents, for the first time, the effects of ox-LDL on transdifferentiation of BMEPCs. BMEPCs might be considered a new member involved in vascular calcification; however, because ox-LDL-induced vascular calcification is a complex process, the cell system *in vitro* is perhaps too simple to represent the actual microenvironment *in vivo*. Oxidative stress alone cannot explain the mechanism clearly, which means that there must be other signaling pathways that participate in the process.

In conclusion, we have shown that BMEPCs can be induced to ossific differentiation. Ox-LDL acts synergistically with β-GP and contributes to calcification to some extent, with an oxidative stress mechanism underlying the phenomenon. Our results offer another target for vascular calcification therapy.

Acknowledgements

This work was supported by the National Basic Research Program of China (973 Program, No 2007CB512503).

Author contribution

Li LIU and Xi-xiong KANG designed the research; Li LIU, Hui CHEN, and Yu-hua KONG performed the research; Li LIU and Zhi-zhong LIU analyzed the data; and Li LIU and Guo-jun ZHANG wrote the manuscript.

References

1 Tyson KL, Reynolds JL, McNair R, Zhang Q, Weissberg PL, Shanahan CM. Osteo/chondrocytic transcription factors and their target genes exhibit distinct patterns of expression in human arterial calcification. Arterioscler Thromb Vasc Biol 2003; 23: 489–94.

2 Tousoulis D, Andreou I, Antoniades C, Tentolouris C, Stefanadis C. Role of inflammation and oxidative stress in endothelial progenitor cells function and mobilization: Therapeutic implications for cardiovascular diseases. Atherosclerosis 2008; 201: 236–47.

3 Iyemere VP, Proudfoot D, Weissberg PL, Shanahan CM. Vascular smooth muscle cell phenotypic plasticity and the regulation of vascular calcification. J Intern Med 2006; 260: 192–210.

4 Gossi M, Modder UI, Atkinson EJ, Lerman A, Khosla S. Osteocalcin expression by circulating endothelial progenitor cells in patients with coronary atherosclerosis. J Am Coll Cardiol 2008; 52: 1314–25.

5 Moeddera UI, Gosslb M, Lerma LO, Khosla S, Lerman A. Circulating endothelial progenitor cells co-expressing an osteogenic phenotype are increased in patients with severe calcific aortic valve stenosis.

Bone 2009; 44: S321.
6 Sata M, Fukuda D, Tanaka K, Kaneda Y, Yashiro H, Shirakawa I. The role of circulating precursors in vascular repair and lesion formation. J Cell Mol Med 2005; 9: 557–68.
7 Côté C, Pibarot P, Després JP, Mohty D, Cartier A, Arsenault BJ, *et al*. Association between circulating oxidized low-density lipoprotein and fibrocalcific remodelling of the aortic valve in aortic stenosis. Heart 2008; 94: 1175–80.
8 Wu Y, Wang Q, Cheng L, Wang J, Lu G. Effect of oxidized low-density lipoprotein on survival and function of endothelial progenitor cell mediated by p38 signal pathway. J Cardiovasc Pharmacol 2009; 53: 151–6.
9 Imanishi T, Hano T, Sawamura T, Nishio I. Oxidized low-density lipoprotein induces endothelial progenitor cell senescence, leading to cellular dysfunction. Clin Exp Pharmacol Physiol 2004; 31: 407–13.
10 Imanishi T, Hano T, Matsuo Y, Nishio I. Oxidized low-density lipoprotein inhibits vascular endothelial growth factor-induced endothelial progenitor cell differentiation. Clin Exp Pharmacol Physiol 2003; 30: 665–70.
11 Taylor J, Butcher M, Zeadin M, Politano A, Shaughnessy SG. Oxidized low–density lipoprotein promotes osteoblast differentiation in primary cultures of vascular smooth muscle cells by up-regulating Osterix expression in an Msx2-dependent manner. J Cell Biochem 2011; 112: 581–8.
12 Sun CK, Lee FY, Sheu JJ, Yuen CM, Chua S, Chung SY, *et al*. Early combined treatment with cilostazol and bone marrow-derived endothelial progenitor cells markedly attenuates pulmonary arterial hypertension in rats. J Pharmacol Exp Ther 2009; 330: 718–26.
13 Van Campenhout A, Moran CS, Parr A, Clancy P, Rush C, Jakubowski H, *et al*. Role of homocysteine in aortic calcification and osteogenic cell differentiation. Atherosclerosis 2009; 202: 557–66.
14 Kuwana M, Okazaki Y, Kodama H, Izumi K, Yasuoka H, Ogawa Y, *et al*. Human circulating $CD14^+$ monocytes as a source of progenitors that exhibit mesenchymal cell differentiation. J Leukoc Biol 2003; 74: 833–45.
15 Zvaifler NJ, Marinova-Mutafchieva L, Adams G, Edwards CJ, Moss J, Burger JA, *et al*. Mesenchymal precursor cells in the blood of normal individuals. Arthritis Res 2000; 2: 477–88.
16 Mody N, Parhami F, Sarafian TA, Demer LL. Oxidative stress modulates osteoblastic differentiation of vascular and bone cell. Free Radic Biol Med 2001; 31: 509–19.
17 Ehara S, Naruko T, Shirai N, Itoh A, Hai E, Sugama Y, *et al*. Small coronary calcium deposits and elevated plasma levels of oxidized low density lipoprotein are characteristic of acute myocardial infarction. J Atheroscler Thromb 2008; 15: 75–81.
18 Cola C, Almeida M, Li D, Romeo F, Mehta JL. Regulatory role of endothelium in the expression of genes affecting arterial calcification. Biochem Biophys Res Commun 2004; 320: 424–7.
19 Mazière C, Savitsky V, Galmiche A, Gomila C, Massy Z, Mazière JC. Oxidized low density lipoprotein inhibits phosphate signaling and phosphate-induced mineralization in osteoblasts. Involvement of oxidative stress. Biochim Biophys Acta 2010; 1802: 1013–9.
20 Johnson RC, Leopold JA, Loscalzo J. Vascular calcification: pathobiological mechanisms and clinical implications. Circ Res 2006; 99: 1044–59.
21 Bear M, Butcher M, Shaughnessy SG. Oxidized low-density lipoprotein acts synergistically with beta-glycerophosphate to induce osteoblast differentiation in primary cultures of vascular smooth muscle cells. J Cell Biochem 2008; 105: 185–93.
22 Liberman M, Bassi E, Martinatti MK, Lario FC, Wosniak J Jr, Pomerantzeff PM, *et al*. Oxidant generation predominates around calcifying foci and enhances progression of aortic valve calcification. Arterioscler Thromb Vasc Biol 2008; 28: 463–70.
23 Lee DH, Lim BS, Lee YK, Yang HC. Effects of hydrogen peroxide (H_2O_2) on alkaline phosphatase activity and matrix mineralization of odontoblast and osteoblast cell lines. Cell Biol Toxicol 2006; 22: 39–46.
24 Matsui S, Takahashi C, Tsujimoto Y, Matsushima K. Stimulatory effects of low-concentration reactive oxygen species on calcification ability of human dental pulp cells. J Endod 2009; 35: 67–72.
25 Francis KR, Wei L. Human embryonic stem cell neural differentiation and enhanced cell survival promoted by hypoxic preconditioning. Cell Death Dis 2010; 1: e22.
26 Wan C, Shao J, Gilbert SR, Riddle RC, Long F, Johnson RS, *et al*. Role of HIF-1alpha in skeletal development. Ann N Y Acad Sci 2010; 1192: 322–6.
27 Shatrov VA, Sumbayev VV, Zhou J, Brune B. Oxidized low-density lipoprotein (oxLDL) triggers hypoxia-inducible factor-1α (HIF-1α) accumulation via redox-dependent mechanisms. Blood 2003; 101: 4847–9.
28 Lu T, Parthasarathy S, Hao H, Luo M, Ahmed S, Zhu J, *et al*. Reactive oxygen species mediate oxidized low-density lipoprotein-induced inhibition of oct-4 expression and endothelial differentiation of bone marrow stem cells. Antioxid Redox Signal 2010; 13: 1845–56.

Acta Pharmacologica Sinica (2011) 32: 1498–1504
 1671-4083/11 $32.00
www.nature.com/aps

Original Article

High cholesterol diet increases osteoporosis risk via inhibiting bone formation in rats

Li YOU[1, *], Zheng-yan SHENG[1], Chuan-ling TANG[2], Lin CHEN[1], Ling PAN[1], Jin-yu CHEN[1]

[1]Department of Osteoporosis, Shanghai First People's Hospital, Shanghai Jiaotong University, Shanghai 200080, China; [2]Laboratory for Reproductive Immunology, Hospital and Institute of Obstetrics and Gynecology, Fudan University Shanghai Medical College, Shanghai 200011, China

Aim: To investigate the effects of high cholesterol diet on the development of osteoporosis and the underlying mechanisms in rats.
Methods: Female Sprague-Dawley rats were randomly separated into 3 groups: (1) the high cholesterol fed rats were fed a high cholesterol diet containing 77% normal diet food, 3% cholesterol and 20% lard for 3 months; (2) ovariectomised (OVX) rats were bilaterally ovariectomised and fed a standard diet; and (3) the control rats were fed the standard diet. Bone mineral density (BMD) of the rats was measured using dual-energy X-ray absorptiometry. Serum levels of oestradiol (E2), osteocalcin (BGP) and carboxy-terminal collagen crosslinks (CTX) were measured using ELISA. Gene expression profile was determined with microarray. Mouse osteoblast cells (MC3T3-E1) were used for *in vitro* study. Proliferation, differentiation and oxidative stress of the osteoblasts were investigated using MTT, qRT-PCR and biochemical methods.
Results: In high cholesterol fed rats, the femur BMD and serum BGP level were significantly reduced, while the CTX level was significantly increased. DNA microarray analysis showed that 2290 genes were down-regulated and 992 genes were up-regulated in this group of rats. Of these genes, 1626 were also down-regulated and 1466 were up-regulated in OVX rats. In total, 370 genes were up-regulated in both groups, and 976 genes were down-regulated. Some of the down-regulated genes were found to code for proteins involved in the transforming growth factor beta (TGF-β)/bone morphogenic protein (BMP) and Wnt signaling pathways. The up-regulated genes were found to code for IL-6 and Ager with bone-resorption functions. Treatment of MC3T3-E1 cells with cholesterol (12.5–50 μg/mL) inhibited the cell proliferation and differentiation *in vitro* in a concentration-dependent manner. The treatment also concentration-dependently reduced the expression of *BMP2* and *Cbfa1*, and increased the oxidative injury in MC3T3-E1 cells.
Conclusion: The results suggest a close correlation between hypercholesterolaemia and osteoporosis. High cholesterol diet increases the risk of osteoporosis, possible via inhibiting the differentiation and proliferation of osteoblasts.

Keywords: high cholesterol diet; hypercholesterolaemia; osteoporosis; osteoblasts; oxidative stress; bone morphogenic protein

Acta Pharmacologica Sinica (2011) 32: 1498–1504; doi: 10.1038/aps.2011.135; published online 31 Oct 2011

Introduction

Osteoporosis is one of the most common bone diseases, affecting millions of people worldwide. Postmenopausal osteoporosis is a major health problem in women. Osteoporosis is associated with an increased risk of low-trauma fractures to the vertebral spine, femoral neck and distal radius that result in substantial morbidity. Even if the age-adjusted incidence of hip fracture remained stable, the estimated number of hip fractures globally will probably increase from 1.7 million in 1990 to an estimated 6.3 million in 2050[1].

Previous human clinical studies have found that hypercholesterolaemia is associated with a lower bone mineral density (BMD). It was reported that postmenopausal women with hypercholesterolaemia have a significantly higher serum bone-specific alkaline phosphatase (BAP) level compared with postmenopausal women with a normal lipid profile[2]. In addition, both BAP and the N-terminal telopeptide of type I collagen (NTx) are significantly and positively correlated with both serum total cholesterol (TC) and low-density lipoprotein cholesterol (LDL-C) in women. Postmenopausal women who have never taken hormone replacement therapy (HRT) show significantly higher cholesterol levels and have lower BMD measurements in the lumbar spine than premenopausal women[3]. In a South Korean population-based study of 375 premenopausal and 355 postmenopausal rural women it was shown that levels of serum TC and LDL-C were inversely cor-

* To whom correspondence should be addressed.
E-mail youlisky2002@126.com
Received 2011-04-17 Accepted 2011-08-23

related with BMD[4]. Furthermore, plasma LDL-C and high-density lipoprotein cholesterol (HDL-C) levels have been shown to be inversely and positively correlated with BMD in both men and women, respectively[5, 6]. However, in some studies, serum triglyceride and HDL cholesterol were found to be correlated with BMD, but no relationship was seen between either total cholesterol or LDL and BMD[7, 8]. D'Amelio *et al* showed that HDL was significantly higher in osteoporotic patients than in controls and the risk of osteoporosis was significantly higher in women with high HDL[9]. The study provided evidence of the relationship between HDL, but not total cholesterol or LDL, and BMD in this cohort of normal-weight women.

Lipid-lowering drugs (statins) increase the BMD of the hip or femoral neck[10–13]. However, some anti-osteoporotic drugs such as selective estrogen receptor modulators (SERMS, *eg* raloxifene) only moderately reduce serum levels of TC and LDL-C[14–16]. All of this evidence points to a clinical correlation between hyperlipidaemia and postmenopausal osteoporosis.

In this study, we investigated the effect of a high cholesterol diet on bone metabolism in rats. We also studied the effect of free cholesterol on the proliferation and differentiation of osteoblasts. We found that hypercholesterolemia in the rat was associated with a reduction of bone density, an increase in bone resorption and a reduction in bone formation. DNA microarray analysis showed that the bone morphogenic protein (BMP)/ transforming growth factor beta (TGF-β) and Wnt pathways, involved in bone formation, were altered by a high cholesterol diet in rats. Furthermore, *in vitro* studies showed that free cholesterol reduced the proliferation and differentiation of osteoblasts, and inhibited the expression of *BMP2* and core binding factor alpha 1 (*Cbfa1*). Free cholesterol also increased the level of malondialdehyde (MDA) and decreased the activity of superoxidase dismutase (SOD) in osteoblasts.

Materials and methods

Animals and experimental treatment

Three-month-old female Sprague-Dawley rats (180–200 g, n=34) were obtained from the Shanghai Laboratory Animal Center. After a 1-week acclimatization, the rats were randomly separated into three groups. The high cholesterol fed rats were fed a high cholesterol diet containing 77% normal diet food, 3% cholesterol and 20% lard (n=12). Ovariectomised (OVX) rats were bilaterally ovariectomised and fed a standard diet. Aseptic surgery was performed via a 1–1.5-cm axillary midline incision and the ovaries were removed. Then the skin was stapled and washed with alcohol (n=12). The control group of rats (n=10) were fed a standard diet. All rats were kept at room temperature (21±2 °C) under a normal 12-h light: 12-h dark regime with good ventilation and convenient access to food and water. The experimental protocol was developed according to the institution's guideline for the care and use of laboratory animals.

Serum cholesterol and BMD measurement

After 3 months of treatment, the rats were sacrificed and blood was collected. The cholesterol concentration was measured by automated biochemistry equipment. Femurs and 1–4 lumbar vertebrae (LV) were also excised. The whole left femur and lumbar vertebrae (1–4) were used for further analysis. The bone mineral content and area was measured, and BMD was automatically calculated via dual-energy X-ray absorptiometry (HOLOGIC, MA, USA).

Serum E2, BGP, CTX, ALP measurement

The sera were collected for the ALP testing according to the manufacturer's instructions (Nanjing Jiancheng Bioengineering Institute, Nanjing, China). In brief, 50 μL serums was mixed with solution I and II and then incubated for 15 min at 37 °C. The chromogenic agent was added and the absorbance at 570 nm was measured. Rat sera were collected and the concentration of estradiol (E2, R&D, MN, USA), osteocalcin (BGP, Immunodiagnostic Systems Limited, Boldon, UK) and carboxy-terminal collagen crosslinks (CTX, Immunodiagnostic Systems Limited, Boldon, UK) were measured according to the description of manufacturers by ELISA. Serum (20 μL) was incubated with the first antibody specifically for each protein at room temperature for 1 h. Then the plate were washed with wash buffer and incubated with biotin-labeled antibody to each first antibody for 1 h at room temperature and washed again. Finally the chromogenic agent was added and incubated for 15 min and the reaction was stopped with H_2SO_4. Absorbance was read at 450 nm (reference wavelength 630 nm).

RNA extraction and microarray analysis

An Affymetrix rat genome 230 2.0 array was used, consisting of more than 31 000 probe sets, representing more than 30 000 transcripts and variants from over 28 000 well-substantiated rat genes. For gene expression analysis by microarray, a procedure from Affymetrix was followed. Total RNA from the proximal femurs was extracted using TRIzol (Invitrogen, CA, USA) and an RNeasy Mini Kit (Qiagen, Hilden, Germany) according to the manufacturer's protocols. All these experiments were performed by Shanghai Biochip Co Ltd (Shanghai, China).

Cell culture and drug administration

The mouse osteoblast cells (MC3T3-E1) were cultured in α-MEM medium (GIBCO BRL, CA, USA) supplemented with penicillin 100 IU/mL, streptomycin 100 IU/mL and 10% fetal bovine serum (GIBCO BRL, CA, USA). Cholesterol (Sigma, MO, USA) was dissolved in ethanol, and different concentrations were used for the experiment.

MTT assay

For the MTT (Sigma, MO, USA) assay, MC3T3-E1 cells at a density of 5×10^3 cells/well were inoculated in 96-well plates in the presence or absence of cholesterol. The concentrations of cholesterol were 0, 12.5, 25, and 50 μg/mL. After 72 h, 20 μL of 5 mg/mL MTT was added to each well and incubated for 5 h. The medium was removed and 150 μL DMSO was added

to each well and incubated for 10 min. The absorbance of the culture plate was read at 570 nm. The inhibition ratio was calculated using the following formula: proliferation ratio=Mean Absorbance of Sample/Mean Absorbance of Control×100%.

ALP, SOD, and MDA measurement

The cell lysate were collected for the ALP, SOD, and MDA measurement according to the manufacturer's instructions (Nanjing Jiancheng Bioengineering Institute, Nanjing, China). The ALP measurement in cell lysate is the same with the serum ALP testing. In brief, for testing SOD, the cell lysate were incubated with solution I, II, III, and IV for 40 min at 37 °C. The chromogenic agent was added and the absorbance was read at 550 nm for SOD activity. For detecting MDA, the cell lysate were incubated with solution I, II and III for 40 min at 95 °C. The absorbance was read at 532 nm for MDA concentration.

Quantitative real-time PCR (qRT-PCR)

For the qRT-PCR assay, MC3T3-E1 cells at a density of 1×10^6 cells/well were inoculated in 6-well plates in the presence or absence of 12.5 μg/mL cholesterol. After 24 h, the cells were collected, and total RNA was extracted using TRIzol reagent (Invitrogen, CA, USA) according to manufacturer's instructions. The qRT-PCR was performed using One Step SYBR PrimeScript™ RT-PCR Kit II (Takara, Tokyo, Japan) following the manufacturer's instructions. Primers for the qRT-PCR assay were as follows: *Col1A1*, forward 5′-TAC AGC ACG CTT GTG GAT G-3′, reverse 5′-TTG GGA TGG AGG GAG TTT A-3′; *ALP*, forward 5′ GAC GGT GAA CGG GAG AAC-3′, reverse 5′-CTC AGA ACA GGG TGC GTA G-3′; *BMP2*, forward 5′-GGA CTG CGG TCT CCT AA AG-3′ reverse 5′-CAG CCT CAA CTC AAA CTC G-3′; *Cbfa1*, forward 5′-AGA CAC AGA GCC TGT GGG-3′ reverse 5′-CTC TGG CTT GGA TTA GGG A-3′; *β-actin*, forward 5′-GAA ATC GTG CGT GAC ATT A-3′, reverse 5′-GGA GCC AGG GCA GTA ATC-3′. For quantification of gene expression changes, the relative quantification method was used.

Statistical analyses

Data were presented as the mean±standard deviation (SD). ANOVA and *post-hoc* analysis were used for comparison. All statistical analyses were performed using SPSS11.0.

Results

BMD was decreased in high cholesterol fed rats and OVX rats

After treatment with a high cholesterol diet containing 77% normal diet food, 3% cholesterol and 20% lard for 3 months, the level of cholesterol was increased, accompanied with an increase in body weight. The level of cholesterol was also increased in OVX rats fed with normal diets. There was no difference in the serum level of triglycerides, calcium and phosphorus between the three groups (Table 1).

BMD in the femurs was significantly decreased in high cholesterol fed rats and OVX rats compared with controls (both $P<0.01$). ALP and BGP levels were reduced and the CTX level was increased in high cholesterol fed rats (both $P<0.05$). The intra- and inter-assay coefficient of variations (CV) of BGP were 4.7% and 5.6%, respectively; the CV of CTX were 4.1% and 5.3%, respectively. Estrogen concentration was reduced in OVX rats. High cholesterol diet had no effect on the estrogen concentration (Table 1), and the CV of E2 were 3.4% and 8.9%, respectively. It suggests that the high cholesterol diet reduces the BMD and bone formation and increases bone resorption in rats.

Table 1. Effect of high cholesterol diet and OVX on weight, total cholesterol (TC), triglycerides (TG), calcium (Ca), phosphorus (P), ALP, osteocalcin (BGP), carboxy-terminal collagen crosslinks (CTX), estrogen (E2), and bone mineral density (BMD) level. Data are presented as the mean±SD. [b]$P<0.05$ *vs* Normal group.

	Normal (*n*=10)	High cholesterol fed rats (*n*=12)	OVX rats (*n*=12)
Weight (g)	311.00±21.95	439.17±65.76[b]	320.83±28.87
TC (mmol/L)	1.87±0.39	3.17±1.06[b]	2.04±0.7
TG (mmol/L)	0.76±0.17	0.58±0.18	0.71±0.26
Ca (mmol/L)	2.40±0.15	2.47±0.19	2.38±0.26
P (mmol/L)	4.16±2.13	4.47±1.68	4.64±1.98
ALP (U/100 mL)	16.15±0.68	12.34±0.46[b]	20.41±0.71[b]
BGP (ng/mL)	500.79±120.51	331.40±124.78[b]	754.87±222.34[b]
CTX (ng/mL)	62.49±31.31	85.55±30.82[b]	95.77±36.96[b]
E2 (ng/L)	4.44±0.33	4.54±0.39	4.05±0.31[b]
Femur BMD	0.15±0.012	0.12±0.014[b]	0.12±0.02[b]
Lumbar vertebrae BMD	0.13±0.03	0.14±0.008	0.13±0.011

Gene expression profiles

In high cholesterol fed rats, 2290 genes were down-regulated and 992 genes were up-regulated. In OVX rats, 1626 genes were down-regulated and 1466 genes were up-regulated. A comparative cluster analysis was carried out with the sets of differentially expressed genes to evaluate the correlation between the two groups of rats. In total, 370 genes were up-regulated in both groups, and 976 genes were down-regulated (Figure 1A). Genes with the most remarkable change in both groups include those coding for proteins involved in apoptosis, binding activity, metabolism, and the cell cycle. The change patterns for these genes were consistent in the two groups (Figure 1B).

GO and pathway analysis for gene expression

Some of the downregulated genes, *Wnt5*, *β-catenin*, *Tgfbr*, *smad4*, *smad6*, *smad7*, *Bmpr2*, and *BMP6*, are involved in the TGF-β/BMP2 and Wnt signalling pathway (Table 2). In addition, the up-regulated genes were found to code for *IL-6* and *Ager* with bone-resorption functions.

The proliferation of osteoblasts *in vitro*

Free cholesterol at 12.5–50 μg/mL inhibited the proliferation

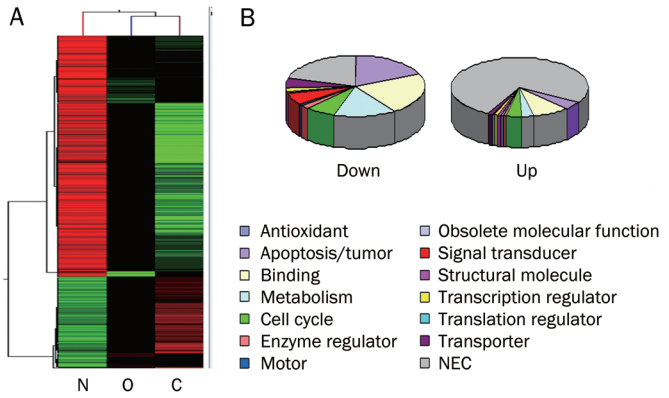

Figure 1. Gene expression profiles. Comparative analysis was performed to show the differentially expressed genes in high cholesterol fed and OVX rats. Cluster analysis of differentially expressed genes in high cholesterol fed rats and OVX rats. (B) The functional distribution of the differentially expressed genes in high cholesterol fed rats and OVX rats. N: normal rats; O: OVX rats with osteoporosis; C: high cholesterol fed rats.

and viability of MC3T3-E1 cells compared with control group (P<0.05, Figure 2A, 2B).

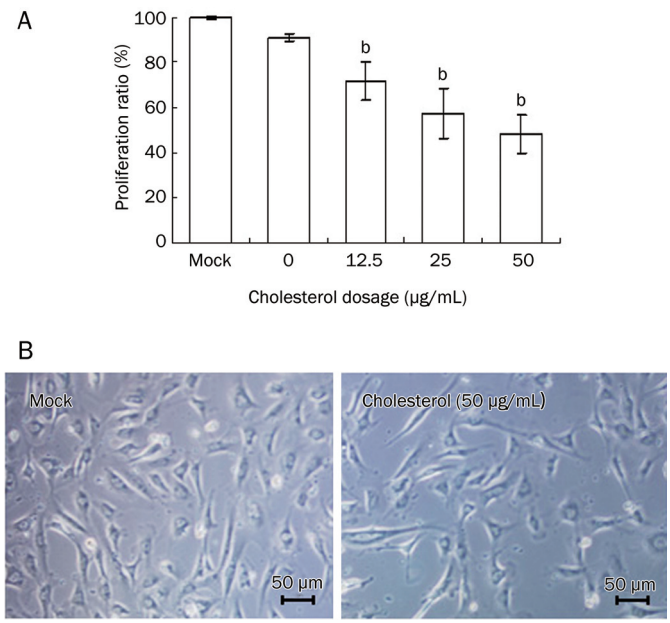

Figure 2. MC3T3-E1 proliferation with the treatment of cholesterol. MC3T3-E1 cells were cultured in medium with 0, 12.5, 25, and 50 μg/mL of cholesterol for 72 h, cell proliferation was tested by MTT assay (A) and cell viability was observed by microscopy (B). Administration schedules are described in Materials and Methods. Data are shown as the mean±SD of eight wells for each group within one experiment, and it was repeated three times. ^{b}P<0.05 *vs* Mock.

The expression of *ALP*, *collagen I*, *BMP2*, and *Cbfa1* genes in MC3T3-E1 cells

Cholesterol 25–50 μg/mL reduced the mRNA expression of *ALP* and *collagen I, BMP2, and Cbfa1* compared with the control group (P<0.05, Figure 3).

Table 2. The expression of bone formation-related genes in the two groups.

Gene name	Gene symbol	High cholesterol fed rats	OVX rats
Insulin-like growth factor binding protein 5	Igfbp5	-7.1	-3.1
Procollagen, Type XII, Alpha 1	Col12a1	-6.3	-4.3
Matrix metallopeptidase 8	Mmp8	-4.8	-2.5
Core binding factor beta	Cbfb	-4.6	-2.4
Caveolin	Cav	-4.6	-3.7
Transforming growth factor, beta receptor II	Tgfbr2	-4.0	-4.2
Leptin receptor	Lepr	-4.0	-2.1
Wingless-type MMTV integration site 5A	Wnt5a	-3.8	-1.0
Bone morphogenetic protein 6	Bmp6	-3.8	-1.4
MAD homolog 6 (Drosophila)	Smad6	-3.8	-1.2
Osteoglycin	Ogn	-3.7	-1.9
Bone morphogenic protein receptor, type II	Bmpr2	-3.7	-2.9
MAD homolog 7	Smad7	-3.7	-2.2
Transforming growth factor, beta receptor III	Tgfbr3	-3.7	-3.2
Insulin-like growth factor binding protein 7	Igfbp7	-3.1	-1.0
Catenin (Cadherin Associated Protein), beta 1	Ctnnb1	-3.1	-1.4
CD276 antigen	Cd276	-3.1	-3.1
Parathyroid hormone receptor 2	Pthr2	-2.9	-1.4
Fibroblast growth factor receptor 2	Fgfr2	-2.9	-1.2
Fibroblast growth factor 9	Fgf9	-2.9	-0.8
Calcitonin receptor	Calcr	-2.8	-2.6
MAD homolog 4 (Drosophila)	Smad4	-2.7	-1.1
Fibroblast growth factor 5	Fgf5	-2.5	-3.7
Procollagen, Type III, Alpha 1	Col3a1	-2.5	-0.8
MAD homolog 9 (Drosophila)	Smad9	-2.3	-0.1
Matrix metallopeptidase 7	Mmp7	-2.3	-3.0
3-Hydroxy-3-methylglutaryl-coenzyme A reductase	Hmgcr	-2.3	-1.0
MAD homolog 5 (Drosophila)	Smad5	-2.2	-2.0
Interleukin 6 signal transducer	Il6st	-2.2	-1.7
Fibroblast growth factor 8	Fgf8	-2.1	-0.7
Apolipoprotein E	Apoe	-2.0	-1.4
Procollagen, Type I, Alpha 2	Col1a2	-1.8	-0.4
Cbp/P300-interacting transactivator with Glu/Asp-rich carboxy-terminal domain 1	Cited1	2.1	0.9
Interleukin 6	IL6	2.2	3.0
Interferon beta 1	Ifnb1	3.1	1.3
Advanced glycosylation end product-specific receptor	Ager	4.6	4.2

The level of ALP, SOD, and MDA in MC3T3-E1 cells

Cholesterol 50 μg/mL reduced the activity of ALP. Cholesterol treatment also reduced the activity of SOD and increased the level of MDA *in vitro* (Figure 4).

Discussion

In our clinical studies, we observed that postmenopausal women with hypercholesterolaemia showed increased bone

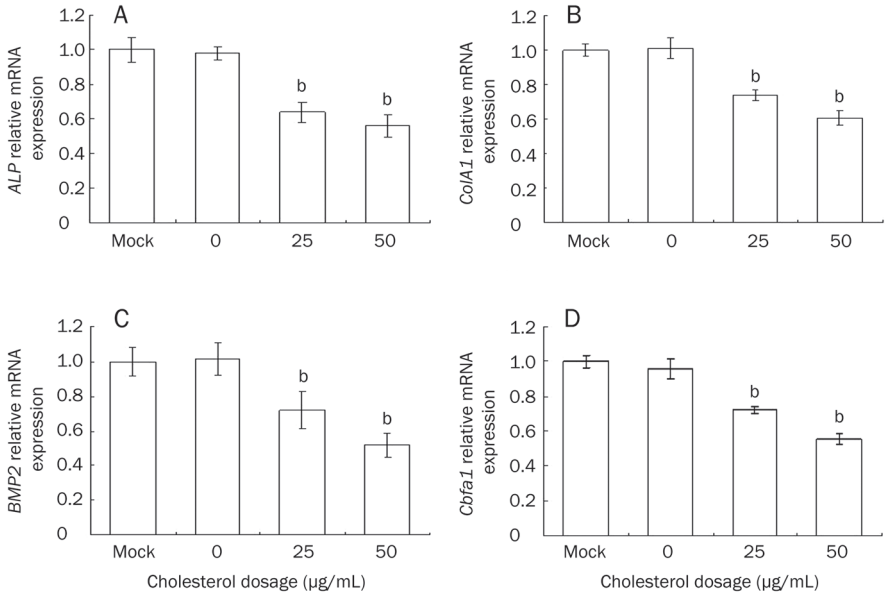

Figure 3. The expression of *ALP*, *ColA1*, *BMP2*, and *Cbfa1* genes in MC3T3-E1 cells after the treatment of cholesterol. (A) ALP, (B) Collagen I, (C) BMP2 and (D) Cbfa1 were analyzed by real-time PCR. Data are shown as the mean±SD of three wells for each group within one experiment, and it was repeated for three times. $^{b}P<0.05$ *vs* Mock.

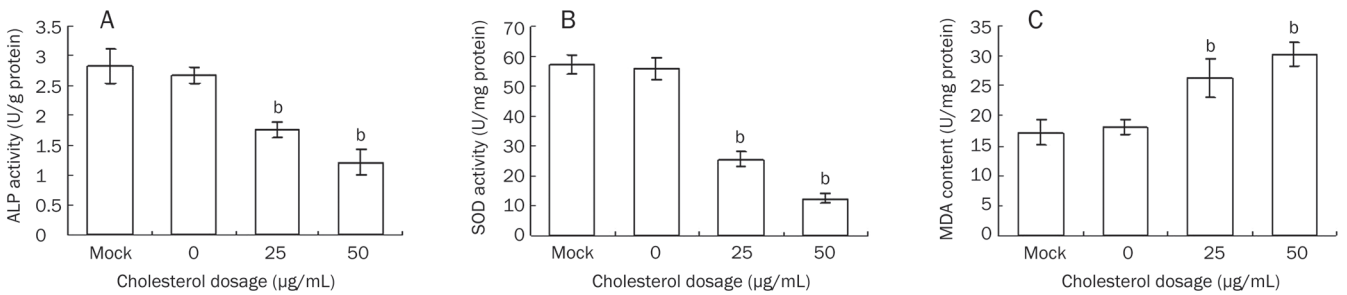

Figure 4. The ALP, SOD activity and the level of MDA in MC3T3-E1 cells treated with cholesterol. Cells were collected after the treatment of 4 d and lysed with 0.1% triton X-100, and the lysate were used for ALP (A), SOD (B) and MDA (C) analysis. Data are shown as the mean±SD of eight wells for each group within one experiment, and it was repeated for three times. $^{b}P<0.05$ *vs* Mock.

turnover and lower BMD, which is consistent with the data reported in other clinical studies[2–4]. We thus hypothesise that a high cholesterol diet induces or promotes the development of osteoporosis. To confirm this hypothesis, we investigate the effects of high cholesterol diet on the development of osteoporosis and the underlying mechanisms. High cholesterol diet significantly increased the weight and the total cholesterol level in serum. BMD decreased in most rats fed with high cholesterol diet. The serum levels of ALP and BGP were decreased and CTX level was increased, indicating that high cholesterol diet increased bone loss. It not only promoted bone resorption, but also reduced bone formation. Interestingly, most OVX rats had developed hypercholesterolaemia, which was similar with the Gurer's study[17]. These data are consistent with our previous findings in clinic that a high cholesterol diet will increase the risk of osteoporosis.

Estrogen deficiency is critical to the pathogenesis of osteoporosis in postmenopausal women, as levels naturally decline, and this results in the imbalance between osteoclast-mediated bone resorption and bone formation[18, 19]. In our experiments, the estrogen level was reduced in the OVX rats, but not in high cholesterol diet fed rats. This suggests that the osteoporosis induced by the cholesterol diet was not the result of estrogen deficiency. High cholesterol fed rats had higher body weights, which is consistent with the view that obesity is related wtih osteoporosis. Kim[20] showed that high percentage body fat and waist circumference correlated with low BMD and risk of a vertebral fracture. Obesity-reduced bone density was associated with activation of PPARgamma and suppression of Wnt/beta-catenin in rapidly growing male rats[21].

Previous studies have shown that increased arterial calcification and blood lipid correlate with an increase in osteoporosis. Lipids have been shown to accumulate in bones of rats and blood vessels around bone in patients with osteoporosis[22, 23]. Osteoporosis has been associated with both atherosclerosis and vascular calcification[24–26]. Serum lipid levels may alter bone mineralization. In Xiao' study, a high fat diet induced the increased expression of genes involved in bone resorption and decreased expression of genes associated with bone formation[27]. In this study, in the high cholesterol fed rats

there was also a decrease in the expression of genes involved in bone formation and an increase in the expression of genes associated with bone resorption. Genes involved in TGF-β/BMP and Wnt pathways promote the differentiation of mesenchymal stem cells into osteoblasts and facilitate the proliferation and maturation of osteoblasts. They also regulate the differentiation of osteoblasts, the secretion of bone matrix and mineralization of the bone matrix[28–30]. Some genes involved in these pathways were also down-regulated in high cholesterol fed rats, which will lead to a suppression of differentiation, proliferation and maturation of osteoblasts, as well as decreased bone formation. The expression of these genes was lower in high cholesterol diet fed rats than those in OVX rats.

Our *in vitro* studies also support a role for high blood lipids in the proliferation and differentiation of osteoblasts. Statins exerted a direct stimulatory effect on osteoblast cells[31, 32] and simvastatin promoted osteoblast differentiation[33]. Parhami *et al*[34] found that minimally oxidized low-density lipoprotein (MM-LDL) inhibited the differentiation of MC3T3-E1 cells. These studies suggest that higher levels of lipids inhibit the differentiation of osteoblasts but treatment with hypolipidemic drugs will recover the differentiation of osteoblasts. Free cholesterol inhibited the proliferation and differentiation of osteoblasts *in vitro*. The proliferation of MC3T3-E1 cells and the level of *ALP* and *collagen I* in osteoblasts were reduced by cholesterol. In addition, cholesterol reduced the expression of *BMP2* and *Cbfa1*. Free cholesterol may inhibits the bone formation via the BMP2 pathway.

Oxidative status influences the pathophysiology of mineralised tissues[35]. The role of oxidative injury is one of the mechanisms for the high lipid-induced osteoporosis. In bone-derived preosteoblasts, oxidized low-density lipoprotein (oxLDL) and other bioactive oxidized lipids inhibit the expression of various markers of osteoblast differentiation[34]. Also OxLDL and oxidative products inhibit osteogenic differentiation of mesenchymal stem cells and preosteoblast in favour of an adipogenic differentiation[36, 37]. We found that free cholesterol inhibited bone formation, reduced the activity of SOD and increased the level of MDA, which indicated that the free cholesterol increased the oxidative injury in osteoblasts *in vitro*.

In conclusion, a close correlation between hypercholesterolaemia and osteoporosis was observed in our study. High cholesterol diet increased the bone resorption and reduced bone formation in rats, accompanied by a reduction in BMD. The results confirmed our hypothesis that a high cholesterol diet increases the risk of osteoporosis. Our *in vitro* experiments showed that free cholesterol inhibited the proliferation and differentiation of osteoblasts, and it reduced bone formation by decreasing *BMP2* expression and increasing oxidative injury. High cholesterol diet increases the risk of osteoporosis, possibly via inhibiting the differentiation and proliferation of osteoblasts.

Acknowledgements

We thank Shanghai Biochip Co Ltd for their excellent technical assistance and appreciate the help of Dr Yan XIONG in the editing of the manuscript. This work was supported by Shanghai First People's Hospital, Shanghai Jiaotong University.

Author contribution

Li YOU designed research; Chuan-ling TANG and Ling PAN performed research; Zheng-yan SHENG contributed new analytical tools and reagents; Lin CHEN and Jin-yu CHEN analyzed data; Li YOU wrote the paper.

References

1 Sambrook P, Cooper C. Osteoporosis. Lancet 2006; 367: 2010–8.
2 Majima T, Shimatsu A, Komatsu Y, Satoh N, Fukao A, Ninomiya K, *et al*. Increased bone turnover in patients with hypercholesterolemia. Endocr J 2008; 55: 143–51.
3 Makovey J, Chen JS, Hayward C, Williams FM, PN S. Association between serum cholesterol and bone mineral density. Bone 2009; 44: 208–13.
4 Cui LH, Shin MH, Chung EK, Lee YH, Kweon SS, Park KS, *et al*. Association between bone mineral densities and serum lipid profiles of pre- and post-menopausal rural women in South Korea. Osteoporos Int 2005; 16: 1975–81.
5 Adami S, Braga V, Zamboni M, Gatti D, Rossini M, Bakri J, *et al*. Relationship between lipids and bone mass in 2 cohorts of healthy women and men. Calcif Tissue Int 2004; 74: 136–42.
6 Yamaguchi T, Sugimoto T, Yano S, Yamauchi M, Sowa H, Chen Q, *et al*. Plasma lipids and osteoporosis in postmenopausal women. Endocr J 2002; 49: 211–7.
7 Dennison EM, Syddall HE, Aihie Sayer A, Martin HJ, Cooper C. Lipid profile, obesity and bone mineral density: the Hertfordshire Cohort Study. QJM 2007; 100: 297–303.
8 Jeong IK, Cho SW, Kim SW, Choi HJ, Park KS, Kim SY, *et al*. Lipid profiles and bone mineral density in pre- and postmenopausal women in Korea. Calcif Tissue Int 2010; 87: 507–12.
9 D'Amelio P, Di Bella S, Tamone C, Ravazzoli MG, Cristofaro MA, Di Stefano M, *et al*. HDL cholesterol and bone mineral density in normal-weight postmenopausal women: is there any possible association? Panminerva Med 2008; 50: 89–96.
10 Uzzan B, Cohen R, Nicolas P, Cucherat M, Perret GY. Effects of statins on bone mineral density: a meta-analysis of clinical studies. Bone 2007; 40: 1581–7.
11 Majima T, Komatsu Y, Fukao A, Ninomiya K, Matsumura T, Nakao K. Short-term effects of atorvastatin on bone turnover in male patients with hypercholesterolemia. Endocr J 2007; 54: 145–51.
12 Solomon DH, Finkelstein JS, Wang PS, Avorn J. Statin lipid-lowering drugs and bone mineral density. Pharmacoepidemiol Drug Safety 2005; 14: 219–26.
13 Lupattelli G, Scarponi AM, Vaudo G, Siepi D, Roscini AR, Gemelli F, *et al*. Simvastatin increases bone mineral density in hypercholesterolemic postmenopausal women. Metabolism 2004; 53: 744–8.
14 Nanetti L, Camilletti A, Francucci CM, Vignini A, Raffaelli F, Mazzanti L, *et al*. Role of raloxifene on platelet metabolism and plasma lipids. Eur J Clin Invest 2008; 38: 117–25.
15 Majima T, Komatsu Y, Shimatsu A, Satoh N, Fukao A, Ninomiya K, *et al*. Clinical significance of 1-year treatment with raloxifene on bone and lipid metabolism in Japanese postmenopausal women with osteoporosis. Endocr J 2007; 54: 855–62.
16 Dayspring T, Qu Y, Keech C. Effects of raloxifene on lipid and lipoprotein levels in postmenopausal osteoporotic women with and without

hypertriglyceridemia. Metabolism 2006; 55: 972–9.
17 Gurer G, Sendur OF, Aydeniz A. Serum lipid profile in postmenopausal women with osteoporosis or osteopenia. South Med J 2006; 99: 95–6.
18 Shoback D. Update in osteoporosis and metabolic bone disorders. J Clin Endocrinol Metab 2007; 92: 747–53.
19 Raisz LG. Pathogenesis of osteoporosis: concepts, conflicts, and prospects. J Clin Invest 2005; 115: 3318–25.
20 Kim KC, Shin DH, Lee SY, Im JA, Lee DC. Relation between obesity and bone mineral density and vertebral fractures in Korean postmenopausal women. Yonsei Med J 2010; 51: 857–63.
21 Chen JR, Lazarenko OP, Wu X, Tong Y, Blackburn ML, Shankar K, *et al*. Obesity reduces bone density associated with activation of PPARgamma and suppression of Wnt/beta-catenin in rapidly growing male rats. PLoS One 2010; 5: e13704.
22 Parhami F, Garfinkel A, Demer LL. Role of lipids in osteoporosis. Arterioscler Thromb Vasc Biol 2000; 20: 2346–8.
23 Rajendran KG, Chen SY, Sood A, Spielvogel BF, Hall IH. The anti-osteoporotic activity of amine-carboxyboranes in rodents. Biomed Pharmacother 1995; 49: 131–40.
24 Hmamouchi I, Allali F, Khazzani H, Bennani L, El Mansouri L, Ichchou L, *et al*. Low bone mineral density is related to atherosclerosis in postmenopausal Moroccan women. BMC Public Health 2009; 9: 388.
25 Barengolts EI, Berman M, Kukreja SC, Kouznetsova T, Lin C, Chomka EV. Osteoporosis and coronary atherosclerosis in asymptomatic postmenopausal women. Calcif Tissue Int 1998; 62: 209–13.
26 Ouchi Y, Akishita M, de Souza AC, Nakamura T, Orimo H. Age-related loss of bone mass and aortic/aortic valve calcification — reevaluation of recommended dietary allowance of calcium in the elderly. Ann N Y Acad Sci 1993; 676: 297–307.
27 Xiao Y, Cui J, Li YX, Shi YH, Le GW. Expression of genes associated with bone resorption is increased and bone formation is decreased in mice fed a high-fat diet. Lipids 2010; 45: 345–55.
28 Yavropoulou MP, Yovos JG. The role of the Wnt signaling pathway in osteoblast commitment and differentiation. Hormones (Athens) 2007; 6: 279–94.
29 Janssens K, ten Dijke P, Janssens S, Van Hul W. Transforming growth factor-beta1 to the bone. Endocr Rev 2005; 26: 743–74.
30 Groeneveld EH, Burger EH. Bone morphogenetic proteins in human bone regeneration. Eur J Endocrinol 2000; 142: 9–21.
31 Maeda T, Matsunuma A, Kurahashi I, Yanagawa T, Yoshida H, Horiuchi N. Induction of osteoblast differentiation indices by statins in MC3T3-E1 cells. J Cell Biochem 2004; 92: 458–71.
32 Mundy G, Garrett R, Harris S, Chan J, Chen D, Rossini G, *et al*. Stimulation of bone formation *in vitro* and in rodents by statins. Science 1999; 286: 1946–9.
33 Maeda T, Matsunuma A, Kawane T, Horiuchi N. Simvastatin promotes osteoblast differentiation and mineralization in MC3T3-E1 cells. Biochem Biophys Res Commun 2001; 280: 874–7.
34 Parhami F, Morrow AD, Balucan J, Leitinger N, Watson AD, Tintut Y, *et al*. Lipid oxidation products have opposite effects on calcifying vascular cell and bone cell differentiation. A possible explanation for the paradox of arterial calcification in osteoporotic patients. Arterioscler Thromb Vasc Biol 1997; 17: 680–7.
35 Wauquier F, Leotoing L, Coxam V, Guicheux J, Wittrant Y. Oxidative stress in bone remodelling and disease. Trends Mol Med 2009; 15: 468–77.
36 Mody N, Parhami F, Sarafian TA, Demer LL. Oxidative stress modulates osteoblastic differentiation of vascular and bone cells. Free Radic Biol Med 2001; 31: 509–19.
37 Parhami F, Jackson SM, Tintut Y, Le V, Balucan JP, Territo M, *et al*. Atherogenic diet and minimally oxidized low density lipoprotein inhibit osteogenic and promote adipogenic differentiation of marrow stromal cells. J Bone Miner Res 1999; 14: 2067–78.

Acta Pharmacologica Sinica (2011) 32: 1505–1512
 1671-4083/11 $32.00
www.nature.com/aps

Original Article

Ganoderma lucidum polysaccharides reduce methotrexate-induced small intestinal damage in mice via induction of epithelial cell proliferation and migration

Li-hua CHEN[1, 2], Zhi-bin LIN[1], Wei-dong LI[1, *]

[1]*Department of Pharmacology, School of Basic Medical Sciences, Peking University Health Science Center, Beijing 100083, China;*
[2]*Department of Clinical Laboratory Science, Changsha Medical University, Changsha 410219, China*

Aim: To study the effects of *Ganoderma lucidum* polysaccharides (G*l*-PS) on methotrexate (MTX)-induced small intestinal damage in mice and the underlying mechanisms.
Methods: BALB/c mice were used for *in vivo* study. The mice were administered with G*l*-PS (50, 100, or 200 mg/kg, ig) for 10 d, and injected with MTX (50 mg/kg, ip) on d 7 and 8 to induce intestinal damage, and then sacrificed on d 11 for morphological study and tissue malondialdehyde (MDA) and superoxide dismutase (SOD) measurements. Before sacrificing, blood samples were collected to analyze immunoglobulin A (IgA). Rat intestinal IEC-6 cells were used for *in vitro* study. Cell proliferation and migration were assessed using MTT method and an *in vitro* wounding model, respectively. Transforming growth factor β (TGFβ) protein expression was determined using ELISA assay. Ornithine decarboxylase (ODC) and c-Myc mRNA expression profiles were determined using RT-PCR.
Results: MTX treatment caused severe mucosal damage, significantly increased small intestine MDA levels, and decreased SOD and serum IgA levels in BALB/c mice. G*l*-PS (100 and 200 mg/kg) markedly reversed the MTX effects. In IEC-6 cells, G*l*-PS (0.1, 1, and 10 μg/mL) significantly stimulated the cell proliferation. Furthermore, G*l*-PS (10 μg/mL) significantly stimulated the cell migration. In addition, G*l*-PS (10 and 20 μg/mL) significantly increased the expression of ODC and c-Myc mRNAs. However, G*l*-PS (up to 20 μg/mL) had no effect on the expression of TGFβ protein.
Conclusion: The results suggest that G*l*-PS protects small intestine against MTX-induced injury via induction of epithelial cell proliferation and migration.

Keywords: *Ganoderma lucidum* polysaccharides; chemotherapy; methotrexate; small intestine injury; IEC-6 cell line

Acta Pharmacologica Sinica (2011) 32: 1505–1512; doi: 10.1038/aps.2011.126; published online 24 Oct 2011

Introduction

The intestinal mucosa barrier (IMB), which is the first line of defense against a hostile environment, is composed of a single layer of columnar epithelium with inter-epithelial tight junctions. Intestinal mucositis is a clinical term that is used to describe the side effects of cancer chemotherapy on the intestinal mucosa surface, resulting from dysfunction of the IMB. Typical symptoms are bloating, abdominal pain and diarrhea. Approximately 40%–100% of cancer patients undergoing chemotherapy develop mucositis[1–4], and 50% of these patients require a reduction in the dose of chemotherapy or occasional cessation of treatment. Mucositis is occasionally fatal. However, no effective treatment for mucositis has been developed.

In recent years, researchers have focused on traditional Chinese medicine for its therapeutic effects and low toxicity. *Ganoderma lucidum* (Leyss, ex Fr) Karst (G*l*) has been widely used to promote health and longevity in China for thousands of years. *Ganoderma lucidum* polysaccharides (G*l*-PS) comprise the critical biological activity components of G*l*. G*l*-PS have been reported to prevent oxidative damage[5], protect the liver, and reduce serum glucose levels without causing toxicity[6, 7]. In addition, G*l*-PS modify biological and immune responses[8].

Unfortunately, little attention has been paid to the effects of G*l*-PS on gastrointestinal mucosal function. In this study, we used a murine model of intestinal damage that was induced using methotrexate (MTX), which is a folate antagonist, to evaluate the protective role of G*l*-PS in IMB. The intestinal epithelial cell line IEC-6 was also used as an *in vitro* wounding

* To whom correspondence should be addressed.
E-mail lwdpharma@126.com
Received 2011-05-06 Accepted 2011-08-12

model to evaluate the role of G*l*-PS on epithelial cell proliferation and cell restitution to elucidate the possible action mechanisms of G*l*-PS in the treatment of IMB.

Materials and methods

Materials

Ganoderma lucidum polysaccharides (G*l*-PS) were isolated from boiling water extracts of fruit bodies of *Ganoderma lucidum* (Leyss, ex Fr) Karst followed by ethanol precipitation, dialysis and protein depletion using the Sevag method. G*l*-PS is glycopeptide with a molecular weight of 584 900. The ratio of polysaccharides to peptides is 93.61%: 6.49%. The polysaccharides consisted of *D*-rhamnose, *D*-xylose, *D*-fructose, *D*-galactose, *D*-mannose and *D*-glucose with a molar ratio of 0.793:0.964:2.944:0.167:0.389:7.94. The polysaccharides were linked together by β-glycosidic linkages. G*l*-PS is a hazel-colored water-soluble powder that was kindly provided by the Fuzhou Institute of Green Valley Bio-Pharm Technology.

Inbred female BALB/c mice (7–8 weeks old) were purchased from the Department of Experimental Animals at the Health Science Centre at Peking University in Beijing, China. The animals were housed in environmentally controlled conditions with 12-h light/12-h dark cycles and were allowed free access to water and standard laboratory chow.

IEC-6 cells were obtained from the Cell Bank of Peking Union Medical College (Beijing, China). IEC-6 cells were routinely maintained in the presence of Dulbecco's modified Eagle's medium (DMEM) (Gibco BRL, USA) containing 5% inactivated fetal calf serum (FCS), 10 μg/mL insulin, 2.8 g/L sodium bicarbonate, 100 U/mL penicillin G sodium and 100 μg/mL streptomycin sulfate.

MTX was purchased from Zhejiang Hengrui Pharmaceutical Co, Ltd. Malondialdehyde (MDA) and superoxide dismutase (SOD) analysis kits were purchased from the Nanjing Jiancheng Biology Research Center. The TGFβ ELISA kit was purchased from Wuhan Boster Bio-engineering Co, Ltd. Primary, and secondary antibodies for the measurement of IgA were obtained from Sigma Chemical Co.

Murine MTX-induced enteritis model

The animals were randomly assigned to five groups that contained nine animals each. Mice received ig once daily for 10 consecutive days of (1) low-dose G*l*-PS (50 mg/kg), (2) intermediate-dose G*l*-PS (100 mg/kg), (3) high-dose G*l*-PS (200 mg/kg), (4) vehicle (*ie*, sterile physiological saline), which was used as a model control, and (5) vehicle (*ie*, sterile physiological saline) as a normal control. With the exception of group (5), the mice were injected intraperitoneally (ip) with MTX (50 mg/kg) on the 7th d and 8th d. Two days after completing the course of MTX (the 11th d), the mice were sacrificed by cervical dislocation. Subsequently, the intestinal tissue samples were harvested and prepared for histological studies. The other segments of the intestine were removed to determine MDA and SOD levels. Before the mice were sacrificed, blood samples were obtained from each animal to perform biochemical analyses (plasma IgA level). The experiments were approved by the Animal Care and Research Ethics Committee of the Peking University Health Science Center.

Intestinal morphology and histopathology

Tissue samples of the intestine (0.5 cm) were obtained at a distance of 15 cm from the pylorus of each animal following laparotomy. Imaging using light microscopy (LM) and transmission electronic microscopy (TEM) was performed for morphological and histopathological studies. The tissue sections were stained with hematoxylin and eosin for imaging using LM.

Measurement of MDA and SOD levels

Quantitative MDA and SOD measurements were performed with tissues that were obtained from the intestine using the MDA and SOD analysis kits.

Measurement of total immunoglobulin A

A sandwich ELISA technique was used as previously described[9].

Determination of IEC-6 cell proliferation

IEC-6 cells (3×10^4) were seeded into 96-well plates (Costar, USA) in the presence of DMEM containing 5% FCS. The cultures were treated with different concentrations of G*l*-PS. After 44 h of incubation at 37 °C and 5% CO_2, a colorimetric MTT assay was performed as previously described[10]. The cultures were incubated with tetrazolium salt thiazolyl blue (20 μL) at a concentration of 5 mg/mL for another 4 h. The cell supernatants were discarded, and the cells were lysed using dimethyl sulfoxide (DMSO). The metabolization of MTT directly correlates with the cell number and was quantitated by measuring the absorbance at 570 nm (reference wavelength 450 nm) using a microplate-reader.

Determination of ODC and c-Myc mRNA expression profiles using RT-PCR analysis

The mRNA expression profiles of ODC and c-Myc in IEC-6 cells were evaluated using reverse transcription polymerase chain reaction (RT-PCR) with the Access RT-PCR system (Takara, Japan) according to the manufacturer's procedures. IEC-6 cells that were treated with or without G*l*-PS were harvested after 12 h of incubation. The total RNA was extracted using TRIzol Reagent (Invitrogen, USA). The concentration of RNA was spectrophotometrically quantified. The cDNA was synthesized using the Advantage RT-for-PCR kit protocol (Promega, USA). Diluted aliquots from these reactions were subsequently used as templates for PCR.

Commercial primers to rat glyceraldehyde 3-phosphate-dehydrogenase (GAPDH) (sense, 5′-GCCAAGGTCATCCATGACAAC-3′ and antisense, 5′-GTCCACCACCCTGTTGCTGTA-3′), rat ODC (sense, 5′-TGCTTGACATTGGTGGTG-3′ and antisense, 5′-TTCTCATCTGGCTTGGGT-3′) and rat c-Myc (sense, 5′-GCTCGCCCAAATCCTGTA-3′ and antisense, 5′-ACCCTGCCACTGTCCAAC-3′) were provided by Shanghai Sangon Biological Engineering Technology and Service Co,

Ltd (Beijing, China) were used to generate products of 498 bp, 355 bp and 385 bp, respectively. The PCR reactions included 0.4 μmol/L of each primer, 0.2 mmol/L dNTPs, 1×PCR-Buffer with 15 mmol/L $MgCl_2$ and 2 U/μL Taq polymerase (Takara, Japan). The PCR cycling protocol was as follows: 45 s at 94 °C, 45 s at 60 °C (GAPDH), 57 °C (ODC), or 59 °C (c-Myc) and 2 min at 72 °C. This protocol was performed for 24 (GAPDH)/26 (ODC)/26 (c-Myc) cycles and included an initial 5-min denaturation at 94 °C and a final 10-min extension at 72 °C. The performed cycles of PCR was chosen to ensure the exponential amplification of all specific cDNA products. The PCR-amplified samples were electrophoresed using 1.5% agarose gels, stained with ethidium bromide, visualized via UV transillumination and quantified via densitometry scanning using AlphaEaseFC V4.0.0 software (Alpha Innotech Corp). ODC and c-Myc expression profiles were normalized relative to that of GAPDH.

Monolayer wounding and measurement of epithelial cell restitution

IEC-6 cell restitution assays were performed using a modified version of a previously described technique[11, 12]. IEC-6 cells were plated in six-well polystyrene plates (Costar) with normal growth medium and allowed to reach confluence. A denuded epithelial wound was created in a standardized fashion by scraping the IEC-6 monolayers with a 200-μL pipet tip. After the scraping, the cells were washed twice with D-Hanks' buffer to remove residual cell debris. The wounded monolayers were cultured for 42 h in DMEM containing 2% FCS in the presence or absence of G*l*-PS. Wound areas were viewed under the microscope at various time points after wounding and photographed with an Olympus IX71 microscope. The denuded wound area (ROI, region of interest) was quantified using LEICA QWIN software (Germany). Two wound areas per well were analyzed. Each group was tested in triplicate, and at least three independent experiments were performed. Restitution was calculated as the migration ratio using the following equation: $(ROI_{0\ h}–ROI_{42\ h})/ROI_{0\ h}×100\%$. The data are expressed as the mean value±SD (standard deviation) representing at least three independent experiments.

IEC-6 cell supernatant collection and determination of TGFβ levels

The collection of IEC-6 cell supernatants was performed as previously described[13]. IEC-6 cells were plated in 6-well culture dishes at a density of $2.5×10^5$ cells/dish. After 24 h, the medium was replaced with medium that had been supplemented with different concentrations of G*l*-PS. IEC-6 monolayers were wounded using a 200-μL pipet tip as previously described. The cells were washed twice with D-Hanks' buffer and subsequently incubated with fresh medium that had been supplemented with G*l*-PS. After 24 h, the cell supernatants were collected. Secretion of TGFβ from supernatants was determined using a sandwich ELISA kit according to the manufacturer's protocol.

Statistical analysis

The data were analyzed using one-way ANOVA followed by the least-significant difference (LSD) test. *P* values that were below 0.05 were considered statistically significant.

Results

Morphological and histological results

As shown in Figure 1, G*l*-PS did not perturb the morphological and histological features of the jejunum in mice. All tissue sections of the intestine of the control group were normal. In the tissue sections of the MTX-treated mice, we observed villus shortening, variable degrees of fusion, epithelial atrophy, a decreased number of crypt cells, crypt loss and the development of abscesses in crypts. In addition, we noted an inflammatory infiltration in the lamina propria. The number of goblet cells was significantly decreased in the villi and the crypts. Although the histopathological features in the MTX+G*l*-PS 100 mg/kg-treated group were similar to the findings in the MTX-treated group, the total small intestine damage in the MTX+G*l*-PS 100 mg/kg-treated group was less than that of the MTX-treated group.

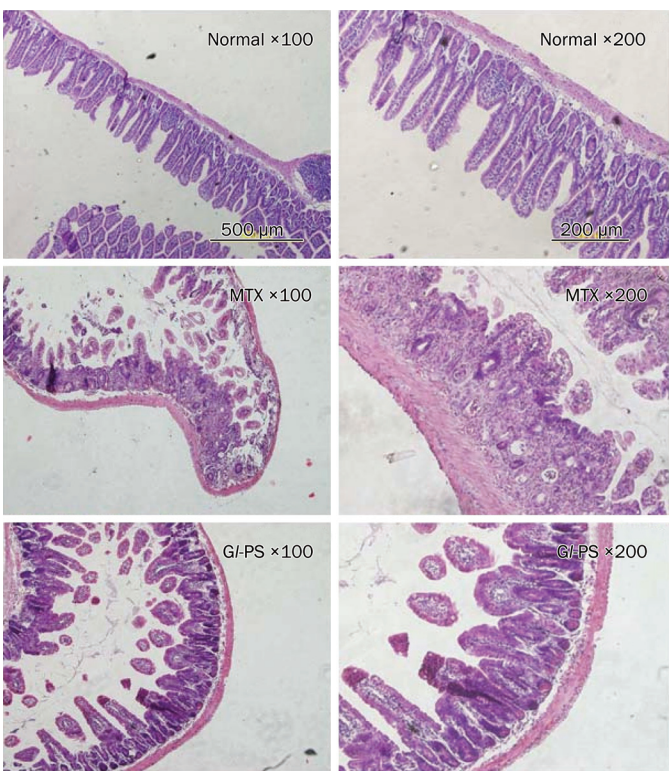

Figure 1. Morphology of the murine jejunum under magnification of 100 and 200. Normal: group of normal control; MTX: group of MTX model; G*l*-PS: group of 100 mg/kg G*l*-PS under MTX stress. These photographs are representative examples of a group of nine mice.

Examination of the intestinal ultrastructure revealed that the microvilli in the normal control group were long, abun-

dant and neatly arranged, whereas the microvilli in the MTX-treated group were reduced, shortened and disordered. Some of the microvilli were ablated. Swelling of the nuclear membrane and mitochondria was observed. The intestinal ultrastructural changes in the MTX+G*l*-PS 100 mg/kg-treated group were ameliorated compared to those in the MTX-treated group (Figure 2).

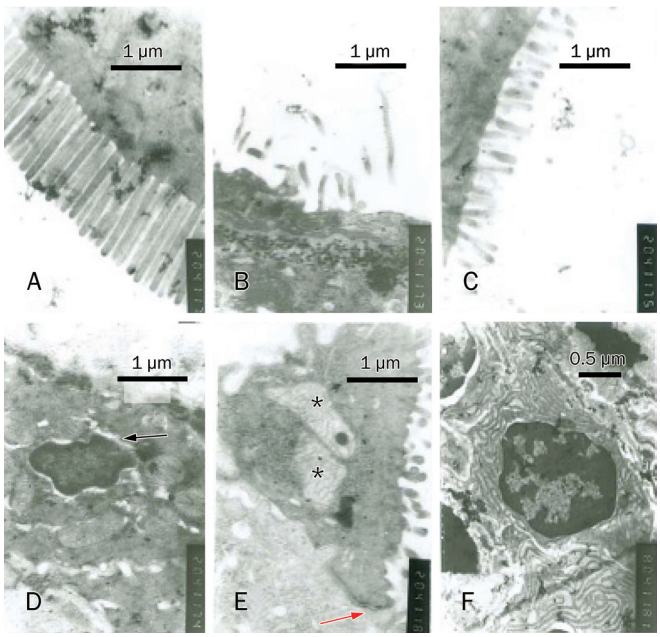

Figure 2. Changes of intestinal ultrastructure. (A) normal control group. (B, D, E) MTX model group. (C, F) group of 100 mg/kg G*l*-PS under MTX stress. The arrow (D) indicates swelling of nuclear membrane. The arrow (D, E) indicates tight junction. * indicates swelling of mitochondria.

G*l*-PS decreased MDA levels but increased SOD levels in mice intestine

We showed that the concentration of MDA in the intestine of mice in the MTX-treated group was significantly higher than that in the normal control group (P<0.001). However, we observed decreases in MDA concentration in MTX+G*l*-PS groups in a dose-dependent manner (Figure 3). However, the level of SOD in the MTX model group was down-regulated compared to that in the control group (P<0.01). MTX-induced decreases in SOD responded to G*l*-PS treatment in a dose-dependent manner (P<0.05) (Figure 4).

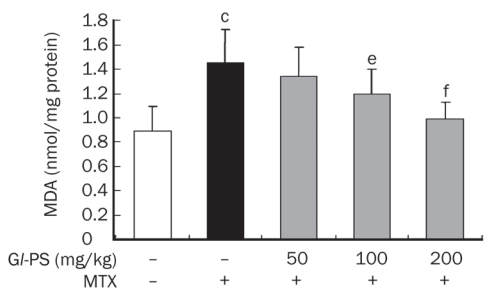

Figure 3. Effect of G*l*-PS on MDA content in supernatant homogenate for intestine in MTX-induced mice. n=9. Mean±SD. ^{c}P<0.01 *vs* normal control. ^{e}P<0.05, ^{f}P<0.01 *vs* MTX model.

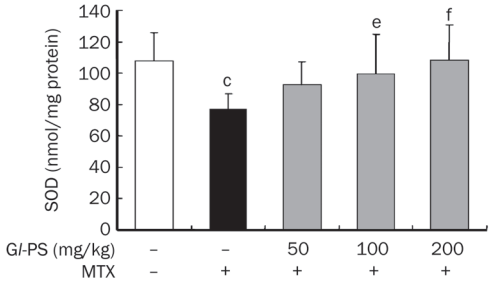

Figure 4. Effect of G*l*-PS on SOD content in supernatant homogenate of intestine in MTX induced mice. n=9. Mean±SD. ^{c}P<0.01 *vs* normal control. ^{e}P<0.05, ^{f}P<0.01 *vs* MTX model.

The concentration of IgA in serum

The concentration of total serum IgA was measured using an ELISA. MTX treatment significantly decreased the total serum IgA concentration compared to the normal control (P<0.05). G*l*-PS treatment elevated the concentration of IgA in a dose-dependent manner (Figure 5).

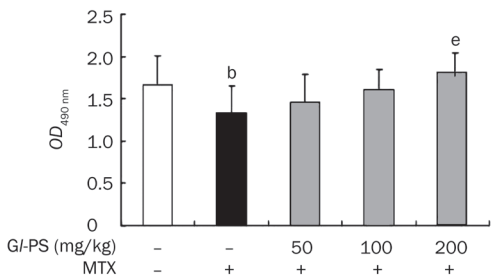

Figure 5. Effect of G*l*-PS on serum IgA level in MTX-induced mice. IgA level show by OD_{490} value. n=7. Mean±SD. ^{b}P<0.05 *vs* normal. ^{e}P<0.05 *vs* MTX model.

Effect of G*l*-PS on the proliferation of IEC-6 cells

The cells were incubated with different concentrations of G*l*-PS (0.1, 1, and 10 μg/mL) for 48 h. As shown in Table 1,

Table 1. Effects of G*l*-PS on IEC-6 cells proliferation. n=8. Mean±SD. ^{b}P<0.05, ^{c}P<0.01 *vs* DMEM.

Group	*OD* value (570 nm)
DMEM	0.626±0.072
G*l*-PS 0.1 μg/mL	0.725±0.080^{b}
G*l*-PS 1 μg/mL	0.751±0.075^{c}
G*l*-PS 10 μg/mL	0.840±0.077^{c}

G*l*-PS significantly promoted the proliferation of IEC-6 cells in a dose-dependent manner compared to the control. The proliferation rate was 34% higher in cells that were treated with 10 μg/mL G*l*-PS compared to that in control cells.

G*l*-PS modulated mRNA expression profiles of ODC and c-Myc in IEC-6 cells

Semiquantitative RT-PCR was used to determine the effect of G*l*-PS on ODC and c-Myc mRNA expression profiles in IEC-6 cells. As shown in Figures 6 and 7, ODC and c-Myc mRNAs were expressed in IEC-6 cells. G*l*-PS (10 and 20 μg/mL) treatment significantly up-regulated the expression of ODC and c-Myc mRNAs compared with that in the normal control group (Figures 6 and 7).

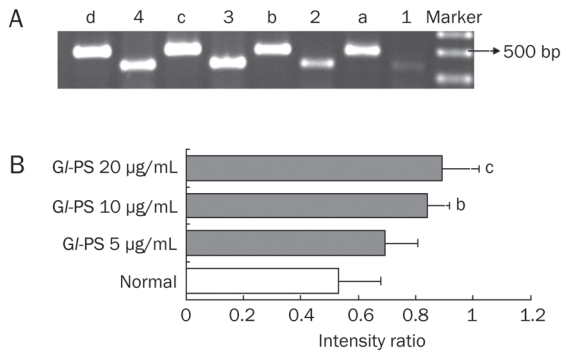

Figure 6. The mRNA expression of ODC and GAPDH in IEC-6 cells by RT-PCR. (A) 1–4: IEC-6 cells were treated with 0, 5, 10, and 20 μg/mL G*l*-PS and it is mRNA expression of ODC. a–d: IEC-6 cells were treated with 0, 5, 10, and 20 μg/mL G*l*-PS and it is mRNA expression of GAPDH. (B) PCR products were quantified by densitometric scanning and ODC expression was normalized relative to the steady-state expression of GAPDH used as internal control (intensity ratio: ODC to GAPDH). Values represent means±SD from three independent experiments. $^{b}P<0.05$, $^{c}P<0.01$ *vs* normal.

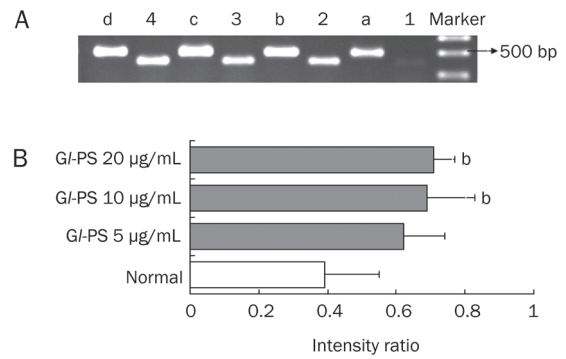

Figure 7. The mRNA expression of c-Myc and GAPDH in IEC-6 cells by RT-PCR. (A) 1–4: IEC-6 cells were treated with 0, 5, 10, and 20 μg/mL G*l*-PS and it is mRNA expression of c-Myc. a–d: IEC-6 cells were treated with 0, 5, 10, and 20 μg/mL G*l*-PS and it is mRNA expression of GAPDH. (B) Quantification of RT-PCR data. $n=3$. $^{b}P<0.05$ *vs* normal control.

G*l*-PS enhanced IEC-6 cell restitution

As shown in Table 2, G*l*-PS caused a dose-dependent enhancement of intestinal epithelial cell restitution in a well-established wounding model with IEC-6 cell monolayers. We detected a 36% increase in the restitution of IEC-6 cells that were treated with 10 μg/mL G*l*-PS compared to that of control cells.

Table 2. The effect of G*l*-PS on IEC-6 cells wound restitution. $n=8$. Mean±SD. $^{b}P<0.05$, $^{c}P<0.01$ *vs* DMEM.

Group	*OD* value (570 nm)
DMEM	0.486±0.054
G*l*-PS 0.1 μg/mL	0.544±0.062
G*l*-PS 1 μg/mL	0.587±0.046[b]
G*l*-PS 10 μg/mL	0.661±0.089[c]

Effects of G*l*-PS on TGFβ levels in IEC-6 cell culture supernatants

Recent evidence has supported a central role for TGFβ in the process of intestinal epithelial restitution[14]. Therefore, the production of TGFβ was measured to determine the possible involvement of this cytokine in G*l*-PS-mediated restitution. No significant effect was observed on the production of TGFβ following G*l*-PS treatment (Table 3).

Table 3. Effects of G*l*-PS on TGFβ level in IEC-6 cells culture supernatants. Values represent means (±SD) from three independent experiments performed in duplicate.

Group	TGFβ (pg/mL)
DMEM	9.602±0.001
G*l*-PS 5 μg/mL	9.603±0.001
G*l*-PS 10 μg/mL	9.605±0.001
G*l*-PS 20 μg/mL	9.607±0.002

Discussion

The intestinal epithelial barrier, including the biotic, mechanical and immunity barriers, is a crucial barrier against pathogen infection. Previous studies have not demonstrated an effective method to prevent IMB damage[15]. It is necessary to develop natural medicines that are effective in treating IMB dysfunction and intercurrent diseases. In the current report, the effects of G*l*-PS on the intestinal epithelial barrier were investigated.

Chemotherapy commonly produces structural damage to the intestinal mucosa in cancer patients[16] and causes side effects such as severe enterocolitis. In agreement with previous studies[17], the results of the present study reveal that MTX induced small intestinal injury, which is characterized by villus shortening and fusion, epithelial atrophy, crypt loss,

inflammatory infiltration of the lamina propria, and goblet cell depletion. G*l*-PS treatment reduced intestinal mucosal damage in this study and reduced gastric mucosal lesions in a previous study[18].

Increased oxidative stress and decreased antioxidant defenses have been demonstrated in intestinal mucosal biopsies of patients with MTX-induced damage to the small intestinal epithelium. These damages may be reduced by antioxidant agents. As previously reported, protective effects of various antioxidants, such as curcumin[19], aged garlic extract[20] and N-acetylcysteine[17], have been shown in MTX-induced small intestinal damage. MDA is frequently used in the measurement of lipid peroxide levels and correlates with the degree of lipid peroxidation. SOD levels correlate with the elimination of free radicals. G*l*-PS have been widely used as antioxidants *in vivo* and *in vitro*[21–23]. Therefore, in the present study, we investigated whether G*l*-PS inhibit MTX-induced small intestine damage via decreasing MDA levels and increasing SOD levels. We showed that the MDA level in the small intestinal mucosa of MTX-treated mice was remarkably increased, suggesting that MTX treatment caused oxidative damage and lipid peroxidation in the intestinal mucosa. MTX-induced increases in MDA levels were attenuated after G*l*-PS administration (Figure 3). These findings may indicate that G*l*-PS protect intestinal tissue against MTX-induced lipid peroxidation. The present study also demonstrated that the MTX-induced downregulation of SOD was inhibited by G*l*-PS treatment in the intestinal mucosa of mice (Figure 4). These results suggest that the effects of G*l*-PS may be achieved via its antioxidant and free radical-eliminating activities.

Immunoglobulin A (IgA) is an important component of the intestinal immunological barrier and is the most abundant immunoglobulin at the mucosal surface where it plays crucial role in mucosal protection[24]. The protective barrier of the gastrointestinal system is impaired in IgA deficiency, and IgA-deficient individuals tend to develop gastrointestinal infections[25, 26]. G*l*-PS are well-known modulators of the immune system[27, 28]. In this study, we found that MTX-treated mice displayed a reduced level of serum IgA. This result indicates that mucosal immune barrier dysfunction occurs during MTX-induced intestine damage. G*l*-PS restored the level of IgA, suggesting that G*l*-PS bolstered intestinal immunity.

Observations over the past several years have demonstrated the ability of the gastrointestinal tract to rapidly restore the continuity of the surface epithelium after extensive destruction. Three different phases have been identified. First, epithelial cells that are adjacent or just beneath the injured surface migrate into the wound to cover the denuded area, which is a process that has been termed epithelial restitution. Secondly, epithelial cell proliferation takes place to replenish the decreased cell pool. Finally, maturation and differentiation of epithelial cells enable the epithelium to maintain its functional activities[12]. The initial mechanism contributing to rapid resealing of epithelial defects after mucosal injury is the migration of viable epithelial cells from the wound margin into the denuded area, which is a process that does not require cell proliferation[29]. The data presented in this study revealed that G*l*-PS at a concentration of 10 μg/mL augmented the migration of intestinal epithelial cells in an *in vitro* model that mimicked the early cell division-independent stages of epithelial restitution. When G*l*-PS were added immediately after wounding, they significantly increased intestinal epithelial cell migration in a dose-dependent manner. Although the exact mechanism of restitution has not been elucidated, the cytokine TGFβ has been shown to play an important role in the stimulation of cell migration after wounding. Some studies have revealed that the intestinal epithelial cell restitution process is stimulated via a TGFβ-dependent pathway[30, 31]. However, in other cases, the intestinal epithelial cell restitution was independent of TGFβ[32]. In our study, we found that G*l*-PS did not affect TGFβ expression in IEC-6 cells after wounding. These results may indicate that G*l*-PS stimulate restitution possibly through a TGFβ-independent pathway.

Epithelial cell proliferation, which is another essential mechanism to mediate resealing of mucosal wounds in the intestine, was substantially promoted by G*l*-PS treatment in our investigation. This effect was dose-dependent, and maximal effects were detected at a concentration of 10 μg/mL G*l*-PS.

The polyamines are a group of ubiquitously distributed organic cations that are intimately involved in the regulation of gastrointestinal mucosal growth[33]. ODC, which is a pyridoxal phosphate-dependent enzyme, is the first rate-limiting enzyme for the biosynthesis of polyamines. The extent of the ODC mRNA expression correlates with the cell proliferation. Treatment of gastrointestinal origin cells with difluoromethylornithine, which is a suicide substrate inhibitor of ODC and induces depletion of intracellular polyamines, inhibits proliferation[34, 35]. In addition, induction of the ODC gene may play an important role in the signaling pathways that are associated with several oncogenes. Transformation by activated *ras*, *v-src* and *myc* appears to be tightly coupled to ODC gene expression and polyamine accumulation[36–38]. ODC is a transcriptional target of c-Myc[39], which has a central role in the proliferation of normal cells. Following mitogenic stimulation of quiescent cells, c-Myc is rapidly induced and remains elevated, suggesting that it is required for continuous cell growth[40]. In the present study, an increase in *c-Myc* and *ODC* gene expression (Figure 6 and 7) was observed in IEC-6 cells 12 h after exposure to G*l*-PS. *c-Myc* and *ODC* gene expression were coincident to the stimulatory effect on cell proliferation (Table 1).

In summary, the present study demonstrated that G*l*-PS reduced MTX-induced intestinal toxicity. We demonstrated that G*l*-PS increased the antioxidation and intestinal immunity *in vivo*, accelerated wound repair by stimulating cell proliferation and migration *in vitro*, and up-regulated *c-Myc* and *ODC* mRNA expression. However, G*l*-PS had no effects on TGFβ levels. Altogether, we demonstrated a new protective effect of G*l*-PS on the intestinal barrier via induction of epithelial cell proliferation and migration. The present study may provide a pharmacological basis for the clinical use of G*l*-PS in preventing enteritis in patients receiving chemotherapeutic agents. Previous studies have shown that cell differentiation

also plays an important role in protecting the intestinal barrier. However, the effect of *Gl*-PS on cell differentiation was not assessed in this study. Therefore, further investigation is required using molecular markers such as sucrase-isomaltase and alkaline phosphatase.

Acknowledgements

The authors are grateful to Dr Mei-hua BAO for her critical reading of the manuscript.

Author contribution

Li-hua CHEN, Wei-dong LI, and Z hi-bin LIN designed the research; Li-hua CHEN performed the research; Wei-dong LI and Zhi-bin LIN contributed new analytical reagents and tools; Li-hua CHEN and Wei-dong LI analyzed the data; and Li-hua CHEN wrote the paper.

References

1 Gupta G, Agarwala S, Thulkar S, Shukla B, Bakhshi S. Jejunal stricture: a rare complication of chemotherapy in pediatric gastrointestinal B-cell non-Hodgkin lymphoma. J Pediatr Hematol Oncol 2011; 33: e69–71.

2 Nicoletto MO, Dalla Palma M, Donach ME, Gusella M, Cappetta A, Shams M, *et al*. Positive experience of intraperitoneal chemotherapy followed by intravenous chemotherapy in heavily pretreated patients with suboptimal residual ovarian cancer and primary peritoneal cancer. Tumori 2010; 96: 918–25.

3 Prisciandaro LD, Geier MS, Butler RN, Cummins AG, Howarth GS. Evidence supporting the use of probiotics for the prevention and treatment of chemotherapy-induced intestinal mucositis. Crit Rev Food Sci Nutr 2011; 51: 239–47.

4 Van Vliet MJ, Harmsen HJ, de Bont ES, Tissing WJ. The role of intestinal microbiota in the development and severity of chemotherapy-induced mucositis. PLoS Pathog 2010; 6: e1000878.

5 You YH, Lin ZB. Protective effects of *Ganoderma lucidum* polysaccharides peptide on injury of macrophages induced by reactive oxygen species. Acta Pharmaco Sin 2002; 23: 787–91.

6 Zhang GL, Wang YH, Ni W, Teng HL, Lin ZB. Hepatoprotective role of *Ganoderma lucidum* polysaccharide against BCG-induced immune liver injury in mice. World J Gastroenterol 2002; 8: 728–33.

7 Zhang HN, He JH, Yuan L, Lin ZB. *In vitro* and *in vivo* protective effect of G*anoderma lucidum* polysaccharides on alloxan-induced pancreatic islets damage. Life Sci 2003; 73: 2307–19.

8 Zhu XL, Lin ZB. Modulation of cytokines production, granzyme B and perforin in murine CIK cells by *Ganoderma lucidum* polysaccharides. Carbohydrate Polymers 2006; 63: 188–97.

9 Ha CL. The inhibitory effect of the Chinese herb *Ganoderma lucidum* mycelium on gut immunoglobulin A responses to cholera toxin in mice. Nutr Res 2003; 23: 691–701.

10 Mossman T. Rapid colorimetric assay for cellular growth and survival: application to proliferation and cytotoxity assays. J Immunol Methods 1983; 65: 55–63.

11 Zou L, Sato N, Kone BC. α- Melanocyte stimulating hormone protects against H_2O_2-induced inhibition of wound restitution in IEC-6 cells via a Syk kinase and NF-κB dependent mechanism. Shock 2004; 22: 453–9.

12 Jung S, Fehr S, Harder-d'Heureuse J, Wiedenmann B, Dignass AU. Corticosteroids impair intestinal epithelial wound repair mechanisms *in vitro*. Scand J Gastroenterol 2001; 36: 963–70.

13 Ruthig DJ, Meckling-Gill KA. N-3 and n-6 fatty acids stimulate restitution by independent mechanisms in the IEC-6 model of intestinal wound healing. J Nutr Biochem 2002; 13: 27–35.

14 Dignass AU, Podolsky DK. Cytokine modulation of intestinal epithelial cell restitution: central role of transforming growth factorβ. Gastroenterology 1993; 105: 1323–32.

15 Daniel C, Baumgart, Dignass AU. Intestinal barrier function. Curr Opin Clin Nutr Metab Care 2002; 5: 685–94.

16 Cunningham D, Morgan RJ, Mills PR, Nelson LM, Toner PG, Soukop M, *et al*. Functional and structural changes of the human proximal small intestine after cytotoxic therapy. J Clin Pathol 1985; 38: 265–70.

17 Ciralik H, Bulbuloglu E, Cetinkaya A, Kurutas EB, Celik M, Polat A. Effects of N-acetylcysteine on methotrexate-induced small intestinal damage in rats. Mt Sinai J Med 2006; 73: 1086–92.

18 Gao Y, Zhou S, Wen J, Huang M, Xu A. Mechanism of the antiulcerogenic effect of *Ganoderma lucidum* polysaccharides on indomethacin-induced lesions in the rat. Life Sci 2002; 72: 731–45.

19 Song WB, Wang YY, Meng FS, Zhang QH, Zeng JY, Xiao LP, *et al*. Curcumin protects intestinal mucosal barrier function of rat enteritis via activation of MKP-1 and attenuation of p38 and NF-κB activation. PLoS One 2010; 5: 1–11.

20 Yüncü M, Eralp A, Celik A. Effect of aged garlic extract against methotrexate-induced damage to the small intestine in rats. Phytother Res 2006; 20: 504–10.

21 Sudheesh NP, Ajith TA, Ramnath V, Janardhanan KK. Therapeutic potential of *Ganoderma lucidum* (Fr) P Karst against the declined antioxidant status in the mitochondria of post-mitotic tissues of aged mice. Clin Nutr 2010; 29: 406–12.

22 Liu W, Wang H, Pang X, Yao W, Gao X. Characterization and antioxidant activity of two low-molecular-weight polysaccharides purified from the fruiting bodies of *Ganoderma lucidum*. Int J Biol Macromol 2010; 46: 451–7.

23 Cherian E, Sudheesh NP, Janardhanan KK, Patani G. Free-radical scavenging and mitochondrial antioxidant activities of Reishi-Ganoderma lucidum (Curt: Fr) P Karst and Arogyapacha-Trichopus zeylanicus Gaertn extracts. J Basic Clin Physiol Pharmacol 2009; 20: 289–307.

24 Kadaoui KA, Corthésy B. Secretory IgA mediates bacterial translocation to dendritic cells in mouse Peyer's patches with restriction to mucosal compartment. J Immunol 2007; 179: 7751–7.

25 Yel L. Selective IgA deficiency. J Clin Immunol 2010; 30: 10–6.

26 Brandtzaeq P. Update on mucosal immunoglobulin A in gastrointestinal disease. Curr Opin Gastroenterol 2010; 26: 554–63.

27 Zhang J, Tang Q, Zhou C, Jia W, Da Silva L, Nguyen LD, *et al*. GLIS, a bioactive proteoglycan fraction from *Ganoderma lucidum*, displays anti-tumour activity by increasing both humoral and cellular immune response. Life Sci 2010; 87: 628–37.

28 Huang SQ, Li JW, Wang Z, Pan HX, Chen JX, Ning ZX. Optimization of alkaline extraction of polysaccharides from *Ganoderma lucidum* and their effect on immune function in mice. Molecules 2010; 15: 3694–708.

29 Rutten MJ, Ito S. Morphology and electrophysiology of guinea pig gastric mucosal repair *in vitro*. Am J Physiol 1983; 244: G171–82.

30 Strauch ED, Wang JY, Bass BL. Bile salt stimulates intestinal epithelial cell migration through TGFbeta after wounding. J Surg Res 2001; 97: 49–53.

31 Bulut K, Meier JJ, Ansorge N, Felderbauer P, Schmitz F, Hoffmann P, *et al*. Glucagon-like peptide 2 improves intestinal wound healing through induction of epithelial cell migration *in vitro*-evidence for a TGF-β-mediated effect. Regul Pept 2004; 121: 137–43.

32 Paclik D, Lohse K, Wiedenmann B, Dignass AU, Sturm A. Galectin-2

and -4, but not galectin-1, promote intestinal epithelial wound healing *in vitro* through a TGF-beta-independent mechanism. Inflamm Bowel Dis 2008; 14: 1366–72.

33 Seidel ER, Scemama JL. Gastrointestinal polyamines and regulation of mucosal growth. Nutrit Biochem 1997; 8: 104–11.

34 Ye YN, Liu ES, Shin VY, Koo MW, Li Y, Wei EQ, *et al.* A mechanistic study of proliferation induced by *Angelica sinensis* in a normal gastric epithelial cell line. Biochem Pharmacol 2001; 61: 1439–48.

35 Lefevre PL, Palin MF, Chen G, Turecki G, Murphy BD. Polyamines are implicated in the emergence of the embryo from obligate diapause. Endocrinology 2011; 152: 1627–39.

36 Hölttä E, Sistonen L, Alitalo K. The mechanism of ornithine decarboxylase deregulation in c-Ha-*ras* oncogene-transformed NIH 3T3 cells. J Biol Chem 1988; 263: 4500–7.

37 Guerrero I, Pellicer A, Alitalo K. Dissociation of *c-fos* from ODC expression and neuronal differentiation in a PC12 subline stably transfected with an inducible n-*ras* oncogene. Biochem Biophys Res Commun 1988; 150: 1185–92.

38 Celano P, Baylin SB, Giardello FM, Nelkin BD, Casero RA. Effect of polyamine depletion on c-myc expression in human colon carcinoma cells. J Biol Chem 1988; 263: 5491–4.

39 Bello-Fernandez C, Packham G, Cleveland JL. The ornithine decarboxylase gene is a transcriptional target for c-Myc. Proc Natl Acad Sci U S A 1993; 90: 7804–8.

40 Evan G, Littlewood TD. The role of c-myc in cell growth. Curr Opin Genet Dev 1993; 3: 44–9.

Acta Pharmacologica Sinica (2011) 32: 1513–1521
 1671-4083/11 $32.00
www.nature.com/aps

Original Article

VEGF ameliorates tubulointerstitial fibrosis in unilateral ureteral obstruction mice via inhibition of epithelial-mesenchymal transition

Yao-guo LIAN[1], Qiu-gen ZHOU[2], Ying-juan ZHANG[1], Fa-lei ZHENG[1, *]

[1]Division of Nephrology, Peking Union Medical College Hospital, Peking Union Medical College and Chinese Academy of Medical Sciences, Beijing 100730, China; [2]Division of Nephrology, Southern Medical University Nanfang Hospital, Guangzhou 510515, China

Aim: Vascular endothelial growth factor (VEGF) has been shown to be a survival factor for renal tubular epithelial cells. In the present study, we investigated whether administration of VEGF ameliorates tubulointerstitial fibrosis in a mouse model of unilateral ureteral obstruction (UUO).

Methods: Thirty-six male CD-1 mice were randomly divided into three groups: sham-operation, UUO and UUO+VEGF group. VEGF (50 μg/kg) was subcutaneously injected twice daily from d 1 to d 14. Mice in each group were killed at d 3, 7, or 14 after the operation, and the tubulointerstitial fibrosis was histopathologically evaluated. Human proximal tubular epithelial cells (HK-2) were used for *in vitro* study. The expression levels of α-SMA, E-cadherin, TGF-β1, CTGF, and BMP-7 in the kidney were determined using Western blot and RT-PCR.

Results: In the UUO mice, the degree of interstitial fibrosis was dramatically increased in a time-dependent manner. At d 3, 7, and 14, both the mRNA and protein expression levels for α-SMA, TGF-β1, and CTGF were significantly upregulated, whereas those for E-cadherin and BMP-7 were significantly downregulated. At d 3 and 7, VEGF treatment significantly reduced interstitial fibrosis and the expression levels for α-SMA, TGF-β1, and CTGF, while significantly increased the expression of E-cadherin and BMP-7, as compared with the UUO mice. At d 14 after operation, no significant differences were observed in the expression of the examined markers between VEGF-treated mice and UUO mice, with the exception of CTGF. In HK-2 cells, VEGF blocked TGF-β1-induced α-SMA and vimentin expression and restored E-cadherin expression in a dose-dependent manner.

Conclusion: VEGF may ameliorate renal tubulointerstitial fibrosis at the early stage in UUO mice. This effect may be related to inhibition of VEGF on renal tubular epithelial-mesenchymal transition (EMT).

Keywords: VEGF; unilateral ureteral obstruction; renal tubulointerstitial fibrosis; epithelial-mesenchymal transition; transforming growth factor-β1

Acta Pharmacologica Sinica (2011) 32: 1513–1521; doi: 10.1038/aps.2011.111; published online 10 Oct 2011

Introduction

Tubulointerstitial fibrosis is closely correlated with the progression of chronic renal disease and is a common final pathway leading to end-stage renal failure. Emerging evidence indicates that renal tubular epithelial-mesenchymal transition (EMT) is an important event in renal interstitial fibrosis[1]. All types of renal injury are potentially able to induce renal tubular cells to undergo EMT, generating mesenchymal cells, as demonstrated by experimental models, *in vitro* experiments, and renal biopsy studies[2]. EMT is the process in which renal tubular epithelial cells lose their epithelial phenotype followed by their acquisition of mesenchymal cell characteristics, contributing to continuous tubulointerstitial fibrosis[3]. Previous studies have demonstrated that transforming growth factor (TGF)-β1 is an inducer of renal tubular epithelial cell EMT, whereas bone morphogenetic protein-7 (BMP-7) counteracts TGF-β1-induced EMT and reverses chronic renal injury[4, 5]. These data imply that there are several factors modulating the phenotype of renal tubular epithelial cells and that imbalance of these factors might lead to their change from the epithelial phenotype.

Vascular endothelial growth factor (VEGF) is an endothelial-specific growth factor that promotes endothelial cell proliferation, differentiation and survival, mediates endothelium-dependent vasodilatation, induces microvascular hyperpermeability and participates in interstitial matrix remodeling. In

* To whom correspondence should be addressed.
E-mail zhengfl46@vip.sina.com
Received 2011-03-23 Accepted 2011-07-11

the kidney, VEGF expression is most prominent in glomerular podocytes and tubular epithelial cells[6, 7]. Several studies have shown that VEGF may relieve experimental renal diseases, such as anti-Thy1 glomerulonephritis, thrombotic microangiopathy and anti-glomerular basement membrane glomerulonephritis[8–10]. Moreover, reduced expression of VEGF has been observed in tubulointerstitial fibrosis[11–13].

VEGF treatment in a rat model of remnant kidneys inhibited loss of peritubular capillaries and improved renal function and peritubular capillary endothelial cell proliferation[14]. Furthermore, VEGF has been shown to induce vasculogenesis and tubulogenesis[15, 16]. In addition, VEGF has been shown to induce a proliferative response and to prevent hydrogen peroxide-induced apoptosis and necrosis in renal tubular epithelial cells[17].

We previously reported that pentoxifylline treatment inhibited tubulointerstitial fibrosis in a rat model of obstructive nephropathy and prevented loss of VEGF[18]. In addition, our previous *in vitro* studies indicated that reduced expression of VEGF might contribute to tubular EMT[19].

The above-mentioned studies suggest that VEGF may be a renoprotective factor important for maintenance of the epithelial phenotype of renal tubular cells. In the present study, we used a mouse model of obstructive nephropathy to test whether VEGF could ameliorate tubulointerstitial fibrosis and EMT and whether it could affect the expression of TGF-β1, connective tissue growth factor (CTGF) and BMP-7.

Materials and methods

Reagents

$VEGF_{121}$ was purchased from R&D Systems (Minneapolis, MN, USA). Blood urea nitrogen and serum creatinine were detected using a kit from Sigma (St Louis, MO, USA). Anti-α-smooth muscle actin (α-SMA) was obtained from Sigma (St Louis, MO, USA); anti-E-cadherin, anti-TGF-β1, anti-CTGF, anti-BMP-7, anti-vimentin and an anti-actin polyclonal antibody and ECL were obtained from Santa Cruz Biotechnology (Santa Cruz, CA, USA). The Histostain™-plus kit was from Zymed Laboratories (South San Francisco, CA, USA). The TRIzol reagent was from Life Technologies/BRL (Rockville, MD, USA). M-MLV reverse transcriptase and Taq polymerase were purchased from Promega (Madison, WI, USA). BCA protein assay kits were purchased from Beyotime (Haimen, China).

Experimental design

Thirty-six male CD-1 mice (21–24 g, Grade III, Peking Union Medical College Hospital) were divided into two 1:2 matched groups. The sham group (group A) was subjected to surgical manipulation without ureteral ligation; the unilateral ureteral obstruction (UUO) group was subjected to left ureteral ligation. The animals were housed in individual cages under conditions of constant temperature and humidity on a 12-h light/dark cycle. Food and water were provided *ad libitum*. Protocols for animal experimentation and maintenance were approved by the Animal Ethics Committee at our institute and carried out in accordance with institutional guidelines. For the surgery, anesthesia with sodium pentobarbital (40 mg/kg, ip) was provided, and the left ureter was ligated with silk sutures at two points and was cut between the ligatures. The UUO mice were randomly divided into two groups: one group (group C) received $VEGF_{121}$ (50 μg/kg, subcutaneous (sc), twice daily, n=12) from d 1 to d 14 after ligation[14], and the other group (group B) received vehicle (normal saline, sc, n=12) as a control. The $VEGF_{121}$ isoform was chosen because it is the only isoform of VEGF that has no heparin-binding ability and, therefore, results in therapeutically effective plasma levels when administered subcutaneously. Four mice from each group (including group A, the sham-operated mice, to serve as negative controls) were killed on d 3 after operation, four mice on d 7, and four mice on d 14. The kidneys were decapsulated and divided into several parts. One part was fixed in 10% neutral buffered formalin and processed for histological analysis. Another part was dissected to isolate the cortex, which was quickly frozen in liquid nitrogen and stored at -70 °C for protein and total RNA extraction. Blood was collected for serum creatinine and blood urea nitrogen measurements according to the protocol of the commercial kit.

Histologic examination

Kidneys were removed, fixed in 10% neutral formalin, embedded in paraffin, sectioned (2.0–3.0 μm thickness), and stained with Masson trichrome using routine procedures. Evaluation of tubulointerstitial fibrosis was performed. In each section, 20 randomly selected fields were examined under ×400 magnification for assessment of the degree of tubulointerstitial fibrosis. The degree of tubulointerstitial fibrosis was scored in Masson-stained sections as the ratio of the positive stain area (blue) to that of the whole area (n=20). Tubulointerstitial fibrosis was examined in each mouse and then averaged for the four mice from each group.

Cell culture

Human proximal tubular epithelial cells (HK-2) (from Dr Xiong-zhong RUAN, Royal Free and University College Medical School, UK) were cultured and maintained in Dulbecco's modified Eagle's medium/Ham's F-12 containing 10% fetal bovine serum as previously described[18]. All studies were carried out in overnight serum-deprived cells at 90%–100% confluency.

Reverse transcription-PCR

Total RNA was isolated from the cortex of the ligated kidneys or from cultured cells using the TRIzol reagent according to the manufacturer's instructions. First-strand cDNA was made from total RNA using the M-MLV transcriptase. PCR was performed in a DNA Thermal Cycler with the primers listed in Table 1. Primers were designed with OLIGO software (version 6) and synthesized by the Shanghai Sangon Biological Engineering Company (Beijing, China).

Reactions were incubated at 95 °C for 5 min, followed by the indicated number of cycles of 30 s at 94 °C and 30 s at 56 °C

Table 1. Primers used in RT-PCR experiments.

Gene	Primers	Sequences	Length of products
Subunit of mouse			
GAPDH	Forward	5′-GCCTTCCGTGTTCCTACCC-3′	166 bp
	Reverse	5′-TGAAGTCGCAGGAGACAACC-3′	
α-SMA	Forward	5′-CCGAGCGTGAGATTGTCC-3′	358 bp
	Reverse	5′-CTTCATGGTGCTGGGTGC-3′	
E-cadherin	Forward	5′-CAAAGTGGCGACAGACGG-3′	483 bp
	Reverse	5′-GACACGGCATGAGAATAGAGG-3′	
TGF-β1	Forward	5′-TGGTGGACCGCAACAACG-3′	394 bp
	Reverse	5′-CGACGTTTGGG GCTGATC-3′	
CTGF	Forward	5′-CTATCCCACCAAAGTGAGAACG-3′	417 bp
	Reverse	5′-TTGCCACAA GCTGTCCAGTC-3′	
BMP-7	Forward	5′-AGGGAGTCGGACCTCTTCTTG-3′	472 bp
	Reverse	5′-CCTCACAGTAGTAGGCAGCATAGC-3′	
Subunit of human			
GAPDH	Forward	5′-CCACCCATGGCAAATTCCATGGCA-3′	323 bp
	Reverse	5′-TGCTAAGCAGTTGTTGGTGCAGGA-3′	
α-SMA	Forward	5′-GCTCACGGAG GCACCCCTGAA-3′	590 bp
	Reverse	5′-CTGATAGGACATTGTTAGCAT-3′	
E-cadherin	Forward	5′-CTCACATTTCCCAACTCC-3′	405 bp
	Reverse	5′-ACCTTCCATGACAGACCC-3′	
Vimentin	Forward	5′-GGCTCAGATTCAGGAACAGC-3′	327 bp
	Reverse	5′-GCTTCAACGGCAAA GTTCTC-3′	

for α-SMA, E-cadherin, vimentin, TGF-β1, CTGF, and BMP-7 (58 °C for GAPDH), 30 s at 72 °C, and a final extension at 72 °C for 10 min. There were 35 cycles of PCR for α-SMA, E-cadherin, vimentin, TGF-β1, CTGF, and BMP-7, and 28 cycles for GAPDH. The PCR products were electrophoresed using 2% agarose and their signal intensity was determined with the UVI soft UVIband Windows application V97.04. The resulting signal intensities were normalized to that of GAPDH.

Western blot analysis

Kidney tissues or cultured cells were homogenized in RIPA lysis buffer (1% NP40, 0.1% SDS, 100 μg/mL phenylmethylsulfonyl fluoride, 0.5% sodium deoxycholate, in PBS) on ice. The supernatants were collected after centrifugation at 12000×*g* at 4 °C for 20 min. Protein concentration was determined using a BCA protein assay kit, and whole lysates were mixed with an equal amount of 2×SDS loading buffer (125 mmol/L Tris-HCl, 4% SDS, 20% glycerol, 100 mmol/L DTT, and 0.2% bromophenol blue). Samples were heated at 100 °C for 5 min and were separated on SDS-polyacrylamide gels. The separated proteins were then transferred to a PVDF membrane. The membrane blots were first probed with a primary antibody. After incubation with horseradish peroxidase-conjugated second antibody, autoradiograms were prepared using the enhanced chemiluminescent system to visualize the protein antigen. The signals were recorded using X-ray film, and the signal intensities were determined using the UVI soft UVI band Windows application V97.04. The primary antibodies that we used included anti-α-SMA (1:300), anti-E-cadherin (1:400), anti-vimentin (1:200), anti-TGFβ1 (1:200), anti-CTGF (1:400), anti-BMP-7 (1:600), and anti-actin (1:2000). The results were normalized to the signal intensity of β-actin, which was used as an internal control.

Confocal microscopy

HK-2 cells treated with TGF-β1 (5 μg/L) alone, co-treated with TGF-β1 (5 μg/L) and different concentrations of VEGF (0.1, 1, 10, and 100 μg/L) or left untreated were cultured in eight-chamber glass slides for 48 h. Cells were fixed with 4% paraformaldehyde in phosphate-buffered saline (PBS) (20 min; room temperature), permeabilized with 0.1% Triton X-100 in PBS (15 min), and incubated in normal goat serum (30 min), followed by application of a monoclonal anti-α-SMA antibody (1:50 in BSA/PBS, Sigma) and a polyclonal anti-E-cadherin antibody (1:100 in BSA/PBS, Santa Cruz Biotechnology) (overnight, 4 °C). The slides were then washed with PBS, incubated in rhodamine (TRITC)-conjugated goat anti-mouse IgG (1:50 in BSA/PBS; Proteintech Group, Chicago, IL, USA) and fluorescein (FITC)-conjugated affinipure goat anti-rabbit IgG (1:50 in BSA/PBS; Proteintech Group, Chicago, IL, USA) (60 min; room temperature), washed with PBS, and incubated in 4′,6-diamidino-2-phenylindole (DAPI) for 3 min, followed by a washing with PBS. Microscopy was performed with a Leica TCS SP2 AOBS confocal microscope (Leica Micro-Systems, Heidelberg, Germany) using an excitation wavelength of 488 nm from an Argon laser and an emission spectra between 520 and 570 nm. Collection parameters remained constant for all samples.

Statistical analyses

All data were expressed as the mean±SD. Statistical analyses were carried out using SPSS 11.5 software for Windows. Statistical significance was evaluated by one-way ANOVA, and the statistical significance between two groups was evaluated by *t*-test. Values of $P<0.05$ were considered statistically significant.

Results

VEGF improves histopathologic changes in UUO mice

After ureteral ligation, mice developed hydronephrosis with progressive dilation of the renal pelvis and thinning of the renal cortex. Serum creatinine and blood urea nitrogen levels remained unchanged at all time points (data not shown). From d 3 to 14, renal tubular damage after UUO increased progressively and was characterized by dilation with flattened epithelium at d 3, atrophy and thickness of the tubular basement membrane at d 7 and destruction of tubules at d 14. In parallel, a progressive expansion of the interstitial space and fibrosis gradually developed, as revealed by Masson trichrome staining (Figure 1). There was no difference in tubulointerstitial fibrosis between the UUO group and the VEGF-treated group at d 14 ($P>0.05$). Meanwhile, the tubulointerstitial fibrosis score was reduced by approximately 8% at d 3 and 18% at d 7 in the VEGF-treated group compared with 15%±1% at d 3

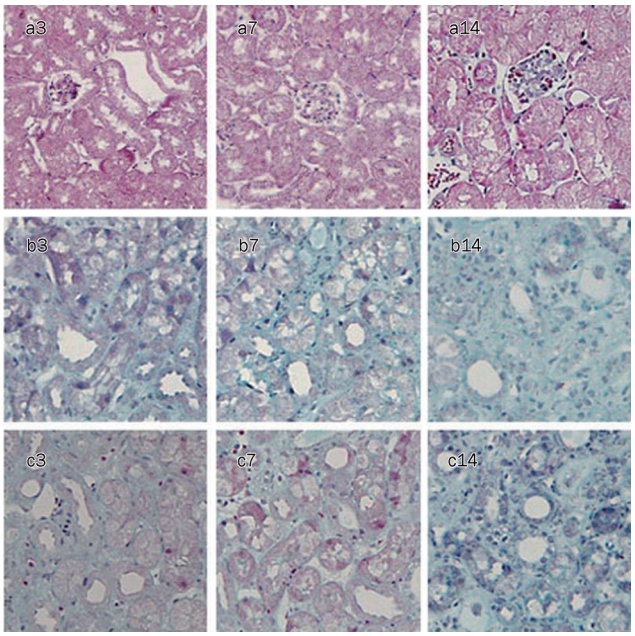

Figure 1. Representative histopathology in sham mice (a), UUO mice (b) and VEGF-treated mice (c) at d 3, 7, and 14, respectively (Masson stain, ×400). D 3 after ligation, few fibrosis appeared in interstitial space. D 7 and 14 after ligation, moderate and severe fibrosis took place, respectively.

and 36%±3% at d 7 in the UUO group (P<0.05, Figure 2).

VEGF inhibits α-SMA expression and restores E-cadherin expression in UUO mice

EMT is an important event in renal interstitial fibrosis. During the process of EMT, epithelial cells lose their polygonal morphology and adhesive cell contacts (E-cadherin) and acquire fibroblast-like characteristics, including an elongated shape, expression of mesenchymal markers (*eg*, α-SMA and vimentin)

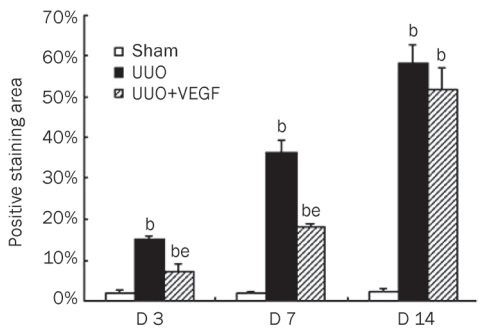

Figure 2. Semiquantitative tubulointerstitial fibrosis score in sham mice, UUO mice and VEGF-treated mice at d 3, 7, and 14, respectively. The fibrosis score was markedly increased in UUO mice compared with sham mice. Compared with UUO mice, the fibrosis score was significantly reduced in VEGF treated mice at d 3 and 7. The values were shown as pecentage of the staining area to selected area and expressed as mean±SD of 3 independent experiments. ^{b}P<0.05 *vs* sham group; ^{e}P<0.05 *vs* UUO group.

and increased motility[20–22]. To investigate the effect of VEGF on EMT in the kidney, α-SMA and E-cadherin protein and mRNA expression levels were determined by Western blot and RT-PCR, respectively, in UUO mice treated with or without VEGF. As shown in Figure 3 and 4, in the UUO group, α-SMA expression was significantly upregulated, whereas E-cadherin expression was significantly downregulated compared with the sham group from d 3 to 14 (P<0.05). VEGF treatment reduced α-SMA expression and improved E-cadherin expression at d 3 and 7 compared with the UUO group (P<0.05). No differences in the expression of α-SMA or E-cadherin were observed between the VEGF-treated and UUO mice at d 14 (P>0.05).

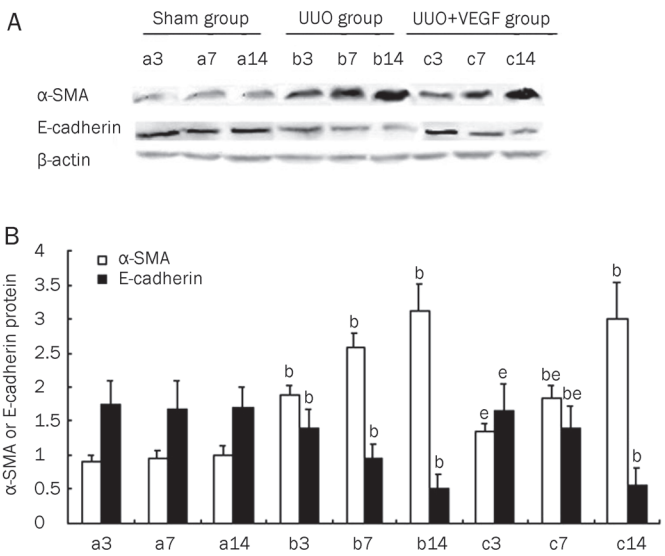

Figure 3. The expressions of α-SMA and E-cadherin protein in sham mice (a), UUO mice (b) and VEGF-treated mice (c) at d 3, 7, and 14, respectively. (A) Representative Western blot of α-SMA and E-cadherin in sham and UUO mice treated with or without VEGF. (B) Compared with UUO group, VEGF treatment significantly inhibited α-SMA expression and increased E-cadherin expression at d 3 and 7. Results were shown as ratio of optical density for α-SMA or E-cadherin to that of β-actin and presented as mean±SD of 3 independent experiments. ^{b}P<0.05 *vs* respective sham mice; ^{e}P<0.05 *vs* respective UUO mice.

VEGF affects the expression of TGF-β1, CTGF, and BMP-7 in UUO mice

Several cytokines, including TGF-β1, CTGF, and BMP-7, are thought to be involved in the pathogenesis of EMT. To examine whether VEGF could modulate the expression of these cytokines, the kidney protein and mRNA levels of TGF-β1, CTGF and BMP-7 were measured in UUO mice treated with or without VEGF. Compared with the sham group, the expression levels of TGF-β1 and CTGF in the UUO group were significantly upregulated, whereas the expression of BMP-7 was significantly downregulated from d 3 to 14 (P<0.05). Importantly, VEGF treatment in the UUO model resulted

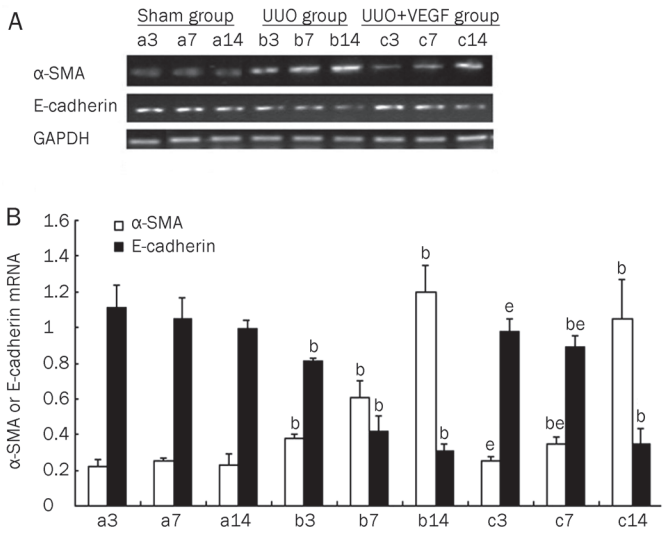

Figure 4. The expressions of α-SMA and E-cadherin mRNA in sham mice (a), UUO mice (b) and VEGF-treated mice (c) at d 3, 7, and 14, respectively. (A) Representative RT-PCR of α-SMA and E-cadherin in sham and UUO mice treated with or without VEGF. (B) Compared with UUO group, VEGF treatment inhibited α-SMA expression and increased E-cadherin expression at d 3 and 7. Results were shown as ratio of optical density for α-SMA or E-cadherin to that of GAPDH and presented as mean±SD of 3 independent experiments. $^{b}P<0.05$ *vs* respective sham mice; $^{e}P<0.05$ *vs* respective UUO mice.

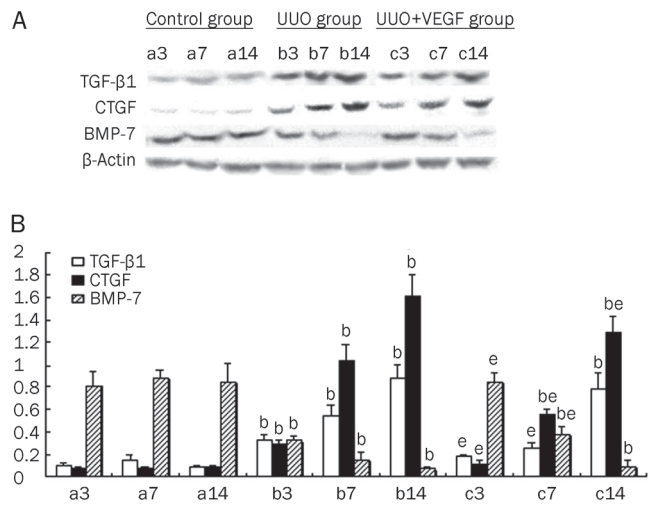

Figure 5. The protein levels of TGF-β1, CTGF and BMP-7 in sham mice (a), UUO mice (b) and VEGF-treated mice (c) at d 3, 7, and 14, respectively. (A) Representative western blot of TGF-β1, CTGF and BMP-7 in sham and UUO mice treated with or without VEGF. (B) Compared with UUO group, VEGF treatment significantly inhibited the expressions of TGF-β1 and CTGF and increased BMP-7 expression. Results were shown as ratio of optical density for TGF-β1, CTGF, or BMP-7 to that of β-actin and presented as mean±SD of 3 independent experiments. $^{b}P<0.05$ *vs* respective sham mice; $^{e}P<0.05$ *vs* respective UUO mice.

in reduced expression of TGF-β1 and CTGF expression and increased BMP-7 expression at d 3 and 7 compared with the untreated UUO group ($P<0.05$). No differences in the expression of TGF-β1 and BMP-7 were observed between the VEGF-treated and untreated UUO mice at d 14 ($P>0.05$). However, VEGF treatment did result in reduced CTGF expression at d 14 ($P<0.05$). Thus, VEGF treatment prevented the production of TGF-β1 and loss of BMP-7 expression at both the mRNA and protein levels at d 3 and d 7, and VEGF treatment inhibited the production of CTGF at d 3, 7, and 14 ($P<0.05$) (Figures 5 and 6).

VEGF inhibits EMT induced by TGF-β1 in cultured HK-2 cells

Confocal microscopy study demonstrated that E-cadherin, a phenotypic marker of epithelial cells, was distributed in the cytoplasm, in the nucleolus and at the cell-cell junctions, whereas α-SMA, a phenotypic marker of mesenchymal cells, was not detected under normal conditions (Figure 7A). The addition of TGF-β1 (5 μg/L) significantly induced α-SMA expression, but inhibited E-cadherin expression (Figure 7B). VEGF (0.1–100 μg/L) treatment restored E-cadherin expression and intercellular junctions and dramatically abrogated TGF-β1-induced α-SMA expression in a dose-dependent manner (Figure 7C).

To further confirm that VEGF blocked TGF-β1-induced EMT in HK-2 cells, we measured the expression of α-SMA, vimentin and E-cadherin in HK-2 cells treated with TGF-β1 (5 μg/L) in the presence or absence of VEGF (0.1–100 μg/L).

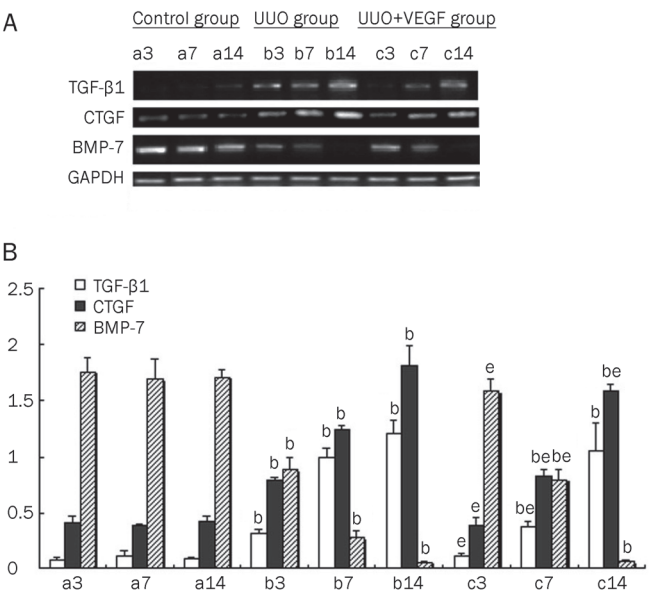

Figure 6. The mRNA levels of TGF-β1, CTGF and BMP-7 in sham mice (a), UUO mice (b) and VEGF-treated mice (c) at d 3, 7, and 14, respectively. (A) Representative RT-PCR of TGF-β1, CTGF, and BMP-7 in sham and UUO mice treated with or without VEGF. (B) Compared with UUO group, VEGF treatment significantly blocked the expressions of TGF-β1 and CTGF and improved expression of BMP-7. Results were shown as ratio of optical density for TGF-β1, CTGF, or BMP-7 to that of GAPDH and presented as mean±SD of 3 independent experiments. $^{b}P<0.05$ *vs* respective sham mice; $^{e}P<0.05$ *vs* respective UUO mice.

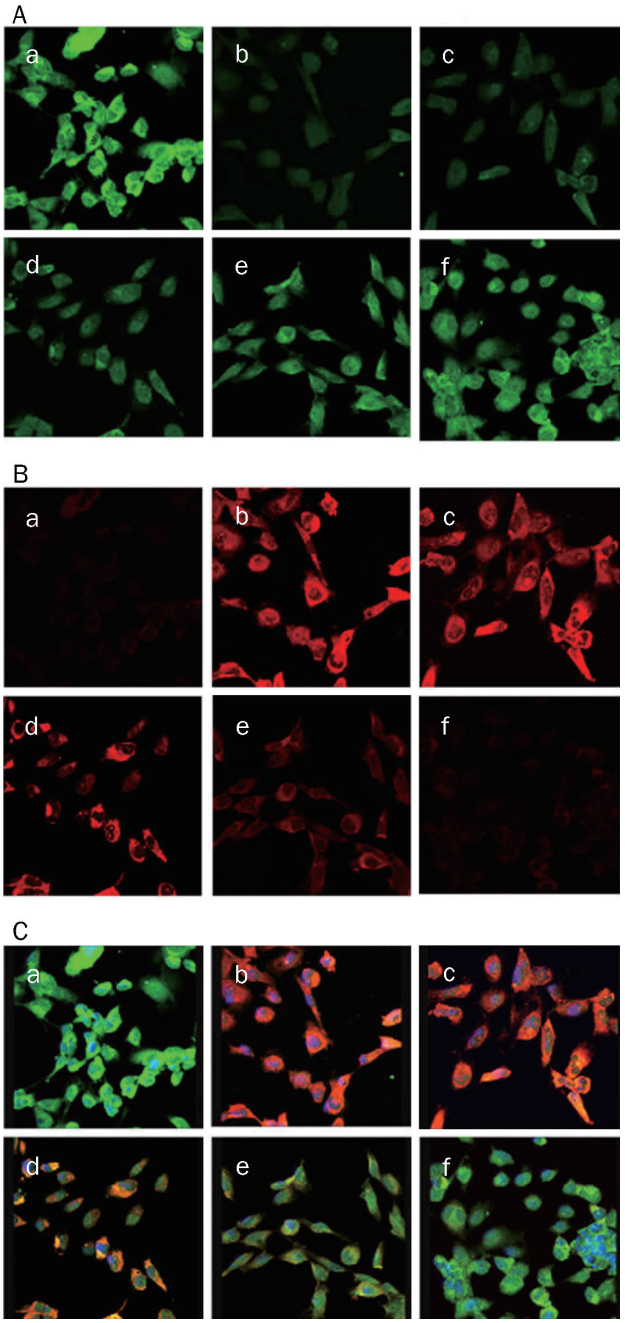

Figure 7. Expressions of E-cadherin and α-SMA in HK-2 cells treated with 5 μg/L TGF-β1 in the presence or absence of VEGF at 0.1–100 μg/L, evaluated by confocal microscopy. The expression of E-cadherin (A) and α-SMA (B) were observed by confocal microscopic image. The colocalization (C) of α-SMA and E-cadherin was stained yellow. a, no treatment; b, 5 μg/L TGF-β1; c, 5 μg/L TGF-β1 and 0.1 μg/L VEGF; d, 5 μg/L TGF-β1 and 1 μg/L VEGF; e, 5 μg/L TGF-β1 and 10 μg/L VEGF; f, 5 μg/L TGF-β1 and 100 μg/L VEGF. ×100.

TGF-β1 alone induced expression of α-SMA and vimentin and inhibited expression of E-cadherin at both the protein and mRNA levels. In contrast, co-treatment with VEGF dramatically abrogated the TGF-β1-induced increases in protein and mRNA expression of α-SMA and vimentin and also restored the protein and mRNA expression of E-cadherin in HK-2 cells in a dose-dependent manner. Moreover, at concentrations of 100 μg/L, VEGF almost completely blocked the TGF-β1-induced changes in α-SMA, vimentin and E-cadherin protein and mRNA expression (P<0.05) (Figures 8 and 9).

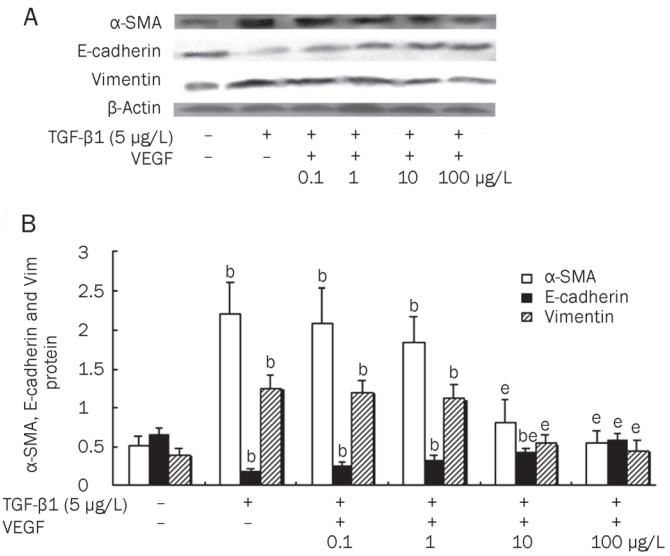

Figure 8. Protein levels of α-SMA, E-cadherin and vimentin in HK-2 cell treated with 5 μg/L TGF-β1 alone, co-treated with 5 μg/L TGF-β1 and VEGF at 0.1–100 μg/L, or untreated for 48 h. (A) Representative Western blot of α-SMA, E-cadherin and vimentin in HK-2 cells. (B) Compared with HK-2 cells treated with TGF-β1 alone, VEGF treatment significantly inhibited the expressions of α-SMA and vimentin and improved the expression of E-cadherin in a dose-dependent manner. Results were shown as ratio of optical density for α-SMA, E-cadherin, or vimentin to that of β-actin and presented as mean±SD of 3 independent experiments. ^{b}P<0.05 *vs* respective HK2 cells untreated; ^{e}P<0.05 *vs* respective HK2 cells treated with 5 μg/L TGF-β1 alone

Discussion

Renal interstitial fibrosis is a common pathological process leading to end-stage renal disease[23]. The UUO model has been widely used as a model of tubulointerstitial fibrosis[24]. The UUO model is characterized by renal myofibroblast activation, tubular atrophy and interstitial fibrosis with minimal glomerular lesions in which TGF-β1 is considered to play an important role[24, 25]. In our study, the obstructed kidneys displayed marked tubulointerstitial injury starting on d 3 after surgery, but glomerular cells remained nearly untouched.

In the present study, the effect of VEGF on tubulointerstitial fibrosis and EMT was tested. Our results from *in vivo* experiments showed that VEGF inhibited tubulointerstitial fibrosis and EMT. The potential mechanisms of VEGF action include inhibition of TGF-β1 and CTGF expression in target cells and the improvement of BMP-7 expression. In addition, we showed that TGF-β1 induced EMT and that VEGF directly

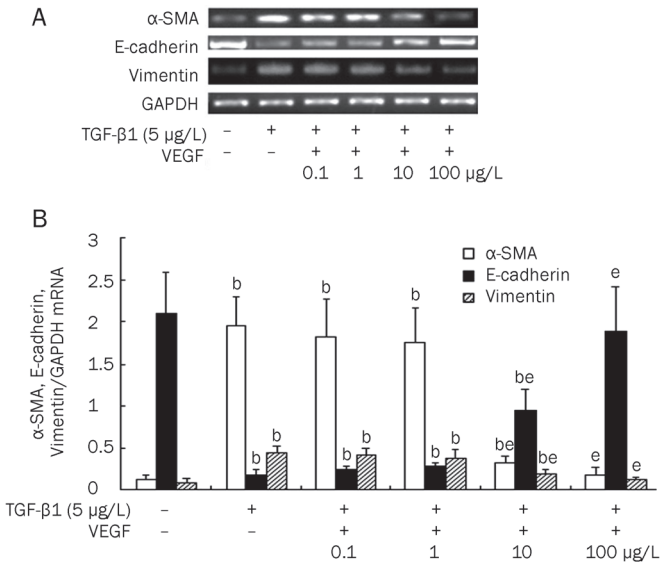

Figure 9. The mRNA levels of α-SMA, E-cadherin and vimentin in HK-2 cell treated with 5 μg/L TGF-β1 in the presence or absence of VEGF at 0.1–100 μg/L for 48 h. (A) Representative RT-PCR of α-SMA, E-cadherin, and vimentin in HK-2 cells. (B) Compared with HK-2 cells treated with TGF-β1 alone, VEGF treatment significantly inhibited the expressions of α-SMA and vimentin and improved the expression of E-cadherin in a dose-dependent manner. Results were shown as ratio of optical density for α-SMA, E-cadherin, or vimentin to that of GAPDH and presented as mean±SD of 3 independent experiments. $^{b}P<0.05$ *vs* respective HK2 cells untreated; $^{e}P<0.05$ *vs* respective HK2 cells treated with 5 μg/L TGF-β1 alone.

inhibited TGF-β1-induced EMT in cultured human renal tubular epithelial cells *in vitro*. Thus, for the first time to our knowledge, we provide evidence that the inhibitory effect of VEGF on tubulointerstitial fibrosis is likely associated with an amelioration of the EMT process.

It is well known that EMT is a novel mechanism involved in renal interstitial fibrosis[26, 27]. In obstructive nephropathy induced by UUO, the tubular epithelial cells lost expression of the epithelial cell marker E-cadherin and acquired mesenchymal features, such as expression of α-SMA and vimentin and production of interstitial matrix components, indicating that they were at a transitional stage between epithelium and mesenchyme[28–30]. In the UUO model, we observed an early induction of α-SMA at d 3 followed by a more robust α-SMA induction at d 7 after surgery. The induction of α-SMA was closely associated with loss of the expression of the epithelial marker E-cadherin. This result is consistent with previous studies[31, 32]. These data suggest that VEGF attenuates α-SMA expression and improves E-cadherin expression on d 3 and 7 after surgery, but fails to function at d 14, indicating that VEGF inhibits EMT during the early stage of injury in the UUO mouse model.

EMT is regulated by many factors and in different ways, with TGF-β1 being the most potent inducer that is capable of initiating and completing the entire EMT course and with BMP-7 acting as an EMT inhibitor both *in vitro* and *in vivo*[33–37]. CTGF can promote EMT both directly and as a downstream mediator of TGF-β1[38]. In our study, VEGF treatment reduced the expression of TGF-β1 and CTGF and upregulated the expression of BMP-7. In accordance with the central role of TGF-β1 and its downstream signaling cascades in the activation of the cellular mechanisms that underlie the progression of EMT[39], VEGF-mediated inhibition of TGF-β1 and CTGF expression would abolish much of their profibrotic effects. Our results demonstrate that VEGF blocked fibrosis and EMT likely through its influence on TGF-β1, CTGF and BMP-7 expression in UUO mice.

VEGF is a survival factor for vascular endothelial cells and plays an important role in the homeostasis of the vascular endothelium in addition to being a survival factor for renal tubular epithelial cells that is involved in renal tubule construction[40–42]. VEGF expression in human and mouse kidney is confined to podocytes and tubular epithelial cells, and renal tubular epithelial cells are an important cellular resource of VEGF in the kidney. There may be intrinsic renoprotective factors that maintain the epithelial phenotype of tubular cells *in vivo*, and loss of these factors may contribute to EMT. VEGF may be a candidate for this type of factor because reduced expression of VEGF has been observed in tubulointerstitial fibrosis[11–13]. Furthermore, it has been reported that depolymerized hyaluronan could inhibit developmental EMT of mouse endocardial cushions by inducing VEGF[43] and that supplementation with VEGF improved cyclosporine-mediated interstitial injury[44]. Therefore, modulation of VEGF expression might be a therapeutic approach for the prevention of progressive renal disease.

In summary, our data provide further *in vivo* and *in vitro* evidence that VEGF may improve tubulointerstitial fibrosis by inhibiting EMT at the early stage of injury. Our findings may have clinical implications for the use of VEGF in patients with early chronic tubulointerstitial injury. It remains to be investigated whether increased dosage of VEGF would be more effective in preventing EMT at later stages of injury.

Acknowledgements

This project was supported by the National Natural Science Foundation of China (No 30570854).

Author contribution

Fa-lei ZHENG designed the research; Yao-guo LIAN performed the research; Fa-lei ZHENG, Yao-guo LIAN, and Ying-juan ZHANG contributed new analytical tools and reagents; Yao-guo LIAN analyzed the data; and Yao-guo LIAN and Qiu-gen ZHOU wrote the paper.

References

1 Kalluri R, Neilson EG. Epithelial-mesenchymal transition and its implications for fibrosis. J Clin Invest 2003; 112: 1776–84.
2 Rastaldi MP. Epithelial-mesenchymal transition and its implications for the development of renal tubulointerstitial fibrosis. J Nephrol 2006; 19: 407–12.

3 Lee JM, Dedhar S, Kalluri R, Thompson EW. The epithelial-mesenchymal transition: new insights in signaling, development, and disease. J Cell Biol 2006; 172: 973–81.
4 Zeisberg M, Hanai J, Sugimoto H, Mammoto T, Charytan D, Strutz F, *et al*. BMP-7 counteracts TGF-beta1-induced epithelial-to-mesenchymal transition and reverses chronic renal injury. Nat Med 2003; 9: 964–8.
5 Xu Y, Wan J, Jiang D, Wu X. BMP-7 counteracts TGF-beta1-induced epithelial-to mesenchymal transition in human renal proximal tubular epithelial cells. J Nephrol 2009; 22: 403–10.
6 Schrijvers BF, Flyvbjerg A, De Vriese AS. The role of vascular endothelial growth factor (VEGF) in renal pathophysiology. Kidney Int 2004; 65: 2003–17.
7 Ferrara N. Role of vascular endothelial growth factor in the regulation of angiogenesis. Kidney Int 1999; 56: 794–814.
8 Wada Y, Morioka T, Oyanagi-Tanaka Y, Yao J, Suzuki Y, Gejyo F, *et al*. Impairment of vascular regeneration precedes progressive glomerulosclerosis in anti-Thy1 glomerulonephritis. Kidney Int 2002; 61: 432–43.
9 Kim YG, Suga SI, Kang DH, Jefferson JA, Mazzali M, Gordon KL, *et al*. Vascular endothelial growth factor accelerates renal recovery in experimental thrombotic microangiopathy. Kidney Int 2000; 58: 2390–9.
10 Shimizu A, Masuda Y, Mori T, Kitamura H, Ishizaki M, Sugisaki Y, *et al*. Vascular endothelial growth factor165 resolves glomerular inflammation and accelerates glomerular capillary repair in rat anti-glomerular basement membrane glomerulonephritis. J Am Soc Nephrol 2004; 15: 2655–65.
11 Song YR, You SJ, Lee YM, Chin HJ, Chae DW, Oh YK, *et al*. Activation of hypoxia-inducible factor attenuates renal injury in rat remnant kidney. Nephrol Dial Transplant 2010; 25: 77–85.
12 Sun D, Feng J, Dai C, Sun L, Jin T, Ma J, *et al*. Role of peritubular capillary loss and hypoxia in progressive tubulointerstitial fibrosis in a rat model of aristolochic acid nephropathy. Am J Nephrol 2006; 26: 363–71.
13 Burt LE, Forbes MS, Thornhill BA, Kiley SC, Chevalier RL. Renal vascular endothelial growth factor in neonatal obstructive nephropathy. I. Endogenous VEGF. Am J Physiol Renal Physiol 2007; 292: F158–67.
14 Kang DH, Hughes J, Mazzali M, Schreiner GF, Johnson RJ. Impaired angiogenesis in the remnant kidney model: II. Vascular endothelial growth factor administration reduces renal fibrosis and stabilizes renal function. J Am Soc Nephrol 2001; 12: 1448–57.
15 Turo A, Norwood VF, Carey RM, Gomez RA. Vascular endothelial growth factor induces nephrogenesis and vasculogenesis. J Am Soc Nephrol 1999; 10: 2125–34.
16 Villegas G, Lange-Sperandio B, Tufro A. Autocrine and paracrine functions of vascular endothelial growth factor (VEGF) in renal tubular epithelial cells. Kidney Int 2005; 67: 449–57.
17 Kanellis J, Fraser S, Katerelos M, Power DA. Vascular endothelial growth factor is a survival factor for renal tubular epithelial cells. Am J Physiol Renal Physiol 2000; 278: F905–15.
18 Zhou QG, Zheng FL, Hou FF. Inhibition of tubulointerstitial fibrosis by pentoxifylline is associated with improvement of vascular endothelial growth factor expression. Acta Pharmacol Sin 2009; 30: 98–106.
19 Zhou QG, Zheng FL, Wen YB, Tan XY, Duan L, Li Y. Altered expression of vascular endothelial growth factor and its receptors in trans-differentiated human proximal tubular epithelial cells induced by transforming growth factor beta1. Zhongguo Yi Xue Ke Xue Yuan Xue Bao 2005; 27: 325–31.
20 Bakin AV, Tomlinson AK, Bhowmick NA, Moses HL, Arteaga CL. Phosphatidylinositol 3-kinase function is required for transforming growth factor β-mediated epithelial to mesenchymal transition and cell migration. J Biol Chem 2000; 275: 36803–10.
21 Fan JM, Ng YY, Hill PA, Nikolic-Paterson DJ, Mu W, Atkins RC, *et al*. Transforming growth factor-β regulates tubular epithelial-myofibroblast transdifferentiation *in vitro*. Kidney Int 1999; 56: 1455–67.
22 Bozic M, de Rooij J, Parisi E, Ortega MR, Fernandez E, Valdivielso JM. Glutamatergic signaling maintains the epithelial phenotype of proximal tubular cells. J Am Soc Nephrol 2011; 22: 1099–111.
23 Isaka Y, Takahara S, Imai E. Chronic deteriorating renal function and renal fibrosis. Contrib Nephrol 2008; 159: 109–21.
24 Chevalier RL. Molecular and cellular pathophysiology of obstructive nephropathy. Pediatr Nephrol 1999; 13: 612–9.
25 Klahr S, Morrissey J. Obstructive nephropathy and renal fibrosis. Am J Physiol Renal Physiol 2002; 283: F861–75.
26 Liu Y. New insights into epithelial-mesenchymal transition in kidney fibrosis. J Am Soc Nephrol 2010; 21: 212–22.
27 Liu YH. Epithelial to mesenchymal transition in renal fibrogenesis: pathologic significance, molecular mechanism, and therapeutic intervention. J Am Soc Nephrol 2004; 15: 1–12.
28 Yang J, Liu Y. Dissection of key events in tubular epithelial to myofibroblast transition and its implications in renal interstitial fibrosis. Am J Pathol 2001; 159: 1465–75.
29 Yang J, Liu Y. Blockage of tubular epithelial to myofibroblast transition by hepatocyte growth factor prevents renal interstitial fibrosis. J Am Soc Nephrol 2002; 13: 96–107.
30 Iwano M, Plieth D, Danoff TM, Xue C, Okada H, Neilson EG. Evidence that fibroblasts derive from epithelium during tissue fibrosis. J Clin Invest 2002; 110: 341–50.
31 Yang J, Dai C, Liu Y. Hepatocyte growth factor gene therapy and angiotensin II blockade synergistically attenuate renal interstitial fibrosis in mice. J Am Soc Nephrol 2002; 13: 2464–77.
32 Yang J, Shultz RW, Mars WM, Wegner RE, Li Y, Dai C, *et al*. Disruption of tissue-type plasminogen activator gene in mice reduces renal interstitial fibrosis in obstructive nephropathy. J Clin Invest 2002; 110: 1525–38.
33 Bottinger EP, Bitzer M. TGF-β signaling in renal disease. J Am Soc Nephrol 2002; 13: 2600–10.
34 Chaudhuri V, Zhou L, Karasek M. Inflammatory cytokines induce the transformation of human dermal microvascular endothelial cells into myofibroblasts: a potential role in skin fibrogenesis. J Cutan Pathol 2007; 34: 146–53.
35 Wahab NA, Mason RM. A critical look at growth factors and epithelial-to-mesenchymal transition in the adult kidney. Nephron Exp Nephrol 2006; 104: e129–34.
36 Morrissey J, Hruska K, Guo G, Wang S, Chen Q, Klahr S. Bone morphogenetic protein-7 improves renal fibrosis and accelerates the return of renal function. J Am Soc Nephrol 2002; 13: S14–21.
37 Nguyen TQ, Goldschmeding R. Bone morphogenetic protein-7 and connective tissue growth factor: novel targets for treatment of renal fibrosis? Pharm Res 2008; 25: 2416–26.
38 Zhang C, Meng X, Zhu Z, Liu J, Deng A. Connective tissue growth factor regulates the key events in tubular epithelial to myofibroblast transition *in vitro*. Cell Biol Int 2004; 28: 863–73.
39 Wendt MK, Allington TM, Schiemann WP. Mechanisms of the epithelial-mesenchymal transition by TGF-beta. Future Oncol 2009; 5: 1145–68.
40 Karihaloo A, Karumanchi SA, Cantley WL, Venkatesha S, Cantley LG, Kale S. Vascular endothelial growth factor induces branching morphogenesis/tubulogenesis in renal epithelial cells in a neuropilin-dependent fashion. Mol Cell Biol 2005; 25: 7441–8.

41 Kang DH, Joly AH, Oh SW, Hugo C, Kerjaschki D, Gordon KL, *et al*. Impaired angiogenesis in the remnant kidney model: I. Potential role of vascular endothelial growth factor and thrombospondin-1. J Am Soc Nephrol 2001; 12: 1434–47.

42 Katavetin P, Miyata T, Inagi R, Tanaka T, Sassa R, Ingelfinger JR, *et al*. High glucose blunts vascular endothelial growth factor response to hypoxia via the oxidative stress-regulated hypoxia-inducible factor/hypoxia-responsible element pathway. J Am Soc Nephrol 2006; 17: 1405–13.

43 Rodgers LS, Lalani S, Hardy KM, Xiang X, Broka D, Antin PB, *et al*. Depolymerized hyaluronan induces vascular endothelial growth factor, a negative regulator of developmental epithelial-to-mesenchymal transformation. Circ Res 2006; 99: 583–9.

44 Kang DH, Kim YG, Andoh TF, Gordon KL, Suga S, Mazzali M, *et al*. Post-cyclosporine-mediated hypertension and nephropathy: amelioration by vascular endothelial growth factor. Am J Physiol Renal Physiol 2001; 280: F727–36.

Acta Pharmacologica Sinica (2011) 32: 1522–1528
 1671-4083/11 $32.00
www.nature.com/aps

Original Article

Specific survivin dual fluorescence resonance energy transfer molecular beacons for detection of human bladder cancer cells

Zhi-qiang WANG[1, #], Jun ZHAO[2, #], Jin ZENG[1], Kai-jie WU[1], Yu-le CHEN[1], Xin-yang WANG[1, 3], Luke S CHANG[1, 3], Da-lin HE[1, 3, *]

[1]Department of Urology, the First Affiliated Hospital of the Medical School of Xi-an Jiaotong University, Xi-an 710061, China; [2]Department of Urology, the Affiliated Hospital of Qingdao University Medical College, Qingdao 266003, China; [3]Oncological Research Lab, Key Laboratory of Environment and Genes Related to Diseases, Ministry of Education, Xi-an Jiaotong University School of Medicine, Xi-an 710061, China

Aim: Survivin molecular beacons can be used to detect bladder cancer cells in urine samples non-invasively. The aim of this study is to improve the specificity of detection of bladder cancer cells using survivin dual fluorescence resonance energy transfer molecular beacons (FRET MBs) that have fluorophores forming one donor-acceptor pair.
Methods: Survivin-targeting dual fluorescence resonance energy transfer molecular beacons with unique target sequences were designed, which had no overlap with the other genes in the apoptosis inhibitor protein family. Human bladder cancer cell lines 5637, 253J and T24, as well as the exfoliated cells in the urine of healthy adults and patients with bladder cancer were examined. Images of cells were taken using a laser scanning confocal fluorescence microscope. For assays using dual FRET MBs, the excitation wavelength was 488 nm, and the emission detection wavelengths were 520±20 nm and 560±20 nm, respectively.
Results: The human bladder cancer cell lines and exfoliated cells in the urine of patients with bladder cancer incubated with the survivin dual FRET MBs exhibited strong fluorescence signals. In contrast, no fluorescence was detected in the survivin-negative human dermal fibroblasts-adult (HDF-a) cells or exfoliated cells in the urine of healthy adults incubated with the survivin dual FRET MBs.
Conclusion: The results suggest that the survivin dual FRET MBs may be used as a specific and non-invasive method for early detection and follow-up of patients with bladder cancer.

Keywords: molecular beacons; fluorescence resonance energy transfer; survivin; human bladder cancer

Acta Pharmacologica Sinica (2011) 32: 1522–1528; doi: 10.1038/aps.2011.122; published online 24 Oct 2011

Introduction

Urinary bladder cancer (BCa) is a common malignancy[1, 2], with the highest recurrence rate of all cancers. The recurrence rate ranges from 50% to 70% and the progression rate to muscle-invasive disease from 10% to 15%[3]. Early detection of BCa and its recurrence is essential for improved prognosis and long-term survival[4]. Therefore, much research has been directed toward identifying the best possible non-invasive, urine-based assays for detection, surveillance and prediction of recurrence and/or progression[4, 5]. However, urine markers have not been used in early detection or screening for BCa to date[6].

Previous studies showed that survivin molecular beacons (MBs) provided a sensitive and convenient method to detect BCa cells in urine samples[7, 8]. However, conventional MBs can be degraded by nucleases or opened by nucleic acid binding proteins, leading to false positive signals[9]. Here, we tried to improve the specificity of detection of BCa using survivin dual fluorescence resonance energy transfer (FRET) MBs whose fluorophores formed one donor-acceptor pair. Each MB pair used sequences complementary to adjacent regions on the same oligonucleotide target so that FRET occurred only when both beacons were hybridized to the target (Figure 1). The dual FRET MBs have been used successfully for mRNA detection in living cells and for monitoring changes in mRNA levels and mRNA cell localization[10, 11]. However, this approach requires a complex permeabilization method for

# These authors contributed equally to the work.
* To whom correspondence should be addressed.
E-mail dalinhexjtu@126.com
Received 2011-04-10 Accepted 2011-08-09

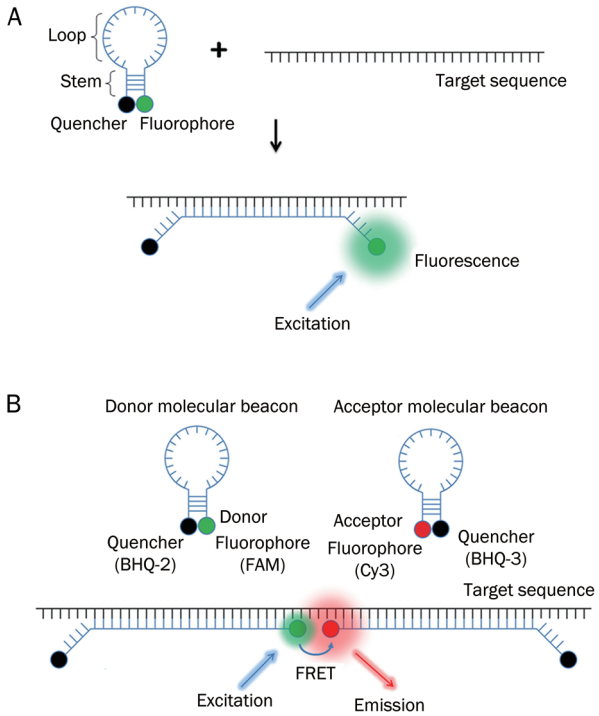

Figure 1. A schematic illustration showing the working mechanism of an MB and a dual FRET MB. (A) The MB adopts a stem-loop structure and thus holds the fluorophore (green) and quencher (black) in close proximity. As a result, the fluorescence emission of the fluorophore is strongly suppressed (in the absence of a target). The target sequence hybridizes with the loop domain of the MB and forces the stem helix to open, whereupon fluorescence is restored because of the spatial separation of the fluorophore from the quencher. (B) Hybridization of donor and acceptor MBs to adjacent regions on the same mRNA target results in FRET between donor fluorophores (FAM, excitation at 490 nm and emission at 520 nm) and acceptor fluorophores (Cy3, excitation at 550 nm and emission at 570 nm) upon donor excitation (490 nm). Because only the donor fluorophore is directly excited, the emission detected from the acceptor fluorophore is due to FRET.

cellular delivery and thus has been hard to popularize in clinical practice[11]. In our previous study, we showed that fixing cells with ice-cold acetone was a simple, effective method to use with MBs[8, 12]. In this study, we aimed to use this simple method to determine whether dual FRET MBs could be used to detect survivin mRNA in BCa cells, which might lay the foundation for clinical applications.

Materials and methods

Survivin dual FRET MBs: design and synthesis

The survivin-targeting MBs were designed so that the target sequences were unique, having no overlap with other genes in the inhibitor of apoptosis protein (IAP) family[11]. As shown in Table 1, we designed two pairs of dual FRET MBs (complementary to target sequences) and one pair of random dual MBs (non-complementary to target sequences). The probe lengths of survivin-targeting donor and acceptor MBs were 15 and 16 bases, respectively. The 'random' beacons had a probe length of 16 bases. All MBs had the shared-stem design, with a stem length of five bases; they had an unmodified oligonucleotide backbone. The survivin MBs and random beacons were synthesized by Invitrogen (Shanghai, China). All of the synthetic targets were synthesized by Sangon Biological Engineering Technology (Shanghai, China).

Solution assays of probe-target hybridization

All solution studies of the probe-target hybridizations were carried out in PBS without calcium and magnesium. After incubation of the probes and targets at 37 °C for 60 min, fluorescence intensity was measured by time-resolved fluorescence spectroscopy (QM4, PTI, Inc, Birmingham, NJ, USA), with 515 nm Cy3 (donor fluorophore) second peak excitation and 530–800 nm emission wavelength detection, and 490 nm FAM (donor fluorophore) excitation and 500–650 nm emission wavelength detection. Concentrations of 200 nmol/L donor, 200 nmol/L acceptor MBs and 200 nmol/L targets were used in a total volume of 2 mL.

Cell culture and glass coverslip preparation

The human BCa cell line 5637 (obtained from ATCC) was maintained at 37 °C, 5% CO_2 in RPMI-1640 (ScienCell Laboratory, USA) medium supplemented with 10% fetal bovine serum (FBS). The human BCa cell lines 253J and T24 (obtained from ATCC) were maintained at 37 °C, 5% CO_2 in Dulbecco's

Table 1. Target sequences and the design of molecular beacons.

Gene	Sequences
Survivin	Target: 5′-ATGGGTGCCCCGACGTTGCCCCCTGCC **TGGCAGCCCTTTCTC** aagg **ACCACCGCATCTCTAC** ATTCAAGAACTGGCCC-3′
	Donor MB: 5′-/Cy3/GAGAAAGGGCTGCCATTCTC/BHQ-2/-3′
	Acceptor MB: 5′-/BHQ-3/ACCACGTAGAGATGCGGTGGT/Cy5/-3′
	Donor MB: 5′-/FAM/GAGAAAGGGCTGCCATTCTC/BHQ-2/-3′
	Acceptor MB: 5′-/BHQ-3/ACCACGTAGAGATGCGGTGGT/Cy3/-3′
Random	Target: 5′-ATCGGTGCGCTTGTCG-3′
	Donor MB: 5′-/Cy3/CACGTCGACAAGCGCACCGATACGTG/BHQ-2/-3′
	Acceptor MB: 5′-/BHQ-3/ACGTGCGACAAGCGCACCGATCACGT/Cy5/-3′

Molecular beacon (MB): underlined bases, bases added to create the stem domain. Target: lowercase bold, bases between two target sequences of the donor and acceptor beacon[11].

modified Eagle medium (DMEM, ScienCell Laboratory, USA) supplemented with 10% FBS. Normal human dermal fibroblasts-adult (HDF-a, ScienCell Laboratory, USA) were grown in fibroblast medium (ScienCell Laboratory, USA) supplemented with 2% FBS, fibroblast growth supplement and penicillin/streptomycin solution. The 5637, 253J, T24, and HDF-a cells were cultured on glass coverslips for 24–48 h. The coverslips, which had cells adhering to them, were then fixed with ice-cold acetone for 5 to 10 min, air-dried and incubated with survivin dual FRET MBs (concentrations of 200 nmol/L donor and 200 nmol/L acceptor MBs) at 37 °C for 60 min in a dark, humid chamber before being examined by laser scanning confocal fluorescence microscopy or fluorescence microscopy.

Western blot analysis

Western blot analysis was performed as previously described[13]. Human BCa cell lines and HDF-a cells were washed with cold PBS twice; then, total cellular protein lysates were prepared with RIPA buffer [50 mmol/L Tris (pH 8.0), 150 mmol/L NaCl, 0.1% SDS, 1% NP40 and 0.5% sodium deoxycholate] containing proteinase inhibitors (1% protease inhibitor cocktail and 1 mmol/L phenylmethanesulfonyl fluoride, both from Sigma, St Louis, MO, USA). A total of 30 μg of protein was separated by 12% SDS-PAGE and transferred to nitrocellulose membranes. The membranes were blocked at room temperature for 1 h with 5% milk in Tris-buffered saline with 0.1% Tween-20 (pH 7.6, TBST). The membranes were incubated with primary antibodies (anti-survivin antibody, Santa Cruz, USA, sc-17779, 1:500 dilution) at room temperature for 2 h. After being washed with TBST, membranes were incubated with secondary antibodies coupled to horseradish peroxidase at room temperature for 1 h and visualized with an ECL chemiluminescence detection system (Pierce, Rockford, IL, USA). Loading differences were normalized using a monoclonal GAPDH antibody.

Urine sample collection and assay

Exfoliated cells were obtained from 50 mL of the second morning voiding of urine from patients with BCa and from healthy adults. Urine samples were processed immediately after collection. After centrifugation for 10 min (2500×*g*), the sediment was resuspended in PBS and placed on glass slides with cytospin. The glass slides with adherent cells were fixed with pre-chilled acetone for 5 to 10 min, air-dried and incubated with survivin dual FRET MBs (concentrations of 200 nmol/L donor and 200 nmol/L acceptor MBs) at 37 °C for 60 min in a dark, humid chamber and then examined with an Olympus fluorescence microscope (Model BX51, Olympus Optical, Tokyo, Japan). Fluorescence images were analyzed using Image-Pro 6.3 software (Media Cybernetics, Inc, USA). The BCa cell line 5637 and HDF-a were used as positive and negative controls, respectively.

The study was approved by the Ethics Committee of Xi-an Jiaotong University, and each patient gave written informed consent prior to the study.

Fluorescence microscopy images

Images of cells on glass coverslips were obtained using an Olympus laser scanning confocal fluorescence microscope (FluoView FV1000, Olympus Optical, Tokyo, Japan). For assays using dual FRET MBs, the excitation wavelength was 488 nm, and the emission detection wavelengths were 520±20 nm (FAM donor fluorescence emission wavelength) and 560±20 nm (Cy3 acceptor fluorescence emission wavelength), respectively. The signal-to-background ratios were then measured by an Olympus Fluoview Ver.1.6a Viewer (Olympus Optical, Tokyo, Japan).

Fluorescence images were acquired using an Olympus fluorescence microscope. The excitation filter range was 470–490 nm, and the emission filter range was 580 nm long-pass interference filters (IF). The signal-to-background ratios were measured using Image-Pro 6.3 software at the same instrument settings used for acquisition.

Statistical analysis

All statistical analyses were performed using SPSS 15.0 (SPSS Inc, Chicago, IL, USA). Quantitative data are presented as the mean±SE. The differences in signal-to-background ratios of different combinations of cells and MBs were compared by one-way ANOVA, followed by Dunnett's *t* test for separate comparisons. Values of $P<0.05$ were considered statistically significant.

Results

Solution studies of FRET signal and specificity

In-solution probe-target hybridization studies were carried out to determine the specificity of dual FRET MBs and the pair of dual MBs that had the better FRET effect. As shown in Figure 2A, Cy3-Cy5 dual FRET MBs and different MBs were detected with synthetic survivin targets. These results implied that even when a large amount of a single (donor or acceptor) MB was present, the resulting fluorescence at the FRET detection wavelength of 665 nm (purple curve) was still much lower than the FRET signal when both were present (blue curve). The FAM-Cy3 dual FRET MB pair had the same fluorescence signal at 515 nm and 565 nm (blue curve), which implied a higher FRET efficiency than the Cy3-Cy5 dual FRET MB pair (Figure 2B). Thus, the FAM-Cy3 dual FRET MB pair was chosen for further studies.

Western blot analysis of survivin protein expression

Western blot analyses were performed to detect the protein level of survivin in human BCa cell lines and HDF-a cells. Using GAPDH as the loading control, we found that survivin was expressed in human BCa cell lines (5637, 253J, and T24 cells) but was not expressed in HDF-a cells (Figure 2C).

Survivin mRNA detection in BCa cells

Our previous study showed that survivin mRNA could be detected in a BCa cell line using survivin MBs[7, 8]. The HDF-a cells were used as a negative control because they do not

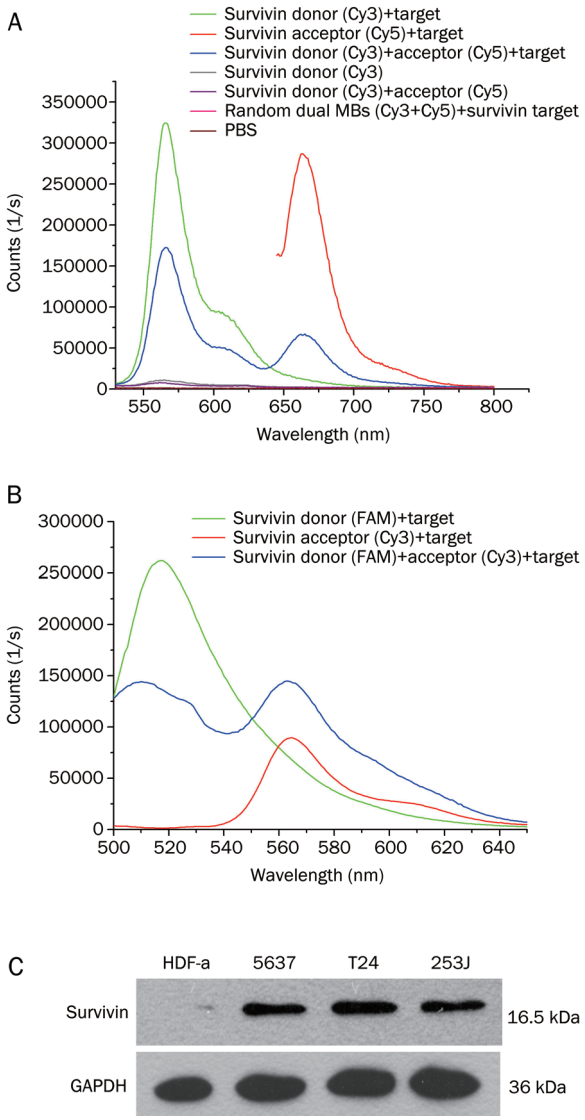

Figure 2. (A) Solution studies of probe-target hybridization of dual FRET MBs. Fluorescence emission spectra of the Cy3 donor and Cy5 acceptor. The green curve was generated from the MB donor in the presence of the target (515 nm excitation, Cy3 second peak excitation). The red curve was generated from the MB acceptor in the presence of the target (645 nm excitation, Cy5 excitation). The blue curve was generated from both donor and acceptor MBs in the presence of the target (515 nm excitation). The gray curve was generated from the MB donor in the absence of the target (515 nm excitation). The purple curve was generated from both donor and acceptor MBs in the absence of the target (515 nm excitation). The pink curve was generated from random dual MBs in the presence of the survivin target (515 nm excitation). The wine-colored curve was generated from PBS. (B) Solution studies of probe-target hybridization of dual FRET MBs. Fluorescence emission spectra of the FAM donor and the Cy3 acceptor under FAM excitation at 490 nm. The green curve was generated from the MB donor in the presence of the target. The red curve was generated from the MB acceptor in the presence of the target. The blue curve was generated from both donor and acceptor MBs in the presence of the target. (C) Western blot analyses of survivin protein expression in BCa cell lines (5637, T24, and 253J) and the normal cell line, HDF-a. GAPDH was the loading control.

express survivin mRNA[11, 12]. In this study, survivin dual FRET MBs, the donor and acceptor beacons, were delivered into 5637 cells and HDF-a cells, respectively. Figure 3A shows the laser scanning confocal fluorescence microscopy images of 5637 cells and HDF-a cells irradiated with 488 nm (the FAM donor fluorescence excitation wavelength). In cells incubated only with survivin dual FRET MBs, the 5637 cells exhibited much stronger fluorescence at 560±20 nm (the Cy3 acceptor fluorescence emission wavelength) than at 520±20 nm (the FAM donor fluorescence emission wavelength), indicating an excellent FRET efficiency. At the same time, almost no fluorescence was detected in HDF-a cells incubated with survivin dual FRET MBs, and only weak fluorescence was detected in 5637 cells incubated with donor beacon and acceptor beacon, respectively.

Because laser scanning confocal fluorescence microscopy is expensive and is not routinely used in clinical settings, we also tried to detect FRET signals using ordinary fluorescence microscopy. The excitation filter range was 470–490 nm, and the emission filter range was 580 nm long-pass IF. As shown in Figure 3B, almost no fluorescence signal was detected in HDF-a cells incubated with dual FRET MBs or in 5637 cells incubated with donor MBs and acceptor MBs, respectively. The signal-to-background ratios of HDF-a cells and 5637 cells incubated with donor MBs or acceptor MBs were 1.1, 1.5, and 1.2, respectively, but obvious fluorescence signal was detected in 5637 cells incubated with dual FRET MBs, with a signal-to-background ratio of 5.8 (Figure 3D). These results demonstrated that ordinary fluorescence microscopy could be used for the detection of survivin mRNA in BCa cells using dual FRET MBs.

Using ordinary fluorescence microscopy, we also evaluated FRET signals in other BCa cell lines (253J and T24) and in exfoliated cells from the urine of healthy adults and patients with BCa. As shown in Figure 4, significant fluorescence was detected in 253J and T24 cells and in exfoliated cells from the urine of patients with BCa; however, fluorescence was not detected in exfoliated cells from the urine of healthy adults.

Discussion

Currently, cystoscopy and cytology remain the gold standard for BCa detection and follow-up. However, conventional cystoscopy is invasive, expensive, and time-consuming. Moreover, several complications can occur after cystoscopy. Additionally, cystoscopy is associated with patient discomfort and is thus refused in some cases[6]. Although urinary cytology has been accepted as the most reliable technique for the monitoring of non-invasive BCa, it lacks adequate sensitivity, particularly for the detection of the low-grade tumors[6, 14]. The development of new non-invasive methods of detection for tumor markers that can reliably predict the presence of a tumor would be clinically important in terms of disease management, quality of life and care cost. However, none of the currently available diagnostic markers can replace cystoscopy[6].

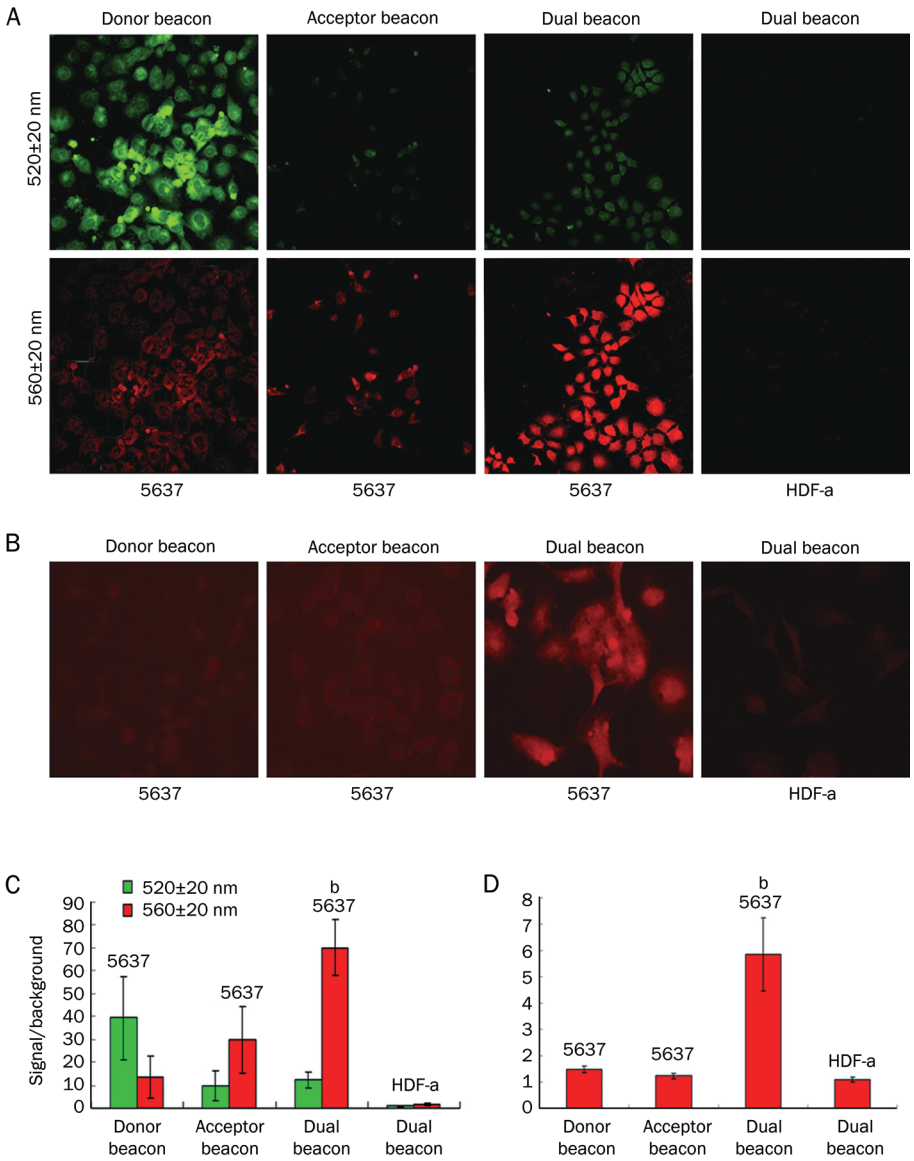

Figure 3. Survivin mRNA detection in BCa cells incubated with survivin dual FRET MBs. (A) At the same excitation wavelength (488 nm), laser scanning confocal fluorescence microscopy images of 5637 cells incubated with the different MBs and HDF-a cells incubated with survivin dual FRET MBs. The fluorescence emission wavelengths were 520±20 nm and 560±20 nm, respectively (magnification×200). (B) The fluorescence microscopy images of 5637 cells incubated with different MBs and HDF-a cells incubated with survivin dual FRET MBs. The excitation filter range was 470-490 nm and the emission filter range was 580 nm long-pass IF (magnification×200). (C) The signal-to-background ratio of laser scanning confocal fluorescence microscopy images of 5637 cells and HDF-a cells. At an emission wavelength of 560±20 nm, the 5637 cells incubated with dual FRET MBs gave a much better signal-to-background ratio than other groups ($^bP<0.05$). (D) The signal-to-background ratios of fluorescence microscopy images of 5637 cells and HDF-a cells. The 5637 cells incubated with FRET MBs gave a much better signal-to-background ratio than other groups ($^bP<0.05$).

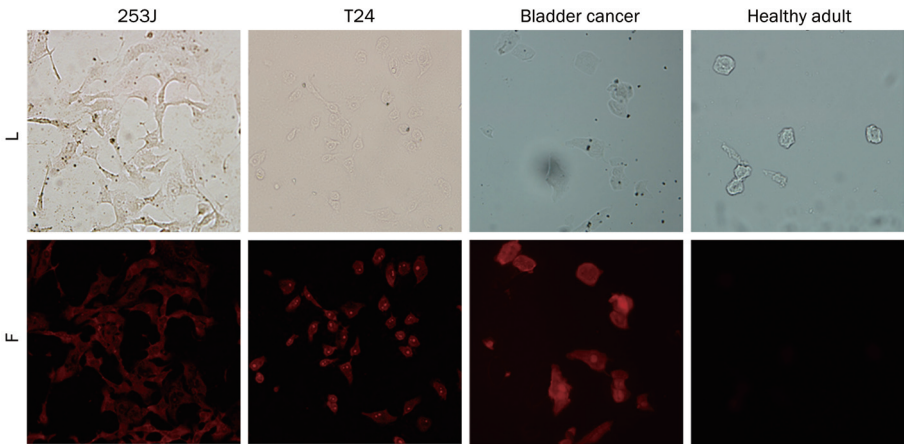

Figure 4. Survivin mRNA detection in BCa cell lines and exfoliated cells in urine from patients with BCa and healthy adults using fluorescence microscopy. Significant fluorescence signal was detected in 253J and T24 cells, and exfoliated cells from the urine of patients with BCa but not in exfoliated cells from the urine of healthy adults. L=light field, F=red fluorescence field (magnification×200).

Survivin, a member of the IAP family, has significantly higher expression in urothelial tumors than in normal tissue[15]. Survivin mRNA in the urine of patients with BCa has been considered to be a potentially useful urinary marker with diagnostic value[16, 17].

Our previous studies applied survivin MBs to detect BCa cells in urine samples, and they showed that MBs are sensitive and simple to use. Although our results held great promise for the diagnosis and follow-up of patients with BCa[7, 8], the specificity of the survivin MBs was inadequate, and a number of patients with nonurothelial tumors tested positive with the MB assay[7, 8]. This was partly due to the degradation of conventional MBs by nucleases and to the MBs being opened by nucleic acid binding proteins, which led to false positive signals[9]. As a result of the low background in the dual FRET MB approach[11], improved detection specificity compared with MBs was achieved. Thus, we designed and synthesized survivin dual FRET MBs to reduce false positive signals while maintaining the advantages of convenience and speed.

The FRET probe pair consisted of two MBs, one labeled with a donor fluorophore (donor beacon) and a second labeled with an acceptor fluorophore (acceptor beacon). These MBs were designed to hybridize to adjacent regions on an mRNA target so that the two fluorophores would lie within the FRET range (about 6 nm) when probe/target binding occurred for both beacons. Excitation of the donor fluorophore would then result in fluorescence emission at a wavelength characteristic of the acceptor fluorophore and a positive FRET signal readily differentiable from non-FRET false positive signals that might result from probe degradation and non-specific probe opening[11].

In this study, we investigated the possibility of using survivin dual FRET MBs in the diagnosis of BCa. Because the higher A/T ratio adjacent to the survivin MB target sequence that we previously chose[8] is unsuitable for the formation of the stems of the dual FRET MBs, we chose another survivin target sequence, which was unique and had no overlap with other genes in the IAP family[11]. The assays of survivin dual FRET MB probe-target hybridization in solution indicated that the FRET signal was much higher than the non-FRET signal, and the FAM-Cy3 dual FRET MB pair had a higher FRET efficiency than Cy3-Cy5 dual FRET MB pair (Figure 2). This was due to the larger overlap between the emission spectrum of FAM (donor fluorophore) and the excitation spectrum of Cy3 (acceptor fluorophore), which allowed a more efficient energy transfer than with the Cy3-Cy5 pair[18]. Thus, in our subsequent studies, FAM and Cy3 were used as the donor and acceptor fluorophores, respectively.

The human BCa cell line 5637, which has been reported to have moderate expression of survivin[7, 8, 19], was used in our previous study[7, 8] and in the present investigation. The laser scanning confocal fluorescence microscopy images (Figure 3) show that the emission at 560±20 nm (the Cy3 acceptor fluorescence emission wavelength) results in a stronger fluorescence signal than the emission at 520±20 nm (the FAM donor fluorescence emission wavelength), indicating the excellent specificity of the dual FRET MBs.

Laser scanning confocal fluorescence microscopy is expensive and is not routinely used in clinical settings compared with fluorescence microscopy. Based on the widespread use and availability of fluorescence microscopy in clinical settings, we investigated the possibility of using dual MBs to detect BCa with a fluorescence microscope. The fluorescence signal could only be detected in BCa cells incubated with dual FRET MBs. To the best of our knowledge, this is the first report of the detection of BCa using dual FRET MBs with either confocal fluorescence microscopy or ordinary fluorescence microscopy. Additionally, a much better signal-to-background ratio was obtained with the dual FRET MBs than with the conventional MBs, indicating a high level of specificity of the dual FRET MBs. Similar effects were also observed with lung cancer, breast cancer, gastric cancer and cervical cancer cell lines (unpublished data), suggesting the potential use of dual FRET MBs in the detection of many different cancers. Moreover, the time required for survivin dual FRET MB detection was 2–3 h in our study. This clearly demonstrates that the dual FRET MB approach is easy to perform and is specific for the detection of survivin mRNA levels in BCa cells.

In conclusion, this study demonstrates that survivin dual FRET MBs provide a simple, fast and non-invasive approach with excellent specificity for the detection of survivin mRNA in BCa cells. The use of dual FRET MBs for the detection of survivin mRNA in urinary exfoliated cells from patients with BCa is under investigation.

Acknowledgements

We thank Prof Xiao-hong FANG from the Institute of Chemistry, Chinese Academy of Sciences, for her helpful support. This work was supported by the National Natural Science Foundation of China (No 30672102).

Author contribution

Zhi-qiang WANG, Jun ZHAO, Luke S CHANG, and Da-lin HE designed the research; Zhi-qiang WANG, Jun ZHAO, Xin-yang WANG, Jin ZENG, Kai-jie WU, and Yu-le CHEN performed the research; Zhi-qiang WANG, Jun ZHAO, and Jin ZENG analyzed the data; and Zhi-qiang WANG and Jin ZENG wrote the paper.

References

1 Jemal A, Siegel R, Ward E, Hao Y, Xu J, Thun MJ. Cancer statistics, 2009. CA Cancer J Clin 2009; 59: 225–49.
2 Sasaki T, Horikawa M, Orikasa K, Sato M, Arai Y, Mitachi Y, *et al*. Possible relationship between the risk of Japanese bladder cancer cases and the CYP4B1 genotype. Jpn J Clin Oncol 2008; 38: 634–40.
3 Tsui KH, Juang HH, Lee TH, Chang PL, Chen CL, Yung BY. Association of nucleophosmin/B23 with bladder cancer recurrence based on immunohistochemical assessment in clinical samples. Acta Pharmacol Sin 2008; 29: 364–70.
4 Van Tilborg AA, Bangma CH, Zwarthoff EC. Bladder cancer biomarkers and their role in surveillance and screening. Int J Urol 2009; 16: 23–30.
5 Schultz IJ, Witjes JA, Swinkels DW, de Kok JB. Bladder cancer

diagnosis and recurrence prognosis: comparison of markers with emphasis on survivin. Clin Chim Acta 2006; 368: 20–32.
6 Van Rhijn BW. Considerations on the use of urine markers for bladder cancer. Eur Urol 2008; 53: 880–1.
7 Zhao J, He D, He H, Li L, Zhang LL, Wang XY. Primary application study in early diagnosis of bladder cancer by survivin molecular beacons. Urology 2007; 70: 60–4.
8 Zhao J, Wang ZQ, Wang XY, Yang XJ, He D. Preliminary study of diagnostic utility of molecular beacons in bladder cancer. Urology 2010; 76: 512–8.
9 Chen AK, Behlke MA, Tsourkas A. Avoiding false-positive signals with nuclease-vulnerable molecular beacons in single living cells. Nucleic Acids Res 2007; 35: e105.
10 Krusinski T, Ozyhar A, Dobryszycki P. Dual FRET assay for detecting receptor protein interaction with DNA. Nucleic Acids Res 2010; 38: e108.
11 Santangelo PJ, Nix B, Tsourkas A, Bao G. Dual FRET molecular beacons for mRNA detection in living cells. Nucleic Acids Res 2004; 32: e57.
12 Yang L, Cao Z, Lin Y, Wood WC, Staley CA. Molecular beacon imaging of tumor marker gene expression in pancreatic cancer cells. Cancer Biol Ther 2005; 4: 561–70.
13 Wu KJ, Zeng J, Zhu GD, Zhang LL, Zhang D, Li L, *et al*. Silibinin inhibits prostate cancer invasion, motility and migration by suppressing vimentin and MMP-2 expression. Acta Pharmacol Sin 2009; 30: 1162–8.
14 Lekili M, Sener E, Demir MA, Temeltas G, Muezzinoglu T, Buyuksu C. Comparison of the nuclear matrix protein 22 with voided urine cytology in the diagnosis of transitional cell carcinoma of the bladder. Urol Res 2004; 32: 124–8.
15 Liu L, Zhang M, Zou P. Expression of PLK1 and survivin in non-Hodgkin's lymphoma treated with CHOP. Acta Pharmacol Sin 2008; 29: 371–5.
16 Vrooman OP, Witjes JA. Urinary markers in bladder cancer. Eur Urol 2008; 53: 909–16.
17 Weikert S, Christoph F, Schrader M, Krause H, Miller K, Muller M. Quantitative analysis of survivin mRNA expression in urine and tumor tissue of bladder cancer patients and its potential relevance for disease detection and prognosis. Int J Cancer 2005; 116: 100–4.
18 Wang Y, Wang N. FRET and mechanobiology. Integr Biol (Camb) 2009; 1: 565–73.
19 Ning S, Fuessel S, Kotzsch M, Kraemer K, Kappler M, Schmidt U, *et al*. siRNA-mediated down-regulation of survivin inhibits bladder cancer cell growth. Int J Oncol 2004; 25: 1065–71.

Acta Pharmacologica Sinica (2011) 32: 1529–1536
 1671-4083/11 $32.00
www.nature.com/aps

Original Article

Crocetin induces cytotoxicity and enhances vincristine-induced cancer cell death via p53-dependent and -independent mechanisms

Ying-jia ZHONG[1, 2], Fang SHI[1], Xue-lian ZHENG[1], Qiong WANG[1], Lan YANG[1], Hong SUN[1], Fan HE[1], Lin ZHANG[1], Yong LIN[1], Yong QIN[3], Lin-chuan LIAO[2, *], Xia WANG[1, *]

[1]Laboratory of Molecular and Translational Medicine, Key Laboratory of Obstetric, Gynecologic and Pediatric Diseases and Birth Defects of the Ministry of Education, West China Second University Hospital, Sichuan University, Chengdu 610041, China; [2]Department of Forensic Analytical Toxicology, West China School of Preclinical and Forensic Medicine, Sichuan University, Chengdu 610041, China; [3]Department of Chemistry of Medicinal Natural Products, Key Laboratory of Drug Targeting and Novel Delivery System of the Ministry of Education, West China School of Pharmacy, Sichuan University, Chengdu 610041, China

Aim: To investigate the anticancer effect of crocetin, a major ingredient in saffron, and its underlying mechanisms.
Methods: Cervical cancer cell line HeLa, non-small cell lung cancer cell line A549 and ovarian cancer cell line SKOV3 were treated with crocetin alone or in combination with vincristine. Cell proliferation was examined using MTT assay. Cell cycle distribution and sub-G_1 fraction were analyzed using flow cytometric analysis after propidium iodide staining. Apoptosis was detected using the Annexin V-FITC Apoptosis Detection Kit with flow cytometry. Cell death was measured based on the release of lactate dehydrogenase (LDH). The expression levels of p53 and $p21^{WAF1/Cip1}$ as well as caspase activation were examined using Western blot analysis.
Results: Treatment of the 3 types of cancer cells with crocetin (60–240 μmol/L) for 48 h significantly inhibited their proliferation in a concentration-dependent manner. Crocetin (240 μmol/L) significantly induced cell cycle arrest through p53-dependent and -independent mechanisms accompanied with $p21^{WAF1/Cip1}$ induction. Crocetin (120–240 μmol/L) caused cytotoxicity in the 3 types of cancer cells by enhancing apoptosis in a time-dependent manner. In the 3 types of cancer cells, crocetin (60 μmol/L) significantly enhanced the cytotoxicity induced by vincristine (1 μmol/L). Furthermore, this synergistic effect was also detected in the vincristine-resistant breast cancer cell line MCF-7/VCR.
Conclusion: Ccrocetin is a potential anticancer agent, which may be used as a chemotherapeutic drug or as a chemosensitizer for vincristine.

Keywords: crocetin; vincristine; cell cycle; apoptosis; p53; neoplasm

Acta Pharmacologica Sinica (2011) 32: 1529–1536; doi: 10.1038/aps.2011.109; published online 10 Oct 2011

Introduction

Saffron, which is the flower of *Crocus sativus* L, is an important dietary ingredient in India and other tropical countries. In addition to its use as a spice and a food colorant, saffron is administered as an analgesic and cardioprotective agent, as well as in treatment of various mental illnesses in traditional Indian medicine. Crocetin (8, 8′-diapo-8, 8′-carotenoic acid), which is the major ingredient of saffron that is responsible for its coloring property, is a low-molecular-weight carotenoid compound characterized by a diterpenic and symmetrical structure with seven double bonds and four methyl groups. This compound exhibits antioxidant[1, 2], antihyperlipidemic[3], antiatherosclerotic[4, 5], cardioprotective[6], hepatoprotective[7], and neuroprotective effects[8] *in vitro* and *in vivo*. Therefore, crocetin exhibits favorable effects in the prevention or treatment of a variety of diseases such as dyslipidemia, atherosclerosis, myocardial ischemia, hemorrhagic shock and arthritis[9].

In recent years, considerable effort has been made to identify new chemotherapeutic or chemopreventive agents for cancer. Naturally occurring compounds in food or medicinal plants are ideal candidates for new anticancer agents because they are generally safe and are associated with low toxicity. Crocetin causes cell growth inhibition or induces cell death in several

* To whom correspondence should be addressed.
E-mail xiawang@scu.edu.cn (Xia WANG);
linchuanliao@scu.edu.cn (Lin-chuan LIAO)
Received 2011-02-16 Accepted 2011-07-13

malignant cells including human rhabdomyosarcoma (RD) cells[10], pancreatic cancer cells[11], and breast cancer cells[12] in *in vitro* studies. In the pancreatic cancer xenograft mouse model, significant regression in tumor growth with inhibition of proliferation and enhanced apoptosis was observed in crocetin-treated animals compared with the control animals[11]. In addition, crocetin inhibits 12-*O*-tetradecanoylphorbol-13-acetate (TPA)-induced skin tumors in the tobacco-specific carcinogen benzo(a)pyrene [B(a)P] initiated mice[13] and exhibits protective effects against B(a)P-induced lung carcinogenesis[14]. Collectively, these studies provide evidence of the antitumor activity of crocetin.

Saffron is expensive and has limited availability. To avoid high costs of saffron, Prof Yong QIN's laboratory (Sichuan University, China) has successfully synthesized crocetin using total synthesis. Given the importance of crocetin as a potential anticancer agent, the present study was designed to examine the effect of crocetin on several types of human cancer cells. Crocetin inhibited cell proliferation by inducing cell cycle arrest in cancer cells that were derived from the cervix (HeLa), ovary (SKOV3), and lung (A549) through p53-dependent and -independent mechanisms. Crocetin induced cytotoxicity in these cancer cells by enhancing apoptosis in a time-dependent manner. In the present study, we demonstrated that crocetin significantly sensitized these cancer cells to vincristine-induced cell death and that the synergistic effect was detected in a vincristine-resistant breast cancer cell line. Altogether, this study suggests that crocetin is a potential chemopreventive agent and a potential anticancer agent that can be used as a chemotherapeutic drug or a chemosensitizer for vincristine.

Materials and methods

Reagents

Crocetin was kindly provided by Prof Yong QIN's laboratory (Sichuan University, Chengdu, China). Vincristine (VCR), propidium iodide (PI), and MTT (3-(4,5-dimethylthiazolyl-2)-2,5-diphenyltetrazolium bromide) were purchased from Sigma (St Louis, MO, USA). The pan-caspase inhibitor Z-VAD-FMK was purchased from Calbiochem (La Jolla, CA, USA). Antibodies against active caspase-3, poly(ADP-ribose) polymerase (PARP) were purchased from BD Biosciences (San Diego, CA, USA). Anti-caspase-9 and anti-p53 were purchased from Cell Signaling (Beverly, MA, USA). Anti-β-actin was purchased from Proteintech (Chicago, IL, USA). Anti-$p21^{WAF1/Cip1}$ was purchased from Santa Cruz Biotechnology (Santa Cruz, CA, USA).

Cell culture

The cervical cancer cell line HeLa, non-small cell lung cancer cell line A549, and ovarian cancer cell line SKOV3 were purchased from the American Type Culture Collection (ATCC, Manassas, VA, USA). These cells were grown in RPMI-1640 or DMEM supplemented with 10% fetal bovine serum (FBS), 1 mmol/L glutamate, 100 units/mL penicillin, and 100 μg/mL streptomycin and cultured in an incubator (37°C, 5% CO_2). The vincristine-resistant mammary cancer cell line MCF-7/VCR was obtained from the Immunology Department at the West China School of Preclinical and Forensic Medicine at Sichuan University. MCF-7/VCR cells are cross-resistant to doxorubicin and were grown in RPMI-1640 containing 10% FBS and 1 μmol/L vincristine under standard conditions. The cells were cultured in the absence of vincristine one week before performing experiments.

MTT assay

Cell proliferation was measured by MTT assays as previously described[15]. Briefly, cells were treated with different doses of crocetin for 48 h. Treated cells were incubated with MTT for approximately 3 h, rinsed two times with phosphate buffered saline (PBS), and dissolved with DMSO. The absorbance of the samples was measured at 570 nm using a plate reader. All the experiments were repeated three times, and the averaged result is shown in each figure.

Flow cytometric analysis

Flow cytometry was used to analyze the cell cycle distribution. After being treated as indicated in each figure legend, the cells were trypsinized, washed once with PBS, and fixed in 70% ethanol on ice for 1 h. Fixed cells were resuspended in PBS containing RNase (100 μg/mL) at 37 °C for 30 min. After digestion of cellular RNA, the cells were stained with propidium iodide (PI) staining solution (0.2% FBS and 25 μg/mL PI in PBS) at room temperature for 1 h in the dark. The stained cells were analyzed using a FAScan flow cytometer (Beckman Coulter Cell). To assess apoptosis, HeLa cells were treated with crocetin as indicated in each figure legend and double stained with Annexin V-FITC and PI using the Annexin V-FITC Apoptosis Detection Kit (Nanjing KeyGen Biotech, Nanjing, China) followed by flow cytometric analysis. Early apoptosis was defined by Annexin V^+/PI^- staining (Q4), and late apoptosis was defined by Annexin V^+/PI^+ staining (Q2).

Cell death assay

After each designated treatment, cell death was detected based on the release of lactate dehydrogenase (LDH) using a cytotoxicity detection kit (Promega, Madison, WI, USA) as previously described[16]. All of the experiments were repeated three to five times, and the averaged result is shown in each figure.

Western blot analysis

Cell lysate was collected by lysing cells in M2 lysis buffer [20 mmol/L Tris-HCl (pH 7.6), 0.5% NP40, 250 mmol/L NaCl, 3 mmol/L EDTA, 3 mmol/L EGTA, 2 mmol/L DTT, 0.5 mmol/L phenylmethylsulfonyl fluoride, 20 mmol/L β-glycerophosphate, 1 mmol/L sodium vanadate, and 1 μg/mL leupeptin]. Cell extracts were subjected to SDS-PAGE and analyzed by Western blot. The proteins were visualized by enhanced chemiluminescence (Millipore, Billerica, MA, USA) using the BIO-RAD Image station. Each experiment was repeated at least three times, and representative results are shown.

Statistical analysis

The data were represented as the mean±standard deviation (SD) from at least three independent experiments. The 95% confidence limits of the IC_{50} values were calculated. Comparisons between groups were performed by paired Student's *t* test using the SPSS statistics software package (IBM SPSS, Chicago, IL, USA). $P<0.05$ was used for statistical significance.

Results

Crocetin inhibits cell proliferation in cancer cells

Crocetin inhibits cell proliferation in pancreatic adenocarcinoma cells and breast cancer cells[11, 12]. We first tested the effect of crocetin on several cancer cell types to determine whether the antiproliferative effect was common in different cancer cell types. We first treated cervical cancer HeLa cells with different doses of crocetin for 48 h. The MTT assay was used to measure viable cells. As shown in Figure 1A, crocetin reduced viable cell numbers in a dose-dependent manner, showing a pronounced effect at the higher concentration, *ie*, with a reduction of viability of approximately 80% at a concentration of 240 μmol/L crocetin. Under these experimental conditions, marginal cell death was observed. The reduction of viable cell numbers detected by the MTT assay was mainly attributed to inhibition of cell proliferation. Similar dose-dependent anti-proliferation effects of crocetin were observed in non-small cell lung cancer A549 cells and ovarian cancer SKOV3 cells (Figure 1B and 1C). The IC_{50} values and 95% confidence limits of crocetin for HeLa, A549, and SKOV3 cells were 119.32 μmol/L (104.24–134.83 μmol/L), 101.34 μmol/L (88.07–117.65 μmol/L), and 119.76 μmol/L (97.14–143.40 μmol/L), respectively. Therefore, these results suggest that crocetin effectively suppresses proliferation in the tested cancer cells.

Crocetin inhibits cancer cell proliferation by inducing cell cycle arrest at the G_1 checkpoint

To investigate the underlying mechanism for crocetin-induced proliferation inhibition, we examined the cell cycle distribution in crocetin-treated cancer cells using flow cytometric analysis based on cellular DNA content. Crocetin significantly increased the number of HeLa cells in the G_1 phase, which was detected at 8 h post crocetin treatment (Figure 2, upper panel). Crocetin-induced G_1 phase distribution was time-dependent, and the percentages of cells in the G_1 phase increased from 33% in untreated HeLa cells to 41% in HeLa cells after 24 h of crocetin treatment. At the same time, the populations of cells in the S or G_2 phases were markedly reduced. Consistent with its effect on HeLa cells, crocetin showed similar effects on the cell cycle of A549 and SKOV3 cells (Figure 2, middle and lower panels). These results indicate that crocetin inhibits cell proliferation by inducing G_1 arrest in cancer cells.

Crocetin induces cell cycle arrest through p53-dependent and -independent mechanisms

p53 regulates the G_1 checkpoint by activating transcription of genes that influence cell-cycle progression, including cyclin-dependent kinase inhibitor $p21^{WAF1/Cip1}$ and GADD45[17]. To explore the role of p53 and its downstream genes in crocetin-induced cell cycle regulation, we detected the expression levels of p53 and $p21^{WAF1/Cip1}$ in crocetin treated cells. As shown in Figure 3A, crocetin induced p53 and $p21^{WAF1/Cip1}$ accumulation in A549 cells, which have functional wild-type p53. Furthermore, crocetin induced the increase of p53 and $p21^{WAF1/Cip1}$ in HeLa cells, which express low basal levels of p53 because p53 is degraded via interactions with the E6 gene product of HPV (Figure 3B). Therefore, crocetin may cause G_1 arrest through p53 and its downstream $p21^{WAF1/Cip1}$. Importantly, the p53-independent pathway may also be involved in cell cycle regulation by crocetin, because crocetin also caused G_1 arrest in SKOV3 cells that have lost p53 expression and function due to a mutation in the p53 gene (Figure 2, lower panel). Crocetin substantially induced $p21^{WAF1/Cip1}$ in SKOV3 cells (Figure 3C). These results indicate that a p53-independent mechanism is involved in upregulation of $p21^{WAF1/Cip1}$, which induces G_1 arrest. Altogether, these results suggest that crocetin regulates cancer cell proliferation through p53-dependent and -independent induction of $p21^{WAF1/Cip1}$.

Crocetin induces cell death by enhancing apoptosis in cancer cells

We further investigated whether crocetin caused cell death in HeLa, A549, and SKOV3 cells after extending the incubation time of drug with the cells. Although marginal cell death was induced by crocetin at early times, significant cell death was detected by the LDH release assay in HeLa cells after crocetin treatment for 72 h (Figure 4A). As shown in Figure 4B, 4C, and 4D, crocetin induced significant cell death in a dose-dependent manner by approximately 40%–50% in all cell lines after treatment with the highest concentration of crocetin. To determine the type of cell death induced by crocetin, HeLa

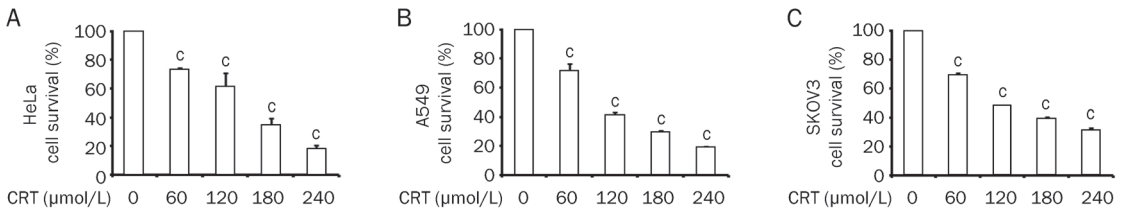

Figure 1. Crocetin (CRT) inhibits cell proliferation in cancer cells. HeLa (A), A549 (B), and SKOV3 cells (C) were treated with different concentrations of crocetin for 48 h. Cell survival was quantitated using MTT assays. $n=3$. Mean±SD. $^cP<0.01$ *vs* control.

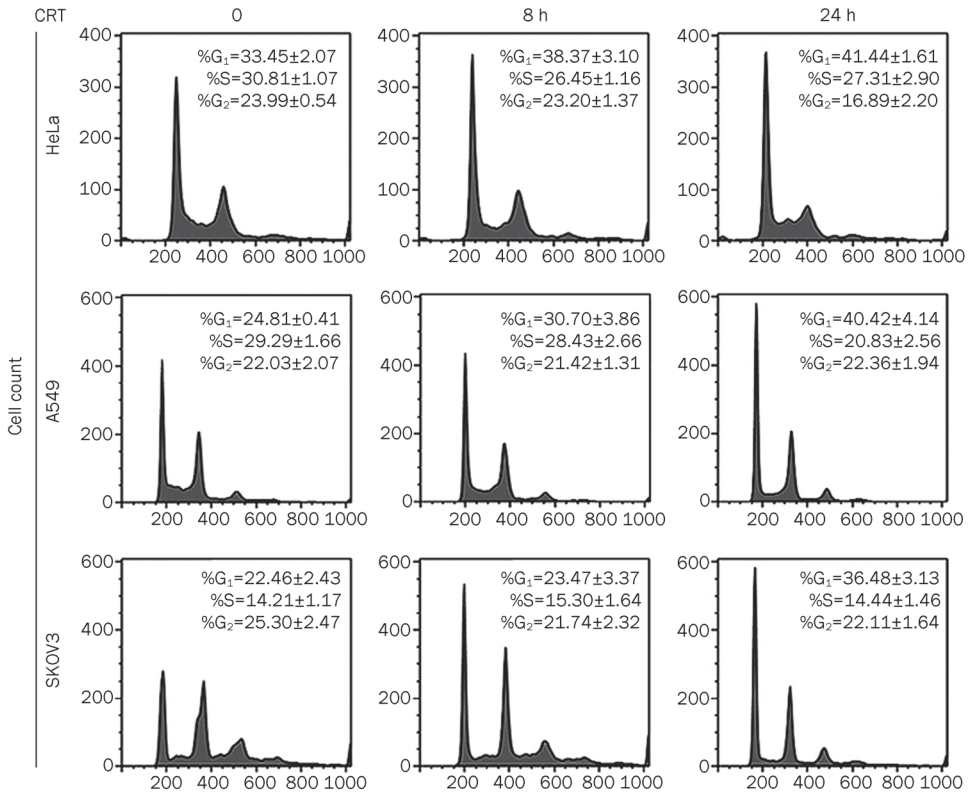

Figure 2. Crocetin induces cell cycle arrest in cancer cells. HeLa, A549, and SKOV3 cells were treated with crocetin (240 μmol/L) for the indicated times. The cells were collected, fixed and stained with PI followed by flow cytometric analysis.

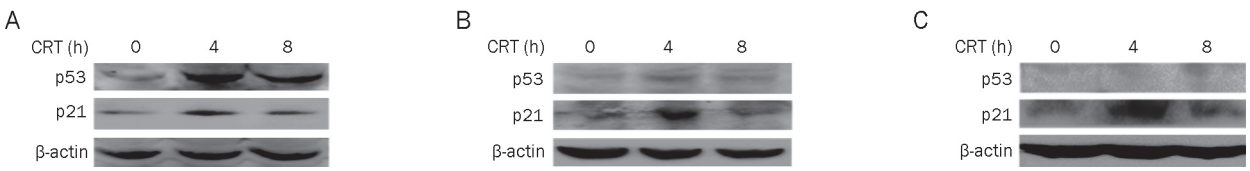

Figure 3. Crocetin induces p53 and p21$^{WAF1/Cip1}$ in cancer cells. HeLa (A), A549 (B), and SKOV3 cells (C) were treated with crocetin (240 μmol/L) for the indicated time. Using Western blot analysis, p53 and p21$^{WAF1/Cip1}$ protein expression were evaluated. β-actin was detected as an input control.

cells were incubated with crocetin for different times as indicated. Floating and attached cells were collected, fixed, and stained with PI. The percentage of cells containing sub-G_1 DNA content, which is a measure of apoptosis, was detected using flow cytometric analysis. Figure 5A shows that crocetin treatment resulted in an increase of sub-G_1 phase in a time-dependent manner, which was most evident at 72 h post-treatment. The crocetin-induced apoptosis was further confirmed using flow cytometry after Annexin V-FITC and PI double staining. Early and late apoptotic cells were increased in a dose-dependent manner in crocetin-treated HeLa cells (Figure 5B). The cell distribution in Q1 (Annexin V^-/PI^+) in samples that were treated with high concentrations of crocetin was slightly increased. These results indicate necrotic and very late apoptotic cell death (Figure 5B) and suggest that the main killing mechanism of crocetin is inducing apoptosis and possibly necrosis. The decrease of pro-caspase 9, which indicates caspase-9 activation, was detected at 24 h post crocetin treatment. Crocetin treatment also markedly triggered caspase-3 activation and PARP cleavage (115 kDa) to generate a 23-kDa fragment, which are hallmarks of apoptosis induction (Figure 5C). These results demonstrate that crocetin treatment activates the caspase cascade to promote apoptosis. Additionally, the pan-caspase inhibitor Z-VAD-FMK effectively suppressed crocetin-induced cytotoxicity in HeLa, A549, and SKOV3 cells (Figure 5D), substantiating that crocetin induced cell death via apoptosis. Collectively, these results suggest that prolonged exposure of crocetin induces cytotoxicity through apoptosis in cancer cells.

Crocetin sensitizes cancer cells to vincristine-induced cytotoxicity

Chemoresistance is a major issue that hinders chemotherapy in the treatment of cancer patients. As a naturally occurring compound, crocetin has been shown to be safe and has low toxicity *in vivo*[11, 18], which indicates a potential role as a chemosensitizing agent. However, the combined effect of crocetin with other conventional chemotherapeutic drugs has never been tested. To address this question, we treated HeLa

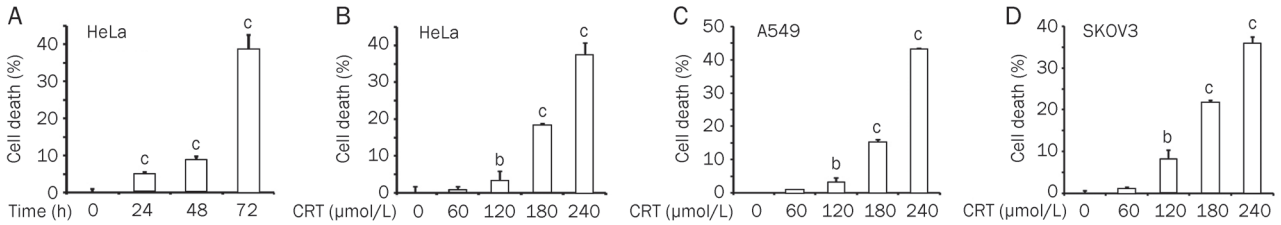

Figure 4. Crocetin induces cytotoxicity in cancer cells in a time-dependent manner. (A) HeLa cells were treated with 240 μmol/L crocetin for the indicated times. Cell death was detected using the LDH assay. HeLa (B), A549 (C), and SK0V3 cells (D) were treated with different concentrations of crocetin for 72 h. Cell death was detected using LDH release assay. Columns, mean of three independent experiments; bars, SD. $^{b}P<0.05$, $^{c}P<0.01$ *vs* control.

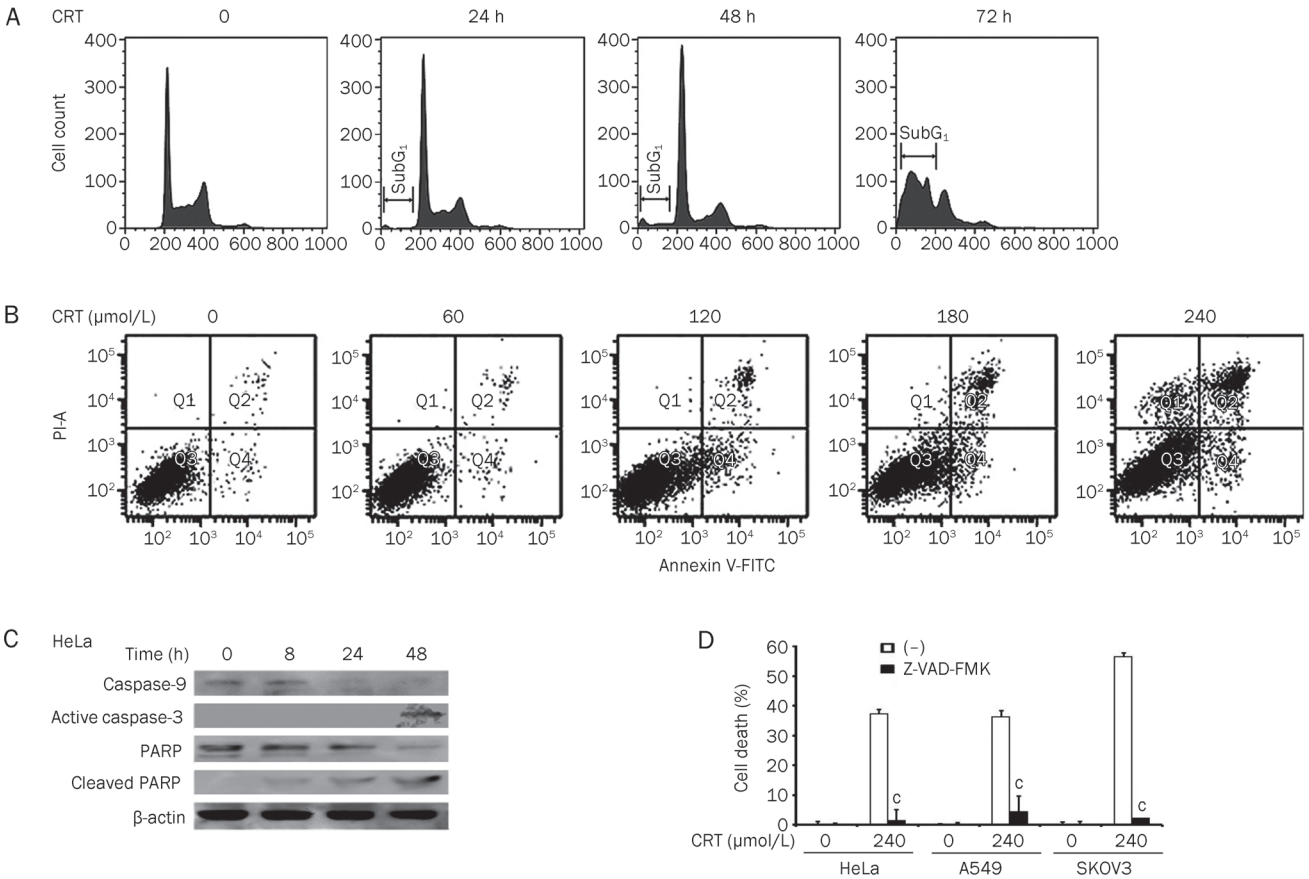

Figure 5. Crocetin induces cytotoxicity by enhancing apoptosis in cancer cells. (A) HeLa cells were treated with crocetin (240 μmol/L) for the indicated time. Floating and attached cells were collected, stained with PI and detected using flow cytometry. (B) HeLa cells were treated with different doses of crocetin for 48 h and stained with Annexin V and PI, followed by flow cytometric analysis. Early apoptosis was defined by Annexin V^+/PI^- staining (Q4), and late apoptosis was defined by Annexin V^+/PI^+ staining (Q2). (C) HeLa cells were treated with crocetin (240 μmol/L) for the indicated times. Caspase-3, -9, and PARP were detected by Western blot. β-actin was used as an input control. (D) HeLa, A549, and SK0V3 cells were pretreated with Z-VAD-FMK (20 μmol/L) for 30 min or left untreated. All cells were treated with crocetin (240 μmol/L) for 72 h. Cell death was measured using the LDH assay. n=3. Mean±SD. $^{c}P<0.01$ *vs* crocetin alone.

cells, A549 cells, and SKOV3 cells with the combination of crocetin and different types of conventional chemotherapeutic drugs. No significant sensitization effects were observed when crocetin was used in combination with cisplatin, carboplatin, etopside, adriamycin, pirarubicin, Taxol, docetaxol, dacarbazine, actinomycin D, or fluorouracil (data not shown). In contrast, simultaneous treatment with crocetin and vincristine synergistically induced cell death (Figure 6A). Notably, the synergistic cytotoxicity was also detected in the vincristine-resistant breast cancer cell line MCF-7/VCR. Although 2 μmol/L vincristine, which is a concentration that kills most of the parental MCF-7 cells, was nontoxic to MCF-7/VCR cells

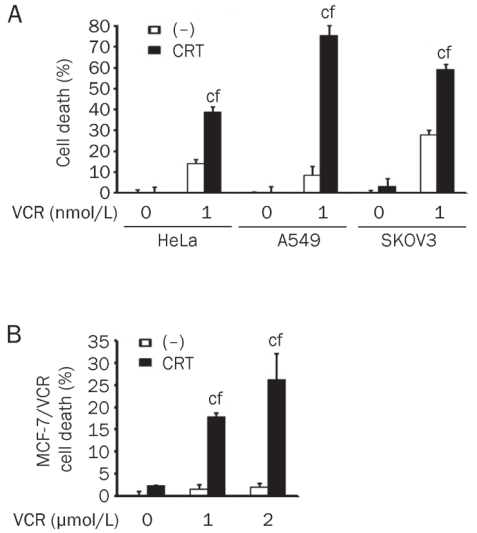

Figure 6. Crocetin sensitizes cancer cells to vincristine-induced cytotoxicity. (A) HeLa, A549, and SKOV3 cells were treated with crocetin (60 μmol/L) or VCR (1 nmol/L) separately or in combination for 72 h. Cell death was detected using the LDH assay. (B) The vincristine-resistant breast cancer cell line (MCF-7/VCR) was treated with crocetin (60 μmol/L) or VCR (1 μmol/L or 2 μmol/L) separately or in combination for 72 h. Cell death was measured using the LDH assay. n=3. Mean±SD. ^{c}P<0.01 *vs* crocetin alone, ^{f}P<0.01 *vs* VCR alone.

(less than 5% of cell death), vincristine in combination with crocetin showed cytotoxicity in approximately 30% of MCF-7/VCR cells (Figure 6B). These results suggest that the combination of crocetin and vincristine would greatly improve the anticancer value of vincristine.

Discussion

In this study, we demonstrated two distinct anticancer functions of crocetin as follows: to inhibit cell proliferation at early time by inducing cell cycle arrest in different human cancer cell types via p53-dependent and -independent $p21^{WAF1/Cip1}$-mediated mechanisms and to kill cancer cells via apoptosis. We demonstrated that crocetin sensitized cancer cells to vincristine-induced cell death. Importantly, crocetin restored vincristine sensitivity in the vincristine-resistant breast cancer cell line MCF-7/VCR. To our knowledge, this is the first report showing the chemosensitizing effect of crocetin on vincristine-induced cytotoxicity in cancer cells. Therefore, our results suggest that crocetin may function as a potential anticancer agent as a chemotherapeutic drug or a chemosensitizer for vincristine.

The molecular mechanism underlying the anticancer property of crocetin remains poorly understood. Crocetin inhibits DNA, RNA, and protein synthesis in malignant cells[14, 19]. Crocetin may also directly interact with DNA and RNA to induce changes in their conformations. Among the three major carotenoids that are derived from saffron (crocin, crocetin, and dimethylcrocetin), crocetin had the highest binding affinity for DNA[20–22]. A previous study has shown that crocetin suppresses TPA-induced expression of oncogenes in the mouse epidermis and inhibits TPA-induced skin carcinogenesis[23]. Another *in vivo* study has shown that crocetin displays antitumor activities in a lung cancer animal model by scavenging free radicals[24].

Because p53 is mutated in approximately 50% of human tumors, we selected three cancer cell lines with different statuses of p53 to study the anticancer effects of crocetin. The results show that crocetin inhibits cell proliferation by inducing G_1 arrest. We demonstrated that crocetin induced cell cycle arrest via p53-dependent and -independent pathways in cancer cell lines with wild type p53 (A549) and mutated p53 (SKOV3). Crocetin slightly increased the p53 expression level in HeLa cells, suggesting that crocetin may partly counteract the p53 suppressive function of the HPV oncogene E6. In turn, p53 induces the expression of downstream $p21^{WAF1/Cip1}$ in HeLa cells to suppress cell proliferation. Further investigation is required to understand how crocetin counteracts the p53-suppressing function of E6. The DNA-damaging agent cisplatin represses virally coded E6 proteins and contributes to the restoration of p53 expression in cisplatin treated HeLa cells[25]. It would be interesting to determine whether crocetin functions to activate p53 through DNA damage. Crocetin-mediated $p21^{WAF1/Cip1}$ induction was detected in the p53-null SKOV3 cells, which have rearrangements in the p53 gene that prevent the production of detectable protein products. These results suggest that crocetin activates $p21^{WAF1/Cip1}$ through a p53-independent mechanism. Consistent with our results, p53-independent induction of $p21^{WAF1/Cip1}$ and concomitant G_1 arrest have been previously reported in malignant cells[26, 27]. The induction of $p21^{WAF1/Cip1}$ may contribute to G_1 arrest in crocetin-treated cancer cells because $p21^{WAF1/Cip1}$ inhibits the activity of cyclin dependent kinases (Cdks) or proliferating cell nuclear antigen (PCNA). Therefore, $p21^{WAF1/Cip1}$ functions as a suppressor of cell cycle progression at the G_1 checkpoint[28, 29]. The roles of cyclins and Cdks in crocetin-induced cell cycle arrest warrant further study.

The MTT assay, which detects viable cells, does not discriminate cell loss that is caused by cell death from that caused by suppression of proliferation. However, the LDH release assay is widely used to detect cell death resulting from apoptosis. Apoptotic cells under tissue culture conditions will eventually leak their cytoplasmic contents because they do not undergo phagocytosis, which occurs *in vivo*. Using the LDH assay and flow cytometric analysis, we showed that prolonged incubation of crocetin killed cancer cells via apoptosis, which was associated with the activation of caspase-9 to initiate the intrinsic apoptosis pathway. Although the exact mechanism for crocetin-induced apoptotic activation requires further investigation, our results demonstrate that induction of apoptosis at least partly contributes to the anticancer activity of crocetin. In addition, crocetin significantly enhanced the anticancer activity of vincristine in cancer cells. The ability of crocetin to restore vincristine sensitivity in the vincristine-resistant cancer cells suggests a potential role as a chemosensitizer for certain anticancer therapeutics such as vincristine. The mechanism

that mediates vincristine-specific sensitization is currently unknown. A vincristine-specific pathway or molecule may be activated in response to crocetin treatment, which enhances the cell killing mechanism of vincristine.

In our study, the IC_{50} values of crocetin on cell proliferation were from 100–120 μmol/L, which are comparable with that from a study by Dhar[11]. Several animal experiments have shown that high doses of crocetin *in vivo* are well-tolerated and relatively nontoxic with a potential to exert anticancer activities[11, 14, 24]. These data indicate the possibility that crocetin may be used at relatively high doses for cancer therapy. The solubility and the bioavailability of crocetin require optimization before being used as an effective anticancer drug. It is also intriguing that the suppression of proliferation and cytotoxic effects of crocetin are not dependent on the p53 status in cancer cells. This advantage is highly relevant because p53 is mutated in approximately 50% of tumors. This study provides novel evidence for the potential use of crocetin as an anticancer agent, which requires further investigation in vivo.

Acknowledgements

This study was supported in part by grants from the National Natural Science Foundation of China (No 30772539 and 30973403), the Young Scientist Fund of Science & Technology Department of Sichuan Province in China (2010JQ0012), the Scientific Research Foundation for the Returned Overseas Chinese Scholar at the State Education Ministry of China, the Program for Changjiang Scholars and the Innovative Research Team in University (IRT0935).

Author contribution

Ying-jia ZHONG performed the research and analyzed data. Fang SHI and Xue-lian ZHENG assisted with cell culture and cell death experiments. Qiong WANG, Lan YANG, Hong SUN, and Fan HE assisted with flow cytometry and Western blot experiments. Lin ZHANG assisted with data analysis. Yong QIN synthesized and provided crocetin. Xia WANG, Yong LIN, and Lin-chuan LIAO designed the research, analyzed data, wrote and revised the manuscript.

References

1 Ordoudi SA, Befani CD, Nenadis N, Koliakos GG, Tsimidou MZ. Further examination of antiradical properties of Crocus sativus stigmas extract rich in crocins. J Agric Food Chem 2009; 57: 3080–6.
2 Kanakis CD, Tarantilis PA, Pappas C, Bariyanga J, Tajmir-Riahi HA, Polissiou MG. An overview of structural features of DNA and RNA complexes with saffron compounds: Models and antioxidant activity. J Photochem Photobiol 2009; 95: 204–12.
3 Lee IA, Lee JH, Baek NI, Kim DH. Antihyperlipidemic effect of crocin isolated from the fructus of *Gardenia jasminoides* and its metabolite Crocetin. Biol Pharm Bull 2005; 28: 2106–10.
4 Zheng S, Qian Z, Tang F, Sheng L. Suppression of vascular cell adhesion molecule-1 expression by crocetin contributes to attenuation of atherosclerosis in hypercholesterolemic rabbits. Biochem Pharmacol 2005; 70: 1192–9.
5 He SY, Qian ZY, Wen N, Tang FT, Xu GL, Zhou CH. Influence of Crocetin on experimental atherosclerosis in hyperlipidamic-diet quails. Eur J Pharmacol 2007; 554: 191–5.
6 Cai J, Yi FF, Bian ZY, *et al*. Crocetin protects against cardiac hypertrophy by blocking MEK-ERK1/2 signalling pathway. J Cell Mol Med 2009; 13: 909–25.
7 Dhar A, Cherian G, Dhar G, Ray G, Sharma R, Banerjee SK. Molecular basis of protective effect by crocetin on survival and liver tissue damage following hemorrhagic shock. Mol Cell Biochem 2005; 278: 139–46.
8 Ahmad AS, Ansari MA, Ahmad M, Saleem S, Yousuf S, Hoda MN, *et al*. Neuroprotection by crocetin in a hemi-parkinsonian rat model. Pharmacology, biochemistry, and behavior 2005; 81: 805–13.
9 Giaccio M. Crocetin from saffron: an active component of an ancient spice. Crit Rev Food Sci Nutr 2004; 44: 155–72.
10 Jagadeeswaran R, Thirunavukkarasu C, Gunasekaran P, Ramamurty N, Sakthisekaran D. *In vitro* studies on the selective cytotoxic effect of crocetin and quercetin. Fitoterapia 2000; 71: 395–9.
11 Dhar A, Mehta S, Dhar G, Dhar K, Banerjee S, Van Veldhuizen P, *et al*. Crocetin inhibits pancreatic cancer cell proliferation and tumor progression in a xenograft mouse model. Mol Cancer Ther 2009; 8: 315–23.
12 Chryssanthi DG, Lamari FN, Iatrou G, Pylara A, Karamanos NK, Cordopatis P. Inhibition of breast cancer cell proliferation by style constituents of different *Crocus* species. Anticancer Res 2007; 27: 357–62.
13 Wang CJ, Lee MJ, Chang MC, Lin JK. Inhibition of tumor promotion in benzo[a]pyrene-initiated CD-1 mouse skin by crocetin. Carcinogenesis 1995; 16: 187–91.
14 Magesh V, DurgaBhavani K, Senthilnathan P, Rajendran P, Sakthisekaran D. *In vivo* protective effect of crocetin on benzo(a) pyrene-induced lung cancer in Swiss albino mice. Phytother Res 2009; 23: 533–9.
15 Chen W, Wang X, Bai L, Liang X, Zhuang J, Lin Y. Blockage of NF-kappaB by IKKbeta- or RelA-siRNA rather than the NF-kappaB super-suppressor IkappaBalpha mutant potentiates adriamycin-–induced cytotoxicity in lung cancer cells. J Cell Biochem 2008; 105: 554–61.
16 Wang X, Ju W, Renouard J, Aden J, Belinsky SA, Lin Y. 17-allylamino-17-demethoxygeldanamycin synergistically potentiates tumor necrosis factor-induced lung cancer cell death by blocking the nuclear factor-kappaB pathway. Cancer Res 2006; 66: 1089–95.
17 Kastan MB, Canman CE, Leonard CJ. P53, cell cycle control and apoptosis: implications for cancer. Cancer Metastasis Rev 1995; 14: 3–15.
18 Abdullaev FI. Cancer chemopreventive and tumoricidal properties of saffron (*Crocus sativus* L). Exp Biol Med (Maywood, NJ 2002; 227: 20–5.
19 Abdullaev FI. Inhibitory effect of crocetin on intracellular nucleic acid and protein synthesis in malignant cells. Toxicol Lett 1994; 70: 243–51.
20 Bathaie SZ, Bolhasani A, Hoshyar R, Ranjbar B, Sabouni F, Moosavi-Movahedi AA. Interaction of saffron carotenoids as anticancer compounds with ctDNA, Oligo (dG.dC)15, and Oligo (dA.dT)15. DNA Cell Biol 2007; 26: 533–40.
21 Kanakis CD, Tarantilis PA, Tajmir-Riahi HA, Polissiou MG. DNA interaction with saffron's secondary metabolites safranal, crocetin, and dimethylcrocetin. DNA Cell Biol 2007; 26: 63–70.
22 Kanakis CD, Tarantilis PA, Tajmir-Riahi HA, Polissiou MG. Interaction of tRNA with Safranal, Crocetin, and Dimethylcrocetin. J Biomol Struct Dyn 2007; 24: 537–46.
23 Hsu JD, Chou FP, Lee MJ, Chiang HC, Lin YL, Shiow SJ, *et al*. Suppression of the TPA-induced expression of nuclear-protooncogenes in mouse epidermis by crocetin via antioxidant activity. Anticancer Res

1999; 19: 4221–7.
24 Magesh V, Singh JP, Selvendiran K, Ekambaram G, Sakthisekaran D. Antitumour activity of crocetin in accordance to tumor incidence, antioxidant status, drug metabolizing enzymes and histopathological studies. Mol Cell Biochem 2006; 287: 127–35.
25 Wesierska–Gadek J, Schloffer D, Kotala V, Horky M. Escape of p53 protein from E6-mediated degradation in HeLa cells after cisplatin therapy. Int J Cancer 2002; 101: 128–36.
26 Lee SJ, Ha MJ, Lee J, Nguyen P, Choi YH, Pirnia F, *et al*. Inhibition of the 3-hydroxy-3-methylglutaryl-coenzyme A reductase pathway induces p53-independent transcriptional regulation of $p21^{WAF1/CIP1}$ in human prostate carcinoma cells. J Biol Chem 1998; 273: 10618–23.
27 Nakano K, Mizuno T, Sowa Y, Orita T, Yoshino T, Okuyama Y, *et al*. Butyrate activates the WAF1/Cip1 gene promoter through Sp1 sites in a p53-negative human colon cancer cell line. J Biol Chem 1997; 272: 22199–206.
28 Aikawa T, Segre GV, Lee K. Fibroblast growth factor inhibits chondrocytic growth through induction of p21 and subsequent inactivation of cyclin E-Cdk2. J Biol Chem 2001; 276: 29347–52.
29 Kelman Z. PCNA: structure, functions and interactions. Oncogene 1997; 14: 629–40.

Acta Pharmacologica Sinica (2011) 32: 1537–1542
 1671-4083/11 $32.00
www.nature.com/aps

Original Article

Identification of serum biomarkers for lung cancer using magnetic bead-based SELDI-TOF-MS

Qi-bin SONG[1, *, #], Wei-guo HU[1, #], Peng WANG[2], Yi YAO[1], Hua-zong ZENG[3, *]

[1]*Department of Oncology, Renmin Hospital of Wuhan University, Wuhan 430060, China;* [2]*Peking Union Medical College Hospital, Beijing 100730, China;* [3]*School of Life Sciences and Technology, Tongji University, Shanghai 200092, China*

Aim: To identify novel serum biomarkers for lung cancer diagnosis using magnetic bead-based surface-enhanced laser desorption/ionization time-of-flight mass spectrum (SELDI-TOF-MS).

Methods: The protein fractions of 121 serum specimens from 30 lung cancer patients, 30 pulmonary tuberculosis patients and 33 healthy controls were enriched using WCX magnetic beads and subjected to SELDI-TOF-MS. The spectra were analyzed using Biomarker Wizard version 3.1.0 and Biomarker Patterns Software version 5.0. A diagnostic model was constructed with the marker proteins using a linear discrimination analysis method. The validity of this model was tested in a blind test set consisted of 8 randomly selected lung cancer patients, 10 pulmonary tuberculosis patients and 10 healthy volunteers.

Results: Seventeen *m/z* peaks were identified, which were significantly different between the lung cancer group and the control (tuberculosis and healthy control) groups. Among these peaks, the 6445, 9725, 11705, and 15126 *m/z* peaks were selected by the Biomarker Pattern Software to construct a diagnostic model for lung cancer. This four-peak model established in the training set could discriminate lung cancer patients from non-cancer patients with a sensitivity of 93.3% (28/30) and a specificity of 90.5% (57/63). The diagnostic model showed a high sensitivity (75.0%) and a high specificity (95%) in the blind test validation. Database searching and literature mining indicated that the featured 4 peaks represented chaperonin (M9725), hemoglobin subunit beta (M15335), serum amyloid A (M11548), and an unknown protein.

Conclusion: A lung cancer diagnostic model based on bead-based SELDI-TOF-MS has been established for the early diagnosis or differential diagnosis of lung cancers.

Keywords: human lung cancer; serum biomarker; magnetic beads; SELDI-TOF-MS

Acta Pharmacologica Sinica (2011) 32: 1537–1542; doi: 10.1038/aps.2011.137; published online 24 Oct 2011

Introduction

Lung cancer is among the leading causes of cancer death in the world, especially in developing countries. In the past several years, the morbidity and mortality related to lung cancer have been on the rise, mostly due to late diagnosis and metastasis[1–3]. Therefore, early diagnosis is an important factor for improving the prognosis of lung cancer patients. The vast majority of lung cancer patients in an early stage exhibit no symptoms, and the cancer is commonly detected as an abnormal shadow on a chest roentgenogram or a chest computed tomography (CT) scan[4]. It is therefore urgent to identify better methods that can provide more information for lung cancer diagnosis, especially during the early stages. The currently used biomarkers for the early diagnosis of lung cancer in the clinic are carcinoembryonic antigen (CEA), cytokeratin-19 fragments (CYFRA-211) and neuron-specific enolase (NSE)[5–7]. However, all of these biomarkers have a poor positive predictive value for lung cancer patients, especially for those in an early stage, and some of these biomarkers are not specific to lung cancer.

Applications of proteomic technologies in recent years have significantly broadened our understanding of the molecular mechanisms of numerous diseases and have aided in biomarker screening and drug target discovery. SELDI-TOF-MS is considered a high-efficiency comparative proteomic approach that possesses diverse advantages over traditional protein separation and identification techniques[8]. Moreover, SELDI-TOF-MS and pattern recognition software have been successfully used in the identification of specific markers for certain diseases, such as prostate cancer, ovarian cancer and

# The first two authors contributed equally to this work.
* To whom correspondence should be addressed.
E-mail qibinsong@yahoo.cn (Qi-bin SONG);
zeng@tongji.edu.cn (Hua-zong ZENG)
Received 2011-05-25 Accepted 2011-08-22

rheumatism[8–10].

In this article, serum specimens from lung cancer patients and non-cancer controls were subjected to magnetic bead-based SELDI-TOF-MS. Characteristic peaks for lung cancer patients were identified, and a diagnostic model was constructed. The diagnostic model was validated using a blind test set, which demonstrated clinical significance of this model in lung cancer diagnosis.

Materials and methods

Patient recruitment and sample collection

Serum specimens from 30 lung cancer patients (CA), 30 pulmonary tuberculosis (benign lung disease) patients (TB), and 33 healthy individuals (HC) were collected. Another 8 randomly selected patients with lung cancer, 10 cases of pulmonary tuberculosis and 10 healthy volunteers were enrolled to test the validity of the diagnostic model constructed in this study. The demographic characteristics of the lung cancer patients and the control subjects are shown in Table 1. Informed consent was obtained from every participant, and the study received ethical committee approval. The blood samples were collected in 4 mL BD vacutainer tubes without anticoagulant, allowed to clot at room temperature for up to 1 h, and centrifuged at 4 °C for 5 min at 1000×*g*. The pooled sera were frozen and stored at -80 °C for future analysis.

Table 1. Demographic characteristics of lung cancer patients and control subjects.

Sample type	Number of samples	Male/ female	Average age, years	Age range, years
Lung cancer	38	26/12	34.4	12–65
Pulmonary tuberculosis	40	17/23	43.9	14–58
Healthy controls	43	20/23	37.2	23–69

Proteomic fraction preparation and SELDI-TOF-MS assay

Serum samples were denatured in the presence of U9 lysis buffer (9 mol/L urea, 2% CHAPS, 50 mmol/L Tris-HCl, pH 9.0; Bio-Rad) and then mixed with WCX-2 (NaAC, pH 4.0) buffer. The sample was then incubated with WCX-2-pretreated magnetic beads (Changchun Bokun Science and Technology, China) for 60 min. The beads were then washed twice with NaAC and eluted with 1% TFA (trifluoroacetic acid)[11]. The protein fraction was then lyophilized and prepared for SELDI-TOF-MS (BioRad, USA) according to the manufacturer's instructions. Masses were acquired from *m/z* 1000-50 000.

Protein identification and bioinformatics analysis

Protein database searching was performed with the MASCOT search engine (http://www.matrixscience.com/; Matrix Science, London, UK), which compared the monoisotopic peaks against the NCBI nonredundant protein database (http://www.ncbi.nlm.nih.gov/). The allowed mass tolerance was less than 0.05%[12–14]. Proteins with MASCOT scores greater than 63 were considered significant (P<0.05).

Data processing and pattern recognition

Principal component analysis (PCA) was performed to cluster the samples (MATLAB, MathWorks, USA). The score plots aided in visualizing the data, and a diagnostic model was constructed with the marker proteins using a linear discrimination analysis method. The classification performance (specificity and sensitivity) was assessed using the AUC values of the ROC curves[15, 16]. The mass spectrometry analysis system was applied to identify the characteristic molecules corresponding to the featured peaks in the Metlin (http://metlin.scripps.edu/) and HMDB (http://www.hmdb.ca/) databases. The protein hits were verified using text mining techniques.

Results

Identification of the serum protein profile

The protein fractions of the serum samples from 30 lung cancer patients, 30 pulmonary tuberculosis patients and 33 healthy controls were enriched using WCX magnetic beads, which is a particularly effective method for the detection of low-molecular-weight proteins and peptides, and were analyzed by SELDI-TOF-MS. Following baseline correction and peak alignment, protein signals were obtained for all samples. Representative mass chromatogram data for lung cancer patients, pulmonary tuberculosis patients and healthy controls are shown in Figure 1.

Protein fingerprint analysis of serum protein from lung cancer patients

The mass spectrum data of the 121 samples were analyzed using Biomarker Wizard (version 3.1.0) to identify the peaks that were different between the lung cancer patients and the control individuals. The Shapiro-Wilk test was used to evaluate the normality of the distribution of the peaks, and the homogeneity of the variance was calculated by the Levene's test. All of the peaks were sorted using the P value from the ANOVA and the Student-Newman-Keuls *post-hoc* test using SPSS 16.0 (SPSS Inc, USA). Seventeen significant discriminating *m/z* peaks (4188.21, 4548.39, 4763.26, 4983.18, 5069.19, 5351.19, 5486.84, 6212.41, 6445.26, 6573.47, 9725.37, 11705.4, 11769.7, 15126.9, 15335.2, 15938.7, and 19790.5) were found between the lung cancer group and the control groups (P<0.05), and are shown in Table 2. The importance of these peaks determined by the Biomarker Pattern Software is listed as well. The most important peak was assigned an importance index of 100. The importance of other peaks was calculated relative to that of the top peak, and a value below 100 was conferred to each peak. The peaks at 4763.26, 5069.19, 5351.19, 5486.84, 6212.41, 11705.4, 11769.7, 15335.2, and 15938.7 Da were higher in the lung cancer patients than that in the control groups, and the peaks at 4188.21, 4548.39, 4983.18, 6445.26, 6573.47, 9725.37, 15126.9, and 19790.5 Da were lower in the lung cancer patients than that in the control groups.

Table 2. Discriminant *m/z* peaks between lung cancer group and the control group.

		Sum of squares	df	Mean square	*F*	*P*
M4188.21	Between groups	3.602	2	1.801	6.822	<0.01
	Within groups	23.757	90	0.264		
	Total	27.358	92			
M4548.39	Between groups	59.255	2	29.628	68.835	<0.01
	Within groups	38.737	90	0.430		
	Total	97.992	92			
M4763.26	Between groups	26.690	2	13.345	31.805	<0.01
	Within groups	37.763	90	0.420		
	Total	64.453	92			
M4983.18	Between groups	13.542	2	6.771	19.539	<0.01
	Within groups	31.188	90	0.347		
	Total	44.730	92			
M5069.59	Between groups	16.088	2	8.044	22.930	<0.01
	Within groups	31.573	90	0.351		
	Total	47.662	92			
M5351.19	Between groups	27.022	2	13.511	10.279	<0.01
	Within groups	118.301	90	1.314		
	Total	145.323	92			
M5486.84	Between groups	21.686	2	10.843	27.912	<0.01
	Within groups	34.963	90	0.388		
	Total	56.649	92			
M6212.41	Between groups	50.416	2	25.208	41.621	<0.01
	Within groups	54.509	90	0.606		
	Total	104.925	92			
M6445.26	Between groups	36.418	2	18.209	84.311	<0.01
	Within groups	19.437	90	0.216		
	Total	55.855	92			
M6573.47	Between groups	22.213	2	11.106	50.560	<0.01
	Within groups	19.770	90	0.220		
	Total	41.983	92			
M9725.37	Between groups	13.078	2	6.539	15.286	<0.01
	Within groups	38.502	90	0.428		
	Total	51.580	92			
M11705.4	Between groups	594.433	2	297.217	6.538	<0.01
	Within groups	4 091.655	90	45.463		
	Total	4 686.088	92			
M11769.7	Between groups	133.933	2	66.967	5.025	<0.01
	Within groups	1 199.450	90	13.327		
	Total	1 333.383	92			
M15126.9	Between groups	141.451	2	70.725	10.306	<0.01
	Within groups	617.657	90	6.863		
	Total	759.107	92			
M15335.2	Between groups	11.583	2	5.791	8.673	<0.01
	Within groups	60.098	90	0.668		
	Total	71.681	92			
M15938.7	Between groups	2 204.907	2	1102.454	3.764	<0.05
	Within groups	26 361.431	90	292.905		
	Total	28 566.339	92			
M19790.5	Between groups	0.660	2	0.330	18.626	<0.01
	Within groups	1.595	90	0.018		
	Total	2.254	92			

Diagnostic model construction and validation

The 17 *m/z* peaks that could discriminate between lung cancer group and the control groups were identified by Biomarker Patterns Software Version 5.0 and analyzed to select peaks for the establishment of a diagnostic biomarker pattern. The *m/z* peaks at 6445, 9725, 11705, and 15126 were selected by the

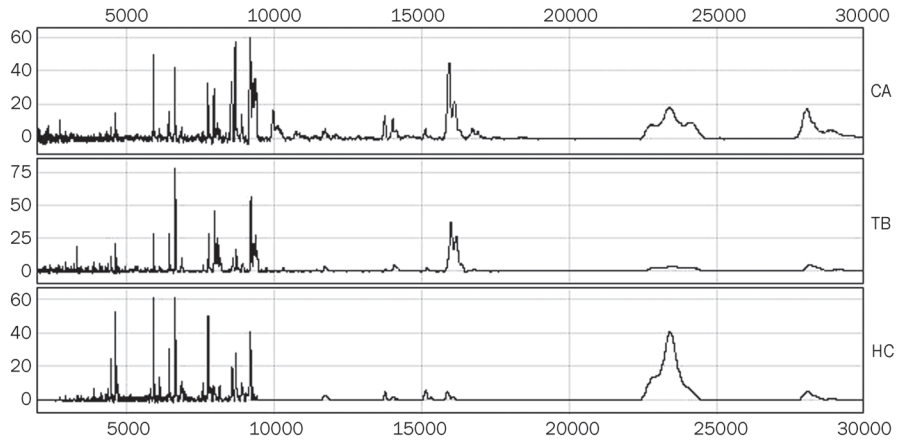

Figure 1. Representative data of mass chromatogram analysis. The data were from MS assay of lung cancer patients, pulmonary tuberculosis patients and healthy controls. The x-axis represents the molecular mass calculation (*m/z*), and the y-axis represents the relative intensity.

pattern recognition software as the best markers to construct a diagnostic model for lung cancer (Figure 2). This four-peak model established in the training set could discriminate lung cancer patients from healthy individuals as well as pulmonary tuberculosis patients with a sensitivity of 93.3% (28/30) and a specificity of 90.5% (57/63). The decision tree is presented in Figure 3, and the characteristics of the diagnostic model are shown in Figure 4. The prediction accuracy was validated using a blind test set consisting of 28 randomly selected individuals. The sensitivity and specificity of the prediction are shown in Table 3. We combined database searching with literature mining to determine the identities of the proteins corresponding to the featured peaks. Three of the featured proteins were identified as chaperonin (M9725), hemoglobin subunit beta (M15335) and serum amyloid A (M11548). There was no protein match for the 6445 Da peak in the searched databases, indicating it might be a novel protein.

Table 3. Sensitivity and specificity of decision tree model.

Classification (clinical diagnosis)	Decision tree classification class		
	CA, *n* (%)	TB, *n* (%)	HC, *n* (%)
In the training set			
CA (*n*=30)	28 (93.3)	2 (6.7)	0 (0)
TB (*n*=30)	3 (10.0)	25 (83.3)	2 (6.7)
HC (*n*=33)	0 (0)	1 (3.0)	32 (97.0)
In the blinded testing set			
CA (*n*=8)	6 (75.0)	2 (25.0)	0 (0)
TB (*n*=10)	1 (10.0)	9 (90.0)	0 (0)
HC (*n*=10)	0 (0)	0 (0)	10 (100.0)

To explore the clinical significance of the constructed model, the validity of the model was tested by a blind test set consisting of 8 randomly selected lung cancer patients, 10 pulmonary tuberculosis patients and 10 healthy volunteers. The sensitivity of the diagnostic model was 75.0% (6/8), and the specificity was 95% (19/20).

Discussion

During the last several decades, the identification of novel biomarkers for complex diseases has become increasingly successful because of the emergence of high-throughput proteomic techniques such as SELDI-TOF-MS[17]. Biomarkers, especially biomarker patterns, are considered to be reliable and powerful tools for the early diagnosis, differential diagnosis, and therapy of some diseases[18, 19]. Analysis of serum proteins by SELDI-TOF-MS provides new information about small proteins with high serum abundances[20, 21]. Magnetic beads with large surfaces are better able to enrich proteins from serum than other materials. Joint application of magnetic beads and SELDI-TOF-MS might be a more powerful strategy to discover novel serum biomarkers with low abundances.

In this study, the protein fingerprints in the sera from 30 lung cancer patients, 30 pulmonary tuberculosis patients and 33 healthy controls were analyzed using magnetic beads and SELDI-TOF-MS, and seventeen characteristic *m/z* peaks were identified using Biomarker Wizard. Theoretically, multiple markers are much more powerful and reliable in the diagnosis of a disease than a single marker alone. In our study, the 17 discriminating *m/z* peaks were analyzed by Biomarker Patterns Software, and only 4 protein peaks, those at 6445, 9725, 11705, and 15126 *m/z*, were capable of serving as markers for lung cancer diagnosis. This four-peak model established in the training set could discriminate lung cancer patients from healthy individuals and from pulmonary tuberculosis patients with a sensitivity of 93.3% (28/30) and a specificity of 90.5% (57/63). The validity of the model was tested using a blind test set, and the sensitivity of the diagnostic model was 75.0% (6/8), and the specificity was 95% (19/20). Despite the limitation of the test set size, these data indicate that our study provides a novel and potent tool to distinguish lung cancer patients from tuberculosis patients and healthy individuals using serum.

In conclusion, our findings suggest that the application of magnetic beads and SELDI-TOF-MS could be a potent strategy for the identification of serum biomarkers. More importantly, the diagnostic model we constructed using the protein peaks at 6445, 9725, 11705, and 15126 *m/z* could successfully dis-

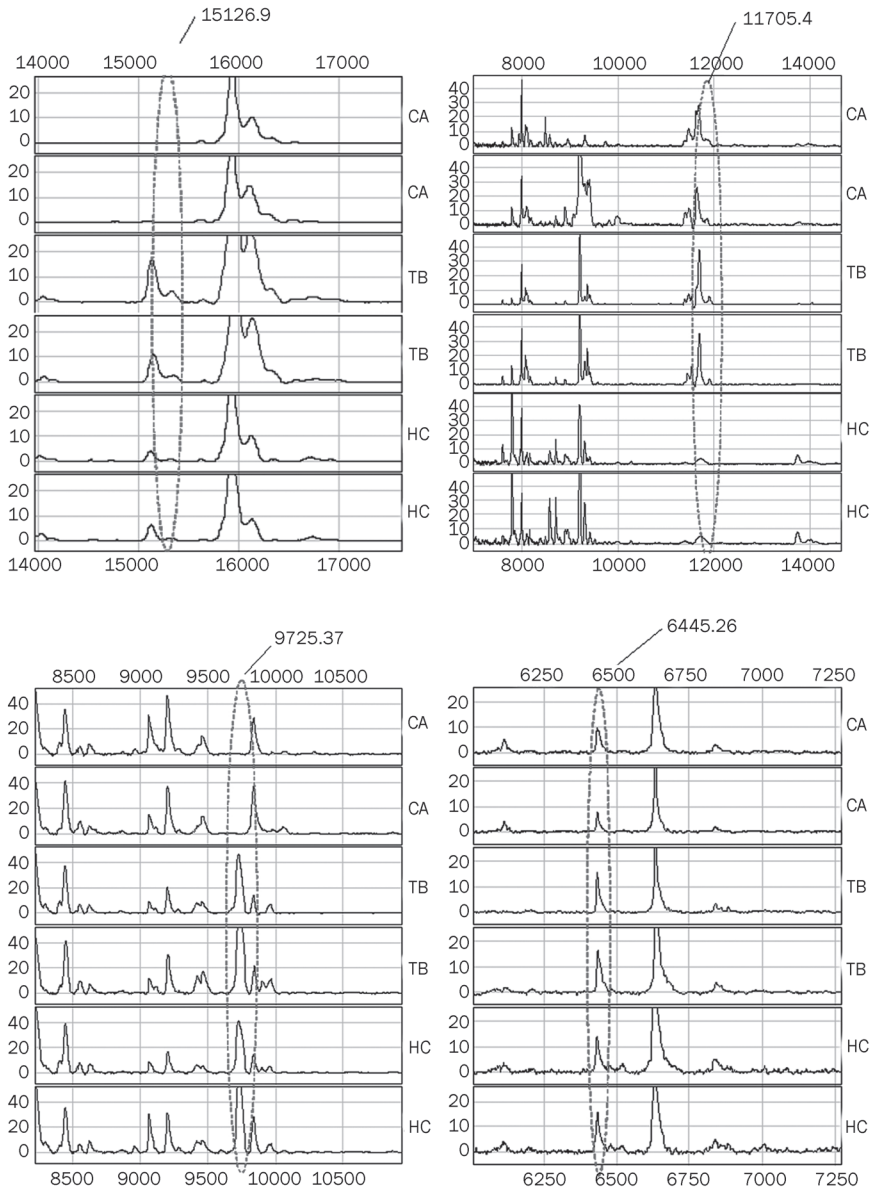

Figure 2. Four characteristic peaks in lung cancer patients. Protein spectrum of serum samples from two different lung cancer patients (CA), two pulmonary tuberculosis patients (TB) and two healthy controls (HC). The x-axis represents the molecular mass calculation (*m/z*), and the y-axis represents the relative intensity.

tinguish lung cancer patients from tuberculosis patients and normal controls, which might be of clinical significance in the early diagnosis of lung cancer. Database searching with literature mining showed that the featured peaks were chaperonin (M9725), hemoglobin subunit beta (M15335), serum amyloid A (M11548) and an unknown protein. A previous report has illustrated that serum amyloid A could be a promising serum biomarker for lung cancer, consistent with the results of our study. However, the clinical significance of chaperonin and hemoglobin subunit beta in lung cancer diagnosis deserves further investigation.

Acknowledgements

The authors also thank Cluster Biotech Co Ltd for the assistance in bio-information analysis.

Author contribution

Qi-bin SONG and Hua-zong ZENG designed research; Wei-guo HU and Yi YAO performed research; Peng WANG contributed new reagents and samples; Wei-guo HU and Peng WANG analyzed data; and Qi-bin song, Wei-guo HU, and Hua-zong ZENG wrote the paper.

References

1 Spira A, Ettinger DS. Multidisciplinary management of lung cancer. N Engl J Med 2004; 350: 379–92.
2 Herbst RS, Heymach JV, Lippman SM. Lung Cancer. N Engl J Med 2008; 359: 1367–80.
3 Singh N, Agarwal R, Aggarwal AN. Quality-of-life assessment in trials of lung cancer. Lancet 2007; 370: 933.
4 Petricoin EF, Zoon KC, Kohn EC, Barrett JC, Liotta LA. Clinical proteomics: translating benchside promise into bedside reality. Nat Rev

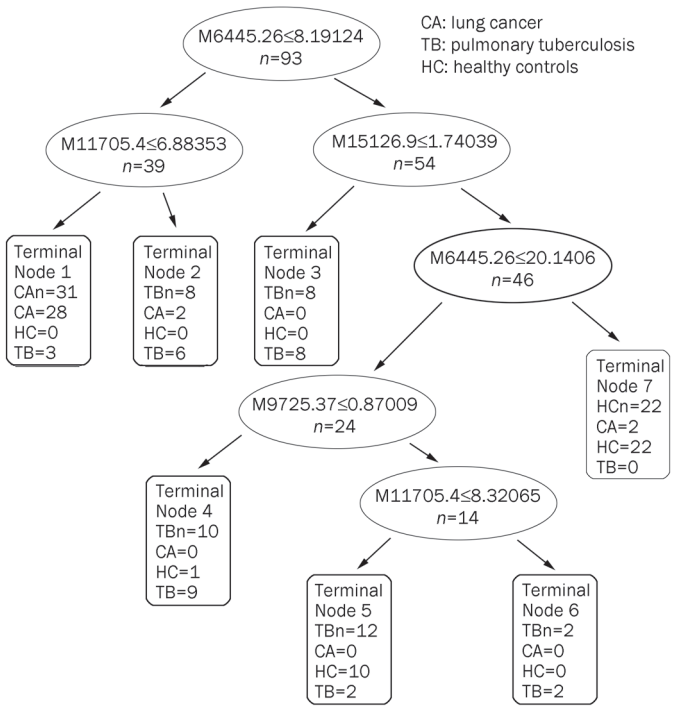

Figure 3. Boosting decision tree classification of the participants. The root node (top) and descendant nodes were shown as ellipses and the terminal nodes (Nodes 1–7) were shown as rectangles. The mass value in the nodes was followed by lower or equal to intensity value. If the answer to the question in a node of the tree is yes, proceed down to the left node, otherwise (*ie* no), proceed down to the right node. When proceeding to the terminal nodes, the decision tree assigned samples to three groups. Samples in terminal nodes 2, 3, 4, and 6 were assigned to TB, terminal node 1 was to CA and terminal nodes 5 and 7 were to HC. The numbers in rectangles represent the actual clinical diagnosis of samples assigned to this terminal node by decision tree (*ie* in terminal node 1, decision tree assigned 31 samples to CA, but actually 28 of them were CA according to the clinical diagnosis).

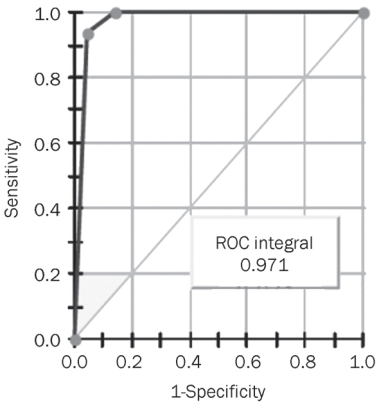

Figure 4. ROC of the boosting decision tree.

Drug Discov 2002; 1: 683–95.
5 Schneider J, Velcovsky HG, Morr H, Katz N, Neu K, Eigenbrodt E. Comparison of the tumor markers tumor M2-PK, CEA, CYFRA21-1, NSE and SCC in the diagnosis of lung cancer. Anticancer Res 2000; 20: 5053–8.
6 Ardizzoni A, Cafferata MA, Tiseo M, Filiberti R, Marroni P, Grossi F, *et al*. Decline in serum carcinoembryonic antigen and cytokeratin 19 fragment during chemotherapy predicts objective response and survival in patients with advanced nonsmall cell lung cancer. Cancer 2006; 107: 2842–9.
7 Holdenrieder S, von Pawel J, Dankelmann E, Duell T, Faderl B, Markus A, *et al*. Nucleosomes and CYFRA 21-1 indicate tumor response after one cycle of chemotherapy in recurrent non-small cell lung cancer. Lung Cancer 2009; 63: 128–35.
8 Petricoin EF, Ardekani AM, Hitt BA, Levine PJ, Fusaro VA, Steinberg SM, *et al*. Use of proteomic patterns in serum to identify ovarian cancer. Lancet 2002; 359: 572–7.
9 Zhang Z, Bast RC Jr, Yu Y, Li J, Sokoll LJ, Rai AJ, *et al*. Three biomarkers identified from serum proteomic analysis for the detection of early stage ovarian cancer. Cancer Res 2004; 64: 5882–90.
10 Goncalves A, Bertucci F, Birnbaum D, Borg JP. Protein profiling SELDI-TOF and breast cancer: clinical potential applications. Med Sci (Paris) 2007; 23: 23–6.
11 Baumann S, Ceglarek U, Fiedler GM, Lembcke J, Leichtle A, Thiery J. Standardized approach to proteome profiling of human serum based on magnetic bead separation and matrix-assisted laser desorption/ionization time-of-flight mass spectrometry. Clin Chem 2005; 51: 973–80.
12 Trygg J, Holmes E, Lundstedt T. Chemometrics in metabonomics. J Proteome Res 2007; 6: 469–79.
13 Smith CA, Want EJ, O'Maille G, Abagyan R, Siuzdak G. XCMS: processing mass spectrometry data for metabolite profiling using nonlinear peak alignment, matching, and identification. Anal Chem 2006; 78: 779–87.
14 Tibshirani R, Hastie T, Narashiman B, Chu G. Diagnosis of multiple cancer types by shrunken centroids of gene expression. Proc Natl Acad Sci U S A 2002; 99: 6567–72.
15 Anthony ML, Rose VS, Nicholson JK, Lindon JC. Classification of toxin-induced changes in ^{1}H NMR spectra of urine using an artificial neural network. J Pharm Biomed Anal 1995; 13: 205-11.
16 Beckonert O, Bollard ME, Ebbels T, Keun HC, Antti H, Holmes E, *et al*. NMR-based metabonomic toxicity classification: hierarchical cluster analysis and k-nearest. Anal Chim Acta 2003; 490: 3–15.
17 Fung ET, Wright GL Jr, Dalmasso EA. Proteomic strategies for biomarker identification: progress and challenges. Curr Opin Mol Ther 2000; 2: 643–50.
18 Skytt A, Thysell E, Stattin P, Stenman UH, Antti H, Wikström P. SELDI-TOF MS *versus* prostate specific antigen analysis of prospective plasma samples in a nested case control study of prostate cancer. Int J Cancer 2007; 121: 615–20.
19 Hundt S, Haug U, Brenner H. Blood markers for early detection of colorectal cancer: a systematic review. Cancer Epidemiol Biomarkers Prev 2007; 16: 1935–53.
20 Wu CC, Chien KY, Tsang NM, Chang KP, Hao SP, Tsao CH, *et al*. Cancer cell-secreted proteomes as a basis for searching potential tumor markers: nasopharyngeal carcinoma as a model. Proteomics 2005; 5: 3173–82.
21 Welsh JB, Sapinoso LM, Kern SG, Brown DA, Liu T, Bauskin AR, *et al*. Large-scale delineation of secreted protein biomarkers overexpressed in cancer tissue and serum. Proc Natl Acad Sci U S A 2003; 100: 3410–5.

Acta Pharmacologica Sinica (2011) 32: 1543–1548
 1671-4083/11 $32.00
www.nature.com/aps

Short Communication

Dimethylenastron suppresses human pancreatic cancer cell migration and invasion *in vitro* via allosteric inhibition of mitotic kinesin Eg5

Xiao-dong SUN[1, #], Xing-juan SHI[1, #], Xiao-ou SUN[1, #], You-guang LUO[1], Xiao-jing WU[1], Chang-fu YAO[1], Hai-yang YU[1], Deng-wen LI[1], Min LIU[2, *], Jun ZHOU[1, *]

[1]*Department of Genetics and Cell Biology, Tianjin Key Laboratory of Protein Science, College of Life Sciences, Nankai University, Tianjin 300071, China;* [2]*Department of Biochemistry, Key Laboratory of Immune Microenvironment and Disease of the Ministry of Education, Basic Medical College, Tianjin Medical University, Tianjin 300070, China*

Aim: The mitotic kinesin Eg5 plays a critical role in bipolar spindle assembly, and its inhibitors have shown impressive anticancer activity in preclinical studies. This study was undertaken to investigate the effect of dimethylenastron, a specific inhibitor of Eg5, on the migration and invasion of pancreatic cancer cells.
Methods: Human pancreatic cancer cell lines PANC1, EPP85, BxPC3, CFPAC1, and AsPAC1 were used. Eg5 expression was examined using immunofluorescence microscopy. Cell migration and invasion were analyzed with wound healing and transwell assays. Cell proliferation was examined using sulforhodamine B and MTT assays. The binding of dimethylenastron to Eg5 was analyzed with a molecular modeling study, and the ADP release rate was examined with the MANT-ADP reagent.
Results: Eg5 expression was 9–16-fold up-regulated in the 5 pancreatic cancer cell lines. Treatment of PANC1 pancreatic cancer cells with dimethylenastron (3 and 10 μmol/L) for 24 h suppressed the migratory ability of the cancer cells in a concentration-dependent manner. The invasion ability of the cancer cells was also reduced by the treatment. However, treatment of PANC1 cells with dimethylenastron (3 and 10 μmol/L) for 24 h had no detectable effect on their proliferation, which was inhibited when the cancer cells were treated with the drug for 72 h. Molecular modeling study showed that dimethylenastron could allosterically inhibit the motor domain ATPase of Eg5 by decreasing the rate of ADP release.
Conclusion: Dimethylenastron inhibits the migration and invasion of PANC1 pancreatic cancer cells, independent of suppressing the cell proliferation. The findings provide a novel insight into the mechanisms of targeting Eg5 for pancreatic cancer chemotherapy.

Keywords: kinesin; Eg5; dimethylenastron; pancreatic cancer; cell migration; cell invasion; cell proliferation; molecular modeling

Acta Pharmacologica Sinica(2011) 32: 1543–1548; doi: 10.1038/aps.2011.130; published online 10 Oct 2011

Introduction

Eg5 (also known as kinesin-5, kinesin spindle protein, or Kif11) is encoded by the *KIF-11* gene located at chromosome 10q24.1. As a member of the BimC family of kinesin-related proteins, Eg5 is a microtubule-dependent motor protein and plays a crucial role in the assembly and maintenance of the bipolar spindle, by hydrolysis of ATP to generate outward forces and push apart anti-parallel microtubules[1, 2]. In addition, accumulating evidence indicates that Eg5 is highly expressed in cancer cell lines and tumor samples[3, 4]. It has been reported that the overexpression of Eg5 leads to abnormal spindle formation, genomic instability, and the development of a broad spectrum of cancers[3, 4].

Eg5 has been demonstrated as an effective target for cancer treatment. Antisense oligonucleotides against Eg5 has been shown to reduce the growth of tumors in xenograft models[5]. In blast crisis chronic myeloid leukemia and prostate cancer cells, in which Eg5 is highly expressed, inhibition of Eg5 causes cell cycle arrest and significantly suppresses cell proliferation[5, 6]. Over the last decade, the effects of various Eg5 inhibitors on the proliferation of cancer cells have been investigated, and the mechanisms of action of several Eg5 inhibitors have been studied[7–11]. Dimethylenastron is a cell-permeable quinazoline-thione compound that acts as a potent inhibitor of Eg5[12]. We have demonstrated previously that dimethylenastron inhibits pancreatic tumor growth by suppressing cell

# These authors contributed equally to this work.
* To whom correspondence should be addressed.
E-mail minliu@tijmu.edu.cn (Min LIU);
junzhou@nankai.edu.cn (Jun ZHOU)
Received 2011-07-13 Accepted 2011-09-06

proliferation and resulting in robust apoptosis[11].

Pancreatic cancer is a highly malignant neoplasm of the pancreas and the fourth leading cause of cancer-related deaths worldwide. The prognosis of this disease is poor, with fewer than 5% of those diagnosed still alive five years after diagnosis[13]. The high mortality rate of pancreatic cancer results mainly from the delay in diagnosis and the high rate of metastasis, of which abnormal cancer cell motility is an essential component[14, 15]. It remains elusive whether Eg5 inhibitors affect cancer cell motility, despite the intensive studies of the mechanisms of action of this group of compounds. In this study, we provide the first evidence that dimethylenastron allosterically inhibits Eg5 activity and reduces the migration and invasion of pancreatic cancer cells, independent of its inhibitory effect on pancreatic cancer cell proliferation.

Materials and methods

Materials

Dimethylenastron was purchased from Calbiochem. Sulforhodamine B, 3-(4,5-dimethyl-2-thiazolyl)-2,5-diphenyl-2*H*-tetrazolium bromide (MTT), and 4′-6-diamidino-2-phenylindole (DAPI) were from Sigma–Aldrich, and the mouse monoclonal antibody against Eg5 was from Abcam. The rhodamine-conjugated anti-mouse secondary antibody was obtained from Amersham Biosciences.

Cell culture

PANC1, EPP85, BxPC3, CFPAC1, and AsPC1 human pancreatic cancer cells were cultured in RPMI-1640 medium supplemented with 2 mmol/L *L*-glutamine and 10% fetal bovine serum at 37 °C in a humidified atmosphere with 5% CO_2. Normal pancreatic epithelial cells were grown as primary cultures as described previously[16].

In vitro cell proliferation assay

Cells grown in 96-well plates were treated with gradient concentrations of dimethylenastron for 24 or 72 h. Sulforhodamine B and MTT assays were then performed as described previously[17]. The percentage of cell proliferation as a function of drug concentration was plotted.

Immunofluorescence microscopy

Cells grown on glass coverslips were fixed with cold (-20 °C) methanol for 8 min and then washed with phosphate-buffered saline (PBS). Nonspecific sites were blocked by incubating with 2% bovine serum albumin diluted with PBS for 20 min at room temperature. Cells were incubated with mouse monoclonal anti-Eg5 antibody (1:100 dilution) for 2 h and then with rhodamine-conjugated anti-mouse secondary antibody for 2 h, followed by staining with DAPI for 5 min. Coverslips were mounted with 90% glycerol in PBS and examined with a Zeiss fluorescence microscope. Images of interphase cells were taken, and 300 cells were analyzed. Eg5 expression in cells was quantified by measuring the fluorescence intensity of Eg5 with AxioVision Rel 4.1 software. To quantify Eg5 distribution in the nucleus, an irregular circle was drawn outside the nucleus, and the fluorescence intensity of Eg5 within this circle was measured. The percentage of Eg5 expression in the nucleus was then calculated.

Wound healing assay

Cells grown in serum-free medium for 12 h as confluent monolayers were treated with dimethylenastron and mechanically scratched with a 20 μL pipette tip to create the wound. Cells were then washed with PBS to remove the debris, and culture medium containing 10% or 5% serum was added to allow for wound healing. Phase-contrast images of the wound were taken 24 h later, and the number of cells that migrated into the wound area was counted in three random fields per wound. The extent of wound closure was quantified as the number of migrating cells in the drug-treatment group divided by the number of migrating cells in the control group.

Transwell invasion assay

Cell invasion in response to dimethylenastron was carried out by transwell assays. The upper surface of the transwell filters was coated with matrigel or fibronectin. Cells suspended in 200 μL serum-free media were added to the chamber, and the chamber was placed in a 24-well plate containing complete medium. After 24 h of incubation at 37 °C, the filters were gently taken out and matrigel on the upper surface of the filters was removed by cotton swabs. Cells on the underside of transwell filters were fixed with 4% paraformaldehyde for 30 min, stained with 0.1% crystal violet for 10 min, and then photographed. For quantitative assessment, the number of invading cells was counted in five random fields per filter. The extent of cell invasion was quantified as the number of invading cells in the drug-treatment group divided by the number of invading cells in the control group.

Molecular modeling

Dimethylenastron was docked onto the coordinates obtained from the crystal structure of Eg5[18], using standard DOCK methodology[19]. The lowest-energy Eg5/dimethylenastron interaction model was presented.

Measurement of ADP release rate

The effects of dimethylenastron on the ADP release rate of the Eg5 motor domain were examined with the MANT-ADP reagent (Molecular Probes), by measuring the changes in MANT-ADP fluorescence as described previously[9, 20]. In brief, purified Eg5 motor domain was incubated with the MANT-ADP racemate at a 1:1 stoichiometry. The Eg5-MANT-ADP complex was then mixed with 1 mmol/L MgATP in the presence or absence of preformed microtubules. The decrease in MANT-ADP fluorescence was then examined over time at an excitation wavelength of 360 nm and an emission wavelength of 460 nm. The observed exponential rate constant was then fit to a hyperbola to obtain the ADP release rate.

Preparation of microtubules

For the preparation of microtubules, 10 μmol/L microtubule

associated protein-free tubulin (cytoskeleton) was incubated at 35 °C for 30 min in a buffer containing 80 mmol/L Na-PIPES (pH 6.9), 1 mmol/L $MgCl_2$, 1 mmol/L EGTA, 1 mmol/L GTP, and 5% glycerol.

Statistical analysis

Student's *t* test was used to determine statistical significance. *P* values less than 0.05 were considered significant, and *P* values less than 0.01 were considered highly significant. Experiments were repeated 3 times, and error bars represent standard deviations between experiments.

Results

Eg5 expression is up-regulated in pancreatic cancer cell lines

To investigate the potential of Eg5 as a target for pancreatic cancer treatment, we examined its expression in several well characterized pancreatic cancer cell lines, including BxPC3, PANC1, EPP85, CFPAC1, and AsPAC1, and compared to Eg5 expression in normal pancreatic epithelial cells. Consistent with previous studies[4], we found that Eg5 was highly expressed in all the pancreatic cancer cell lines examined (Figure 1A–1B). Interestingly, while only a small portion of Eg5 was localized in the nucleus in normal cells, a significant increase in its nuclear localization was observed in pancreatic cancer cells (Figure 1C).

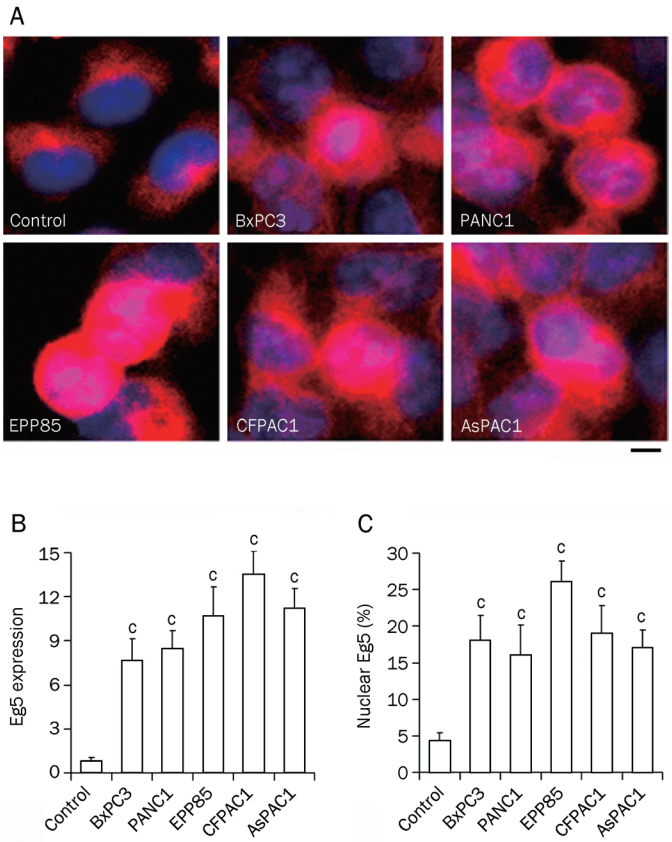

Figure 1. Overexpression of Eg5 in pancreatic cancer cell lines. (A) Immunofluorescence microscopic analysis of Eg5 (red) in pancreatic cancer cells and control normal pancreatic epithelial cells. Cells were also stained with the DNA dye DAPI to show the nuclei (blue). All the cells shown in this figure are interphase cells. Scale bar, 10 μm. (B) Experiments were performed as in A, and the expression of Eg5 in cells was quantified. (C) Experiments were performed as in A, and the distribution of Eg5 in the nucleus was quantified. Mean±SD. *n*=3. $^cP<0.01$ *vs* control.

Inhibition of Eg5 activity suppresses pancreatic cancer cell migration

The overexpression of Eg5 in pancreatic cancer cells prompted us to examine whether the inhibition of Eg5 activity affects the motility of pancreatic cancer cells. PANC1 cells were used for the analysis of cell motility because of their well-characterized genetic background, growth conditions, and migratory ability[21]. Serum-starved PANC1 cells grown as confluent monolayers were treated with the Eg5 inhibitor dimethylenastron and mechanically scratched to create the wound. Culture medium containing 10% serum was then added to allow wound healing, and phase-contrast images of the wound were taken 24 h later to examine the extent of wound closure as a measure of cell migration. As shown in Figure 2A–2B, dimethylenastron inhibited pancreatic cancer cell migration in a concentration-dependent manner, as evidenced by compromised wound closure in response to dimethylenastron treatment. The inhibitory effect of dimethylenastron on cell migration was more evident when culture medium containing 5% serum was used for wound healing (Figure 2C).

Dimethylenastron inhibits pancreatic cancer cell invasion

We then performed transwell assays to evaluate the effect of inhibition of Eg5 activity on pancreatic cancer cell invasion. PANC1 cells were treated with dimethylenastron and loaded to the transwell chambers (the upper surface of the transwell filters was coated with matrigel). After 24 h, cells migrated to the underside of the transwell filters were stained with crystal violet solution and imaged. As shown in Figure 3A–3B, inhibition of Eg5 activity by dimethylenastron significantly suppressed the ability of pancreatic cancer cells to invade to the underside of the transwell filters. Similar results were achieved when the upper surface of the transwell filters was coated with fibronectin (Figure 3C).

Dimethylenastron inhibits pancreatic cancer cell proliferation in a concentration-dependent manner

We then examined whether the reduced migration and invasion of pancreatic cancer cells in response to dimethylenastron results from its effect on cell proliferation. To investigate this possibility, sulforhodamine B and MTT-based cell proliferation assays were performed. As shown in Figure 4A, both sulforhodamine B and MTT assays revealed that at concentrations 1 to 10 μmol/L, dimethylenastron did not obviously affect PANC1 cell proliferation when cells were treated for 24 h. In contrast, 1 to 10 μmol/L dimethylenastron could significantly inhibit cell proliferation when cells were treated for 72 h (Figure 4B). These results thus demonstrate that the inhibitory

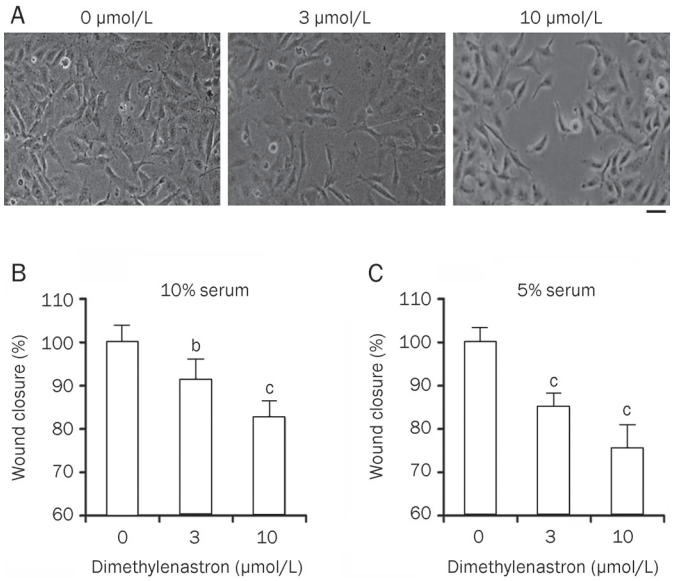

Figure 2. Determination of the effect of dimethylenastron on pancreatic cancer cell migration by wound healing assay. (A) PANC1 cells grown in serum-free medium were treated with 0, 3, or 10 μmol/L dimethylenastron and scratched. Culture medium containing 10% serum was added to allow for wound healing, and wound margins were imaged 24 h later. Scale bar, 50 μm. (B) Experiments were performed as in panel A, and the extent of wound closure was quantified by counting the number of migrating cells. (C) Experiments were performed as in A and B, except that culture medium containing 5% serum was used for wound healing. Mean±SD. n=3. ^{b}P<0.05, ^{c}P<0.01 *vs* control.

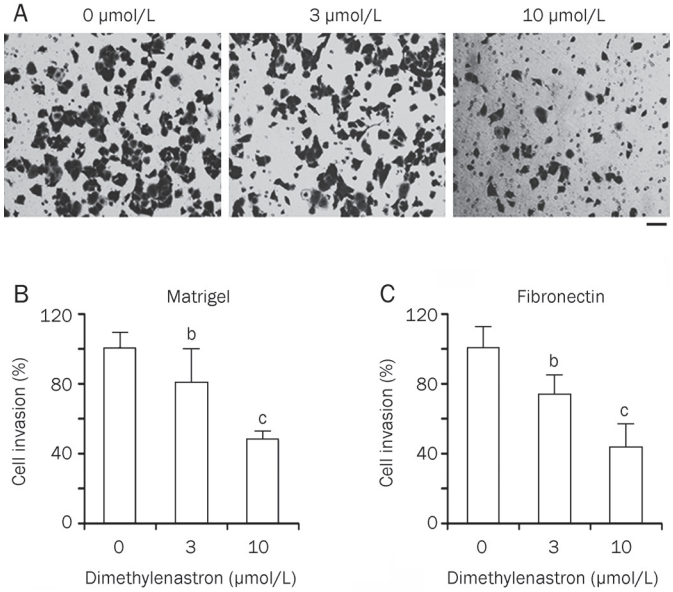

Figure 3. Dimethylenastron inhibits pancreatic cancer cell invasion as measured by transwell assay. (A) PANC1 cells were treated with 0, 3, or 10 μmol/L dimethylenastron and loaded to the transwell chambers (the upper surface of the transwell filters was coated with matrigel). After 24 h, cells migrated to the underside of the transwell filters were stained with crystal violet solution and imaged. Scale bar, 50 μm. (B) Experiments were performed as in panel A, and the extent of cell invasion was determined by counting the number of invading cells. (C) Experiments were performed as in A and B, except that the upper surface of the transwell filters was coated with fibronectin. Mean±SD. n=3. ^{b}P<0.05, ^{c}P<0.01 *vs* control.

effects of dimethylenastron on pancreatic cancer cell migration and invasion are independent of its effect on cell proliferation.

Dimethylenastron allosterically inhibits the motor domain ATPase of Eg5

To gain more mechanistic insight into how dimethylenastron inhibits Eg5 activity, we analyzed their interaction by molecular modeling. Dimethylenastron was docked onto the coordinates obtained from the crystal structure of Eg5[18], using standard DOCK methodology[19], and the lowest-energy Eg5/dimethylenastron interaction model was presented (Figure 5A). Detailed analysis revealed that dimethylenastron binds to the motor domain of Eg5 in a pocket close to the ATP/ADP binding pocket on Eg5; there exist a loop (E116-R119) and an α-helix (G110-F113) between the two binding pockets (Figure 5B). This model suggests that in the absence of ATP/ADP, dimethylenastron does not bind to Eg5 stably. Following ATP binding and hydrolysis to ADP, the ADP molecule pushes the aforementioned loop and α-helix to the dimethylenastron pocket and promotes the interaction between Eg5 and dimethylenstron.

Analysis of the ADP release rate has been useful for studying the effect of Eg5 inhibitors on its activity towards ATP hydrolysis[9]. To investigate whether dimethylenastron inhibits Eg5 activity by affecting ADP release, we analyzed the ADP release rate of Eg5 motor domain with the MANT-ADP reagent, a fluorescent analog of ADP that displays increased fluorescence when bound to Eg5[20]. As shown in Figure 5C, dimethylenastron significantly inhibited the basal rate of ADP release (in the absence of microtubules). In the presence of microtubules, dimethylenastron inhibited the rate of ADP release to a similar extent. These data thus suggest that dimethylenastron allosterically inhibits the motor domain ATPase of Eg5 by decreasing ADP release, independently of the binding of Eg5 to microtubules.

Discussion

The incidence of pancreatic cancer has been increasing at an alarming rate on a global scale over the past two decades. In spite of recent improvement in patient survival, the treatment of pancreatic cancer is still difficult. Our previous studies have shown that the Eg5 inhibitor dimenthylenastron inhibits the growth of pancreatic tumor both *in vitro* and in the mouse model[11]. In the present study, our results show that dimethylenastron inhibits pancreatic cancer cell migration and invasion. These findings thus provide novel mechanistic insight into the anticancer effect of dimethylenastron, suggesting the potential of using this agent for pancreatic cancer treatment. Given that the ability to rapidly metastasize is the most deadly aspect of pancreatic cancer and that tumor metastasis results

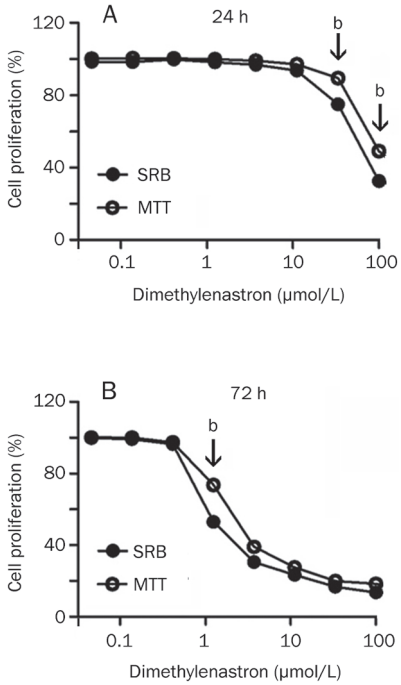

Figure 4. Dimethylenastron inhibits the proliferation of pancreatic cancer cells in a concentration-dependent manner. PANC1 cells were treated with gradient concentrations of dimethylenastron for 24 h (A) or 72 h (B). The percentage of cell proliferation was measured by sulforhodamine B (SRB)- or MTT-based cell proliferation assays. $^{b}P<0.05$ (SRB data versus MTT data).

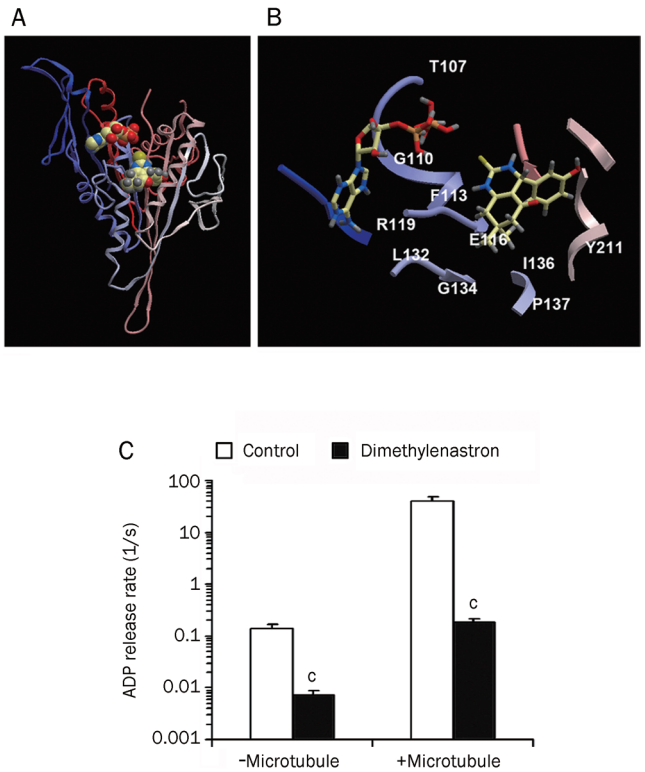

Figure 5. Dimethylenastron allosterically inhibits Eg5 activity by decreasing the rate of ADP release. (A) Schematic models showing the structure of Eg5 bound with ADP (upper) and dimethylenastron (lower). (B) Details of important interactions of ADP (left) and dimethylenastron (right) with the motor domain of Eg5, with red depicting oxygen, blue depicting nitrogen, yellow showing carbon, and grey representing hydrogen. Amino acid residues of Eg5 involved in the interaction with ADP and dimethylenastron are labeled. (C) Effects of dimethylenastron on the ADP release rate of Eg5 motor domain in the presence or absence of microtubules. Mean±SD. $n=3$. $^{c}P<0.01$ *vs* control.

mainly from cancer cell migration and invasion[14], the use of dimethylenastron for pancreatic cancer management might decrease cancer metastasis and improve patient survival.

Our study has also demonstrated that the inhibitory effects of dimethylenastron on pancreatic cancer cell migration and invasion are independent of its effect on cell proliferation. At present, the molecular mechanism of how dimethylenastron decreases cancer cell motility remains elusive. It has been shown in a previous study that knockdown of myosin II in fibroblasts could enhance cell migration and that the increase in cell motility by knockdown of myosin II could be rescued by the inhibition of Eg5 activity[22]. Therefore, it would be important to investigate whether the inhibition of Eg5 activity in pancreatic cancer cells by dimethylenastron could trigger the myosin II-associated signaling pathway.

The effectiveness of most chemotherapeutic agents has been impaired by various side effects. In this study, by molecular modeling and analysis of ADP release rate, we find that dimethylenastron allosterically inhibits the motor domain ATPase of Eg5, independent of the Eg5/microtubule interaction. Although the relationship between the allosteric inhibition of Eg5 activity and the inhibition of migration and invasion of pancreatic cancer cells remains unclear, our data suggest that dimethylenastron might have few (if any) side effects as a chemotherapeutic agent, because it would not affect the normal physiological functions of Eg5 that require its interaction with microtubules.

Another important question is how Eg5 expression is regulated in normal cells and how it is highly expressed in pancreatic cancer cells. In our previous study, we presented evidence that cellular Eg5 level is down-regulated by parkin, an E3 ubiquitin ligase well known for its role in Parkinson's disease. Interestingly, parkin represses Eg5 gene transcription by Hsp70 monoubiquitination-dependent inactivation of the c-Jun NH_2-terminal kinase pathway and blocking c-Jun binding to the activator protein 1 site in the Eg5 promoter, instead of triggering Eg5 protein degradation through the ubiquitin-proteasome pathway[23]. In addition, the Bcr-Abl tyrosine kinase has been reported to regulate Eg5, although the molecular details remain unclear[6]. Considering that both parkin and Bcr-Abl have been implicated in tumorigenesis, it would be interesting to examine whether abnormalities in these proteins play a role in triggering Eg5 overexpression in pancreatic cancer cells.

Acknowledgements

This work was supported by grants from the National Natural Science Foundation of China (31170820 and 90913021) and the Fok Ying Tung Education Foundation (111036).

Author contribution

Min LIU and Jun ZHOU designed research; Xiao-dong SUN, Xing-juan SHI, Xiao-ou SUN, Xiao-jing WU, Chang-fu YAO, and Hai-yang YU performed research; Deng-wen LI and Min LIU contributed new reagents or analytic tools; You-guang LUO and Jun ZHOU wrote the paper.

References

1 Valentine MT, Gilbert SP. To step or not to step? How biochemistry and mechanics influence processivity in Kinesin and Eg5. Curr Opin Cell Biol 2007; 19: 75–81.
2 Kapitein LC, Peterman EJ, Kwok BH, Kim JH, Kapoor TM, Schmidt CF. The bipolar mitotic kinesin Eg5 moves on both microtubules that it crosslinks. Nature 2005; 435: 114–8.
3 Castillo A, Morse HC 3rd, Godfrey VL, Naeem R, Justice MJ. Overexpression of Eg5 causes genomic instability and tumor formation in mice. Cancer Res 2007; 67: 10138–47.
4 Liu M, Wang X, Yang Y, Li D, Ren H, Zhu Q, *et al*. Ectopic expression of the microtubule-dependent motor protein Eg5 promotes pancreatic tumourigenesis. J Pathol 2010; 221: 221–8.
5 Hayashi N, Koller E, Fazli L, Gleave ME. Effects of Eg5 knockdown on human prostate cancer xenograft growth and chemosensitivity. Prostate 2008; 68: 1283–95.
6 Carter BZ, Mak DH, Shi Y, Schober WD, Wang RY, Konopleva M, *et al*. Regulation and targeting of Eg5, a mitotic motor protein in blast crisis CML: overcoming imatinib resistance. Cell Cycle 2006; 5: 2223–9.
7 Kapoor TM, Mayer TU, Coughlin ML, Mitchison TJ. Probing spindle assembly mechanisms with monastrol, a small molecule inhibitor of the mitotic kinesin, Eg5. J Cell Biol 2000; 150: 975–88.
8 Hotha S, Yarrow JC, Yang JG, Garrett S, Renduchintala KV, Mayer TU, *et al*. HR22C16: a potent small-molecule probe for the dynamics of cell division. Angew Chem Int Ed Engl 2003; 42: 2379–82.
9 Sakowicz R, Finer JT, Beraud C, Crompton A, Lewis E, Fritsch A, *et al*. Antitumor activity of a kinesin inhibitor. Cancer Res 2004; 64: 3276–80.
10 Tao W, South VJ, Zhang Y, Davide JP, Farrell L, Kohl NE, *et al*. Induction of apoptosis by an inhibitor of the mitotic kinesin KSP requires both activation of the spindle assembly checkpoint and mitotic slippage. Cancer Cell 2005; 8: 49–59.
11 Liu M, Yu H, Huo L, Liu J, Li M, Zhou J. Validating the mitotic kinesin Eg5 as a therapeutic target in pancreatic cancer cells and tumor xenografts using a specific inhibitor. Biochem Pharmacol 2008; 76: 169–78.
12 Gartner M, Sunder-Plassmann N, Seiler J, Utz M, Vernos I, Surrey T, *et al*. Development and biological evaluation of potent and specific inhibitors of mitotic Kinesin Eg5. Chembiochem 2005; 6: 1173–7.
13 Jemal A, Siegel R, Ward E, Hao Y, Xu J, Thun MJ. Cancer statistics, 2009. CA Cancer J Clin 2009; 59: 225–49.
14 Ghaneh P, Costello E, Neoptolemos JP. Biology and management of pancreatic cancer. Gut 2007; 56: 1134–52.
15 Hezel AF, Kimmelman AC, Stanger BZ, Bardeesy N, Depinho RA. Genetics and biology of pancreatic ductal adenocarcinoma. Genes Dev 2006; 20: 1218–49.
16 Furukawa T, Duguid WP, Rosenberg L, Viallet J, Galloway DA, Tsao MS. Long-term culture and immortalization of epithelial cells from normal adult human pancreatic ducts transfected by the E6E7 gene of human papilloma virus 16. Am J Pathol 1996; 148: 1763–70.
17 Zhou J, Liu M, Aneja R, Chandra R, Lage H, Joshi HC. Reversal of P-glycoprotein-mediated multidrug resistance in cancer cells by the c-Jun NH_2-terminal kinase. Cancer Res 2006; 66: 445–52.
18 Turner J, Anderson R, Guo J, Beraud C, Fletterick R, Sakowicz R. Crystal structure of the mitotic spindle kinesin Eg5 reveals a novel conformation of the neck-linker. J Biol Chem 2001; 276: 25496–502.
19 Kick EK, Roe DC, Skillman AG, Liu G, Ewing TJ, Sun Y, *et al*. Structure-based design and combinatorial chemistry yield low nanomolar inhibitors of cathepsin D. Chem Biol 1997; 4: 297–307.
20 Gilbert SP, Mackey AT. Kinetics: a tool to study molecular motors. Methods 2000; 22: 337–54.
21 Lieber M, Mazzetta J, Nelson-Rees W, Kaplan M, Todaro G. Establishment of a continuous tumor-cell line (panc-1) from a human carcinoma of the exocrine pancreas. Int J Cancer 1975; 15: 741–7.
22 Even-Ram S, Doyle AD, Conti MA, Matsumoto K, Adelstein RS, Yamada KM. Myosin IIA regulates cell motility and actomyosin-microtubule crosstalk. Nat Cell Biol 2007; 9: 299–309.
23 Liu M, Aneja R, Sun X, Xie S, Wang H, Wu X, *et al*. Parkin regulates Eg5 expression by Hsp70 ubiquitination-dependent inactivation of c-Jun NH_2-terminal kinase. J Biol Chem 2008; 283: 35783–8.

Acta Pharmacologica Sinica (2011) 32: 1549–1554
 1671-4083/11 $32.00
www.nature.com/aps

Original Article

Tolerance and pharmacokinetics of single-dose intravenous hemoporfin in healthy volunteers

Pei-hong SUN[1], Xia ZHAO[1], Ying ZHOU[1], Yan LIANG[1], Hui-lin ZHANG[1], Yi-min CUI[1, *], Ji-ning TAO[2, *]

[1]*Department of Pharmacy, Peking University First Hospital, Beijing 100034, China;* [2]*Shanghai Fudan-Zhangjiang Bio-Pharmaceutical Co, Ltd, Shanghai 201203, China*

Aim: To investigate the safety, tolerability and pharmacokinetics of intravenous hemoporfin, a novel photosensitive drug for the treatment of port-wine stain (PWS), in healthy Chinese volunteers following single-dose administration.
Methods: Thirty-six healthy Chinese subjects were enrolled. The subjects were administered hemoporfin (2.5, 5, 7.5 or 10 mg/kg) via single-dose intravenous infusion. Pharmacokinetics of the drug were studied in the groups with doses of 2.5, 5 and 7.5 mg/kg, and tolerability was studied in all the 4 groups. Safety and tolerance were evaluated by monitoring adverse events and laboratory parameters, and pharmacokinetics were assessed by determining hemoporfin content with a validated high-performance liquid chromatography with fluorescence detection (HPLC/FLD) method.
Results: Mild and transient adverse events occurred in the trial (n=10), but none were serious, and no subjects were withdrawn from the trial. The gastrointestinal tract adverse events, such as nausea, stomach upset, abdominal pain and vomiting, were observed in the groups with doses of 7.5 and 10 mg/kg. Increased alanine aminotransferase (ALT) concentration was found in 3 subjects, and increased alkaline phosphatase (ALP) concentration in one subject. The half-life of hemoporfin for doses of 2.5, 5, and 7.5 mg/kg was 1.26 h, 1.31 h, and 1.70 h, respectively. C_{max} and AUC increased with dose for intravenous single-dose administration of hemoporfin in the 2.5, 5, and 7.5 mg/kg groups. Urinary excretion of hemoporfin within 12 h was less than 0.2%.
Conclusion: Hemoporfin is safe and well-tolerated in healthy Chinese volunteers at a single intravenous dose of up to 10 mg/kg. It was rapidly cleared from the blood and had a short half-life, which insures a short light-avoidance period.

Keywords: port-wine stain; photosensitive drug; hemoporfin; hematoporphyrin monomethyl ether; pharmacokinetics; tolerance; healthy volunteers; safety

Acta Pharmacologica Sinica (2011) 32: 1549–1554; doi: 10.1038/aps.2011.132; published online 31 Oct 2011

Introduction

Port-wine stain (PWS) is a congenital vascular malformation of the dermis that affects 0.3% to 0.5% of newborns and is commonly associated with psychosocial impairment[1]. In China, photodynamic therapy (PDT) has been applied for the treatment of PWS since 1991[2]. In this therapy, an exogenous chromophore-like porphyrin derivative is administered in the blood and concentrates in the ectatic capillaries. Subsequent irradiation using light of appropriate wavelength generates reactive oxygen species (ROS) in the presence of porphyrin derivatives and oxygen, selectively damaging the capillary wall[3]. PDT has been shown to be effective for PWS[4–6]. However, previously used photosensitive drugs, such as hematoporphyrin derivative (HpD) or Photocarcinorin, are complex mixtures of porphyrins containing more than 10 chemicals, with a long elimination half-life of >30 h[7]. This led to prolonged systemic photosensitivity to visible light, which lasted for one to three months following drug administration, limiting the clinical application of PDT[2, 8].

Hemoporfin (hematoporphyrin monomethyl ether) is a novel porphyrin-related photosensitive drug first developed in China. Hemoporfin consists of two positional isomers of 7(12)-(1-methoxyethyl)-12(7)-(1-hydroxyethyl)-3,8,13,17-tetramethyl-21*H*,23*H*-porphin-2,18-di-propionic acid (Figure 1). Previous reports have shown that hemoporfin has strong photodynamic effects and hemoporfin-based PDT induces significant cell death[9, 10]. An experimental study using chicken comb as an animal model of PWS showed that hemoporfin-based PDT could selectively destroy the microvasculature of the superficial portion of the dermis and thus cause the red combs to completely fade without damaging the overlying

* To whom correspondence should be addressed.
E-mail cuiymzy@126.com (Yi-min CUI);
taojining@hotmail.com (Ji-ning TAO)
Received 2011-06-20 Accepted 2011-09-14

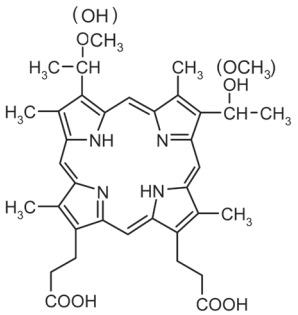

Figure 1. Chemical structure of hemoporfin.

skin[11]. Pharmacokinetic studies utilizing hemoporfin have been performed in various animals. Studies in rats showed that the drug was distributed rapidly to tissues, particularly to the liver, stomach, intestines, and spleen (JG Sun and GJ Wang, unpublished data). Hemoporfin was rapidly transferred from the central compartment to the peripheral compartment in rabbits following intravenous injection. Data for the elimination phase showed that hemoporfin was quickly eliminated (the elimination half-life was approximately 2.5 h) and not accumulated[12]. These preclinical data indicate that hemoporfin could achieve satisfactory clinical results and enable the use of shorter light-avoidance time periods during the course of therapy.

This Phase I clinical trial of hemoporfin was approved by the State Food and Drug Administration of China (SFDA, 2005L01082). The objectives of the present study were to assess the safety, tolerance and pharmacokinetics of hemoporfin in healthy Chinese volunteers. Results of this trial are herein reported to provide evidence for the next phase of clinical trials.

Materials and methods

This study was performed at Base for Drug Clinical trial and approved by the ethics committee of the First Hospital of Peking University, and conducted in accordance with the Declaration of Helsinki and Good Clinical Practice.

Subjects

Subjects (of Han nationality) were enrolled according to the following criteria: (i) 18–45 years old with body mass index (BMI) of 19–27 kg/m^2; (ii) normal vital signs, physical and laboratory findings, negative for HIV and hepatitis B/C, no abnormalities on ECG, no history of heart, liver, renal, digestive system disorders, nervous or psychological disease or metabolic disorders; (iii) no history of allergy to any components of hemoporfin for injection; (iv) no smoking, drinking or drug addiction prior to or during the study; (v) no pregnancy or lactation for female subjects; (vi) no drugs or other medication, or participation in any clinical trial that might interfere with absorption, distribution, metabolism or excretion of hemoporfin or be harmful to human organs three months prior to or during the study; and (vii) voluntary signature on an informed consent form. Subjects with systemic disease or inherited/acquired coagulation defects were excluded.

Drug

Hemoporfin for injection was formulated and supplied by Shanghai Fudan-Zhangjiang Bio-Pharmaceutical Co, Ltd (Shanghai, China). It was a sterile lyophilized powder containing 100 mg of hemoporfin per vial.

Study design

A randomized, open-label, dose-escalation study was conducted to assess the safety and tolerance of hemoporfin. Thirty-six healthy Chinese subjects were enrolled, ten subjects each in the 2.5, 5, and 7.5 mg/kg dose groups and six subjects in the 10 mg/kg dose group. The trial was designed to begin with the 2.5 mg/kg dose group and not proceed to the higher dose group until the safety and tolerance to the lower doses were confirmed. Within each cohort, toxicity was considered unacceptable if any subject experienced a severe adverse event or half of the subjects in any dose group experienced mild adverse events that were attributed to the study medication and were not resolved within a reasonable time period. Pharmacokinetics of hemoporfin were studied in the 2.5, 5, and 7.5 mg/kg dose groups, and tolerability was studied in all four groups. All subjects were required to fast overnight (10 h) before and for 4 h following administration. After drug administration, patients were instructed to avoid exposure to sunlight or bright indoor light for one week.

The medication was prepared in normal saline (60 mL) and was administered by iv infusion over a 20-min period, using an injection pump at a constant speed. The solution was protected from light and used within 4 h after preparation. A volume of 2 to 4 mL of normal saline was intravenously injected following the end of infusion of the drug to reduce drug concentration in the vessels. This prevented the occurrence of photosensitive reactions at the injection site.

Safety and tolerance

All subjects were maintained in the study unit and continuously observed. The variables used to assess safety and tolerability included adverse events, physical examination, vital signs, and 12-lead electrocardiogram, routine blood and urine test, coagulation test and blood biochemical test. The blood biochemical test included urea nitrogen (BUN), creatinine (Cr), uric acid (UA), total protein (TP), albumin (ALB), albumin/globulin ratio (A/G), alanine aminotransferase (ALT), aspartic transaminase (AST), γ-glutamyltransferase (GGT), alkaline phosphatase (ALP), total bilirubin (TBIL), direct bilirubin (DBIL), fasting blood glucose (GLU), triglyceride (TG) and total cholesterol (TCHO). Safety tests were conducted 24 to 48 h before and on days 1, 2, 3, and 7 after drug administration.

Adverse event data were obtained voluntarily from subjects and by daily monitoring and questioning of subjects by study personnel. The expected adverse event associated with hemoporfin was photosensitivity reaction. All subjects who received hemoporfin are photosensitive and must observe pre-

cautions to avoid exposure of skin and eyes to direct sunlight or bright indoor light (*eg*, from examination lamps, including dental lamps, operating room lamps, unshaded light bulbs at close proximity) for at least seven days. Adverse events were evaluated for their intensity, seriousness, and relationship to the study medication. Adverse events were defined as mild (awareness of a sign or symptom but easily tolerated), moderate (discomfort sufficient to cause interference with normal activities), or severe (incapacitating, with an inability to perform normal activities). Causality between the study drug and an adverse event, described as "certainly," "probably," "possibly," "suspected," or "not related," was defined using the criteria developed by the World Health Organization[13].

Sample collection

Blood samples (3 mL) were collected into tubes containing ammonium heparinate and centrifuged immediately to obtain plasma samples. These samples were then transferred to polypropylene vials and kept frozen below -20 °C until analyses were conducted. Samples were collected as follows: prior to dosing (0 h); 5, 10, and 20 min during dosing; and 5, 10, 20, 30 min and 1, 1.5, 2, 3, 4, 6, 8 h post-dosing. Urine was collected prior to dosing (10 mL), and was also pooled at 0 to 2, 2 to 4, 4 to 8, and 8 to 12 h post-dosing. Preliminary analyses showed that no analyte was present in urine 12 h following drug administrations. After the total volume of urine for each time range was measured, 10 mL was maintained at -20 °C until analyses were conducted.

Drug analysis

Concentrations of hemoporfin in plasma and urine were determined using high-performance liquid chromatography with fluorescence detection (HPLC/FLD). Fluorescein was used as the internal standard. This method was previously developed and fully validated for determination of hemoporfin in plasma[14]. In brief, plasma (0.5 mL) and urine samples (diluted) were pretreated using liquid-liquid extraction with ethyl acetate, and the supernatant was evaporated to dryness and reconstituted with 200 μL of mobile phase. The analyte was separated on a Diamonsil C18 column (4.6 mm×150 mm, 5 μm) by isocratic elution with tetrahydrofuran-20 μmol/L sodium acetate buffer (adjusted to pH 6.0 with acetic acid; 40:60, *v/v*) at a flow rate of 1.0 mL/min and analyzed using a fluorescence detector with the excitation and emission wavelengths set at 395 and 613 nm, respectively. Analyses of blank serum and urine indicated no interference of endogenous components with detection of hemoporfin in the final extract. The weighted (1/x) calibration curve was linear over the plasma concentration range of 0.025–5 μg/mL and urine concentration range of 0.025–1 μg/mL with a correlation coefficient (r) of 0.9982 and 0.9998, respectively. The lower limit of quantification for hemoporfin was 0.025 μg/mL. The inter- and intra-day accuracies and precisions were all within 10%. In plasma, the mean method recoveries were 95.1%–97.3% and the mean extraction recoveries were 55.9%–61.4%. In urine, the mean method recoveries were 92.7%–101.7% and the mean extraction recoveries were 75.9%–79.0%.

Pharmacokinetic calculations

The mean hemoporfin concentration in plasma at each time point and in urine over each interval was determined by averaging of the data, and pharmacokinetic parameters were calculated using Winnonlin 5.0 (Pharsight Corporation; Sunnyvale, CA, USA). Single-dose pharmacokinetic parameters were calculated from plasma concentration-time data by the non-compartment method. Peak plasma concentration (C_{max}) and the time to reach peak concentration (T_{max}) were recorded from experimental observations. The parameters of the model were used to calculate values for clearance (CL), volume of distribution [V(L)], elimination half-life ($t_{1/2}$), area under the curve (AUC) from time zero to infinity ($AUC_{0-\infty}$), AUC from time zero to the time of the last quantifiable concentration (AUC_{0-tn}), mean residence time (MRT) from time zero to infinity ($MRT_{0-\infty}$), MRT from time zero to the time of the last quantifiable concentration (MRT_{0-tn}), and the elimination rate constant (K_e). The fraction of the drug excreted in urine (Ae%) was calculated by dividing Ae by the dose administered, where Ae is the cumulative amount of unchanged drug excreted into the urine.

Statistical analyses

The analyses of safety were performed with SPSS (version 11.5). Descriptive statistics were used to summarize demographic data and assess safety variables including adverse events, laboratory assays, vital signs and electrocardiograms. The variations of laboratory parameters before and after drug administration were analyzed using paired t-test and the variances among groups were analyzed using ANOVA. Adverse events are summarized by reported frequencies and percentages.

Results

Study population

Thirty-six (19 male, 17 female) subjects were enrolled in this study. All subjects completed the trials as planned. Demographic characteristics of the study population are presented in Table 1. There were no significant differences in age, weight, height or BMI among the four groups.

Safety and tolerability

A single dose of hemoporfin was well tolerated in these healthy volunteers at doses up to 10 mg/kg, with no severe adverse events occurring during the study, and all subjects were in good compliance. The most commonly reported adverse events were related to the gastrointestinal tract. Nausea (3 subjects, 8.3%), upset stomach (2 subjects, 5.6%), abdominal pain (2 subjects, 5.6%) and vomiting (1 subjects, 2.8%) were observed in the 7.5 mg/kg and 10 mg/kg dose groups. Increased ALT concentrations were found in three subjects, one in the 2.5 mg/kg group and two in the 7.5 mg/kg group. Increased ALP concentration was also found in one subject in the 5 mg/kg group. High ALT and ALP concentrations

Table 1. Demographic characteristics of the study population. All values are given as mean±SD (range) and are considered significantly different when $P<0.05$.

Group	*n*	Gender (Male/Female)	Age (years)	Weight (kg)	Height (m)	BMI (kg/m^2)[a]
2.5 mg/kg	10	5/5	34.9±3.0 (30–39)	64.3±8.8 (50–75)	1.62±0.08 (1.49–1.72)	24.5±2.3 (20.3–26.7)
5.0 mg/kg	10	5/5	35.1±3.8 (30–39)	60.4±7.2 (50–73)	1.62±0.07 (1.51–1.76)	22.9±1.7 (20.7–25.5)
7.5 mg/kg	10	5/5	35.7±2.9 (30–39)	61.0±8.0 (50–76)	1.62±0.07 (1.54–1.75)	23.2±2.1 (20.3–26.8)
10 mg/kg	6	4/2	36.8±2.1 (33–39)	61.0±6.4 (54–66)	1.65±0.07 (1.55–1.70)	22.5±0.8 (20.8–23.0)

[a] BMI, body mass index.

(ALT<3×ULN, ALP<2×ULN; where ULN=upper limit of normal) were observed on d 4 or d 7 following drug administration but returned to normal on d 14 without additional treatment. The aforementioned adverse events were considered to be related to the study drug; ten of the thirty-six (27.8%) hemoporfin-treated subjects had drug-related adverse events (details shown in Table 2). All adverse events and laboratory abnormalities were mild and tolerable, did not lead to discontinuation of the study, and recovery was achieved without treatment. Blood pressure, pulse rate, body temperature, electrocardiographic findings, physical examination findings, hematology results, and urinalysis results following dosing did not show any clinically relevant differences from baseline.

Table 2. Drug-related adverse events reported during single-dose iv administration of hemoporfin in the studied healthy Chinese subjects.

Subject No	Dose (mg/kg)	Gender	Drug-related adverse events reported
101	2.5	M	ALT concentration increased
202	5	M	ALP concentration increased
301	7.5	M	ALT concentration increased
305	7.5	M	ALT concentration increased
307	7.5	F	Nausea and abdominal pain
310	7.5	F	Abdominal pain
402	10	M	Upset stomach
404	10	F	Nausea
405	10	F	Upset stomach
406	10	F	Nausea and vomiting

F, female; M, male.

Pharmacokinetics

The mean plasma concentration-versus-time profiles after the administration of a single dose of hemoporfin are shown in Figure 2. As expected, C_{max} was observed at 20 min following intravenous administration (at the end of the infusion). Plasma hemoporfin levels rapidly decreased, exhibiting a bi-exponential decline with a rapid distribution phase followed by a moderately rapid elimination phase. Hemoporfin was not detectable in most plasma samples after 6 h.

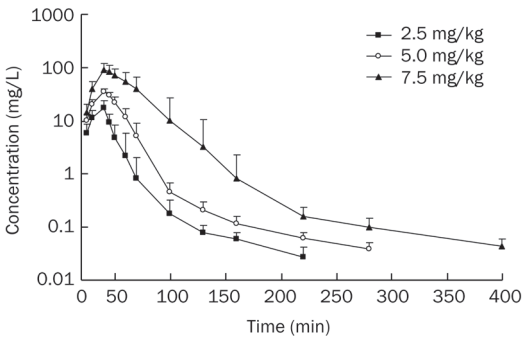

Figure 2. Plasma concentration-time curves of hemoporfin following iv administration of doses of 2.5, 5, 7.5 mg/kg. The data are the means±standard deviations for 10 subjects in each group.

The mean values for the pharmacokinetic parameters of hemoporfin are summarized in Table 3. Hemoporfin had a short half-life ($t_{1/2}$): 1.26 h, 1.31 h, and 1.70 h for doses of 2.5, 5, and 7.5 mg/kg, respectively, and a short mean residence time (MRT): 12.2 min, 17.7 min, and 26.6 min for doses of 2.5, 5, and 7.5 mg/kg, respectively. For doses of 2.5, 5, and 7.5 mg/kg, mean C_{max} values were 17.49, 35.72, and 92.18 mg/L, respectively, and the mean $AUC_{0-\infty}$ values were 6.41, 17.61, and 64.39 mg·h/L, respectively. C_{max} and AUC both increased with dosage.

For the 2.5, 5, and 7.5 mg/kg dose groups, urinary excretion of the prototype drug within a 12-h period after drug administration was 0.14%±0.07%, 0.15%±0.03%, and 0.12%±0.05%, respectively.

Significant differences were observed in pharmacokinetic parameters between male and female subjects in the 7.5 mg/kg dose group. Plasma concentrations of hemoporfin in female subjects were higher than those in the male subjects at the same time point following drug administration. For male and female subjects, the mean C_{max} values were 67.64±7.97 mg/L and 116.72±20.27 mg/L, respectively; the mean AUC_{0-tn} values were 39.99±4.96 mg·h/L and 88.58±36.00 mg·h/L, respectively; the mean volume values were 30.9±4.9 L and 12.4±4.5 L, respectively; and the mean CL values were 11.5±1.1 L/h and 5.5±1.3 L/h, respectively. There were no significant differences in pharmacokinetic parameters in plasma between male and female subjects in the 2.5 and 5 mg/kg groups.

Table 3. Pharmacokinetic parameters of hemoporfin following single ascending intravenous infusions. Values are expressed as mean±standard deviation.

	Hemoporfin dose (mg/kg)				
	2.5 (*n*=10)	5.0 (*n*=10)	7.5 (*n*=10)	7.5 (male, *n*=5)	7.5 (female, *n*=5)
AUC_{0-tn} (mg·h/L)	6.34±2.82	17.53±3.47	64.28±35.25	39.99±4.96	88.58±36.00
$AUC_{0-\infty}$ (mg·h/L)	6.41±2.82	17.61±3.47	64.39±35.28	40.09±4.98	88.69±36.04
C_{max} (mg/L)	17.49±7.05	35.72±4.54	92.18±29.66	67.64±7.97	116.72±20.27
T_{max} (min)	20±0	20±0	20±0	20±0	20±0
$t_{1/2}$ (h)	1.26±0.33	1.31±0.33	1.70±0.27	1.85±0.14	1.55±0.29
MRT_{0-tn} (min)	12.2±3.5	17.7±3.0	26.6±6.3	22.9±1.6	30.3±7.1
$MRT_{0-\infty}$ (min)	15.5±2.9	19.4±2.7	27.5±6.0	24.0±1.7	31.0±7.0
CL (L/h)	29.8±15.2	17.3±3.8	8.5±3.4	11.5±1.1	5.52±1.3
V (L)	55.9±34.9	32.9±11.2	21.6±10.7	30.9±4.9	12.4±4.5
K_e (h^{-1})	0.58±0.15	0.56±0.16	0.42±0.077	0.38±0.033	0.46±0.088
Ae % (%)	0.14±0.07	0.15±0.03	0.12±0.05	0.13±0.04	0.11±0.06

Discussion

This study showed that iv administration of hemoporfin at doses from 2.5 to 10 mg/kg is safe and well tolerated. Adverse events were generally mild in intensity and required no treatment or intervention. Nausea, upset stomach, abdominal pain and vomiting were the most frequently reported adverse events considered to be related to hemoporfin. These events were dose dependent and found only in the high-dose groups of 7.5 mg/kg and 10 mg/kg. Increases in ALT and ALP concentrations were the most frequently reported laboratory abnormalities. They might be caused by individual variances as they were not relevant to the dose and no significant differences among the different groups were found when analyzed using ANOVA.

Hemoporfin is primarily cleared by the liver, with less than 0.2% of the drug excreted in urine. Hemoporfin has a molecular weight of 612.72 and is poorly water soluble, which favor hepatobiliary elimination. A previous pharmacokinetic study in rats showed that following a single intravenous dose of 10 mg/kg hemoporfin, biliary excretion within 12 h was about 81.8%±9.0%. Urinary excretion within 48 h was about 0.19%±0.17%. Fecal excretion within 48 h was about 57.55%± 15.5% (JG Sun and GJ Wang, unpublished data). The results showed that hemoporfin was excreted predominantly into the bile and eventually into the feces.

After iv administration, hemoporfin was distributed rapidly throughout the body during the first 1 to 3 h, followed by an elimination phase with a $t_{1/2}$ of approximately 1 to 2 h. For the 2.5 and 5 mg/kg dose groups, the mean C_{max} and AUC increased proportionately with dosage. For the 7.5 mg/kg dose group, drug metabolism in the plasma of female subjects was different than the male subjects. The mean C_{max} and AUC of male subjects increased proportionately with dosage, but the C_{max} and AUC values in the female subjects increased significantly to almost twice the values in the male subjects. The *V* and CL values of the females were half of the males. No significant differences in drug metabolism in plasma were observed between male and female subjects in the 2.5 and 5 mg/kg groups. These data suggested that females given the same high dose would have substantially decreased hemoporfin clearance and higher levels of systemic exposure. The gender differences indicate that female subjects should be observed for variations in drug metabolism and drug reaction when receiving a large dose of hemoporfin.

The presence of the decreased hemoporfin clearance in female subjects at the high dose needs to be confirmed in clinical trials with larger sample sizes. The mechanisms responsible for the phenomenon are still under investigation. Drug transporters such as P-glycoprotein are likely to be involved in the gender differences. P-glycoprotein is an energy-dependent efflux pump responsible for transporting drugs (usually high molecular weight substances) out of cells and can be expressed in normal tissues such as the luminal surface of biliary hepatocytes[15]. This pump might play an important role in the elimination of hemoporfin to the bile. P-glycoprotein level in female liver is only 30% to 50% of that in male liver[16], and P-glycoprotein may be saturated at higher drug concentrations, so the low P-glycoprotein level in female liver may account for the decreased clearance of hemoporfin in females given large doses.

Compared to the 7.5 and 10 mg/kg dose groups, fewer adverse events were found in the two lower-dose groups, as expected. In addition, hemoporfin exhibited linear pharmacokinetics and no gender-dependent differences in the 2.5 and 5 mg/kg dose groups. Based on the above results, we decided to choose the dosage range from 2.5 to 5 mg/kg for future phase II clinical trials.

A goal of PDT for the treatment of PWS is to selectively destroy the abnormal vasculature but spare adjacent normal skin structures. It is very important to determine the light dose and the time between drug dosing and light application. While shining the light at the PWS lesions during or shortly

following iv injection of a photosensitizing drug, when the drug is still highly concentrated inside the circulation (including the PWS vessels) and undergoes little diffusion to the surrounding tissue, the photochemically-induced reactive oxygen species (ROS) would most likely be located within the vessels and, therefore, selectively damage the vascular endothelial cells, induce thrombosis and obstruct capillary vessels. Because the amount of photosensitizing drug outside the vessels is low, the vascular-acting, PDT-induced skin lesion is negligible or reversible[8]. For the 2.5 and 5 mg/kg dose groups, the pharmacokinetics of hemoporfin indicate that within 50 min after infusion, hemoporfin concentration in vessels were maintained at relatively high levels. Thereafter, the vascular concentrations decreased to a low level and it was presumed that the drug achieved a significant extravascular distribution. This suggests that light application should be within certain time limits (*ie*, 50 min after infusion) in hemoporfin-based PDT for the treatment of PWS.

The short $t_{1/2}$ of hemoporfin (1–2 h) suggests that no accumulation would be expected with repeated doses at intervals of one week or shorter. The current recommended dosing schedule is every two months for patients with PWS. The rapid elimination of hemoporfin contributed to a short light-avoidance period. In this study, precautions to avoid photosensitivity were required for one week after treatment, and no photosensitivity reaction was observed throughout the study.

In conclusion, hemoporfin is safe and well tolerated in healthy Chinese subjects at a single dose of between 2.5 mg/kg and 10 mg/kg. No serious adverse events occurred during the study and all subjects remained in good compliance. C_{max} and AUC values increased with dose for intravenous, single-dose administration of hemoporfin in the 2.5, 5, and 7.5 mg/kg groups. Hemoporfin is rapidly cleared from the blood and has a short $t_{1/2}$ of <2 h, which supports a short light-avoidance period of one week.

Acknowledgements

We appreciate all the volunteers participating in this research. We are grateful to the nurses who participated in this study. We appreciate our colleagues X LIU and Q XIANG, who provided editorial assistance.

This study was sponsored by Shanghai Fudan-Zhangjiang Bio-Pharmaceutical Co, Ltd. The work was funded by National Mega Project on Major Drug Development Research (2009ZX09401-001), key project of Science and Technology commission of Shanghai Municipality (064319003).

Author contribution

Yi-min CUI, Pei-hong SUN, and Ji-ning TAO designed research; Pei-hong SUN, Xia ZHAO, Ying ZHOU, Yan LIANG, and Hui-lin ZHANG performed research; Xia ZHAO and Ying ZHOU analyzed data; Pei-hong SUN wrote the paper; Yi-min CUI and Ji-ning TAO critically revised the manuscript.

References

1 Jacobs AH, Walton RG. The incidence of birthmarks in the neonate. Pediatrics 1976; 58: 218–22.
2 Gu Y, Li J, Shan H, Wang K, Jiang Y, Zhang Y, *et al*. Clinical application of copper vapor laser in pdt for fifty cases of PWS. Chin J Laser Med Surg 1994; 3: 215–7.
3 Jasim ZF, Handley JM. Treatment of pulsed dye laser-resistant port wine stain birthmarks. J Am Acad Dermatol 2007; 57: 677–82.
4 Jiang L, Gu Y, Li X, Zhao X, Li J, Wang K, *et al*. Changes of skin perfusion after photodynamic therapy for port wine stain. Chin Med J (Engl) 1998; 111: 136–8.
5 Ouyang T, Cheng Y, Xing X. Clinical application of photodynamic therapy combined with non-coherent light (red light) for treatment of port-wine stains. Chin J Plast Surg Burn 1998; 14: 163–5.
6 Chen Y, Li H, Liu S. Treatment of nevas flammeus with copper vapor laser in photodynamic therapy. Acta Acad Med Hubei 1999; 20: 162–3.
7 Xu DY, Editor. Tumor photodynamic therapy. Beijing: Chinese Medical Science and Technology Press; 1996.
8 Qin ZP, Li KL, Ren L, Liu XJ. Photodynamic therapy of port wine stains-a report of 238 cases. Photodiagn Photodyn Ther 2007: 4: 53–9.
9 Song K, Kong B, Qu X, Li L, Yang Q. Phototoxicity of hemoporfin to ovarian cancer. Biochem Biophys Res Commun 2005; 337: 127–32.
10 Wei Y, Kong B, Song K, Qu X, Jin Q, Yang Q. Involvement of mitochondria-caspase pathway in hemoporfin-mediated cell death. Photochem Photobiol 2007; 83: 1319–24.
11 Liu F, Gu Y, Liu H, Fu Q, Zhu J, Pan Y, *et al*. An experimental study on the comparison of photodynamic effects of hematoporphyrin monomethyl ether and hematoporphyrin derivative. Chin J Laser Med Surg 2001; 10: 69–73.
12 Chen WH, Yu JX, Yao JZ, Shen WD, Liu JF, Xu DY. Pharmacokinetic studies hematoporphyrin monomethyl ether: a new promising drug for photodynamic therapy of tumors. Chin J Laser Med Surg 2000; 9: 105–8.
13 Du WM, Wang YM, Cheng NN. ADR confirmation and its research methods (2). Chin J Pharmacovigilance 2005; 2: 11–3.
14 Li P, Sun JG, Huang CR, Xu MJ, Li J, Lu H, *et al*. Determination of hematoporphyrin monomethyl ether in dogs plasma by HPLC using fluorescence detection. Chin J Laser Med Surg 2005; 14: 212–6.
15 Yu DK. The contribution of P-glycoprotein to pharmacokinetic drug-drug interactions. J Clin Pharmacol 1999; 39: 1203–11.
16 Schuetz EG, Furuya KN, Schuetz JD. Interindividual variation in expression of P-glycoprotein in normal human liver and secondary hepatic neoplasms. J Pharmacol Exp Ther 1995; 275: 1011–8.

Acta Pharmacologica Sinica (2011) 32: 1555–1560
 1671-4083/11 $32.00
www.nature.com/aps

Original Article

Pharmacokinetics and safety of calcium *L*-threonate in healthy volunteers after single and multiple oral administrations

Hong-yun WANG, Pei HU, Ji JIANG*

Clinical Pharmacology Research Center, Peking Union Medical College Hospital, Chinese Academy of Medical Science and Peking Union Medical College, Beijing 100730, China

Aim: To evaluate the pharmacokinetics of *L*-threonate after single or multiple oral administrations and its safety profile in healthy Chinese volunteers.
Methods: This was an open-label, single- and multiple-dose study. The subjects were assigned to receive a single dose, 675, 2025, or 4050 mg, of calcium *L*-threonate (n=12) or repeated doses of 2025 mg twice daily for 4 d (n=12). Serial plasma and urine samples were analyzed with HPLC-MS/MS. Pharmacokinetic parameters of *L*-threonate were calculated using non-compartmental analysis with WinNonlin software.
Results: In the single dose group, C_{max} reached at 2.0 h and the mean $t_{1/2}$ was approximately 2.5 h. Area under curve (AUC) and C_{max} increased with dose escalation, but dose proportionality was not observed over the range of 675 to 4050 mg. AUC and C_{max} in the fasted subjects were lower compared with those in the non-fasted subjects. Cumulative urinary excretion of *L*-threonate over 24 h represented 5.9% of the administered dose with a mean Cl/r of 0.8 L/h. In the multiple-dose study, no accumulation appeared upon repeated doses of 2025 mg twice daily for 4 d. There were no serious adverse events that occurred during this study.
Conclusion: Calcium *L*-threonate was well tolerated in healthy Chinese subjects, with no pattern of dose-related adverse events. Plasma exposure increased with dose escalation, but linear pharmacokinetics were not observed over the studied doses. *L*-threonate was absorbed rapidly, and its absorption was enhanced by food intake. No systemic accumulation appeared after repeated administrations.

Keywords: osteoporosis; calcium *L*-threonate; *L*-threonic acid; pharmacokinetics; safety; Chinese; open-label, single dose; multiple dose

Acta Pharmacologica Sinica (2011) 32: 1555–1560; doi: 10.1038/aps.2011.138; published online 10 Oct 2011

Introduction

Osteoporosis is a bone disease that leads to an increased risk of fracture. Due to its significant prevalence worldwide, osteoporosis is now considered a serious public health concern. In 1992, there were 1.6 million people worldwide suffering from this disease[1], and this number is estimated to reach 6 million by 2050[2]. Aging of populations worldwide is responsible for the major increase in the incidence of osteoporosis[3]. Osteoporosis can be treated with lifestyle changes and medications. Typical medications include bisphosphonates, estrogen analogs, raloxifene, calcium salts and sodium fluoride. These medications are classified as antiresorptive or bone anabolic agents. Antiresorptive agents reduce bone resorption, whereas bone anabolic agents build bone, rather than inhibit resorption[4].

L-Threonic acid is an active metabolite of vitamin C[5–8]. It has been reported that *L*-threonic acid exhibits significant stimulatory action on vitamin C uptake and prolongs the retention of vitamin C in human T-lymphoma cells[9, 10]. It is also well known that vitamin C is a marker for osteoblast formation and has been shown to stimulate procollagen and enhance collagen synthesis[11–14]. Therefore, *L*-threonic acid may play a role in the mineralization process through its positive action on vitamin C. This hypothesis was confirmed in 1999 by Rowe DJ[15]. It was reported that *in vitro* treatment with ascorbate-containing vitamin C metabolites enhanced the formation of the mineralized nodules and collagenous proteins and that *L*-threonate was one of the metabolites that was found to influence the mineralization process[15]. Recently, a preclinical study was performed to investigate the effect of *L*-threonate on bone resorption of rabbit osteoclasts[16]. This study contained a total of six culture groups, including one control group and

* To whom correspondence should be addressed.
E-mail pk.frosh@gmail.com
Received 2011-05-26 Accepted 2011-08-17

five groups treated with drugs (calcium *L*-threonate, sodium *L*-threonate, alendronate, 17β-estradiol and calcium gluconate). The levels of type I collagen C-telopeptide (CT_x) and bone slice resorptive area were measured. This study found that *L*-threonate, especially calcium *L*-threonate, inhibited the bone resorption of osteoclasts *in vitro*; however, the reductive effects on the CT_x level and resorptive area were not as significant as alendronate and 17β-estradiol at the same concentration.

Calcium *L*-threonate ((*2R*,*3S*)-2,3,4-trihydroxy butyric acid calcium) (Figure 1) is a novel drug developed for the treatment of osteoporosis and as a calcium supplement. Phase I clinical trials of calcium *L*-threonate, including tolerance, pharmacokinetics and calcium absorption evaluation, were performed in Peking Union Medical College Hospital. In this paper, the pharmacokinetics of *L*-threonate after single or multiple oral administrations and its safety profile in healthy Chinese volunteers are presented.

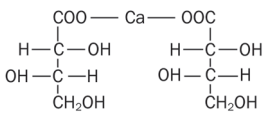

Figure 1. Calcium *L*-threonate, (*2R*,*3S*)-2,3,4-trihydroxy butyric acid calcium.

Materials and methods

Drugs, chemical standards and reagents

Calcium *L*-threonate tablets (675 mg/tablet) and chemical standards of *L*-threonic acid (purity 99.8%) were provided by JuNeng Pharmaceutical Co (Beijing, China). HPLC-grade acetonitrile and acetic acid were purchased from ThermoFisher (New Jersey, USA). Other reagents utilized were all of analytical grade, and distilled water was produced by a Milli-Q water purification system (Millipore, Bedford, USA).

Subjects

This study was conducted in accordance with Good Clinical Practice regulations, the ethical principles stated in the Declaration of Helsinki, and other applicable regulatory requirements. Approval of the study was obtained from the Ethical Committee of the Peking Union Medical College Hospital (Beijing, China) prior to subject enrollment. All of the subjects provided written informed consent after the nature of the study was fully explained.

The subjects were enrolled based on the following inclusion criteria: men and women of Han Chinese ethnicity between 19 and 40 years of age with a body mass index of 19 to 25 kg/m^2; and no evidence of clinically significant abnormalities in cardiac, hepatic, renal, pulmonary, neurological, gastrointestinal, hematological or psychiatric function, as determined by medical history, physical examination and laboratory screens. Pregnant and lactating women were excluded from the study. Female subjects were required to be surgically incapable of pregnancy or to practice effective double-barrier birth control methods. Exclusion criteria included a history of a clinically important disease that, in the opinion of the investigator, might place the subject at risk; a history of allergy to drugs; participation in a clinical study during the preceding 4 weeks; blood donation within a period of 4 weeks prior to study drug administration; positive test results for HBV, hepatitis C virus (HCV), or human immunodeficiency virus (HIV); positive test results for drugs of abuse; or a history of alcohol abuse. Additionally, all of the enrolled subjects were required to avoid vitamin C medications 1 month prior to and during the study.

Study design

This was a phase I, open-label, single and multiple-dose study. In the single-dose study, a randomized, 4-way crossover design was used, and the washout period between dosing was 1 week. Twelve male Chinese subjects were randomized into 4 treatment groups in which they received a single oral dose of 675, 2025, or 4050 mg calcium *L*-threonate after an overnight fasting or 2025 mg within 30 min after consuming breakfast. A standard meal was provided at 4 and 10 h after dosing. Serial blood samples (3 mL at each time point) were collected in heparinized vacutainers at the following time points: 0 (pre-dose), 0.5, 1, 1.5, 2, 2.5, 3, 3.5, 4, 6, 8, 12, 24, and 48 h. Fractionated urine samples were collected at the following time intervals: 0 (pre-dose), 0–3, 3–6, 6–9, 9–12, and 12–24 h. In the multiple-dose study, 14 healthy Chinese subjects (50% male and 50% female) received an oral dose of 2025 mg after overnight fasting on the morning of d 1 and d 7, and serial blood samples (3 mL at each time point) were drawn at the following time points: 0 (pre-dose), 0.5, 1, 1.5, 2, 2.5, 3, 3.5, 4, 6, 8, 12, 24, and 48 h. From d 3 to d 6, the subjects received an oral dose of 2025 mg twice daily with a dose interval of 12 h. Blood samples prior to dosing (0 h) were collected in the morning for trough plasma level monitoring. During the study, blood samples were separated by centrifugation at 2500×*g* for 10 min, and plasma was collected. The volume of urine samples at each time interval was recorded, and 10 mL was collected. All of the plasma and urine samples were stored at -30 °C until analysis.

All of the subjects were hospitalized in the phase I unit ward of Peking Union Medical College Hospital during the study. The subjects were required to refrain from smoking, alcohol and caffeinated beverages. Strenuous exercise was not allowed on each dosing day. Medications (including vitamins, herbal supplements and traditional Chinese medicines) were not permitted, although paracetamol (acetaminophen) was allowed as a mild analgesic.

Plasma and urine sample analysis

The concentrations of *L*-threonate in plasma and urine samples were determined using the high-performance liquid chromatography-tandem mass spectrometry (HPLC-MS/MS) method developed in our lab[17]. Briefly, 0.1 mL volume of plasma sample was vortexed with 0.3 mL of methanol for 3 min. After centrifugation at 10 000×*g* for 5 min, 0.2 mL of

the supernatant was collected and diluted with 1.5 mL of water; 20 μL of the sample was injected for analysis. Each 0.1 mL volume of urine was diluted with 2 mL of water and vortexed for 1 min, and then 20 μL of the sample was injected for analysis. The analyte was separated on an YMC J'Sphere C_{18} column (50 mm×4.6 mm; id, 3.5 μm)(Waters, MA; USA) with methanol-acetonitrile-10 mmol/L ammonium acetate (20:5:75, *v/v*) as the mobile phase and at a flow rate of 0.2 mL/min. Detection was performed on a Quattro Ultima triple-quadruple mass spectrometer (Waters, MA, USA) equipped with an electrospray source (ESI) operated in the negative ionization mode. Multiple reactions monitoring (MRM) was used to monitor *L*-threonate by the ion transition of *m/z* 134.5→74.7. The linear calibration curves of *L*-threonate in plasma and urine were obtained over the concentration range of 0.25 to 50 mg/L and 2.5 to 500 mg/L. Low-, medium-, and high-quality control samples (plasma: 0.75, 12.5, 40 mg/L; urine: 7.5, 125, 400 mg/L) were analyzed with the study samples to ensure the quality of analysis.

Pharmacokinetic and statistical analysis

Pharmacokinetic analysis was performed with WinNonlin software (Pharsight 4.0.1; NC, USA) utilizing non-compartmental analysis. The maximum plasma drug concentration (C_{max}) and time to C_{max} (t_{max}) were directly obtained from the plasma concentration-time curves. The terminal-phase elimination half-life ($t_{1/2}$) was calculated as $0.693/\lambda_z$, where λ_z was the slope of the apparent elimination phase of the natural logarithmic (ln) transformation of the plasma concentration-time curve, which was estimated using liner regression. The area under the plasma concentration-time curve from time zero to t (AUC_{0-t}), where t is the time of last measurable sample, was calculated according to the linear trapezoidal rule. The AUC from time zero to infinity ($AUC_{0-\infty}$) was estimated as $AUC_{0-t}+C_t/\lambda z$, where C_t was the plasma concentration of the last measurable sample. Apparent total clearance (*Cl/F*) was calculated as $Dose/AUC_{0-\infty}$ or $Dose/AUC_{ss}$ and apparent total volume of distribution (V_z/F) as calculated as CL/λ_z. Renal clearance was estimated as Au_{0-t}/AUC_{0-t}, where Au_{0-t} was the cumulative amount of drug excreted in urine from time zero to t (24 h). Attainment of steady state by d 7 was evaluated by regressing the natural logarithmic (ln) transformation of trough concentrations on d 3, 4, 5, and 6 over time. Steady-state was attained if the slope was not statistically different from zero. The steady-state AUCs (AUC_{ss}) over the dosing interval (τ=12 h) and C_{avg} ($AUC_{ss/\tau}$) were calculated. The degree of fluctuation (DF%) was calculated as $(C_{max}-C_{min})/C_{avg}\times 100\%$. Accumulation ratios were defined as the steady-state $AUC_{0-\tau}$ to the single-dose $AUC_{0-\tau}$ ratio or the steady state C_{max} to the single-dose C_{max} ratio, namely, R_{AUC} = $AUC_{0-\tau}$ (steady state)/$AUC_{0-\tau}$ (single-dose) (τ=12 h) and $R_{C_{max}}=C_{max}$ (steady state)/C_{max} (single-dose), respectively.

Statistical analysis was performed using SPSS software (version 11.0; SPSS Inc; Chicago, IL, USA). The results were expressed as the mean±SD. The linearity of plasma *L*-threonate pharmacokinetics within the 675 to 4050 mg dose range was assessed with respect to pharmacokinetic parameters underlying drug exposure, *ie*, AUC and C_{max}. After log-transformation, 90% confidence intervals (CI_s) for the ratios of dose-normalized, geometric mean values of AUC and C_{max} were calculated using mixed-effects models. The approach was developed by Smith *et al* on the basis of the criteria for the assessment of bioequivalence[18]. Dose proportionality is declared if the CI for the dose ratio is contained within the limits, 80%–125% for AUC and 70%–143% for C_{max}. Based on a 2025 mg dose level, the food intake effect on the pharmacokinetics of *L*-threonate was assessed between the fasted and fed subjects using a paired-*t* test, where $P\leq 0.05$ was considered statistically significant.

Safety evaluation

Safety and tolerability were evaluated through adverse events reported by the investigators and subjects and based on clinical laboratory measurements (blood chemistry, hematology, urinalysis, and liver functions), 12-lead ECG, physical examination, and vital signs. Adverse events were assessed by the investigators with regard to severity (mild, moderate, severe or life-threatening) and the relationship to the study treatment (reasonably or possibly related, not reasonably or possibly related).

Results

Subject demographics

Twenty-six healthy Han Chinese volunteers were recruited and randomized into the phase I clinical study. In the single-dose study, all of the subjects (12 males) completed the 4-way, crossover trial. In the multiple-dose study, 14 subjects (7 males and 7 females) were enrolled, and two subjects withdrew on d 3 due to personal reasons. There were no significant differences among the 26 subjects with regard to age, height, weight, or body mass index (Table 1).

Table 1. Subject demographics, mean±SD (range).

	Single-dose (*n*=12)	Multiple-dose (*n*=14)
Age (year)	28.2±4.8 (24–38)	28.1±5.3 (21–37)
Sex	12 male	7 male, 7 female
Height (cm)	169.9±4.2 (162–178)	166.1±4.5 (160–174)
Weight (kg)	64.6±4.1 (57–71)	58.6±4.1 (52–64)
BMI*	22.4±1.8 (19.3–25.1)	21.0±1.4 (19.1–22.5)

BMI*: body mass index

Single-dose pharmacokinetics

The mean plasma concentration-time curves in 12 healthy Chinese subjects after oral administration of 675, 2025, or 4050 mg calcium *L*-threonate are shown in Figure 2, and the pharmacokinetic parameters are presented in Table 2. The results indicated that *L*-threonate was absorbed rapidly with a

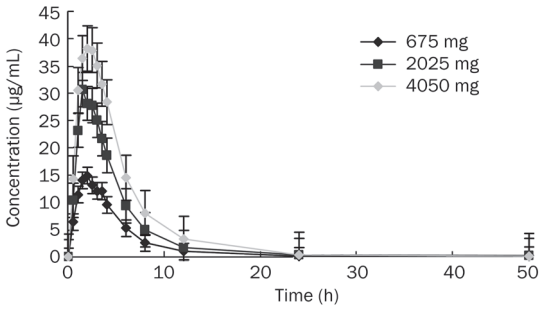

Figure 2. Mean plasma concentration-time curves in healthy Chinese subjects after single oral administration of calcium *L*-threonate 675, 2025, and 4050 mg (*n*=12).

median t_{max} of 2.0 h across all of the dose cohorts. After reaching peak exposure, the plasma disposition of *L*-threonate was also rapid, having a mean $t_{1/2}$ of 2.5 h, which was independent of dose. The mean oral apparent total plasma clearance (*Cl/F*) and V_z/F were 9.8 L/h and 28.9 L, 14.5 L/h, and 53.6 L, and 21.3 L/h and 76.5 L for the 675, 2025, and 4050 mg dose cohorts, respectively. Over the dose range of 675 to 4050 mg, the mean C_{max} increased from 15.5 to 42.8 mg/L and $AUC_{0-\infty}$ increased from 77.7 to 220.9 h·mg/L; however, the 90% CI for the ratio of dose-normalized, geometric mean values of C_{max} and AUC indicated that there was no apparent dose proportionality over the range of 675 mg to 4050 mg (Table 3).

The effect of food intake on the pharmacokinetics of L-threonate was studied in the 2025 mg dose group, in which 12 subjects received calcium *L*-threonate after overnight fasting or breakfast. The results showed that C_{max} and AUC in fed subjects were increased compared to fasted subjects (Figure 3). The mean C_{max} increased from 32.3 to 39.1 mg/L, and the mean $AUC_{0-\infty}$ increased from 152.9 to 203.6 h·mg/L. There was a statistically significant difference between the fasted and fed groups using a paired *t* test ($P<0.05$); therefore, it was concluded that the absorption of *L*-threonate was improved by food intake.

Table 3. 90% CI for the ratio of dose-normalized, geometric mean values of AUC and C_{max}.

	90% CI			
	AUC_{0-t}		C_{max}	
	Mean*	90% CI+	Mean*	90% CI+
675 mg: 2025 mg	1.486	1.276–1.697	1.441	1.300–1.582
4050 mg: 2025 mg	0.701	0.491–0.912	0.658	0.517–0.800
CVw (%)#	30.50%	20.25%		

CI=(A-B)(+/−)*t*_value*sqrt(MSE)*sqrt(1/nA+1/nB), where A–B=mean difference between the treatment A and B under log scale, t_value is the crirical values from t-distribution with degree of freedom of MSE, CVw%(within–subject coefficients of variation)=sqrt(exp(MSE)–1)*100, where MSE is the residual error from ANOVA).

(*)=geometric mean

(+): lower limit–upper limit

(#): within-subject coefficients of variation=sqrt[exp(MSE)–1]×100, where MSE is the residual error from ANOVA

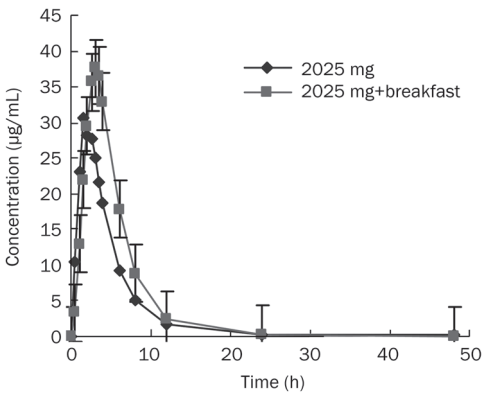

Figure 3. Mean plasma concentration-time curves in healthy Chinese subjects receiving 2025 mg calcium *L*-threonate after overnight fasting or breakfast (*n*=12).

Table 2. Pharmacokinetic parameters of *L*-threonate in healthy Chinese subjects following single oral administration (mean±SD).

	Dose (mg)			
	675 (*n*=12)	2025 (*n*=12)	2025 (fed) (*n*=12)	4050 (*n*=12)
t_{max} (median, h)	2.0±0.5	2.0±0.4	3.0±0.5	2.0±0.7
C_{max} (mg/L)	15.5±4.6	32.3±9.9	39.1±12.0	42.8±15.1
$t_{1/2}$ (h)	2.4±1.3	2.7±0.8	2.3±0.4	2.7±0.6
AUC_{0-t} (mg/L·h)	76.2±30.1	150.1±41.8	199.7±69.5	218.3±90.8
$AUC_{0-\infty}$ (mg/L·h)	77.7±30.7	152.9±42.9	203.6±70.4	220.9±90.0
V_z/F (L)	28.9±6.0	53.6±14.8	37.4±13.6	76.5±22.4
Cl/F (L/h)	9.8±3.3	14.5±4.9	11.4±4.9	21.3±8.7
Cl/r (L/h)	1.0±0.7	0.7±0.5	0.7±0.3	0.8±0.5
Au_{0-t} (mg)	69.8±48.2	84.6±75.7	132.8±62.4	135.5±136.6
Urinary excretion rate (%)	10.30	4.20	6.60	3.30

BMI*: body mass index

Following single administration, urine samples were collected over a period of 24 h. Cumulative urinary excretion of *L*-threonate over the collection interval was 10.3%, 4.2%, and 3.3% of the administered dose of 675, 2025, and 4050 mg, respectively, with a mean renal clearance of 0.8±0.5 L/h.

Multiple-dose pharmacokinetics

The mean plasma concentration-time curves of *L*-threonate in 12 healthy Chinese subjects following multiple-dose administration of 2025 mg calcium *L*-threonate are presented in Figure 4, and the pharmacokinetic parameters are presented in Table 4. Attainment of steady-state was achieved by d 7 because the regression slope of natural logarithmic (ln) transformation of trough concentrations on d 3, 4, 5, and 6 over time was not statistically different from zero. The mean steady-state $t_{1/2}$ was 2.1±0.6 h, which was comparable to the value of a single-dose (2.0±0.7 h). The accumulation index was 1.086 (90% CI, 0.967–1.204) based on AUC_{0-t} and 1.102 (90% CI 1.004–1.2) based on C_{max}, indicating that there was no further accumulation of *L*-threonate after multiple administrations.

Safety evaluation

There were no serious adverse events (AEs) reported in this study. The major adverse event was diarrhea (1/26, 3.8%), which was observed in one subject after administration of 2025 mg calcium *L*-threonate during the single-dose period. This AE was mild, transient, and without fever, nausea or bellyache; the subject recovered without medication or other treatment. No additional AEs were reported in this study. There were no clinically significant changes in laboratory parameters (clinical chemistry, hematology or urinalysis) or vital signs after treatment with calcium *L*-threonate. When compared to baseline values acquired in the screening period, there were no clinically significant changes in the ECG data. Therefore, calcium *L*-threonate was shown to be safe and well tolerated in healthy Chinese subjects.

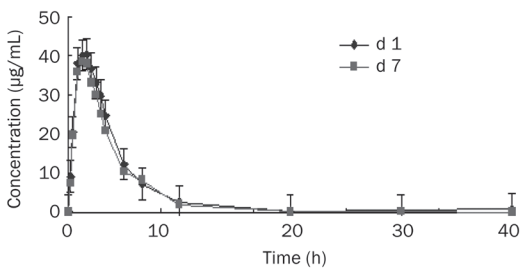

Figure 4. Mean plasma concentration-time curves in healthy Chinese subjects after multiple doses of 2025 mg calcium *L*-threonate (*n*=12).

Table 4. Pharmacokinetic parameters of calcium *L*-threonate in healthy Chinese subjects following multiple-dose of 2025 mg calcium *L*-threonate (mean±SD).

	d 1 (*n*=12)	d 7 (*n*=12)
t_{max} (median, h)	1.6±0.6	1.6±0.4
C_{max} (mg/L·h)	43.8±16.4	47.7±15.3
$t_{1/2}$ (h)	2.1±0.6	2.0±0.7
AUC_{0-t} (mg/L·h)	204.1±88.2	216.2±68.1
$AUC_{0-\infty}$ (mg/L·h)	207.5±87.0	220.4±67.1
V_z/F (L)	34.4±16.5	29.3±10.2
Cl/F (L/h)	12.3±6.6	13.6±3.62
C_{avg} (mg/L)	–	14.6±2.66
AUC_{ss} (mg/L·h)	–	176.0±31.6
DF (%)*		3.1±1.1
$R_{C_{max}}$	–	1.102
R_{AUC}	–	1.086

*: DF, degree of fluctuation.

Discussion

Calcium *L*-threonate is a novel drug developed for the treatment of osteoporosis. In this study, the pharmacokinetics and safety of *L*-threonate in healthy Chinese volunteers were reported for the first time. This study was divided into two parts: single- and multiple-dose studies. In the single-dose study, a 4-way, crossover design was used; 12 male Chinese subjects received 675, 2025, 2025 (after breakfast) or 4050 mg calcium *L*-threonate. It indicated that *L*-threonate was absorbed rapidly, with C_{max} being reached at a median time of 2.0 h. Over the dose range of 675 mg to 4050 mg, the plasma exposure of *L*-threonate increased with dose escalation; however, dose proportionality was not observed. The reason was not clear, but it could be due to the saturate absorption of *L*-threonate. After reaching peak exposure, the disposition of *L*-threonate was rapid, as $t_{1/2}$ ranged from 2.4 to 2.7 h. AUC_{0-t} contributed to over 98% of the total AUC, indicating that a sampling period of 48 h was adequate for assessing plasma exposure of *L*-threonate. Cumulative urinary excretion of *L*-threonate over 24 h represented only 5.9% of the administered dose. Because *L*-threonate is an acidic compound that has hydroxyl and carboxyl groups, we hypothesized that this drug might be eliminated as a conjugated form. However, no phase II metabolites were found in plasma or urine when we screened the samples using a TOF mass spectrometer (QSTAR XL, AB Sciex, USA). Therefore, we hypothesize that *L*-threonate may be involved in the anabolism of other endogenous substances after administration. The metabolic pathway of *L*-threonate is still being investigated in our lab.

In the multiple-dose study, there was no accumulation after repeated doses of 2025 mg twice per day for 4 d. The mean $t_{1/2}$ was similar to that of the single-dose study, indicating that the elimination rate of *L*-threonate did not change during repeated administrations. However, concerning the 2025 mg dose group, AUC and C_{max} in the multiple-dose study were significantly higher than those of the single-dose study (fasted group), approximately 30% higher based on the C_{max} and AUC. A combined total of 24 Chinese subjects (18 male, 6 female) completed this study. Half of the subjects in the multiple-dose group were male (*n*=6), and half were female (*n*=6), whereas all of the subjects (*n*=12) in the single-dose group were male. Therefore, is the difference in AUC and C_{max} between the

single- and multiple-dose studies due to gender effect? Pharmacokinetic parameters (C_{max} and AUC_{0-t}) were compared using subject, gender and period as fixed factors using a three-way ANOVA analysis. This analysis indicated that the differences among subjects and periods were significant ($P<0.01$); however, there was no statistical difference between male and female subjects ($P>0.05$). Therefore, the differences in plasma exposure were due to the study period and individual variation, and not gender.

The safety evaluation during the study demonstrated that calcium *L*-threonate was well tolerated in healthy Chinese volunteers over the studied dose range. The reported AE was diarrhea (1/26, 3.8%), which was possibly due to mannitol, an excipient used in the tablet, increasing the intestinal osmotic pressure. This reported AE was mild and transient; the subject recovered without any medication or further treatment.

In summary, this study demonstrated the single- and multiple-dose pharmacokinetics of calcium *L*-threonate and its safety profile in healthy Chinese volunteers. *L*-threonate was absorbed rapidly and exhibited dose-related plasma exposure. After reaching peak exposure, this drug was quickly cleared from the plasma, but renal excretion was not its major elimination route. The absorption of *L*-threonate was enhanced by food intake, and there was no accumulation after multiple administrations. Calcium *L*-threonate was well tolerated in healthy Chinese volunteers over the studied dose range.

Acknowledgements

This study was supported by JuNeng Pharmaceutical Co (Beijing, China). The authors thank all of the volunteers enrolled in this study. We also thank the staff of the clinical ward and bioanalytical lab of Phase I Unit in Peking Union Medical College Hospital.

Author contribution

Ji JIANG and Pei HU designed the research and revised the manuscript; Hong-yun WANG performed the research, analyzed the data, and wrote the paper.

References

1 Cooper C, Campion G, Melton LJ 3rd. Hip fractures in the elderly: a world-wide projection. Osteoporosis Int 1992; 2: 285–9.
2 Sambrook P, Cooper C. Osteoporosis. Lancet 2006; 367: 2010–8.
3 Reginster JY, Burlet N. Osteoporosis: A still increasing prevalence. Bone 2006; 38: 4–9.
4 Mauck KF, Clarke BL. Diagnosis, screening, prevention, and treatment of osteoporosis. Mayo Clin Proc 2006; 81: 662–72.
5 Thomas M, Hughes RE. A relationship between ascorbic acid and threonic acid in guinea-pigs. Food Chem Toxicol 1983; 21: 449–52.
6 Chamberlin BA, Sweeley CC. Metabolic profiles of urinary organic acids recovered from absorbent filter paper. Clin Chem 1987; 33: 572–6.
7 Thomas M, Hughes RE. Evaluation of threonic acid toxicity in small animals. Food Chem 1985; 17: 79–83.
8 Isbell HS, Frush HL. Oxidation of *L*-ascorbic acid by hydrogen peroxide: Preparation of *L*-threonic acid. Carbohydr Res 1979; 72: 301–4.
9 Fay MJ, Verlangieri AJ. Stimulatory action of calcium *L*-threonate on ascorbic acid uptake by a human T-lymphoma cell line. Life Sci 1991; 19: 1377–81.
10 Fay MJ, Bush MJ, Verlangieri AJ. Effect of aldonic acids on the uptake of ascorbic acid by 3T3 mouse fibroblasts and human T lymphoma cells. Gen Pharmacol 1994; 25: 1465–9.
11 Morton DJ, Barrett-Connor EL, Schneider DL. Vitamin C supplements use and bone mineral density in postmenopausal women. J Bone Miner Res 2001; 16: 135–40.
12 Hall SL, Greendale GA. The relation of dietary vitamin C intake to bone mineral density: results from the PEPI study. Calcif Tissue Int 1998; 63: 183–9.
13 Franceschi RT, Lyer BS. Relationship between collagen synthesis and expression of the osteoblast phenotype in MC3T3-E1 cells. J Bone Miner Res 1992; 7: 235–46.
14 Franceschi RT, Lyer BS, Cui Y. Effects of ascorbic acid on collagen matrix formation and osteoblast differentiation in murine MC3T3-E1 cells. J Bone Miner Res 1994; 9: 843–54.
15 Rowe DJ, Ko S, Tom XM, Silverstein SJ, Richards DW. Enhanced production of mineralized nodules and collagenous proteins *in vitro* by calcium ascorbate supplemented with vitamin C metabolites. J Periodontol 1999; 70: 992–9.
16 He JH, Tong NW, Li HQ, Wu J. Effects of *L*-threonate on bone resorption by osteoclasts *in vitro*. J Sichuan Univ (Med Sc Edi) 2005; 36: 225–8.
17 Wang HY, Jiang J, Hu P. Determination of *L*-threonate in human plasma and urine by high performance liquid chromatography-tandem mass spectrometry. J Chromatogr B 2006; 834: 155–62.
18 Smith BP, Vandenhende FR, DeSante KA, Farid NA, Welch PA, Callaghan JT, *et al*. Confidence interval criteria for assessment of dose proportionality. Pharm Res 2000; 17: 1278–83.